



## Review

# Rayleigh–Taylor and Richtmyer–Meshkov instabilities: A journey through scales<sup>☆</sup>



Ye Zhou <sup>a,\*</sup>, Robin J.R. Williams <sup>b</sup>, Praveen Ramaprabhu <sup>c</sup>, Michael Groom <sup>d</sup>, Ben Thornber <sup>d</sup>, Andrew Hillier <sup>e</sup>, Wouter Mostert <sup>f,g</sup>, Bertrand Rollin <sup>h</sup>, S. Balachandar <sup>i</sup>, Phillip D. Powell <sup>a</sup>, Alex Mahalov <sup>j</sup>, N. Attal <sup>k</sup>

<sup>a</sup> Lawrence Livermore National Laboratory, Livermore, CA, 94550, USA

<sup>b</sup> Atomic Weapons Establishment, Aldermaston, Reading RG7 4PR, UK

<sup>c</sup> Department of Mechanical Engineering and Engineering Science, University of North Carolina at Charlotte, Charlotte, NC 28223, USA

<sup>d</sup> School of Aerospace, Mechanical and Mechatronic Engineering, The University of Sydney, Sydney, Australia

<sup>e</sup> Department of Mathematics, CEMPS, University of Exeter, Exeter, UK

<sup>f</sup> Department of Mechanical and Aerospace Engineering, Princeton University, Princeton, NJ 08544, USA

<sup>g</sup> Department of Mechanical and Aerospace Engineering, Missouri University of Science and Technology, Rolla, MO 65401, USA

<sup>h</sup> Department of Aerospace Engineering, Embry-Riddle Aeronautical University, Daytona Beach, FL 32114, USA

<sup>i</sup> Department of Mechanical and Aerospace Engineering, University of Florida, Gainesville, FL 32611, USA

<sup>j</sup> School of Mathematical and Statistical Sciences, Arizona State University, Tempe, AZ 85281, USA

<sup>k</sup> Convergent Science Inc, Northville, MI 48167, USA

## ARTICLE INFO

## Article history:

Received 8 September 2020

Received in revised form 22 December 2020

Accepted 23 December 2020

Available online 17 February 2021

Communicated by V.M. Perez-Garcia

## Keywords:

Rayleigh–Taylor instability  
Richtmyer–Meshkov instability  
Kelvin–Helmholtz instability  
Turbulence  
Magnetohydrodynamics  
Mixing

## ABSTRACT

Hydrodynamic instabilities such as Rayleigh–Taylor (RT) and Richtmyer–Meshkov (RM) instabilities usually appear in conjunction with the Kelvin–Helmholtz (KH) instability and are found in many natural phenomena and engineering applications. They frequently result in turbulent mixing, which has a major impact on the overall flow development and other effective material properties. This can either be a desired outcome, an unwelcome side effect, or just an unavoidable consequence, but must in all cases be characterized in any model. The RT instability occurs at an interface between different fluids, when the light fluid is accelerated into the heavy. The RM instability may be considered a special case of the RT instability, when the acceleration provided is impulsive in nature such as that resulting from a shock wave. In this pedagogical review, we provide an extensive survey of the applications and examples where such instabilities play a central role. First, fundamental aspects of the instabilities are reviewed including the underlying flow physics at different stages of development, followed by an overview of analytical models describing the linear, nonlinear and fully turbulent stages. RT and RM instabilities pose special challenges to numerical modeling, due to the requirement that the sharp interface separating the fluids be captured with fidelity. These challenges are discussed at length here, followed by a summary of the significant progress in recent years in addressing them. Examples of the pivotal roles played by the instabilities in applications are given in the context of solar prominences, ionospheric flows in space, supernovae, inertial fusion and pulsed-power experiments, pulsed detonation engines and Scramjets. Progress in our understanding of special cases of RT/RM instabilities is reviewed, including the effects of material strength, chemical reactions, magnetic fields, as well as the roles the instabilities play in ejecta formation and transport, and explosively expanding flows. The article is addressed to a broad audience, but with particular attention to graduate students and researchers who are interested in the state-of-the-art in our understanding of the instabilities and the unique issues they present in the applications in which they are prominent.

© 2021 Elsevier B.V. All rights reserved.

## Contents

1. Introduction.....	3
----------------------	---

<sup>☆</sup> Contains material copyright by the UK Ministry of Defence © Crown Owned Copyright 2020/AWE.

\* Corresponding author.

E-mail address: [yezhou@llnl.gov](mailto:yezhou@llnl.gov) (Y. Zhou).

2. Fundamental equations.....	4
3. Analytical models of single-mode linear instability growth.....	5
3.1. The classical Rayleigh–Taylor problem .....	5
3.2. From RTI to RMI: Linear stability .....	7
3.3. Vorticity paradigm .....	7
4. Instability development from multi-modal perturbations: linear through turbulent regimes.....	8
4.1. Linear regime .....	8
4.2. Nonlinear regime .....	9
4.3. Mix measures .....	10
4.4. Mixing transition criteria.....	12
4.5. The minimum state .....	12
4.6. Turbulent flows.....	13
5. Numerical methods and formulations .....	14
5.1. Trade-off between tractability and complexity.....	14
5.2. Compressible formulations .....	15
5.3. Incompressible formulations .....	16
5.3.1. Variable density.....	16
5.3.2. Boussinesq approximation .....	17
5.4. Interface tracking.....	18
6. State of the art in numerical simulations .....	19
6.1. Direct numerical simulation.....	19
6.2. Large eddy simulation.....	20
6.2.1. Explicit subgrid modeling .....	21
6.2.2. Implicit subgrid modeling .....	21
7. Effects of material strength on RT instabilities .....	23
7.1. Preliminary remarks .....	23
7.2. Experimental Rayleigh–Taylor strength platform .....	23
7.3. Material strength models .....	24
7.3.1. Steinberg–Guinan model .....	25
7.3.2. Steinberg–Guinan–Lund model .....	25
7.3.3. Other material models .....	25
7.4. Inferring material strength through hydrodynamic simulation .....	25
8. Ejecta.....	26
8.1. Surface ejecta physics .....	28
8.2. Spike formation.....	28
8.3. Particle formation .....	31
8.3.1. Primary breakup .....	31
8.3.2. Secondary breakup and atomization .....	31
8.3.3. Experimental particle sizing .....	31
8.4. Modeling .....	31
8.4.1. Direct simulation .....	31
8.4.2. Particle transport .....	32
9. Reactive flows .....	32
9.1. Preliminary .....	32
9.2. Applications .....	33
9.3. Flame physics .....	34
9.4. RM flames .....	36
9.5. RT flames .....	38
9.6. Concluding remarks .....	39
10. Explosively expanding single and multiphase flows .....	39
10.1. Preliminary remarks .....	39
10.2. Some examples of explosives flows .....	40
10.3. Phenomenology of explosively driven flows .....	41
10.4. Simulations of RT and RM instabilities .....	42
10.4.1. Single phase flows .....	42
10.4.2. Multiphase flows .....	43
10.5. Experiments of RT and RM instabilities .....	44
10.6. Summary .....	45
11. Magnetohydrodynamics: Governing equations .....	45
12. The magnetic Rayleigh–Taylor instability .....	47
12.1. Studying the magnetic Rayleigh–Taylor instability in an incompressible 2D model .....	47
12.1.1. Lagrangian displacements in linear MHD .....	47
12.1.2. Derivation of the dispersion relation .....	48
12.2. Beyond 2D – the role of 3D effects and additional physics .....	49
12.2.1. Variations in the direction of the magnetic field at the interface .....	49
12.2.2. Role of magnetic diffusion .....	49
12.2.3. Compressibility .....	50
12.3. The nonlinear phase of the magnetic Rayleigh–Taylor instability .....	50
12.4. MHD extensions to the self-similar mixing model .....	51
13. The magnetic Richtmyer–Meshkov instability .....	51
13.1. Shock waves .....	51

13.2.	The RM instability in MHD.....	52
13.2.1.	Suppression of the instability.....	52
13.3.	Magnetic field amplification in the MHD RM and RT.....	55
13.4.	Beyond ideal MHD.....	56
14.	RT instability in solar prominences .....	57
14.1.	Prominences and their dynamics.....	57
14.2.	Prominence plumes as observational evidence of the magnetic RTI.....	59
14.3.	Linear and nonlinear modeling of prominence plumes.....	59
14.3.1.	Linear behavior.....	59
14.3.2.	Theoretical developments connected to prominence plume observations.....	60
14.3.3.	Nonlinear modeling.....	60
14.4.	Discussion and outlook.....	61
15.	Space physics: Ionospheric flows .....	62
15.1.	Equatorial spread F.....	62
15.2.	Spacecraft and general circulation model data.....	63
15.3.	Nested simulation studies .....	64
15.4.	Challenges .....	65
16.	Z-pinch, pulsed-power experiments and other applications .....	67
16.1.	Z-pinch .....	67
16.2.	Supernovae .....	68
16.3.	Inertial fusion .....	69
17.	Conclusion .....	69
	Declaration of competing interest .....	70
	Acknowledgments .....	70
	Appendix A. Surfaces of discontinuity .....	70
	Appendix B. Definitions .....	71
B.1.	Abbreviations .....	71
B.2.	Notations .....	71
B.3.	Symbols .....	71
	References .....	73

## 1. Introduction

The Rayleigh–Taylor (RT) and Richtmyer–Meshkov (RM) instabilities are canonical fluid dynamic phenomena which are readily observed in several engineering applications and natural situations [1–3]. They occur when a corrugated boundary, or interface separating two different fluids of different properties,<sup>1</sup> is subjected to either a gradual (RT) or sudden, impulsive (RM) acceleration. RT is most familiarly seen on Earth when a heavier fluid is placed on top of a lighter fluid; gravity destabilizes the interface separating the fluids resulting in the growth of imposed perturbations and ultimately culminating in vigorous turbulent mixing. More generally, the RT instability occurs when a lighter fluid is accelerated into a heavier fluid or conversely when a heavier fluid is decelerated by a lighter fluid. Where RT instability is the result of a constant acceleration, the RM instability corresponds to the case of impulsive acceleration of an interface. A typical example of the RM instability is that of a shock wave traveling through such an interface. The shock *impulsively* accelerates the interface, which in turn becomes unstable.

RT instability was first described and analyzed by Lord Rayleigh [4] and subsequently by G.I. Taylor in 1950 [5]. Perturbations present at the interface are amplified by the baroclinic vorticity ( $\frac{1}{\rho^2} \nabla p \times \nabla \rho$ ) deposited as a result of the misalignment between the pressure gradient and the local density gradient. Generally, the evolution of an RT unstable fluid–fluid interface can be decomposed into three regimes: (i) the linear phase in which the amplitude of the interfacial perturbation grows exponentially and is obtained from a linearization of the perturbation equations; (ii) the non-linear phase which is marked by saturation of the amplitudes, and the appearance of the characteristic mushroom shapes; (iii) the late-time development characterized

by a wide range of scales and intense turbulent mixing. The evolution of RM instability follows a similar path, but the linear stage is marked by perturbation amplitudes that grow *linearly* in time. The structures formed by the light fluid penetrating into the heavy fluids are termed bubbles, while the structures formed by the heavy fluid penetrating into the light fluid are called spikes, as nonlinear mode interactions tend to broaden intrusions of light material into heavy and sharpen intrusions of heavy into light.

The RM instability follows the passage of a shock wave across a perturbed interface between two fluids of different densities [6,7], and can be treated as an impulsive analogue of the RT instability. A major distinction between the two instabilities is that a perturbed interface between two fluids of different densities is RM unstable, regardless of the direction of shock wave propagation (i.e. shocks originating in either the light or the heavy fluid can lead to instability), whereas the interface is RT unstable only when the acceleration is directed toward the heavy fluid (e.g., [8]). This aspect is relevant to physical phenomena that arise during the interaction between the shock and the material interface, which are also included in the later sections, e.g. Sections 9 and 10. As with RT, the instability typically proceeds via linear and nonlinear stages, until the fluids eventually become subject to turbulent mixing.

The RT and RM instabilities feature in some of the most dramatic phenomena in the universe. Accounting for them and the hydrodynamic mixing they induce is crucial for understanding supernova dynamics [9–13], and consequently the behavior of exploded star material (supernova remnants, or SNRs) moving into the interstellar medium long after the initial catastrophe [14]. Such instabilities also feature strongly in extreme applications in engineering, most notably in inertial nuclear fusion. RT and RM instabilities have been identified as two of the main impediments to the achievement of net energy gain in inertial confinement fusion (ICF) efforts [15–17]. Indeed, hydrodynamic instability in general is a key concern in all forms of nuclear fusion, as any textbook on plasma physics will attest (see for example, and

<sup>1</sup> We use “properties” here to allow for density variations that were not present initially, but could arise due to (for example) a shock interaction.

appropriately for this article, the volumes by Goedbloed and Poedts [18] and Goedbloed, Keppens, and Poedts [19]). Similarly, RT has also been observed to occur in geological flows, where it is an example of this instability in solids (e.g., [20]) and in magma mushes (see, for example, [21]).

While the focus of this article is on flows driven by RT and RM instabilities, it is also important to note the role played by the Kelvin–Helmholtz (KH) [22,23] instability here as it is often the mechanism that underlies mixing in RTI and RMI flows, as a result of the shear between the growing bubble and spike structures. Note that the RT, RM, and KH instabilities are frequently collectively termed *hydrodynamic instabilities*.

Fundamentally, these instabilities rely on the existence of a source of free energy which can drive the growth of perturbations at an interface beyond the ability to be restrained by any relevant restoring forces. The sources of free energy for the above instabilities differ: (i) for RT instability, the source is from gravitational forces (or, equivalently, surface acceleration) which tend to drive flows where denser material falls through lighter material which might otherwise support it, displacing the lighter material into buoyant bubbles. (ii) The RM instability is an impulsive analog of the RT instability, in which a sudden intense acceleration, such as a shock, sets the material in motion, and this induced motion continues once the acceleration ceases. (iii) In KH instability, by contrast, the source of free energy is the tangential relative motion between the two components across a shearing surface. This instability is familiar as the source of ocean waves, for example.

The process just described can, however, be stalled at any stage through the action of dissipative or restoring forces. For KH instability, the action of a stabilizing gravitational force can lead to the wave amplitude growing very slowly, if at all. For all the above instabilities, viscosity [24–27], surface tension [28–30], material strength [31,32], rotation [33–36], and magnetic fields [37] can act to stifle growth, or in some cases completely arrest perturbation growth.

As will quickly become evident in this article, RT, RM and KH instabilities manifest themselves in an extremely wide variety of physical systems [1–3]. While these physical systems may vary in their detail, some fundamental principles are shared in common. Here, we seek to outline this fundamental physics, to provide a common framework in which the instabilities and the systems in which they occur can be described, and from which more detailed, system-specific analyses can be developed.

There are two major issues that this survey attempts to tackle: First, the pace of high-quality publications in this area is simply too rapid with outputs from vast and diverse scientific and engineering disciplines, with thousands of manuscripts appearing each year. While this phenomenon is a testament to the vibrancy and richness of the field, it has also elevated the barriers to entry for scientists, engineers, and applied mathematicians who are setting out to undertake research in these areas. There is thus a pressing need to alleviate this challenge by offering a repository of significant findings that reflect the current state of the art in these areas.

Second, while supernovae [10,12,13,38] and inertial confinement fusion [15,16,39] are often almost exclusively discussed as two prime examples of the applications of hydrodynamic instabilities, several other equally important (and interesting) applications in natural and engineering flows are less familiar and have attracted relatively limited attention. This work endeavors to rectify this gap, and elevate these key applications to the attention of a broad and heterogeneous audience.

This pedagogical review starts with fundamental and general descriptions of the RT, RM, and KH instabilities, describing in detail the different stages in their time-dependent development. This is followed by a review of progress, along with the challenges in numerically solving the problem, with emphasis on

the turbulent phase. The review is then extended to include discussions of more complicated and relevant settings for RT and RM instabilities in applications – chemically reactive and explosively expanding flows, MHD flows, flows with material strength, ejecta, space plasma and astrophysics, etc. Readers that are interested in exploring specific topics in greater detail will also benefit from the comprehensive list of papers included in the bibliography. This tutorial is written keeping in mind the needs of a broad audience, spanning graduate students who are setting out in this field, engineers tackling a specific aspect associated with these flows, or researchers seeking to identify fruitful directions of potential research in these areas.

In what follows, we will describe more fully the mathematical formulation of the instability growth problem, the computational models which may be applied to them, and numerous practical and experimental examples of interfacial instability growth phenomena. In the next section, we first describe the mathematical formulation which must underlie an understanding of these flows.

## 2. Fundamental equations

The underlying governing equations of fluid dynamics are the dynamical equations for the trajectories of the tracers from which the fluid is constituted, together with the evolution equations of fields to which the tracers are coupled. However, typically it is neither useful nor practical to describe the properties of a fluid at such microscopic detail, so the equations are reduced by statistical averaging. In this paper we focus on flows where the fluids may be represented as a continuum. As a first step, the equations for the trajectories of the individual tracers are averaged over an ensemble to generate the collisional Boltzmann equation for the evolution of the tracer's probability density function (pdf)  $f(\mathbf{x}, \mathbf{v}, t)$  as a function of time  $t$  in a six-dimensional phase space of spatial position,  $\mathbf{x}$ , and velocity  $\mathbf{v}$ . Then a hierarchy of equations can be derived for the velocity moments of this probability density function, such as the density and velocity

$$\rho = \int \mu_m f(\mathbf{x}, \mathbf{v}, t) d\mathbf{v}, \quad (1)$$

$$\rho \mathbf{u} = \int \mu_m f(\mathbf{x}, \mathbf{v}, t) \mathbf{v} d\mathbf{v}, \quad (2)$$

where  $\mu_m$  is the molecular mass. Often the conservation equations for mass, momentum (i.e., Newton's second law) and energy (see, e.g., [40])

$$\frac{\partial \rho}{\partial t} + \nabla \cdot (\rho \mathbf{u}) = 0, \quad (3)$$

$$\frac{\partial}{\partial t} (\rho \mathbf{u}) + \nabla \cdot (\rho \mathbf{u} \mathbf{u}) = \nabla \cdot \boldsymbol{\sigma} + \mathbf{f}_b, \quad (4)$$

$$\frac{\partial}{\partial t} (\rho E) + \nabla \cdot (\rho \mathbf{u} E) = \nabla \cdot (\boldsymbol{\sigma} \cdot \mathbf{u} + \mathbf{q}) + \mathbf{f}_b \cdot \mathbf{u} \quad (5)$$

are chosen as a suitable model, as these are sufficient to capture local thermodynamic equilibrium. Here, the specific total energy  $E$ , is given by  $E = e + \frac{1}{2}u^2$ , where  $e$  is the specific internal energy. The Cauchy stress tensor  $\boldsymbol{\sigma}$  and energy flux  $\mathbf{q}$  capture the effects of both inter-particle forces and higher moments of the pdf than the mass, momentum and energy, and must be provided either by evolution equations for these higher-order statistics, or through an empirical closure. We have also included an applied body force  $\mathbf{f}_b$ , specified per unit volume. These equations may be augmented by additional conservation equations for species densities, electromagnetic fields, etc., with additional source terms for processes such as species diffusion and resistivity.

For a continuous flow, the momentum conservation equation can be written as

$$\rho \frac{D\mathbf{u}}{Dt} = \nabla \cdot \boldsymbol{\sigma} + \mathbf{f}_b. \quad (6)$$

The *advective* or *material derivative*  $D/Dt = \partial/\partial t + \mathbf{u} \cdot \nabla$  represents the rate of change of a local variable due to both the intrinsic time dependence of the variable, and the differential flow rate of the variable into a particular point owing to its spatial gradient. The first term on the right side of Eq. (6) represents the net force per unit volume on a fluid element due to internal stresses. This Cauchy stress term can be separated into isotropic and anisotropic components

$$\boldsymbol{\sigma} = -p\mathbf{I} + \boldsymbol{\tau}, \quad (7)$$

where  $p = \sigma_{ii}/3$  and  $\tau_{ii} = 0$ . The tensor  $\boldsymbol{\tau}$  corresponds to *shearing*, or *tangential* stresses, and is often referred to as the *deviatoric stress tensor*. The simplest, most common, and (fortunately) widely applicable form for the deviatoric stress tensor is one that is linear in the velocity gradients:  $\tau_{ij} = A_{ijkl}\partial u_k/\partial r_l$ . An isotropic fluid for which this approximation holds is known as a *Newtonian* fluid, in which case Eq. (6) becomes the Navier–Stokes equations [41–44]

$$\rho \frac{D\mathbf{u}}{Dt} = -\nabla p + \nabla \cdot \left[ 2\mu \left( \mathbf{S} - \frac{1}{3} (\nabla \cdot \mathbf{u}) \mathbf{I} \right) \right] + \nabla [\zeta (\nabla \cdot \mathbf{u})] + \mathbf{f}_b, \quad (8)$$

where  $\mu$  is the shear viscosity and  $\mathbf{S}$  is the symmetric strain rate tensor

$$\mathbf{S} = \frac{1}{2} (\nabla \mathbf{u} + (\nabla \mathbf{u})^T). \quad (9)$$

We have written Eq. (8) in a form applicable to compressible and variable-density flows, as these are considered widely in this paper, and included the term containing the bulk viscosity  $\zeta$ .

The Navier–Stokes statement of momentum conservation is supplemented with that of mass conservation, which takes the form of a *continuity* equation. In the general case of three-dimensional flows, Eqs. (3) and (5) represent four equations in five unknowns ( $\rho$ ,  $p$ , and the three components of  $\mathbf{u}$ ). The final and “closing” equation is provided by the fluid’s *equation of state*, which specifies the pressure in terms of the density and internal energy of the fluid:

$$p = p(\rho, e). \quad (10)$$

It is not necessary to integrate the energy equation in a number of physically-relevant limits, such as incompressible flow (when the material speed is small relative to the speed of sound), isothermal flow (when the material temperature is maintained constant for example by radiative energy losses), or isentropic flow, which will apply in the absence of shocks and allows the effects of gradual expansion or compression of the fluid to be treated.

### 3. Analytical models of single-mode linear instability growth

In this section, we provide a formal introduction of single-mode linear stability theory for RT instabilities, a treatment of RM linear growth as a special case, and a reinterpretation of these results through a vorticity paradigm. When the amplitude of surface perturbations is significantly than the wavelength, the resulting flows may be treated as a linear superposition of independent Fourier single modes. The next section will use this as a basis for more complete models which extend into the nonlinear regime. We note certain deviations from the idealized classical problem and the impact these “real life” fluid and material properties have on the RTI.

#### 3.1. The classical Rayleigh–Taylor problem

The classical RT problem consists of two semi-infinite incompressible ( $\nabla \cdot \mathbf{u} = 0$ ) and inviscid ( $\mu = 0$ ) fluids in a gravitational field (see Fig. 2), with the denser fluid at a higher gravitational potential [4]. The question posed is then: *how does an arbitrarily small perturbation to the fluid interface evolve from a static initial condition?*

The key to solving the classical RT problem is to first expand the governing equations about the static initial condition, then to linearize the system by considering small deviations in  $\rho$ ,  $p$ , and  $\mathbf{u}$ . In this approach, the governing equations are written for a system which is varied from some equilibrium state by a small perturbation. The smallness of the perturbation allows one to neglect high-order terms in the governing equations, thereby linearizing the equations and simplifying the analysis. The linearized equations are then solved for the growth of perturbations, to determine whether the perturbations will grow or decay in time; that is, whether the system will return to equilibrium (stable), or depart from it (unstable). In fact, the vanishing derivatives of  $\rho$  in the bulk of either fluid (i.e., anywhere *except* at the two-fluid interface) reduce the continuity equation to

$$\nabla \cdot \mathbf{u} = 0. \quad (11)$$

Further, continuity of the velocity field requires that while this condition is derived away from the fluid interface, it must nonetheless be maintained there. However, the density discontinuity at the interface means that its derivatives certainly *cannot* be ignored there. Thus, expanding about the unperturbed state ( $\rho = \rho_0$ ,  $\mathbf{u} = \mathbf{0}$ ) by writing  $\rho = \rho_0 + \delta\rho$ , we find to the lowest order in the perturbation variables

$$\frac{\partial(\delta\rho)}{\partial t} + u_z \frac{\partial\rho_0}{\partial z} = 0. \quad (12)$$

For the following equations, we have adopted Cartesian coordinate system for convenience and selected  $z$  as  $n$ , the direction normal to the interface.

The Navier–Stokes equations reduce in the present case to the Euler equations with  $\mathbf{f}_b = -\rho g \hat{\mathbf{z}}$  [45]:

$$\rho \frac{D\mathbf{u}}{Dt} = -\nabla p - \rho g \hat{\mathbf{z}}, \quad (13)$$

where the constant gravitational field is taken to point along  $-\hat{\mathbf{z}}$ . Expanding about the unperturbed state (now also writing  $p = p_0 + \delta p$ ), requiring the resulting equations to be satisfied for the unperturbed equilibrium and writing to first order in the perturbed variables ( $\delta\rho$ ,  $\delta p$ ,  $\mathbf{u}$ ) yields

$$\nabla p_0 + \rho_0 g \hat{\mathbf{z}} = 0, \quad (14)$$

$$\rho_0 \frac{\partial \mathbf{u}}{\partial t} + \nabla(\delta p) + (\delta\rho)g \hat{\mathbf{z}} = 0. \quad (15)$$

The  $\mathcal{O}(1)$  equation produces the usual result for hydrostatic pressure in a fluid,

$$p_0(z) = p_0(0) - \rho_0 g z, \quad (16)$$

while the next order equation of perturbation expansion constitutes the linearized Navier–Stokes equations for the Rayleigh–Taylor problem.

Fourier transforming Eqs. (11), (12), and (15) in  $x$ ,  $y$ , and  $t$ , then algebraically eliminating  $u_x$ ,  $u_y$ ,  $\delta p$ , and  $\delta\rho$  yields

$$\frac{\partial}{\partial z} \left( \rho_0 \frac{\partial u_z}{\partial z} \right) - k_r^2 \rho_0 u_z = \frac{k_r^2 g}{\omega^2} \frac{\partial \rho_0}{\partial z} u_z, \quad (17)$$

where  $k_x$ ,  $k_y$ , and  $\omega$  are the Fourier transform variables corresponding to  $x$ ,  $y$ , and  $t$ , respectively, and  $k_r^2 = k_x^2 + k_y^2$ . In the

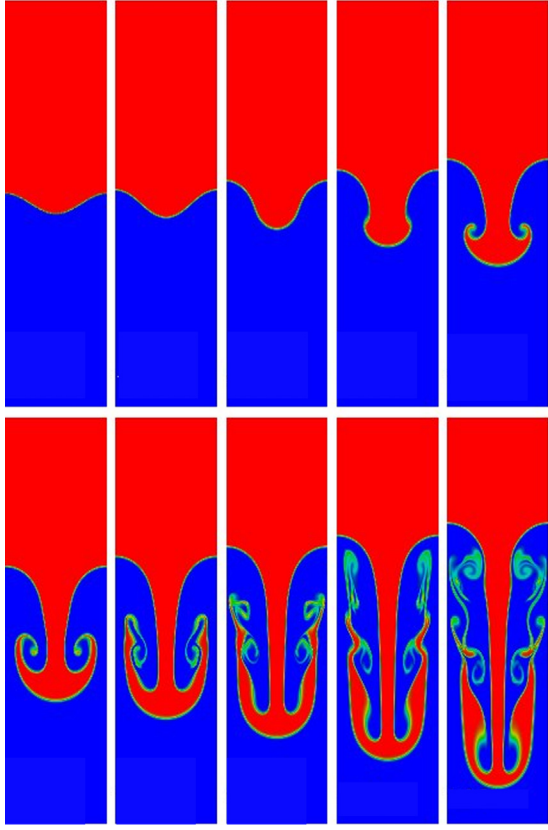


**Fig. 1.** Simulation of the classical Rayleigh-Taylor instability in a two fluid system. During the linear phase of growth (roughly the first three panels), the interface amplitude grows exponentially. As the system transitions to the non-linear regime, it develops the characteristic “bubbles and spikes” shown clearly in the fourth, fifth and sixth panels. Finally, as the perturbation evolves further, turbulence develops as shown in the seventh and subsequent panels [46]. Reproduced with permission. ©Elsevier.

bulk of either fluid, we have  $\partial\rho_0/\partial z = 0$ , so that Eq. (17) reduces to

$$\frac{\partial^2 u_z}{\partial z^2} - k_r^2 u_z = 0, \quad (18)$$

which admits the solution

$$u_z(z) = u_{z0} e^{-k_r |z|}, \quad (19)$$

where  $u_{z0}$  is a constant and we have imposed both continuity of  $u_z$  at the interface  $z = 0$ , as well as the boundary condition that  $u_z$  remains finite as  $z \rightarrow \pm\infty$ . In order to determine the dispersion relation  $\omega = \omega(k_r)$ , we next integrate Eq. (17) across the interface to obtain

$$\left[ \rho_0 \frac{\partial u_z}{\partial z} \right] = \frac{k_r^2 g}{\omega^2} [\rho_0] u_z(0). \quad (20)$$

Finally, substituting Eq. (19) into this expression yields the result

$$\omega = \sqrt{\left( \frac{\rho_1 - \rho_2}{\rho_1 + \rho_2} \right) k_r g}, \quad (21)$$

where  $\rho_1$  and  $\rho_2$  are the “bottom” and “top” fluid densities, respectively. Thus, we find that if  $\rho_1 > \rho_2$  (the denser fluid is on the bottom) then  $\omega$  is real and the system is stable, while if  $\rho_1 < \rho_2$  (the denser fluid is on top) the frequency is imaginary and the velocity grows exponentially in time,  $u_z(t) = u_z(0)e^{st}$ ,

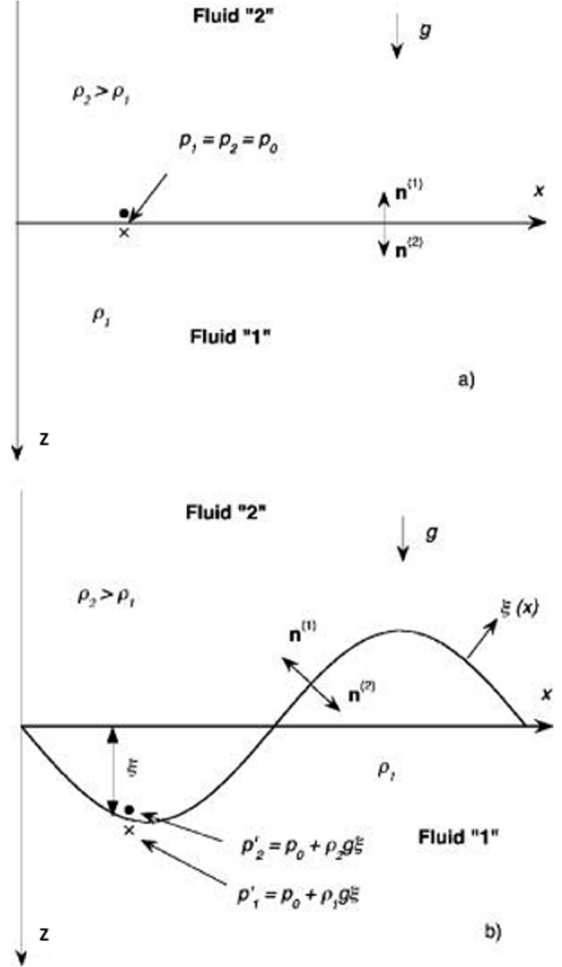


**Fig. 2.** Diagram of the RT interface between the fluids: (a) planar interface in equilibrium, (b) perturbed interface. [47]. Reproduced with permission. ©AAPT.

with a growth rate  $s = i\omega$ :

$$s = \sqrt{k_r g \mathcal{A}} \quad \mathcal{A} = \frac{\rho_2 - \rho_1}{\rho_1 + \rho_2}, \quad (22)$$

where  $\mathcal{A}$  is known as the *Atwood number* of the system (In this scenario, we say that the light fluid is being accelerated into the heavy fluid).

Clearly,  $s$  is either pure real or pure imaginary. The latter possibility indicates oscillation around equilibrium i.e. neutral stability. The former indicates instability. A few general observations may be made regarding the classical Rayleigh-Taylor problem, which will prove useful as we move to consider more general cases of instability. First, shorter wavelength perturbations are more unstable (grow faster) than longer ones since  $s \propto \sqrt{k_r} = \sqrt{2\pi/\lambda}$ . Second, the degree of instability increases with the external pressure gradient, which in the classical case is supplied by the gravitational field,  $g$ . Third, the degree of instability increases with the Atwood number, which ranges between 0 for fluids of equal density, and 1 for a light fluid of vanishing density. Thus, the greater the density contrast between the fluids, the stronger the instability.

It is important to note that the analysis developed in this section is predicated on the validity of the linearization of the Navier-Stokes equations: the so-called *linear regime* of the RT instability. In particular, the interface amplitude and velocity must be small compared to the natural scales of the problem, the

wavelength  $\lambda$  and  $\sqrt{\lambda g}$ , respectively. When this approximation breaks down the system transitions to the *non-linear* regime, in which the characteristic “bubble and spike” pattern develops as a manifestation of the higher harmonics which were previously neglected, as shown in the later frames of Fig. 1.

### 3.2. From RTI to RMI: Linear stability

We now elaborate the results for the RT instability in greater detail, and make connections to the RM instability. As shown above, the RT instability predicts exponential growth rate of perturbations in the linear phase of the instability, which increases with the perturbation wavenumber  $\tilde{k}$ , ( $\equiv k_r$ ). It is sometimes written as an equation of motion for the interface perturbation amplitude  $a(t)$ ,

$$\frac{d^2a(t)}{dt^2} = \tilde{k}ga(t)\mathcal{A}, \quad (23)$$

whose solutions are exponential functions of  $t$ .

More generally and in many practical applications, RT can occur under any time-dependent acceleration of the interface  $g(t)$ ; constant gravitational acceleration is just a convenient special case. In the case where the acceleration  $g(t) = \Delta u \delta(t)$  (i.e. applied instantaneously at  $t = 0$ ) on an initial amplitude of  $a_0$ , such that  $\int g(t)dt = \Delta u$  is the velocity imparted by the impulse, we can immediately integrate Eq. (23) to get,

$$\frac{da}{dt} = \tilde{k}a_0\Delta u\mathcal{A}. \quad (24)$$

Richtmyer first derived the compressible perturbed equations and determined that the  $\mathcal{A}$  and  $a_0$  terms on the right hand of Eq. (24) must take their post-shock values. Here, the impact of compressibility can then be separated from that of nonlinear and multi-modal growth treated in the following sections and given its due emphasis. Hereafter, the + signs will be introduced to indicate post-shock quantities. This means that  $\mathcal{A}^+$  is calculated using the post-shock compressed densities  $\rho_2^+$  and  $\rho_1^+$ , while  $a_0^+ = (1 - \Delta u/U_s)a_0$  where  $U_s$  is the velocity of the incident shock wave. This introduces another key non-dimensional parameter, the Mach number  $M$  which governs compressibility effects (properties of shock waves and discontinuities are discussed in detail in the Appendix). The Mach number  $M_s$  of the incident shock appears implicitly in Eq. (27) through the mean compression rate (the factor that pre-multiplies  $a_0$ ) and the induced velocity, hence modifying the growth rate. Additionally, Mach numbers defined based on the mean velocity of the interface and perturbation growth rate are also useful in characterizing compressibility effects in both RT and RM mixing layers [48]. Flows with Mach numbers significantly greater than one exhibit fundamentally different behaviors from the incompressible case, and must be described using modified governing equations and numerical methods.

It should be stressed that this is an approximation based on incompressibility and impulsiveness of the applied acceleration, and other formulae have been suggested (among others, see for example, Meyer-Blewett [49] and Vandenboomgaerde [50]) that provide better agreement with experimental data in certain circumstances.

The above equation reveals an amplitude growth rate that is linear in time rather than an exponential, and in fact constitutes the RM instability. While the RM instability canonically involves a shock-interface interaction (Fig. 3), and hence compressible bulk fluids, the growth rate in the linear phase closely approximates the incompressible, impulsive solution at early times in many practical applications [6].

Linear stability analysis generally has the limitation that it becomes inconsistent at later times (or when the perturbation has a

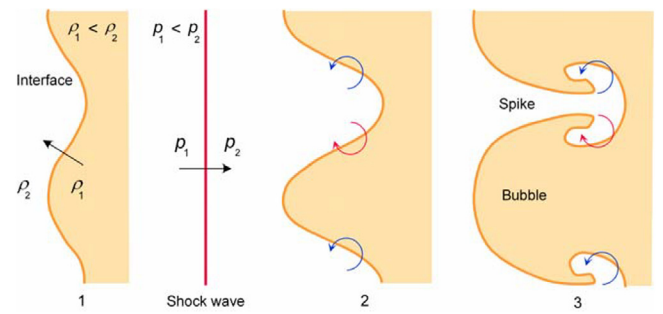


**Fig. 3.** The three initial stages in the evolution of the RM instability are (from top): Initial perturbation before shock interaction, vorticity deposited by shock interaction causing instability growth and bubble/spike configuration when significant roll-up has occurred. Figure 1 of [51] with color added by [52]. With permission from Shock Waves, ©Springer.

finite initial amplitude); eventually the perturbation grows large enough to invalidate the linearizing assumption, and nonlinear effects begin to dominate (when  $k_r a(t) > 1$ ). The characteristic bubble-spike configurations of RT, and the mushroom-shapes in RM instability, are due to the effects of higher harmonics which come into effect beyond the range of validity of the linear analysis. In the case of RT and RM instabilities in particular, the linear growth phase may be very short-lived (and thus the utility of linear theory limited) in experiments and applications, which evolve from finite amplitude (rather than infinitesimal) perturbations. In the next subsection, we briefly describe an alternative way to interpret the RT and RM instabilities that provides additional physical insight.

### 3.3. Vorticity paradigm

The *vorticity paradigm* provides a physically intuitive perspective, which is useful in understanding the evolution of the RT and RM instabilities [53]. Vorticity ( $\mathbf{w} = \nabla \times \mathbf{u}$ ) [54] that is localized to a density interface, will lead to interface perturbation growth under the influence of the induced velocity.

In a compressible, viscous fluid, the vorticity equation can be obtained by taking the curl of Eq. (8), [55]:

$$\begin{aligned} \frac{\partial \mathbf{w}}{\partial t} + \mathbf{u} \cdot \nabla \mathbf{w} &= \mathbf{w} \cdot \nabla \mathbf{u} - \mathbf{w}(\nabla \cdot \mathbf{u}) + \frac{1}{\rho^2}(\nabla \rho \times \nabla p) \\ &+ \frac{\mu}{\rho^2}(\nabla \rho \times \nabla \times \mathbf{w}) - \frac{4\mu}{3\rho^2}(\nabla \rho \times \nabla(\nabla \cdot \mathbf{u})) + \frac{\mu}{\rho}\nabla^2 \mathbf{w} \\ &+ \left( \nabla \times \left[ \frac{1}{\rho} \left( -\frac{2}{3}(\nabla \cdot \mathbf{u})(\nabla \mu) \right) \right] \right. \\ &\left. + 2(\nabla \mathbf{u}) \cdot (\nabla \mu) + (\nabla \mu) \times \mathbf{w} \right]. \end{aligned} \quad (25)$$

The left-hand side of Eq. (25) is the rate of change of vorticity in a Lagrangian packet of fluid; the first term on the right describes the stretching of vorticity by the velocity; the second describes dilation of vorticity by the compressible flow; and the third term is the *baroclinic* generation term. The fourth to last terms on the right describe the effect of viscosity and particularly variable viscosity in the last term. These viscous terms may be non-negligible in general flows [55]. While shock waves – agents of the RM instability – occur in compressible flows, and physically involve strong gradients in fluid viscosity over very short length scales, it is the third, baroclinic term in Eq. (25) which is most pertinent to our immediate discussion of the RT and RM instabilities. In particular, if the pressure and density gradients at a point are not directionally aligned, then the baroclinic term

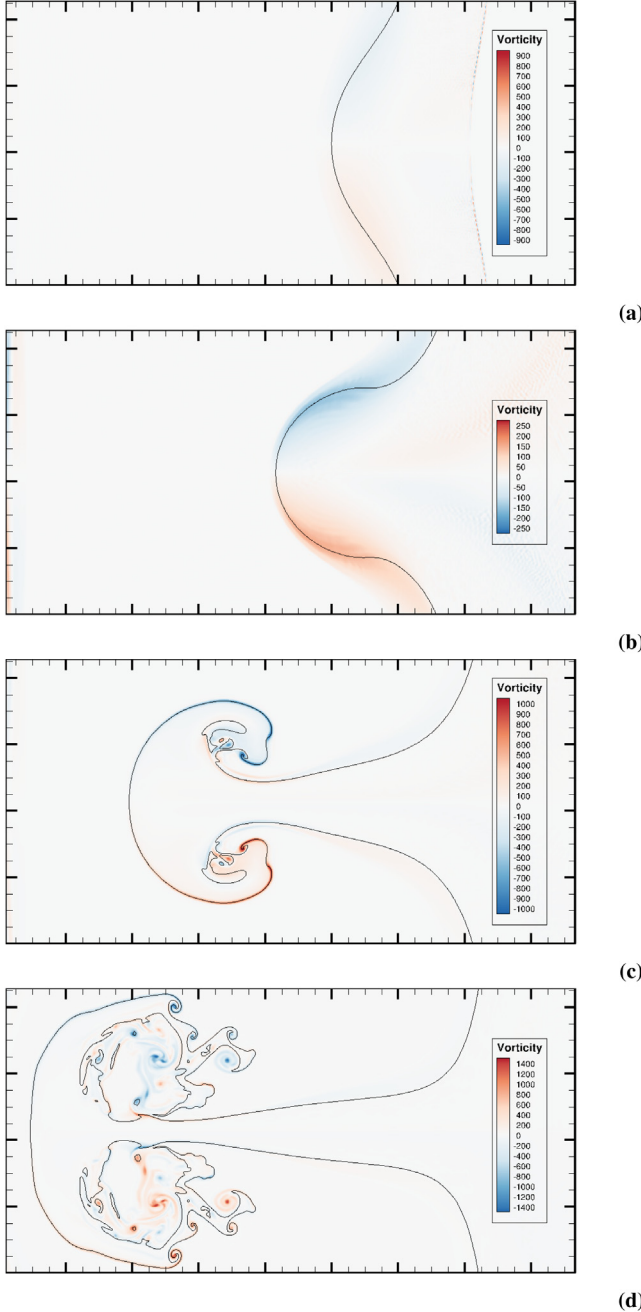


**Fig. 4.** Contours of vorticity in the two-dimensional RM instability between air and  $\text{SF}_6$ , from implicit large eddy simulations (ILES). Also shown are the contour lines denoting the mass fraction  $Y_1 = 0.5$ . Upon shock interaction, baroclinic vorticity is deposited at the interface, causing perturbations to grow and the interface to roll up into the classic mushroom shape.

is activated and vorticity is generated or destroyed. Thus, the strength of the pressure or density gradients, and their degree of alignment, determine the amount of vorticity that is deposited on the interface. This mechanism is present in both RT and RM instabilities [55]. In the RT instability, the pressure gradient is supplied by the acceleration field (for example, gravity) which imposes hydrostatic pressure on the fluid. At the interface, if the pressure gradient opposes the density gradient, but is at a finite angle to it, vorticity will be gradually generated, leading to instability. A similar mechanism operates in RM, where the pressure gradient is supplied by the shock wave and the baroclinic vorticity deposited at the interface upon shock passage causes the

perturbations on the interface to grow. The resulting evolution of the interface including the appearance of roll-ups is shown in Fig. 4, using implicit large eddy simulations (ILES) of RMI cases. (See also, Refs. [56] and [57] for reshocked single- and multi-mode RMI induced flows, respectively.) Recently, ILES was used to elucidate the differences between two- and three-dimensional dynamics of single-mode reshocked RMI [58]. Finally, we remark that vorticity can also be generated on a shock structure itself, particularly from nonlinear *triple-points* that form on the shock geometry, and this can also be a source of turbulence [55].

#### 4. Instability development from multi-modal perturbations: linear through turbulent regimes

In this section, we provide a more detailed treatment of the various stages of development in RT and RM instabilities arising from *multimodal* initial perturbations. Hydrodynamic instabilities in experiments and engineering applications are typically seeded by perturbations that can be characterized as multimodal, and often contain a broad spectrum of modes. For simplicity, we consider perturbations that consist of a range of initial wavelength bands  $[\lambda_1, \dots, \lambda_N]$ , all of which are initially growing in the linear regime. In other words, the amplitude  $a_k$  of each mode with a wavenumber  $k = 2\pi/\lambda_k$  is growing at a rate that is well described by linear stability analysis [59]. For the Rayleigh–Taylor instability, the initial growth in  $a_k$  is given by rewriting Eq. (23) for mode  $k$

$$\ddot{a}_k = \mathcal{A}gka_k, \quad (26)$$

the solution of which is an exponential with exponent  $s = \sqrt{\mathcal{A}gk}$ . Similarly, the RM growth rate due to the initial impulse is given here by rewriting Eq. (24) according to

$$\dot{a}_k = k\Delta u \mathcal{A}^+ [a_k(0)]^+, \quad (27)$$

where  $[a_k(0)]$  is the initial amplitude of mode  $k$ . Recall that Section 3.2 discusses the behavior which is linear in “mode amplitude”. That is still the case for the analysis that gets us to Eq. (27) and discussion thereafter, even though the shock compression is nonlinear for the acoustic characteristics.

In the following subsections, each distinct stage of the development in multimodal RTI and RMI will be discussed in greater detail alongside corresponding flow visualizations. Note that although the discussion implicitly pertains to planar geometries, it may be qualitatively applied to more complicated configurations, for example cylindrical and spherical geometries.

##### 4.1. Linear regime

If individual modes in the initial perturbation wavepacket are of sufficiently small amplitudes, their early evolution can be described by the linear theories discussed earlier. An implicit assumption here is that the interface separating the two fluids is initially smooth and continuous, such that it can be described as an expansion in some orthonormal basis (e.g. as a Fourier series). This allows for analysis in terms of amplitudes and wavelengths of individual modes (i.e. harmonics) in the perturbation.

A single mode  $k$  is considered linear, while its amplitude  $a_k$  satisfies  $ka_k < 1$  [60,61], provided  $ka_k \ll 1$  initially. More generally for broadband spectra, this threshold applies to the r.m.s. amplitude in bands of width roughly a factor 2 in wavenumber. Typically a more conservative estimate is taken, such as  $a_k \leq 0.1\lambda_k$  [62], beyond which the mode is considered nonlinear or saturated. Note that there are a wide range of factors such as viscosity, finite thickness, strong shocks and additional physics that modify the initial growth rate compared to the basic forms given in Eqs. (26) and (27), a detailed discussion of which can be

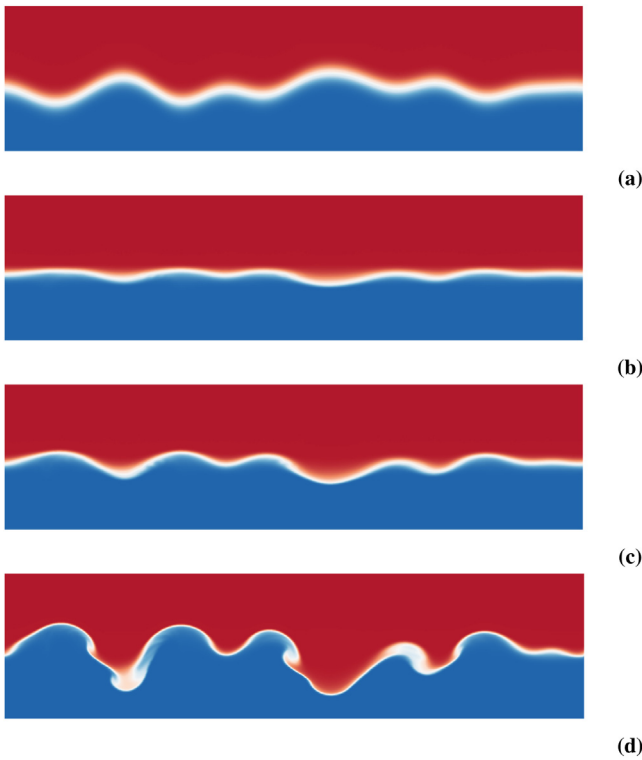


**Fig. 5.** Early time evolution of multimode RM instability. Shown are contours of volume fraction  $f_1$  where  $f_1 = 1$  (red) indicates unmixed heavy fluid and  $f_1 = 0$  (blue) indicates unmixed light fluid. (For interpretation of the references to color in this figure legend, the reader is referred to the web version of this article.)

Source: Data from Thornber et al. (2017) [63].

found in [1]. These factors may also affect the amplitude at which each mode saturates, however for simplicity it will be assumed that a multimode perturbation is growing in the linear regime provided the r.m.s. amplitude in the wavenumber band satisfies  $a_k \leq 0.1\lambda_{\min}$ .

Fig. 5(a) shows the initial condition used in a recent fundamental study of turbulent mixing induced by the RM instability [63], while the image sequence represents early time development and shares the same general trends as observed in other studies of RT mixing layers (see Youngs [64]). The initial surface perturbation shown in Fig. 5(a) contains a superposition of modes in the interval  $k_{\min} = 4$  to  $k_{\max} = 8$ , while the total standard deviation of the perturbation is taken as  $\sigma = 0.1\lambda_{\min}$  to ensure that all modes are initially linear. The interface also has an initial diffusive thickness, which modifies the initial growth rate but has a negligible impact on the subsequent evolution [65].

Shortly after the initiation of the instability (in this case by a  $M = 1.84$  shock wave), the layer growth is in the linear regime, as shown in Fig. 5(b). For this particular case, the incident shock travels from the heavy to light fluids, resulting in a phase inversion of the initial perturbation (due to the negative Atwood number and as a result a negative growth rate). The initial diffusive thickness of the interface has also been compressed by the shock. While the evolution of RTI growth rates from the same initial surface perturbation would differ from this case, the layer would look qualitatively similar at an equivalent early time. In both cases, the evolution of the instability is due to baroclinic torque at the interface that results from a misalignment between the density and pressure gradients.

#### 4.2. Nonlinear regime

Once the r.m.s. amplitude  $a_{k,\max} > 0.1\lambda_{\min}$ , the layer can be considered to have entered the weakly nonlinear regime. In this regime, the growth of the highest amplitude modes is no longer well described by linear theory, however the interface is still smooth and simply connected. Fig. 5(c) shows a visualization of the previously shown RMI mixing layer in this regime.

For a single mode, the bubble (spike) amplitudes are defined by computing the distance between the location of the bubble (spike) tips and the position of the corresponding unperturbed interface. Thus far, we have used the amplitude  $a$  to describe the linear and nonlinear phases of perturbation growth, but as the perturbation further develops into the highly nonlinear stage, new notations of  $h_b$  ( $h_s$ ) are introduced to measure the corresponding mixed zones for the bubble (spike) amplitudes (e.g., [66]).

While the unperturbed interface has been frequently taken as the reference from which to calculate  $h_b/h_s$ , the mixing layer center is only collocated with the unperturbed interface at low  $\mathcal{A}$ , but not high Atwood numbers. In practice, this can be defined in multiple ways, however, a robust definition is to define the mixing layer center  $z_c$  as the position of equal mixed volumes [67], given by

$$\int_{-\infty}^{z_c} \langle f_2 \rangle \, dz = \int_{z_c}^{\infty} \langle f_1 \rangle \, dz, \quad (28)$$

where  $\langle \dots \rangle$  indicates a plane average in the statistically homogeneous direction(s).

For multimode perturbations, *average amplitudes* of the bubble and spike fronts are more representative of the spread of the mixing layer than the amplitudes of individual peaks. The mixing zones of bubble and spike layers, once again denoted as  $h_b$  and  $h_s$ , can be defined in several ways (see, e.g., [68] for details), with the overall width of the layer given by  $h = h_b + h_s$  [69,70]. The threshold or “visual” width, perhaps the most often used definition, is obtained from large experimental or numerical datasets by tracking the 1% and 99% surfaces of the planar-averaged fluid volume fractions (i.e. averaged over the homogeneous directions). Other analysis has been performed with volume fraction thresholds of other values, e.g. 5%, and 95%, with nearly identical results to very late times for the single-mode cases [71]. The locations of the bubble and spike tips (i.e. the 1% and 99% planar-averaged volume fraction thresholds) are then used to mark the width of the mixing layer  $h$ .

In the literature, there is considerable interest to evaluate the development of asymmetries in the growth of the bubbles and spikes at high  $\mathcal{A}$ . Ratios of spike-to-bubble mixing widths based on 1% 5% and 10% concentration thresholds have been widely utilized. Using the previous definition for  $z_c$  given in Eq. (28), bubble and spike integral widths may also be defined [68,72] as

$$W_b = \int_{-\infty}^{z_c} \langle f_1 \rangle \langle f_2 \rangle \, dz, \quad (29)$$

$$W_s = \int_{z_c}^{\infty} \langle f_1 \rangle \langle f_2 \rangle \, dz. \quad (30)$$

This allows for the assessment of asymmetries in the growth of the bubbles and spikes at high  $\mathcal{A}$ , while also retaining the favorable statistical properties of  $W$ . The total integral width is given by,

$$W = \int_{-\infty}^{\infty} \langle f_1 \rangle \langle f_2 \rangle \, dz. \quad (31)$$

For a symmetric (low  $\mathcal{A}$ ), linear volume fraction profile, the width of the mixing layer is of the order of  $6W$  [73,74].

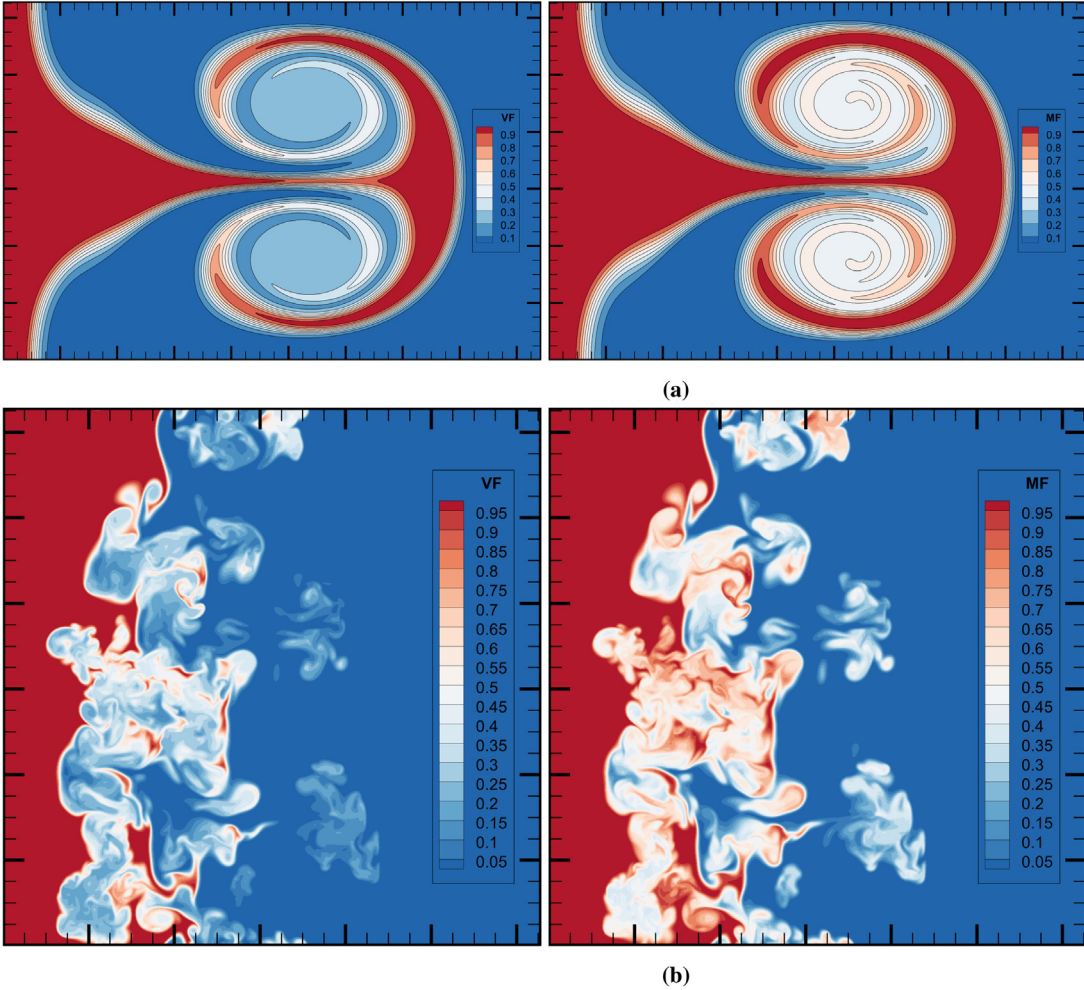


**Fig. 6.** Contours of heavy-fluid volume fractions (VF) and mass fractions (MF) in the (a) 2D single-mode and (b) 3D multi-mode RM instability at an Atwood number of  $\mathcal{A} = 0.5$ , taken from direct numerical simulations. Note the subtle differences in the locations of contour lines for equal values of volume and mass fractions.

The so-called the “product width” is defined with respect to a “stoichiometric” mole fraction and is analogous to the product in fast reactions [68,75]. For brevity, we will not discuss this further here and refer the reader to the above-mentioned references for details.

Note that some publications (e.g., Ref. [68]) use mole fractions instead of the volume fractions used in the original definitions, while others use similar definitions based on mass fractions. Under the assumption that the constituent species of the mixture are intimately mixed at the molecular level and that the species temperatures  $T_i$  are equal locally, the volume fraction and mole fraction of each species are identical. The mass fraction and volume fraction of each species will be different however. Fig. 6 shows contour plots of the volume and mass fractions of the heavier fluid in direct numerical simulations of both the 2D single-mode and 3D multi-mode RM instability in order to highlight these differences.

A distinction is generally drawn between weakly nonlinear and strongly nonlinear regimes. An RTI/RMI mixing layer may be considered strongly nonlinear when the interface has become multi-valued, as shown in Fig. 5(d). This occurs due to the intense vorticity that is generated/deposited at the interface, causing it to roll up into saturated vortex structures dominated by localized KH instabilities. These roll-ups are also the sites of intense molecular mixing between the two fluids, due to the stirring motions and increased surface area. The interface may no longer be simply connected as regions of strong circulation cause material to pinch

off and advect away from the main layer. This is more pertinent to RMI than RTI, due to the initial impulsive acceleration.

#### 4.3. Mix measures

In addition to the primary roll-ups that occur due to baroclinic vorticity, as the mixing layer continues to evolve it begins to develop secondary instabilities within the roll-ups and at other sites along the interface. This is due to shearing motion that occurs at the interface, across which a jump in the tangential component of velocity exists. In regions where there is strongly sheared flow, the interface becomes KH unstable, resulting in the production of increasingly fine-scale vortical motions. It is these motions that accelerate the transition of the mixing layer from a laminar to turbulent state, often generating modes outside the range present in the initial perturbation. Since the interfacial surface area also rapidly increases, mixing occurs much more effectively as the layer becomes progressively more turbulent. Fig. 7(a) shows a visualization of the RMI mixing layer in this transitional regime.

It is often useful to quantify the degree to which the two fluids are mixed by considering a dimensionless measure of the mixing state. One such measure is the molecular mixing fraction [76], given by

$$\Theta = \frac{\int \langle f_1 f_2 \rangle \, dz}{\int \langle f_1 \rangle \langle f_2 \rangle \, dz}. \quad (32)$$

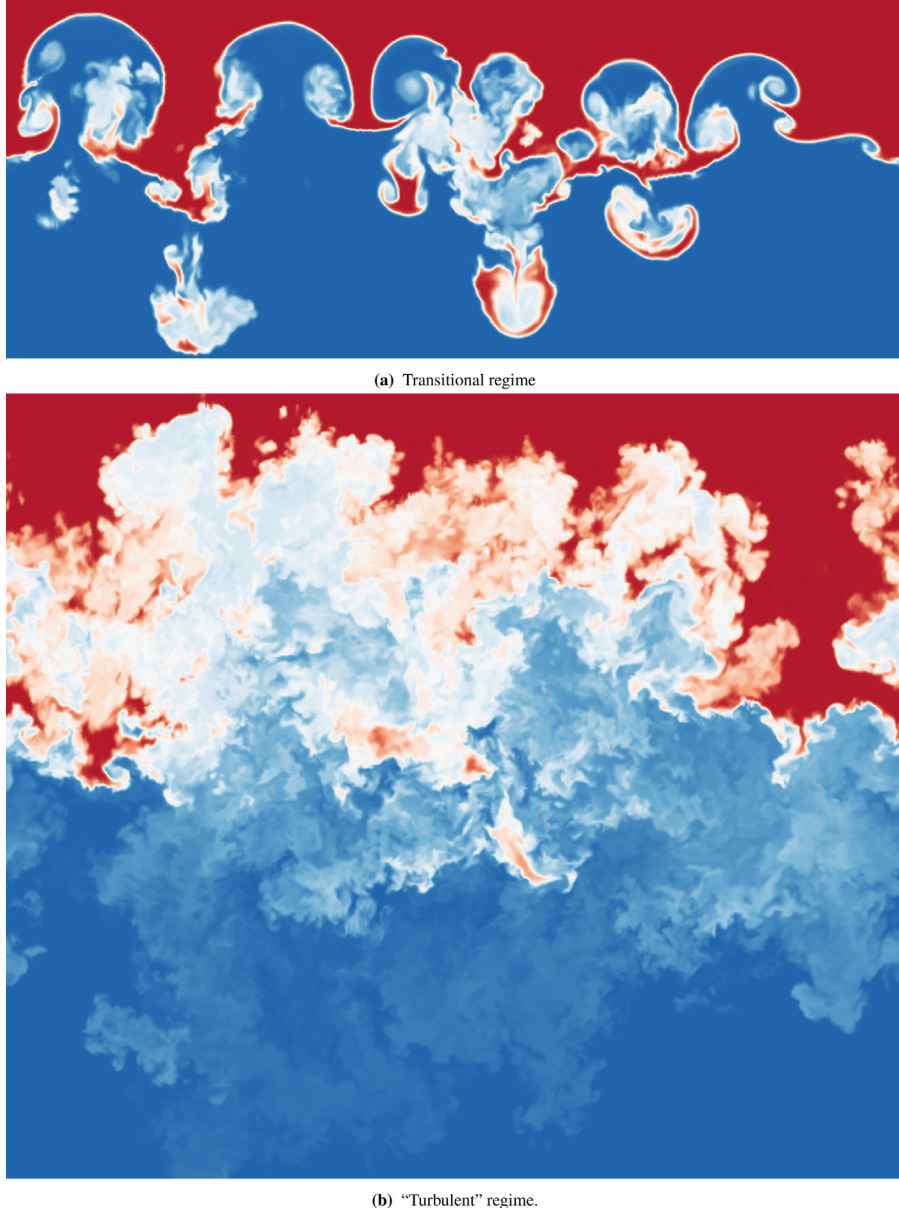


**Fig. 7.** Transitional and “turbulent” flows in a multimode RMI mixing layer.

Another measure,  $\mathcal{E}$ , is quantified based on the amount of mixed fluid by considering a passive, equilibrium chemical reaction between the light and heavy fluids. Both  $\mathcal{E}$  and  $\Theta$ , often termed the *mixedness* parameters, provide extremely similar measure of the amount of molecularly mixed fluid within the layer [77–79].

This pair of mix measures,  $\{\Theta, \mathcal{E}\}$ , can take values between 0 and 1, with  $\{\Theta, \mathcal{E}\} = 0$  corresponding to complete heterogeneity and  $\{\Theta, \mathcal{E}\} = 1$  corresponding to complete homogeneity of mixing. It can also be shown that  $\{\Theta, \mathcal{E}\}$  are related to the variance of the density probability density function (PDF) [80]. The variations of  $\{\Theta, \mathcal{E}\}$  in time can be used to estimate when the layer has entered the transitional regime. From typical simulations of conventional RTI/RMI configurations  $\{\Theta, \mathcal{E}\}$  will have an initial value close to 1, as the only heterogeneity present the flow is due to the surface perturbation (e.g., Zhou et al. 2016). As the instability develops,  $\{\Theta, \mathcal{E}\}$  will decrease and eventually reach a minimum, beyond which they increase again and tends toward some asymptotic value. The decrease in  $\{\Theta, \mathcal{E}\}$  is due to the inter-penetration of bubbles and spikes, a process accompanied by stretching of the layer. As the roll-ups of the primary and

secondary instabilities develop however, fine-scale mixing begins to occur and eventually overcomes the stretching effect. Thus the minimum in  $\{\Theta, \mathcal{E}\}$  values can be considered to correspond approximately to the time when the layer has begun to transition to turbulence.

More recently, the mixed mass is defined as [79],

$$\mathcal{M} = \int 4\rho Y_1 Y_2 dV, \quad (33)$$

where  $Y_1$  and  $Y_2$  are the mass fractions and  $\rho$  is the mixture density.

The mixed mass has several attractive features:

- It is measured from ICF experiments to elucidate the degradation of the yield from the mixing induced by hydrodynamic instabilities (e.g., [81]).
- It is a conserved quantity, in the absence of species diffusion. The conservation of mass is given by

$$\frac{\partial \rho Y_m}{\partial t} + \nabla \cdot (\rho Y_m \mathbf{u}) = \nabla \cdot \mathbf{J}_m \quad (34)$$

for  $m = 1$ , or 2.

The mass flux for species 1 is given by  $\mathbf{J}_1 = -\rho Y_1 \mathbf{V}_1$ , and the application of Fick's law of diffusion gives

$$\mathbf{J}_1 = \rho D_{12} \nabla Y_1, \quad (35)$$

where  $D_{12}$  is the binary diffusion coefficient. Often in fundamental studies  $D_{12}$  (as well as the viscosity  $\mu$  and conductivity  $\kappa_T$ ) is assumed to be constant, however this need not be the case in general. For mixtures of more than two species, Fick's law is often still used but with an additional correction velocity to ensure mass conservation [82], while a more accurate representation is the Hirschfelder–Curtiss approximation [83].

- The normalized mixed mass

$$\Psi = \frac{\int \rho Y_1 Y_2 dV}{\int \langle \rho \rangle \langle Y_1 \rangle \langle Y_2 \rangle dV}. \quad (36)$$

has demonstrated to provide more consistent results for both the RTI and RMI flows when compared with the traditional mixedness parameters.

#### 4.4. Mixing transition criteria

It is important to note that diffusive effects (viscosity, diffusivity, conductivity) will act to moderate the fluid instabilities, most strongly at small scales, with potentially important ramifications for the evolution of the mixing layer. To quantify the significance of the diffusivities of mass, momentum and temperature, it is necessary to introduce the Reynolds, Schmidt and Prandtl numbers. The Reynolds number is the ratio between inertial and viscous forces and is given by

$$Re = \frac{\mathcal{L}U}{\nu}, \quad (37)$$

which results in an outer-scale Reynolds number that represents the effect of large scales dominating the flow [3]. For sufficiently low values of this Reynolds number, the growth of secondary instabilities will be suppressed, and the mixing layer will not reach a state of fully developed turbulence.

For stationary flows, Dimotakis [84] identified a so-called mixing transition that is characterized by a reduction in the sensitivity of the flow parameters to the Reynolds (and Schmidt) numbers, and occurs for an outer-scale Reynolds number of  $Re \approx 1-2 \times 10^4$ . The order-one constant, 1–2, was estimated from several experimental datasets and the precise value of which may be flow or geometry dependent. Results from shear layers, jets, and other flows depicted a marked increase in mixing quantities and small scale features, once the flow has surpassed the mixing transition Reynolds number  $1-2 \times 10^4$  [84].

The notion of a mixing transition can also be adapted to flows that are evolving in time [85]. The Zhou–Robey hypothesis [85–87] extended this theory to statistically unsteady flows [88], showing that an additional, temporal criterion must be satisfied to allow the flow to have sufficient time to evolve and fill out various scales. Since the flow is self-similar, time and length scales are related. More specifically, the diffusion layer scale  $\lambda_D$ , must also be considered and the criteria for the new “temporal mixing transition” becomes  $\min(\lambda_{LT}, \lambda_D) \geq \lambda_v$ . Here, the “Liepmann–Taylor” scale,  $\lambda_{LT}$ , is defined by the outer scale and the Reynolds number (Eq. (37)) as  $\lambda_{LT} = 5\mathcal{L}Re^{-1/2}$  [84], and the diffusion layer length scale is given by  $\lambda_D = C_d(vt)^{1/2}$ .

We now describe in greater detail the Liepmann–Taylor and diffusion layer length scales. The “Liepmann–Taylor” scale,  $\lambda_{LT}$ , is taken as a multiple of the Taylor microscale  $\lambda_T$ , e.g.,  $\lambda_{LT} = (5/2)^{1/2}\lambda_T$  [68]. The viscous diffusion length,  $\lambda_D$ , is proportional to  $(vt)^{1/2}$  with various proposed numerical prefactors [85–87,89],

and is comparable to the species diffusion length  $(4Dt)^{1/2}$  for order-unity Schmidt numbers. For RTI flow, an analogous diffusion length for the mixing region is given by  $\lambda_h = (10v\tau_h)^{1/2}$  where the growth time scale  $\tau_h = h/h$  for a mixing width  $h$ .

The time scale  $\tau_h$  is not very sensitive to the exact definition of  $h$ . In the asymptotic limit of  $t^2$  growth,  $\lambda_h \rightarrow (5vt)^{1/2}$ . We also note that  $\lambda_h$  and other diffusion lengths are comparable in size to the vertical Taylor microscale shown in Ref. [68], hence their classification as intermediate length scales.

#### 4.5. The minimum state

It is critical to stress that a mixing layer that has surpassed the Reynolds number required for the mixing transition does not mean that the flow is fully developed turbulence. To illustrate this point, we recall the standard definition of fully-developed turbulent flows: The requirement that an extended inertial range exist between the energy-containing scales, where the large-scale eddies might be subject to external forcing, and the dissipation scales, where the small-scale motions are subject to viscous action.

The key length scales in isotropic and anisotropic flows are detailed in [84,89] and [68], respectively. The “Liepmann–Taylor” scale,  $\lambda_{LT}$ , is the upper boundary of the inertial range that separates the energy-containing and inertial ranges. The “inner viscous” scale,  $\lambda_v$ ,  $\lambda_v = 50\mathcal{L}Re^{-3/4}$  is the lower boundary of the inertial range. This length scale separates the inertial and dissipation ranges.

Recall that the mixing transition occurs for an outer-scale Reynolds number of  $Re \approx 1-2 \times 10^4$ . This corresponds to the requirement that  $\lambda_L \simeq \lambda_v$ , indicating that an inertial range does not exist for such Reynolds number. Therefore, the flow field just surpassing the mixing transition does not qualify as a turbulent flow, but the mixing transition requirement is a gateway for an evolving time-dependent flow to eventually become a turbulent flow. It is a necessary, but not sufficient condition for a turbulent flow [89].

For a sufficiently high Reynolds number, the mixing layer will eventually transition to a state of fully developed turbulence. As for what constitutes a sufficiently high Reynolds number in order to achieve fully developed turbulence, a “minimum state” outer-scale Reynolds number,  $Re^*$ , has been introduced as the lowest Reynolds number beyond which there is an *established* inertial range [89], the textbook definition of fully-developed turbulence. Based on a consideration of interacting scales, Zhou [89] found that  $Re^* = 1.6 \times 10^5$ , an order of magnitude higher than that of the mixing transition.

For flows that have achieved this “minimum state” criterion, there is a complete decoupling between the energy-containing scales and dissipation range scales, so that the statistics of the energy-containing scales becomes independent of Reynolds number. The  $Re^*$  is a stringent requirement that has not been met in almost all experiments and simulations carried out heretofore. See however, the very recent work by Mansoor et al. [90] with shock tube experiments (Fig. 8).

This “minimum state” criterion also allows for an estimate of the time for turbulence to achieve a fully developed state in statistically unsteady flows [3]. Rose and Sulem [91] noted the eddy turnover time as the length scale of an eddy divided by the typical velocity difference across the eddy. The eddy turnover time is therefore proportional to the time required for the eddy to be distorted, and in this distortion process, generate smaller eddies. Approximately one dominant, energy-containing eddy turnover time corresponds to the mixing transition, as noted by Drake et al. [88]. Using the same notions, it can be shown that about four eddy-turn over times will be needed for the flow to qualify for the fully-developed turbulent flows as defined by the minimum state [68].

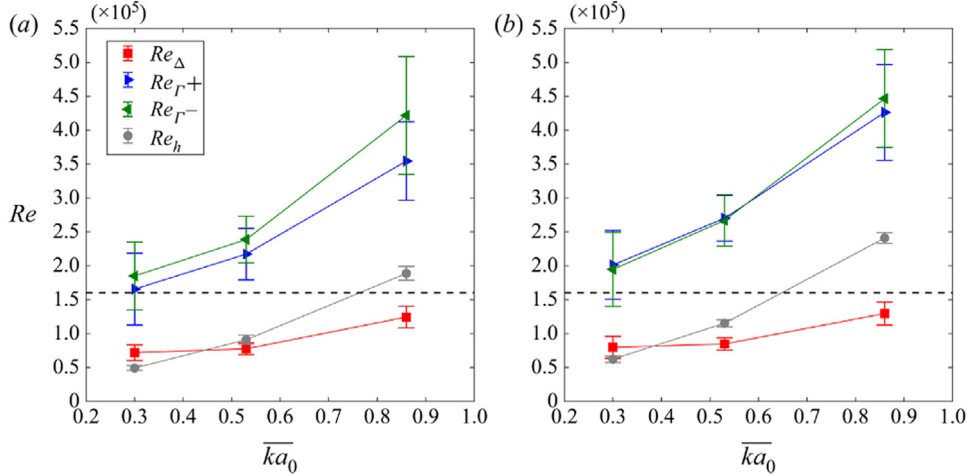


**Fig. 8.** Reynolds numbers based on local and global information, plotted against the initial conditions  $\overline{k}a_0$  at (a)  $t = 2.65$  ms and (b)  $f = 5.65$  ms. Fig. 8 of Mansoor et al. [90]. The dashed lines indicate the minimum state criterion of  $Re = 1.6 \times 10^5$  in Ref. [89]. The authors found that the Reynolds number defined by Eq. (37) better characterizes the flow in terms of mixing transition compared to other methods used (see Ref. [90] for detailed definitions) and demonstrates the physical significance of the minimum state criterion in the context of RMI studies. This is an Open Access article, distributed under the terms of the Creative Commons Attribution license.

#### 4.6. Turbulent flows

The particular case shown here (Figs. 7(a) and 7(b)) was initialized using a narrowband spectrum of modes, so that the low wavenumber modes saturate shortly after the saturation of the highest wavenumber modes. In contrast, for a broadband spectrum of modes in the initial perturbation, the lowest wavenumber modes will continue to grow linearly, while higher wavenumber modes have already saturated. For RT flows, a perturbation of wavelength  $\lambda$  and initial amplitude  $h_0$  will saturate upon reaching an amplitude  $h_{sat} \sim \lambda/2\pi$ , and at a time  $t_{sat} = \sqrt{\lambda/2\pi}\mathcal{A}g \log(\lambda/2\pi h_0)$ . Thus, the low wavenumber modes will reach nonlinearity over a longer saturation non-dimensional time  $t_{sat}\sqrt{2\pi\mathcal{A}g/\lambda}$ .

For broadband perturbations, Youngs [92] proposed the higher saturation amplitudes of low wavenumber modes would allow them to continue growing after the short wavelengths have saturated, thereby dominating the overall growth rate of the layer at late times. This implies the self-similar growth rate of RT and RM mixing in this regime is dependent on the initial conditions [3,93,93–95], when initialized with broadband perturbations.

Thus, when a broadband spectrum of modes is present at the initial interface, the late-time RT development progressively samples longer wavelengths since they are favored as discussed above. This results in a mixing front that is self-similar [69, 74, 76, 96–101] (i.e. the lateral scale of dominant structures is proportional to the amplitude), and grows according to

$$h = \alpha \mathcal{A}gt^2, \quad (38)$$

where  $\alpha$  is the turbulent growth rate and  $h$  is a measure of the amplitude of the mixing layer. A more complete expression for  $h$  was obtained from a similarity analysis by [102–104] (and independently from a mass flux and energy balance argument by [77]) resulting in a differential equation for  $h$ :  $\dot{h}^2 = c_{RT}\mathcal{A}gh$ , with the solution

$$h(t) = \frac{1}{4}c_{RT}\mathcal{A}gt^2 + \sqrt{c_{RT}h_0\mathcal{A}g}t + h_0. \quad (39)$$

In the above equation,  $h_0$  is the initial amplitude and creates a virtual origin effect, while  $c_{RT}$  can depend on the initial conditions and be identified as  $4\alpha$  at  $t \gg t_0$ . Thus, the behavior suggested by the above equations can be interpreted as describing the envelope of the Fourier modes as they saturate, which will

move to longer wavelengths and hence larger layer width as time progresses. Since in this scenario (termed bubble competition [97,105]), the late-time behavior is dictated by the behavior of wavelengths that were prescribed in the initial spectrum,  $\alpha$  can depend on the amplitudes of these initial modes as shown in [104–107]. An alternate pathway to self-similarity involves starting with a narrow-band spectrum of high- $k$  modes, so that the longer wavelengths that dominate the flow late in time are seeded through the merger of modes that have recently saturated. This behavior is referred to as bubble merger, and is expected to result in values of the growth rate  $\alpha$  that is only weakly dependent on the initial amplitudes [108–114]. Of course, the growth rate  $\alpha$  can also depend on additional factors such as the entrainment of heavy fluid into the bubbles resulting in densification of the bubbles and diminished buoyancy [115].

Elbaz & Shvarts [116] showed that at least  $\mathcal{G} = 3$  mode coupling generations must occur in order for self-similar growth to be obtained for both the RT and RM flows. Here, time is represented by the number of wavelength doublings or “generations”—a physical measure of the instability evolution. In terms of mode coupling generations, Elbaz & Shvarts assessed that the constant acceleration linear electric motor (LEM) experiments achieved  $\mathcal{G} = 3.3\text{--}4.9$  and therefore the reported values of  $\alpha$  are representative of the self-similar asymptotic limit. For the impulsive LEM experiments, however, it is estimated that  $\mathcal{G} = 1.25\text{--}1.85$  generations, hence it can be concluded that they did not reach self-similarity [116].

For the turbulent RT mixing layer, self-similar growth of the form  $h = \alpha \mathcal{A}gt^2$  is observed, where  $\alpha = \alpha_b + \alpha_s$ . As with  $\theta$ , the constant  $\alpha$  can depend on  $\mathcal{A}$  [68,117–121] as well as on the initial conditions [64]. For immiscible fluids, surface tension may also influence the value of  $\alpha$  obtained [122], by inhibiting mixing. Results from the LEM experiments show that the ratio  $\alpha_s/\alpha_b$  varies significantly with Atwood number.

In this regime, the RM mixing layer experiences self-similar decay in a manner analogous to homogeneous decaying turbulence. During this period, integral mix measures such as the mixing fraction  $\Theta$  approach an asymptotic value, while the mixing layer width grows as  $h = h_b + h_s = c_{RM}t^\theta$  for some constant exponent  $\theta$ . The specific value of  $\theta$  can depend weakly on the Atwood number as well as the initial conditions as mentioned previously, a consequence of the permanence of large eddies [123], while  $c_{RM}$

also depends on the initial conditions [116]. Note that experimental results have indicated that the bubble and spike amplitudes may grow as  $h_b \sim t^{\theta_b}$  and  $h_s \sim t^{\theta_s}$ , where  $\theta_s > \theta_b$ , particularly for large Atwood numbers, implying asymmetry between bubbles and spikes [124]. However, recent numerical results [125] show for  $0.5 < A < 0.9$  that while the ratio  $h_s/h_b$  varies initially, it eventually approaches a constant value which implies that  $\theta_b = \theta_s$  (see also, Refs. [103] and [85]).

It is important to note that in general, a RT mixing layer will achieve self-similarity on a shorter timescale than a RM mixing layer due to the different dependence on  $t$  (i.e., distinctive self-similarity scalings:  $t^2$  for RT vs  $t^\theta$  for RM), hence why it is easier for RT to achieve self-similarity in experiments and simulations. This can also be explained in terms of the time between successive mode generations, which becomes progressively shorter for RT but longer for RM, where each new mode generation requires  $\sim 10$  times longer to reach than the previous one [116]. The different dependence of  $h$  on  $t$  also implies that the dependence of the Reynolds number on  $t$  is different. For Rayleigh–Taylor, the outer-scale Reynolds number grows as  $Re \propto t^3$ , whereas for Richtmyer–Meshkov it grows as  $Re \propto t^{2\theta-1}$ . Thus for  $\theta < 1/2$  (as is the case for all but the most extreme broad-band perturbation spectra), the outer-scale RM Reynolds number decreases in time [3].

A visualization of a “turbulent” RM mixing layer is shown in Fig. 7(b). The flow field was generated from an implicit large-eddy simulation. Thus, for Fig. 7(b), its verified provenance as “turbulence” cannot be given in terms of the *minimum state* Reynolds number discussed above. Instead, it is “indicated” by a number of indirect indicators that can be gleaned from the simulations. First, we look at “turbulence” as the establishment of an inertial range, and the stabilization of mixing measures as a first indicator. We then look at the time variation of theta estimates and ensure they have stabilized, finally we check that there are still reasonable statistics in that the integral length has not grown too large.<sup>2</sup>

## 5. Numerical methods and formulations

The focus of this section will be on fundamental numerical studies of turbulence induced by RT and RM instabilities, the various formulations of the governing equations used in these studies and the different approaches taken to solving these equations numerically. In particular, emphasis will be placed on the regimes for which each description is valid due to the varying levels of approximation made, as well as the strengths, limitations and requirements of the numerical methods used for each description. Note that only continuum methods will be considered here.

### 5.1. Trade-off between tractability and complexity

In solving the governing equations of fluid dynamics, the trade-off between tractability and complexity is an important one as it generally guides the choice of numerical methods for a particular study. First, assumptions are made in deriving the governing equations not only to improve tractability but also place restrictions on the range of validity of the results with respect to real flows due to the increasing level of approximation. An additional level of approximation is introduced when the equations are discretized and solved numerically, which the researcher seeks to minimize by choosing an appropriate numerical method.

<sup>2</sup> As the flow field is from an implicit large-eddy simulation, it is difficult to ascertain if such a flow is from the “minimum state” criterion. There is much effort, however, to investigate how an effective Reynolds number can be estimated [126–129]. See also, Section 6.2.2.

However, the level of complexity contained in the system of governing equations places a certain number of requirements that the numerical method must satisfy, which narrows the choice of numerical methods for a given problem.

As discussed in earlier sections, the different formulations of governing equations used to study RT/RM may be grouped according to their treatment of the advective terms and the mixture. Starting from the assumption that the mixture may be treated as a continuum, a hierarchy of descriptions can be derived where each successive level becomes increasingly tractable but has a decreasing range of validity. Generally, the first aspect to consider is whether the mixture contains multiple phases of matter. Historically, numerical studies of turbulence arising from RT/RM have focused almost exclusively on single-phase fluids as this greatly reduces the range of physical phenomena that must be considered. We also draw a distinction between whether fluids of the same phase are miscible or immiscible, as each case typically requires a different numerical approach. This distinction is important, since many experiments, particularly for Rayleigh–Taylor, use immiscible fluids to study turbulent mixing.

Perhaps the biggest distinction however, from an algorithmic point of view, is whether advection of the fluids may be treated as compressible or incompressible. Assuming incompressibility greatly improves the numerical tractability of the problem, as now the pressure and velocity fields may be considered to remain smooth and continuous, which allows for the use of numerical methods that can take advantage of this assumption. Needless to say this also reduces the range of validity of the results, which will be limited to applications where acoustic effects are negligible.

If acoustic effects are important, as quantified by the Mach number, then a fully compressible formulation must be used, which allows for the possibility of discontinuous changes in the flow properties. This requires the use of numerical methods that converge to (or approximate) the weak solution of the governing equations, which places restrictions on the ability of the method to resolve fine-scale turbulent features (discussed below).

Another assumption commonly made within the context of incompressible formulations relates to the Atwood number. In the limit of  $A \rightarrow 0$ , variations in density can be assumed to be small (and influential only through the buoyancy term), and the governing equations may be simplified, known as the Boussinesq approximation. This may be considered the simplest formulation that still permits the study of buoyancy-driven turbulence.

Based on this hierarchy of descriptions, the following subsections will detail each of the main formulations used for the study of turbulence induced by RT and RM instabilities; fully compressible, incompressible variable-density, and incompressible Boussinesq formulations as well as the use of various forms of interface treatments.

A review of studies that investigate the effects of viscosity, conductivity, diffusion, variable-density, compressibility and surface tension on turbulence arising from these instabilities is also included. The different approaches to modeling turbulence in these settings will be discussed. Studies of the effects of other phenomena such as reactions [130], phase transition [131] and magnetohydrodynamics [132] on RMI and RTI will be deferred to later sections. For a discussion of the application of non-continuum, particle-based methods such as the lattice Boltzmann method [133] to these flows, see Livescu [119]. Lately, Banerjee [134] surveyed insights gained into the RTI driven mixing process with a focus on low to high Atwood number ( $>0.1$ ) experiments, while a summary of the small Atwood number experiments can be found in Andrews and Dalziel [135]. A recent review of numerical simulation and modeling of RTI experiments is available in Ref. [136]. Also, Prestridge [137] provided examples of experimental studies from Los Alamos in variable-density mixing in multiple regimes.

## 5.2. Compressible formulations

The governing equations for multicomponent mixtures of compressible, inert, miscible materials are given in Livescu et al. [119] in a very general form. Here the presentation will be restricted to binary mixtures of ideal gases with linear constitutive relations. With these restrictions, the standard form of the governing equations is (e.g., [138])

$$\frac{\partial \rho}{\partial t} + \nabla \cdot (\rho \mathbf{u}) = 0, \quad (40a)$$

$$\frac{\partial \rho \mathbf{u}}{\partial t} + \nabla \cdot (\rho \mathbf{u} \mathbf{u} + p \mathbf{I}) = \nabla \cdot \boldsymbol{\tau} + \rho \mathbf{g}, \quad (40b)$$

$$\frac{\partial \rho E}{\partial t} + \nabla \cdot ([\rho E + p] \mathbf{u}) = \nabla \cdot (\boldsymbol{\tau} \cdot \mathbf{u} - \mathbf{q}_c - \mathbf{q}_d) + \rho \mathbf{g} \cdot \mathbf{u}. \quad (40c)$$

In Eq. (40), (40a), (40b) and (40c) are statements of the conservation of mass, momentum and total energy of the mixture. In addition, these formulations are supplemented by the equation for the conservation of mass for species  $k$ , Eq. (34). The total energy is given by  $E = e + \frac{1}{2} \mathbf{u} \cdot \mathbf{u}$ , where the internal energy  $e$  is related to the state variables  $\rho$  and  $p$  through the equation of state. For ideal gases in thermal equilibrium this relation is

$$\rho e = \frac{p}{\bar{\gamma} - 1}, \quad (41)$$

where  $\bar{\gamma}$  is the ratio of mass-weighted specific heats, given by

$$\bar{\gamma} = \frac{\sum Y_k c_{p,k}}{\sum Y_k c_{v,k}}. \quad (42)$$

In the general case where  $\bar{\gamma}$  varies with the mixture composition, many numerical methods which have been used to solve the weak form of Eq. (40) are unable to preserve pressure equilibrium across a material interface in the inviscid limit [139,140]. Various treatments for this pathology have been proposed, some of which are purely numerical [141], while others involve the use of additional equations for “color functions” such as volume fraction [142,143]. In many of these treatments some form of conservation is lost, the most benign being a lack of conservation of species energy and the most severe being mass conservation. In addition, many of the approaches involving additional equations do not allow for the inclusion of molecular diffusion. However, this was recently rectified by Thornber et al. [144]. Minimal, fully-conservative, thermodynamically-consistent advection schemes have been proposed in context of WENO methods by [145], and more generally by [146].

The specification of a fully defined system of equations is completed by the constitutive relations for viscous dissipation, thermal conductivity and molecular diffusion. Newton’s law of viscosity gives the form of the viscous stress tensor  $\boldsymbol{\tau}$  previously defined in Eq. (47) (note that Stokes’ hypothesis of zero bulk viscosity is invoked), while the heat flux vector is given by Fourier’s law of conductivity to be

$$\mathbf{q}_c = -\kappa_T \nabla T. \quad (43)$$

Finally, changes in mixture composition due to species diffusion give rise to changes in energy which must be accounted for. This is done via the enthalpy diffusion flux, defined as

$$\mathbf{q}_d = \sum h_k \mathbf{j}_k, \quad (44)$$

where  $h_k = e_k + p/\rho_k$  is the enthalpy of species  $k$ . Note that in general, the system of equations and constitutive laws given above does not satisfy the second law of thermodynamics due to the exclusion of terms relating to the diffusion of mass due to pressure and temperature gradients and the energy changes associated with these processes [147]. These terms are typically

neglected for the sake of simplicity but may be non-negligible at large molecular weight ratios [119].

Comparing the (already simplified) compressible formulation above to the incompressible variable-density formulation given in Section 5.3, numerical methods must be able to robustly handle shocks and resolve acoustic waves, in addition to capturing fine-scale vortical motions and material interfaces. This represents the key challenge that compressible solvers must overcome and in general some form of trade-off must be made between stably capturing discontinuities and resolving fine-scale structures. For this reason, a more diverse range of numerical methods is available in the literature for compressible formulations as each approach has its strengths and weaknesses. For example, Gauthier [48] used an auto-adaptive multidomain Chebyshev–Fourier spectral method to perform direct numerical simulations (DNS) of the compressible Rayleigh–Taylor instability. However, for this study the maximum (fluctuating and mean) Mach number was  $M < 0.04$  to prevent the formation of shock waves, which lead to Gibbs oscillations and non-uniform convergence in spectral methods. This inability of spectral methods to robustly handle shock waves is one of the main reasons why fundamental studies of compressible turbulence induced by RTI and RMI are typically performed using some form of high-order finite-difference, finite-volume or arbitrary Lagrangian–Eulerian (ALE) methods.

Compact difference schemes are one such substitute for spectral methods in fundamental studies of compressible turbulence, and their performance relative to spectral methods is reasonably well known from studies using incompressible formulations such as Cook et al. [78]. Olson & Greenough [148] assessed the resolution requirements for numerical simulations of a RM turbulent mixing layer using the Miranda and ARES simulation codes. A similar study was also performed using the same codes for compressible RTI [149]. Miranda uses a 10th order compact difference scheme for spatial differentiation combined with a 5-stage, 4th order Runge–Kutta scheme for temporal integration. Artificial fluid properties are used to regularize sharp gradients and discontinuities in the flow. An 8th order compact filter is also applied to the conserved variables at each time step to smoothly remove the highest 10% of wavenumbers to ensure numerical stability. The other code used in these studies, ARES, is an arbitrary Lagrangian–Eulerian method that uses a 2nd order predictor–corrector method in the Lagrange step and 2nd order finite-difference for spatial gradients. Artificial viscosity is used to damp oscillations that occur near shocks and material interfaces. Comparisons between these two methods showed that, as expected, the higher order of accuracy in the Miranda code was important in capturing a broader range of length scales and also resulted in better convergence of large-scale integral quantities. In both methods, a disadvantage of using artificial viscosity to capture shock waves is that a penalty is incurred on the timestep size in order to meet the viscous stability condition, particularly for strong shocks.

Another example of the successful application of central-upwind schemes to study RTI/RMI is the hybrid method of Hill et al. [150], which uses a combination of a 5th order weighted essentially non-oscillatory (WENO) conservative finite difference scheme for shock capturing and a five-point tuned center-difference (TCD) scheme away from shocks. The TCD scheme is optimized for low-dissipation by minimizing the spatial truncation error, at the cost of a reduction in order of accuracy from 4th to 2nd order. To ensure numerical stability, the momentum, energy and scalar convective terms are written in a skew-symmetric form and time integration is performed using a 3rd order strong stability-preserving Runge–Kutta scheme. An issue that is pertinent to all hybrid numerical methods of this form is how to efficiently detect shocks and other discontinuities such

that the more dissipative upwind method is isolated to the region surrounding the discontinuity and is not activated prematurely or in a large region of the flow. There is also an additional computational cost associated with this detection function, see Johnsen et al. [151] for a comparison of various numerical methods for shock-turbulence interaction, including hybrid central-upwind schemes, and their respective computational cost estimates.

The use of front tracking methods (discussed in further detail in Section 5.4) in conjunction with physical mass diffusion has been applied to model mixing between miscible fluids [152]. The main idea behind this approach is to minimize numerical diffusion across an interface so that it does not dominate contributions from physical diffusion and/or sub-grid models. In Glimm et al. [153], the use of front tracking and large eddy simulation (LES) with dynamically modeled sub-grid terms gave favorable comparisons with data from the Rayleigh–Taylor water channel experiment of Mueschke et al. [154].

An important consideration in compressible formulations is preserving stability and high-order accuracy at non-periodic boundaries, while also avoiding unwanted wave reflections, since the objective often is to represent a very large (or even infinite) physical domain with a finite computational one. In incompressible simulations of RTI, the boundary conditions applied in the inhomogeneous direction are typically no-slip or free-slip conditions, placed sufficiently far away that the pressure and velocity fields are always uniform at the boundaries. For compressible simulations, the presence of acoustic phenomena mean that more advanced treatments are required. These fall broadly into two categories; the use of an absorbing buffer zone or the use of analytical solutions of the system external to the domain. In the buffer zone approach, the computational domain is extended (but typically calculations are only performed in one dimension) and numerical/physical viscosity is gradually increased such that the intensity of any reflected waves is reduced to the point where the impact on the interior domain is negligible. Buffer zones are generally quite effective for arbitrary systems of equations and are also easy to implement, however they often require user interaction and tuning for different simulations.

Analytical approaches use one-dimensional characteristic analysis of the hyperbolic part of the governing equations to relate the amplitudes of incoming and outgoing waves [155]. For non-reflecting boundary conditions, setting the reflected amplitude to zero results in the system of equations becoming ill-posed and hence some degree of reflection must be allowed. In practice, the amount of reflection required to maintain well-posedness is minimal and is typically still smaller than reflections that occur using buffer zones. Incoming waves must also be sufficiently planar for the analysis to be valid and the viscosity must be sufficiently small (i.e. the Reynolds number must be large) if the full Navier–Stokes equations are being simulated, since the wave propagation is assumed to only be due to the inviscid part of the equations. The choice by researchers to use one approach over the other therefore depends on the nature of the flow field being simulated, as well as other factors such as ease of implementation and computational cost (with characteristic boundary conditions typically being slightly more expensive).

### 5.3. Incompressible formulations

#### 5.3.1. Variable density

The generalization of the equations governing buoyancy-driven incompressible flow to arbitrary density ratios was given in Sandoval [156], who considered the incompressible limit of a two-fluid mixture of ideal gases. For a general derivation including non-ideal gas effects and heat conduction, as well as the associated discussion, see [157]. Note that the incompressible

limit may be obtained mathematically as either  $p \rightarrow \infty$  or  $\gamma \rightarrow \infty$  [119]. The  $p \rightarrow \infty$  limit leads to uniform density in regions of pure fluid (as opposed to a non-constant background density) and is the one used in [156]. In this limit, the ideal gas equation of state reduces to

$$\rho = \frac{1}{Y_1/\rho_1 + Y_2/\rho_2}, \quad (45)$$

where  $Y_1$ , and  $Y_2$  are the mass fractions of species 1 and species 2 respectively and  $Y_1 + Y_2 = 1$ . Each species mass fraction obeys a transport equation (of the same form as Eq. (34)), which when summed over both species yields the continuity equation. The governing equations are therefore

$$\frac{\partial \rho}{\partial t} + \nabla \cdot (\rho \mathbf{u}) = 0, \quad (46a)$$

$$\frac{\partial \rho \mathbf{u}}{\partial t} + \nabla \cdot (\rho \mathbf{u} \mathbf{u}^t) = -\nabla p + \nabla \cdot \boldsymbol{\tau} + \rho \mathbf{g}, \quad (46b)$$

$$\nabla \cdot \mathbf{u} = -\nabla \cdot \left( \frac{\mathcal{D}}{\rho} \nabla \rho \right), \quad (46c)$$

where  $D$  is the mass diffusion coefficient (assumed constant) and the viscous stress tensor is given by

$$\boldsymbol{\tau} = \mu \left[ \nabla \mathbf{u} + (\nabla \mathbf{u})^t - \frac{2}{3} (\nabla \cdot \mathbf{u}) \mathbf{I} \right]. \quad (47)$$

Considering the Reynolds number in isolation does not give the full picture, as in addition to viscous dissipation (diffusion of momentum) there will invariably also be some diffusion of mass and heat. To characterize the degree to which these processes affect the flow, the Schmidt number  $Sc$  and Prandtl number  $Pr$  are required. These parameters are a measure of the ratio of the rate of momentum diffusion to mass and heat diffusion respectively, and are given by

$$Sc = \frac{\nu}{\mathcal{D}}, \quad (48)$$

$$Pr = \frac{\nu}{\mathcal{D}_T}. \quad (49)$$

Here  $\mathcal{D}$  is the mass diffusivity between two species and  $\mathcal{D}_T = \kappa_T / (\rho c_p)$  is the thermal diffusivity, with  $\kappa_T$  being the thermal conductivity and  $c_p$  the specific heat capacity at constant pressure. For many gases,  $Sc \approx Pr \approx 0.7$ , and it is common in fundamental turbulent mixing studies to set  $Sc = Pr = 1$  [64]. Thus at very low Reynolds numbers, for  $Pr$  and  $Sc \sim \mathcal{O}(1)$  there will be significant amounts of heat and mass transfer by diffusion, which in such cases will constitute the primary mixing mechanism (rather than turbulent stirring) between the two fluids.

Compared to the Boussinesq approximation (next subsection), the inclusion of variable density introduces additional cubic nonlinearities in the momentum equations as well as a non-zero divergence of velocity, which is a consequence of the change in specific volume that occurs when the two fluids mix. This divergence term on the right-hand side of Eq. (46c) is derived from Eq. (45) and the species mass fraction equations, with the full diffusion operator in the limit of an infinite speed of sound.

This term is also the principal source of additional difficulty that is encountered when solving these equations numerically, compared to incompressible constant-density or Boussinesq formulations. In incompressible solvers, the velocity divergence constraint is satisfied by deriving an elliptic equation for pressure. This equation is obtained by taking the divergence of the momentum equation, combined with the divergence constraint. In constant-density and Boussinesq formulations, combining Eq. (51a) and the divergence of Eq. (51b) results in a constant-coefficient Poisson equation for pressure, which is readily solved through a variety of techniques [158]. For the variable-density

formulation however, combining Eq. (46c) and the divergence of Eq. (46b) leads to a Poisson equation with a factor of  $1/\rho$  in the coefficients, making its solution more complicated and computationally demanding.

Approaches for tackling this problem vary. Sandoval [156] and Cook & Dimotakis [75] use a constant-coefficient Poisson equation for pressure and estimate the  $\nabla \cdot (\rho \mathbf{u})^{n+1}$  term using finite differences of  $\mathbf{u}$  from previous timesteps  $n$  and  $n - 1$ , the divergence constraint and the fact that  $\rho^{n+1}$  is already known at that point in the solution process. This approach has the advantage that no iteration is required for pressure, however the overall accuracy of the temporal discretization is reduced. When used in conjunction with a third-order Adams–Bashforth–Moulton time integration method, the scheme remains stable up to a density ratio of 4, while with third-order Runge–Kutta timestepping density ratios up to 10 can be simulated (A. Cook, private communication).

Livescu & Ristorcelli [80] overcome the reduction in accuracy of the temporal discretization by deriving an exact nonlinear equation for pressure (i.e. no finite difference approximation required for  $\mathbf{u}^{n+1}$ ). The trade-off for eliminating temporal discretization errors is that the pressure equation now requires an iterative solution, increasing the overall computational cost of the scheme. This approach also only works for triply periodic flows.

A third approach is given by Chung & Pullin [159], who use a Helmholtz–Hodge decomposition on the pressure gradient terms in the momentum equation. This leads to a constant-coefficient Poisson equation being obtained for the scalar potential of this decomposition and a nonlinear equation for the divergence-free component that is solved by iteration. This approach ensures that temporal discretization errors are isolated to the divergence-free component. The iteration introduces additional computational cost however, with the convergence rate depending on the Atwood number. In addition,  $\ln(\rho)$  is used instead of  $\rho$  in the timestepping as this ensures  $\rho$  is always positive after dealiasing, but at the cost of not discretely conserving mass (D. Chung, private communication). To date, computations have been run using this method up to a density ratio of 10 [160]. A similar procedure was used by Livescu et al. [161] to simulate planar RTI between fluids with density ratios as high as 19. Recent simulations have also been performed of shear-driven mixing layers between hydrogen and air (density ratio 16) using this method [162]. A key difference with the method of Chung & Pullin is that  $\rho$  is advanced in the timestepping, which ensures that mass is conserved but at the cost of a smaller timestep (D. Livescu, private communication). Other approaches have also been presented, typically in the context of incompressible two-phase flows, such as the method of Dodd & Ferrante [163] who use a pressure-correction technique coupled with a volume-of-fluid method. This approach is quite similar to that of [80], but using only the first step of the iteration.

Finally, we note the recent emergence of novel penalty-based approaches [164] that circumvent altogether solving the computationally expensive variable density Poisson equation. Instead, a penalty function  $\varepsilon$  on the divergence of the velocity field is introduced, while the governing equations are recast in perturbation form, with  $\varepsilon$  as the perturbation parameter [164]. This results in a Poisson equation with constant coefficients that can be solved efficiently without preconditioning. In Guermond & Salgado [164], the authors show that a numerical scheme formulated around these ideas is stable when coupled with monotone methods.

There are also a variety of different configurations used in studies of variable-density turbulent mixing. Sandoval [156] and Livescu & Ristorcelli [80] considered the variable-density extension of the homogeneous problem studied by Batchelor et al. [165]. Chung & Pullin [159] also used a triply periodic

domain but with the fringe-region technique [166], thus producing a statistically stationary flow. Cook & Cabot [75] performed simulations of a planar Rayleigh–Taylor mixing layer at an Atwood number of  $A = 0.5$  and Schmidt number  $Sc = 1$ . Spatial derivatives in the inhomogeneous direction were computed using an eighth-order compact difference scheme to account for aperiodicity. Due to the decreased fidelity of the compact difference scheme versus the spectral scheme used in the homogeneous directions, the grid spacing used in the inhomogeneous direction was decreased by a factor of  $8/13$ . Mueschke & Schilling [167] used this numerical method to perform a DNS of planar RTI with experimentally measured initial conditions, and to compute a variety of statistical quantities that could not be measured in the experiments [168]. Livescu et al. [161] used a similar approach in the inhomogeneous direction (sixth-order compact differences) to perform numerical simulations of planar Rayleigh–Taylor mixing layers for Atwood numbers ranging from 0.04 to 0.9.

While the variable-density formulation allows for accurate results to be obtained for mixtures of miscible fluids at arbitrary Atwood numbers, its range of applicability is still limited to low-speed flows. Typically, departures from incompressibility are considered to occur starting at a Mach number (mean and/or fluctuating) of  $M \approx 0.3$  [169]. In general, this precludes the study of the RM instability using this formulation, as although the development of the instability at late time is virtually incompressible for small to moderate shock Mach numbers, the shock wave itself is an inherently compressible phenomenon. This is not always the case however and deviations from the incompressibility approximation are typically handled using two approaches mentioned here. The first approach uses a hybrid solver that switches between compressible and incompressible formulations based on the maximum local Mach number. This was the approach taken by Oggian et al. [170], who found that a threshold value of  $M = 0.2$  was optimal. The second approach, valid for initial perturbations that are entirely linear, is to use an equivalent velocity perturbation [95], thus circumventing the need to initialize a shock wave. This approach has been used in conjunction with compressible solvers [95,171], however it also represents an intriguing way to apply state-of-the-art incompressible solvers to RMI flows.

### 5.3.2. Boussinesq approximation

The basic formulation for buoyancy-driven incompressible flow in the Boussinesq approximation is given in Batchelor et al. [165]. In this approximation, fluctuations in density  $\rho'$  are assumed to be small relative to the mean density  $\rho_0$  and are due to the dependence of instantaneous density  $\rho = \rho_0 + \rho'$  on a conserved scalar  $\phi = \phi_0 + \phi'$  (such as concentration, temperature). Fluctuations in  $\rho$  and  $\phi$  are related linearly by

$$\rho' = \beta_B \phi', \quad (50)$$

where  $\beta_B$  is a constant (e.g. in the case where  $\phi$  is temperature,  $\beta_B = -\rho_0 \kappa$  where  $\kappa$  is the coefficient of thermal expansion). The density variations are assumed to affect the flow only through changes in the buoyancy force. The equations governing the motion of Boussinesq fluids can therefore be written as

$$\nabla \cdot \mathbf{u} = 0, \quad (51a)$$

$$\frac{\partial \mathbf{u}}{\partial t} + \mathbf{u} \cdot \nabla \mathbf{u} = \nu \nabla^2 \mathbf{u} + \frac{\rho' \mathbf{g} - \nabla(p - \rho_0 \mathbf{g} \cdot \mathbf{x})}{\rho_0}, \quad (51b)$$

$$\frac{\partial \rho'}{\partial t} + \mathbf{u} \cdot \nabla \rho' = D \nabla^2 \rho', \quad (51c)$$

where  $\nu = \mu/\rho_0$  is the kinematic viscosity and  $D$  is the diffusivity associated with  $\phi$ . The dot product of the acceleration vector

$\mathbf{g}$  and the position vector  $\mathbf{x}$  gives the specific potential energy (e.g. due to gravity). The equations may also be equivalently formulated in terms of the fluctuation  $\phi'$ , for example see Landau & Lifshitz [147] for full details of the derivation of Eq. (51) in the context of free convection. Note that Eqs. (51) also apply to mixing of a single gaseous species at two different temperature (for that case  $D$  is the heat diffusivity,  $D_T$ ). A recent review of Boussinesq Rayleigh–Taylor turbulence is given in Boffetta & Mazzino [172].

In Batchelor et al. [165], Eqs. (51a)–(51c) were solved numerically using the Fourier pseudo-spectral code of Rogallo [173] developed for homogeneous turbulence. This is an important advantage of using the Boussinesq approximation; accurate and efficient codes developed for studying homogeneous turbulence may be applied with little modification to study buoyancy-driven effects. In general, the choice of numerical methods is guided by wanting to minimize dissipation and dispersion errors for a given amount of computational effort. For incompressible flows, this is typically achieved with spectral methods [174].

A triply periodic domain was used in [165] and the flow was initialized with homogeneous, isotropic perturbations to the density field. This homogeneous configuration may be considered to be an approximation of the interior of a fully developed Rayleigh–Taylor mixing layer at a small Atwood number. Planar Rayleigh–Taylor mixing layers have also been studied using the Boussinesq approximation, with various approaches taken for dealing with modeling the inhomogeneous direction. Young et al. [175] applied no flux, no slip boundary conditions in the inhomogeneous direction and used spatial discretization with a Chebyshev polynomial basis to handle the aperiodicity. That same study also used a spectral-element method for comparison, an approach that was also taken by Vladimirova & Chertkov [176] who studied a similar configuration. An alternative approach is to retain periodicity in all three directions by applying a second density interface far away from the primary mixing layer, which will remain Rayleigh–Taylor stable since the top fluid is lighter. This allows for the use of a Fourier pseudo-spectral code in all three directions, as in the studies of Boffetta et al. [177] and Matsumoto [178].

Given that changes in density only produce changes in momentum through the buoyancy force in the Boussinesq approximation, the equations of motion are independent of the Atwood number, written here as  $\mathcal{A} \Delta \rho / (2\rho_0)$ . In this formulation, the role of the Atwood number is merely to rescale the non-dimensional time of the simulation. As explained in Section 4.6, for RTI in the self-similar regime  $h = \alpha_{RT} \mathcal{A} g t^2$  and therefore  $\text{Re} \propto \mathcal{A}^2$ , so that a higher Reynolds number may be obtained for the same computational effort if the Atwood number is increased. This is why studies exploring the scaling of various quantities in the self-similar regime have used a relatively high Atwood number of  $\mathcal{A} = 0.1$  [177,179] or even  $\mathcal{A} = 0.15$  [178]. Physically, the Boussinesq approximation is valid only for very low Atwood numbers. For Rayleigh–Bénard convection in air at standard atmospheric conditions, Gray & Gioginy [180] found the Boussinesq approximation to give results with at most a  $\pm 10\%$  error so long as the maximum temperature difference does not exceed 28.6 K (i.e. roughly 10% of the mean). This corresponds to an Atwood number of  $\mathcal{A} = 0.05$ , hence studies aiming to match laboratory conditions or investigate transition to turbulence have typically used  $\mathcal{A} = 0.01$  or lower [104,175].

For RT flows, the suitability of the Boussinesq approximation at different Atwood numbers was investigated in [181] in the linear, nonlinear, single-mode and turbulent cases using dimensional analysis and scaling arguments. If the Boussinesq approximation is applied by taking  $\mathcal{A} = 0$  everywhere, except when it couples with gravity, the solution to the linear stage

of growth is immune to this approximation since the waveform retains symmetry between the light and heavy fluids. However, the approximation will significantly affect spike calculations and (to a lesser extent) bubbles in the nonlinear stages when the density ratio is  $\gg 1$ . For bubbles, applying this approximation to the potential flow models of [181], the terminal velocity in the Boussinesq approximation is  $V_b^{\text{Boussinesq}} \sim \sqrt{2\mathcal{A}g/k}$ , and thus overpredicts the true bubble velocity by  $V_b^{\text{Boussinesq}}/V_b \sim \sqrt{1+\mathcal{A}}$ . Similarly, the asymptotic ratio of bubble amplitudes is obtained from integrating the corresponding expressions for bubble velocities in time and taking the limit  $t \rightarrow \infty$  to give,

$$h_b^{\text{Boussinesq}}/h_b \sim \sqrt{1+\mathcal{A}}. \quad (52)$$

Mikaelian [181] obtained the above results by applying the Boussinesq approximation ( $\mathcal{A} = 0$  except in  $g\mathcal{A}$ ) to the analytic model in [181], and taking the asymptotic limit. Thus, bubbles are moderately over-estimated by the constant density approximation, and this leads to a maximum error of  $\sim 41\%$  at  $\mathcal{A} = 1$  [181]. In contrast, spikes exhibit differentiated behavior for  $\rho_2/\rho_1 > 1$ , culminating in free-fall at  $\mathcal{A} = 1$ , and thus cannot be described by the Boussinesq approximation.

#### 5.4. Interface tracking

The above formulations and numerical approaches are strictly valid for simulating turbulence between miscible fluids. Thus, physical diffusion across a material interface is either explicitly modeled or treated using interface capturing schemes where the interface is “smeared” across some finite width region within the computational domain. However, there are often compelling reasons for modeling an interface as exactly discontinuous without numerical or physical diffusion. One such scenario is when the fluids being studied are immiscible or of different phases (multiphase). Another scenario is when the interface is of negligible thickness compared to the size of the computational grid, which is the case for flame fronts or the early stages of RM/RT instabilities. Indeed, early research into RT and RM instabilities focused on understanding single-mode growth and typically some form of interface tracking was used for this purpose, particularly due to the limited computational resources available at the time [100]. Such simulations were also typically inviscid. When examining turbulence induced by RTI/RMI, interface tracking was deemed to no longer be appropriate in situations where significant fine-scale breakup of the interface occurs. However, for situations where the interface radius of curvature is greater than the grid size, such as those discussed above, some form of interface tracking remains a viable and sometimes necessary approach to modeling the interface evolution in time. In addition to studies of turbulence, other areas of application include the modeling of various multiphase processes such as RTI/RMI in liquid–gas mixtures and shock-induced ejecta.

There are three main approaches that have been used to perform interface tracking in fluid dynamic simulations: (Eulerian) level set methods [182], (Lagrangian) front tracking methods [183] and volume-of-fluid or interface reconstruction methods [184]. In level set methods, the location of the interface is implicitly defined through the use of a level set function  $\phi$ , the evolution of which is given by

$$\frac{\partial \phi}{\partial t} + \mathbf{u} \cdot \nabla \phi = 0. \quad (53)$$

The zero level set  $\phi = 0$  corresponds to the location of the interface and the level set method consists of approximating the solution of Eq. (53) by discretizing the operators on a fixed grid. In general,  $\phi$  is initialized as a signed distance function, and is

adverted according to the numerical solution of Eq. (53). Near the interface, the level set function is constantly reinitialized to remain a signed distance function, whenever information about the interface location is required. In front tracking methods, the interface is described explicitly by topologically-linked marker particles which are propagated according to the underlying velocity field (which may depend on the front geometry). A key aspect of such methods is the handling of topological bifurcations, particularly in 3D, and typically some form of interface reconstruction is used in regions where bifurcation is detected. Interface reconstruction methods, specifically the volume-of-fluid method, represent the interface implicitly through a scalar field  $C$  that gives the volume fraction of a reference fluid in each cell. The color function  $C$  takes values  $0 < C < 1$  in cells cut by the interface, either 0 or 1 away from the interface, and is governed by an advection equation of the same form as Eq. (53). At each timestep, a reconstruction (typically piecewise linear) of the interface is performed based on the  $C$  field. Each interface segment is then advected according to the velocity field and the resulting volume, mass and momentum fluxes are determined.

The relative advantages and disadvantages of each approach are discussed in Sethian & Smereka [182] for level set methods, Du et al. [185] for front tracking methods and Scardovelli & Zleski [186] for volume-of-fluid methods and will be briefly summarized here. Level set methods are advantageous for their ease of calculating geometric quantities such as curvature, extension to three-dimensions, and the handling of topological changes. Volume-of-fluid methods also handle topological changes implicitly, can also be easily extended to 3D and conserve mass well. They are also simple to parallelize, since the reconstruction scheme is local. Front tracking methods are inherently more accurate than the other two approaches, due to their ability to represent the interface with a much larger number of points. This increased accuracy comes at the cost of requiring explicit handling of topological changes however.

The use of interface tracking methods in simulations of turbulent mixing due to RT and RM instabilities has primarily been to study the effects of immiscibility. The level set method was used by Young & Ham [29] to simulate the incompressible RT between two viscous fluids with varying amounts of surface tension. George et al. [187] also performed simulations of RT instability with physical surface tension, using the front tracking code FronTier. Indeed, front tracking has proven useful in determining the degree to which surface tension influences mixing between partially immiscible fluids [122]. Volume-of-fluid methods have also been used in simulations of turbulent RT/RM [63,69,188], however, due to a lack of surface tension the results are only useful in distinguishing between heterogeneous and homogeneous mixing by inhibiting numerical diffusion and do not constitute a true study on the effects of immiscibility. This is not a fundamental limitation of the volume-of-fluid approach however and there is potential to use a volume-of-fluid approach to study the effects of immiscibility on RT/RM flows, with surface tension implemented through the continuum surface force method [184].

The use of some form of interface tracking to resolve gradients that are sharp with respect to the computational grid is also potentially beneficial for modeling early time development of RM and RT flows between miscible fluids. As previously mentioned, front tracking has also been used to simulate mixing between miscible fluids [152], where the front being tracked is typically an isosurface of concentration or temperature. In addition to the front tracking approach, there is potential for combining volume-of-fluid interface reconstruction with a diffuse interface model, such as the newly proposed five-equation model of Thornber et al. [144]. This would allow for steep gradients present during the early time evolution of RM and RT to be accurately resolved, while also retaining the simplicity of a diffuse interface approach once the gradients are captured sufficiently on the computational grid.

## 6. State of the art in numerical simulations

The mathematical formulations discussed in Section 5 describe completely, at the continuum level, the evolution of the flow field that ensues from a given initial condition (assuming well-posedness). Under suitable conditions, as discussed in Section 4.6, the flow will become turbulent. The wide range of scales accompanying turbulence is described in full by the governing equations. However, in order to obtain a numerical solution, these equations must be discretized without losing a significant amount of information about the fine-scale structure of the flow in the process. In particular, turbulent motions at scales smaller than the Nyquist wavelength of the computational grid employed will be lost (or reappear as an aliased wavenumber), while scales that are close to the grid scale will be severely impacted by the numerics. This will in turn affect the evolution of the grid-resolved flow field in time, since there exists a cascade of energy from large to small scales, and this energy is only dissipated at the very smallest scales by viscosity [189]. The handling of the impacts of finite grid resolution when simulating unsteady, turbulent flow is addressed in this section.

### 6.1. Direct numerical simulation

In order to retain a complete description of the turbulent flow field numerically, all the scales of motion must be resolved in the discretization (both spatially and temporally). Approaches that conform to this requirement are referred to as DNS, whereby the numerical solution that is obtained is considered to be independent of the numerical method and the grid resolution used. This can be achieved at the continuum level through simulations in which the following criteria are met: (i) the Navier–Stokes equations are solved with all relevant transport terms using an appropriate high-order method and (ii) the numerical resolution employed is such that the entire dynamic range of scales of motion is resolved. Simulations in which only condition (i) is satisfied are sometimes referred to as Navier–Stokes simulations. As a result of the above criteria, in computational terms DNS is often prohibitively expensive, particularly for problems of practical interest (i.e. flows at high Reynolds numbers and/or complex geometries). In fully developed RT/RM turbulence, multiple scales must be adequately resolved: the initial interface thickness, the dominant wavenumber in the initial condition, the Kolmogorov scale  $\eta$  at which viscous dissipation occurs and when mass diffusion is present, the Batchelor scale  $\eta_B$  at which scalar dissipation occurs. For RT turbulence, the outer-scale Reynolds number is typically defined by Eq. (37),

$$Re \equiv \frac{h\dot{h}}{\nu}, \quad (54)$$

where  $\mathcal{L} = h$  and  $\mathcal{U} = \dot{h}$ . Combining Eq. (54) with Eq. (38) and  $h/\eta = Re^{3/4}$ , the following expression for  $\eta$  is obtained:

$$\eta = \frac{(\frac{\nu}{2})^{0.75} t^{-0.25}}{\sqrt{\alpha A g}}. \quad (55)$$

The above scaling has also been suggested by [75,104] and verified through DNS in [75,77,104]. Thus, scale separation in self-similar RT implies a Kolmogorov scale nearly independent of time (while the large scales grow as  $\sim t^2$ ), a result that is fortuitous to the design of numerical simulations since the smallest flow scales dictate the grid resolution. A second concern, is the growth of grid-generated, spurious modes that can nevertheless be driven by the buoyant forces in the flow. The criterion for the growth of such numerical modes may be given in terms of a grid Grashof number

$$Gr_{\Delta x} = \frac{g \Delta \rho V}{\rho v^2} \sim \frac{2A g \Delta x^3}{v^2}, \quad (56)$$

where  $\Delta x$  is the mesh size. For mesh-generated numerical modes to be stabilized by viscous diffusion,  $\Delta x$  must be such that  $Gr_{\Delta x} < 1$ . When mass diffusion is present, this condition for resolution requirement may be further modified to  $Gr_{\Delta x} = 2.4g \Delta x^3 / (\nu + D)^2 < 1$ .

However, there are a few issues with the above definitions and analyses. Firstly, the assumption that the Kolmogorov scale is representative of the smallest eddies in the flow is predicated upon the presence of an inertial range in the turbulent kinetic energy spectrum i.e. the turbulence is fully developed. In a temporally developing flow, such as a mixing layer, this is not always the case. Secondly, mixing layers can be anisotropic as well as inhomogeneous, making the definition of a single Kolmogorov scale problematic. Typically, in planar mixing layer configurations, the definition of length scales such as the Kolmogorov scale, as well as the calculation of spectra is restricted to the homogeneous directions in which isotropy prevails [75]. A Kolmogorov scale can also be defined in the inhomogeneous direction, but will not necessarily equal the value of  $\eta$  defined in the other directions for significant degrees of anisotropy (e.g. the early time RMI mixing layer). It is also difficult to estimate a priori the value(s) of  $\eta$  for the duration of the simulation, as well as the contributions of motions smaller than  $\eta$ .

Given the above considerations, the DNS label is applied in practice if the grid resolution in a simulation is fine enough to accurately resolve most of the dissipation in the flow, since this will result in reliable first and second order statistics [174]. This can be ensured by verifying the higher-order statistics such as the dissipation rate  $\varepsilon$  are sufficiently converged in the temporal, spatial and spectral domains. This requirement also translates to the smallest resolved length scale being of  $\mathcal{O}(\eta)$ , not equal to  $\eta$ . For Schmidt numbers greater than one, it is also necessary to ensure that scalar dissipation is accurately resolved. In addition to requiring sufficient grid resolution at the small scales, the domain size must ensure the largest scales in the flow are accurately represented. In the inhomogeneous directions, this will be dictated by physical constraints (e.g. mixing layer width), while in the homogeneous directions two-point correlations of the solution should decay to zero within half the domain length in order to obtain a proper statistical representation. If this is not the case, the solution is said to be "box-constrained" and multiple independent realizations must be performed [190].

In spite of the above restrictions, DNS still plays an important role in fundamental studies of turbulent mixing, where the problem can be designed such that it contains a tractable range of scales. Such canonical problems are used to gain insights into the nature of turbulent mixing in an idealized configuration, so that such insights may then be applied to developing reduced-order models for complex scenarios such as inertial confinement fusion implosions, core-collapse supernovae or the many other applications that are discussed in the following sections of this paper.

There are multiple ways in which numerical errors arise and affect the flow field during simulations. One major source of errors are truncation errors that result from approximating gradients or interpolation, which reduce the level of fidelity with which fine-scale motions in the flow can be resolved. These errors correspond to numerical sources of dissipation and dispersion, due to similarities with their physical counterparts in their effect on the flow field. Errors also stem from the finite representation of continuous functions, known as aliasing errors. These errors arise through nonlinear interactions leading to the spurious generation of modes that are not in the set of modes being represented and whose contributions are added incorrectly to the flow field. Finally, errors due to finite grid resolution are also introduced at scales near the grid spacing, where triadic

interactions that occur between scales (because of nonlinearities in the governing equations) are not represented properly. In principle, these errors will diminish as the grid resolution is increased and should be negligible in a fully resolved DNS. As stated previously in Section 5.3, a suitable numerical method for DNS should minimize the effects of the various errors for a given computational effort. This aim guides much of the choice of numerical algorithms in DNS studies.

Flows with shock waves present an additional complication, since the thickness of the shock is typically much smaller than  $\eta$ . Hence, resolving the shock to the point where its thickness is determined by physical viscosity is often prohibitively expensive. The conventional form of the governing equations is also not valid within the shock wave, particularly for strong shocks, due to non-equilibrium effects and ill-posedness [191]. Some calculations have been performed with fully resolved shock waves, for example the simulations of early-time RMI by Margolin & Reisner [192] or shock-turbulence interaction by Ryu & Livescu [193]. However, the typical approach when simulating such flows is to use a shock-capturing approach [194], where the internal structure of the shock is lost but the jump conditions across the shock are still enforced. With this approach, it is important to minimize the impacts of the extra numerical dissipation that is introduced in order to stably capture the shock, as discussed in Section 5.2.

## 6.2. Large eddy simulation

As previously discussed, for Reynolds numbers of practical interest, DNS is not a feasible approach, simply due to the prohibitive amount of computational effort needed to simulate the full range of scales present in a turbulent flow for any significant period of time. Furthermore, most of this effort is expended in computing the evolution of scales that contain a minority of the energy in the flow, viz. the small-scales. These considerations motivate the modeling approach known as large-eddy simulation (LES), where the unsteady dynamics of the largest scales are explicitly computed while the influence of the smaller scales, which are statistically universal, is modeled. Conceptually, LES involves a low-pass filtering operation, where the flow field is decomposed into a filtered and residual component. The equations of motion for the filtered component are derived from the original governing equations and will contain contributions arising from residual motions, which are supplied by some form of closure model [195]. It is important to note that the filtering operation must be independent of the grid resolution and defined as

$$\bar{f}(\mathbf{x}, t) = \int G(\mathbf{r}, \mathbf{x}) f(\mathbf{x} - \mathbf{r}, t) d\mathbf{r} \quad (57)$$

for some function  $f(\mathbf{x} - \mathbf{r}, t)$ . In other words, the filtering operation is a convolution of  $f$  with some kernel function  $G$ , where  $G$  depends on a characteristic filter width  $\Delta$  and potentially also the grid position  $\mathbf{x}$ . In practice, the ratio of the grid spacing  $h$  to the filter width is fixed, so that the following trade-off exists: for a given grid resolution, resolving a wider range of modes comes at the expense of improving the accuracy of the approximation for modes that are already resolved. If  $\Delta = h$  then the residual component of the flow field may also be called the subgrid component, while the filtered component may also be called the resolved component [196]. This is the terminology used in the following sections which, although formally inappropriate when  $\Delta > h$ , is convenient for the purposes of the present discussion.

### 6.2.1. Explicit subgrid modeling

If a closure model for the residual stresses is provided, either in physical or wavenumber space, then the modeling approach is referred to as explicit subgrid modeling or explicit LES. Within explicit LES, a further distinction is made based on whether or not the error of the numerical approximation for the filtered governing equations is negligible, similar to the requirement of negligible numerical error when conducting DNS of the full governing equations. In order to obtain grid-independent solutions the filtering operation must be performed explicitly, with negligible numerical error produced when  $\Delta/h \gg 1$ . This approach is sometimes referred to as pure LES [196]. However, in order for the LES to generate useful results, a significant portion of the turbulent kinetic energy in the flow should be resolved. Considering homogeneous turbulence as an example, assuming a Kolmogorov  $k^{-5/3}$  model spectrum and requiring that 80% of the TKE be resolved gives  $k_c L_{11} = 15$  [197], where  $k_c$  is the cutoff wavenumber and  $L_{11}$  the integral length scale. Calculating accurate statistics at large scales requires that  $L \geq 20L_{11}$  [190], therefore at least 48 modes need to be resolved, requiring a minimum grid resolution of  $96^3$ . In addition, for negligible numerical error a filter width to grid spacing ratio of at least  $\Delta/h = 4$  is required for most schemes [198], bringing the minimum required grid resolution in this example to  $384^3$ . If instead 90% of TKE is required to be resolved, then the grid resolution requirement now becomes at least  $960^3$ . Therefore, as noted by Pope [196], the optimal value of  $\Delta/h$  for a given grid resolution most likely corresponds to some non-negligible amount of numerical error being retained, so that the modeling error is reduced. In the limit of  $\Delta = h$  the explicit filter may be dropped altogether, with the filtering instead being performed implicitly by the numerical method [199]. Despite some obvious drawbacks, this approach is often desirable for multicomponent flows. This is due to the fact that an explicit convolutional filter cannot satisfy positivity/boundedness of the flow variables (i.e. density, mass fractions) without also introducing aliasing errors [200].

For flow at high Reynolds numbers, the requirement that the majority of TKE in the flow be resolved implies that the filter width  $\Delta$  be located in the inertial subrange of the energy spectrum. This represents the ideal case for the application of LES, as (i) it is in this regime that the various assumptions inherent in simple subgrid models (i.e. eddy viscosity models) are well justified and (ii) accurate estimates of the residual quantities are available. This second point becomes increasingly valuable when estimates of the residual motions are required in models for other subgrid processes such as chemical or nuclear reactions. For cases where the filter width is not located in the inertial subrange, such as under-resolved, transitional or laminar flow, the subgrid model can provide too much dissipation, particularly if it is relatively simple in construction [197]. For laminar and transitional flows, it may be possible to obtain accurate results using DNS or more sophisticated subgrid modeling techniques. In the case of the flow being under-resolved, which is commonly the case in applied computations (as opposed to canonical problems), it can often be challenging to satisfy both the resolution of the full problem at hand and the necessary separation between the large and filter length scales.

In incompressible flows, there is only a handful of terms in the filtered governing equations requiring closure; namely the residual stress tensor as well as subgrid mass/scalar fluxes in the case of multicomponent flow. A wide range of closure models exist for these terms, and the most commonly used models are summarized in the review articles of Lesieur & Métais [201] and Meneveau & Katz [202] and the book by Sagaut [203]. In contrast, for compressible flows there are more terms requiring more complicated closures due to the presence of the energy equation.

Additional complications also occur in flows with discontinuities such as shock waves, where the combination of a subgrid model and numerical dissipation can be excessively dissipative. The subgrid motion in a computational cell containing a shock is also significantly different from the case of canonical turbulence that subgrid models are typically constructed to represent, hence a common approach is to set the subgrid interaction to zero in these zones [204]. Some popular models include those of Vreman et al. [205], the stretched-vortex model as well as the use of artificial fluid properties [200].

The above approaches are in contrast to so-called ‘structural’ models [206], which aim to represent structural aspects of some sub-grid field (typically vorticity), and compute the effect of such a field on the resolved scales. An example of this approach is the Nonlinear LES (NLES) method of Burton [117,207] which was applied to RT mixing at  $A > 0.9$ . In [207], the subgrid stress is not modeled using an eddy viscosity approach, but is computed directly from a sub-grid velocity field  $u_{SGS}$ . In the approach of [207],  $u_{SGS}$  is constructed from a corresponding multifractal sub-grid vorticity field generated by the repeated application of a scale-invariant multiplicative operator. This process ensures the sub-grid vorticity field  $\omega_{SGS}$  satisfies multifractal scale-similarity as found in experimental observations. The corresponding sub-grid velocity field is obtained by integrating the vorticity field through the Biot–Savart integral. The advantage of such structural LES schemes is that they imply sub-grid fields with the same scale-similarity as observed in experiments, while the computational cost is comparable to conventional LES. The NLES model belongs to a broader class of structural models, of which the sub-grid stretched vortex model suggested by [208,209] was an early successful example. In the stretched vortex model, sub-grid stresses are computed from an assumed distribution of nearly cylindrical sub-grid vortex structures that are aligned with the resolved field strain rate over a fast timescale.

### 6.2.2. Implicit subgrid modeling

Calculations that exclude the use of an explicit filter and subgrid model are referred to as ILES or Monotone Integrated LES (MILES) and can be used to obtain accurate statistics of the large scales in very high Reynolds number flows [76,210–212]. ILES aims to tackle several of the identified challenges for explicit LES with non-dissipative algorithms, namely the need to (i) ensure monotonic behavior at shock waves and contact surfaces, (ii) provide minimal dissipation in the early linear and non-linear stages of instability growth, (iii) formally separate the filter and mesh scale or ensure numerical dissipation and dispersion do not conflict with the explicit model, and (iv) consider non-equilibrium effects.

ILES use the numerical dissipation of the underlying algorithm to provide the dissipation necessary to remove energy from the smallest resolved scales – acting as an implicit sub-grid model. In principle, any sufficiently dissipative numerical method can be used to perform ILES, provided there is sufficient scale separation in the flow being simulated so that the largest scales of motion are insensitive to the specific mechanism by which energy is removed from the flow. Although some numerical methods do aim to mimic specific sub-grid models, or have explicit stabilization terms, for most algorithms the dissipation rate is a complex function of the pressure, density and velocity field and does not directly map to an explicit sub-grid model. However, this does not preclude the use of ILES, since Kolmogorov’s assumption of the independence of large scales from the dissipative scales may be applied directly to any sub-grid dissipation mechanism. Thus, as long as the specific numerical dissipation mechanism does not impact the resolved large scales, the large scales will evolve physically. This may be seen in the very good agreement in large

scale quantities between substantially different ILES codes when applied to an identical problem [63], including individual terms in the turbulent transport budgets [213].

For the majority of numerical methods which do not attempt to mimic a specific subgrid model, numerical dissipation is introduced to control ringing of the solution at shocks. This is introduced as higher-order modeling approaches appropriate to incompressible flows with low density contrasts may lead to unphysical results around shocks and strong contact discontinuities. For the purposes of numerical stability, energy must be removed from the flow at high wavenumbers by the numerics, using physically-motivated limiting approaches, and thus plays a similar function to an explicit sub-grid model. In practice, this is typically achieved by using a non-oscillatory numerical method, such as the flux-corrected transport, piecewise parabolic or Godunov finite-volume methods. Most approaches employ at least second-order accurate schemes. The advantage of higher-order methods is that the implicit subgrid model is nonlinear and heavily weighted toward the smallest scales resolved by the grid, which improves the computational efficiency of the calculation since it increases scale separation. Use of these schemes also allows for discontinuities such as shock waves and material interfaces to be robustly handled in an ILES calculation. The implicit filtering operation is also naturally anisotropic wherever there is anisotropy in the grid (this is also true of explicit LES schemes with implicit filtering).

Given that each numerical method has a unique dissipation mechanism and magnitude, an ILES practitioner must pay careful attention to the properties of their numerical method to choose the appropriate grid resolution for a given problem. This is typically established by undertaking computations of single mode instability development at very coarse grid resolution (e.g. 8–16 grid points per wavelength), equivalent to the resolution of very high wavenumber modes on a much larger grid. The total needed grid size for a specific problem can then be computed once the minimum number of points to accurately evolve a single mode is established, along with the expected integral scale and the requirement for the resolution of a given proportion of total kinetic energy (as already discussed).

There are three key caveats to consider in the application of ILES. The first is that the dissipation from the subgrid model may not enforce any expected universality of the unresolved scales. The second is that there is no formal point-wise grid independence, which may be gained in explicitly filtered LES. This means that for each grid, a different flow is being computed. While methods exist for defining the effective Reynolds number (and hence viscosity) in an ILES calculation [69,126–129], it remains problematic to evaluate during the simulation itself, although this is also true of many explicit LES models. Thirdly, when estimates of subgrid motions are required for models of other subgrid processes (such as reactions), it is only possible to use methods based on the resolved scales (see e.g. [214]).

To expand on the third point, the flows being solved in ILES have the same rate of subgrid transfer for mass, momentum and energy (assuming the same numerical scheme is used for each equation) and therefore the Schmidt and Prandtl numbers are nominally equal to one [119]. However, flows of sufficiently high Reynolds numbers that have passed the mixing transition (as described in Section 4.6) should be insensitive to specific values of viscosity and diffusivity [3,84,89], at least when the rate-controlling processes in the flow are determined by the resolved large scales. With this in mind, most ILES of compressible turbulent mixing are performed in the nominally inviscid limit, as the contributions from viscous terms to the resolved scales of motion will be negligible in comparison with numerical dissipation.

Therefore, an appropriate application of ILES is in computing the high Reynolds number limit of statistical quantities that

depend on the energy containing scales, in flows where the rate-controlling processes are also determined by these scales. Free shear flows, as well as RT and RM induced mixing layers, satisfy this requirement in the self-similar regime, and hence ILES is expected to be effective at accurately computing integral quantities such as mix width for these flows in the high Reynolds number limit.

During linear, non-linear growth of perturbations, and transition to turbulence, the small scale properties may become under-resolved on a given grid, but may not yet be turbulent. In that period of mixing layer development, both explicit and implicit LES may not give accurate results for properties of the subgrid scales such as mixing. Until models of unresolved mixing during transition are developed, an approach is a combination of DNS of the initial, laminar and transitional growth and then LES (implicit or explicit) of the late time self-similar growth. In RM in particular, the Reynolds number varies as  $t^{2\theta-1}$ , and thus may reduce in time for some initial conditions. In that case, DNS may also need to be employed at late-time.

A comprehensive analysis of the applicability of several numerical methods to RT/RM turbulence can be found in the comparative numerical studies known as the  $\alpha$ -group and  $\theta$ -group collaborations respectively, which mostly comprised results from ILES codes. In the  $\alpha$ -group study [69], six compressible codes and one incompressible code were used to investigate self-similar Rayleigh–Taylor turbulence evolving from a high-wavenumber, narrowband, multimodal perturbation in the nearly incompressible regime. The codes used in the  $\alpha$ -group study included three solvers based on the Piecewise Parabolic Method (PPM); FLASH, WP/PPM and NAV/STK. Three other compressible codes were used including ALEGRA and HYDRA, both ALE codes with optional interface reconstruction capabilities, and the Lagrange-remap code TURMOIL. The Lagrange-remap method used in TURMOIL is similar to an ALE method and operates on a staggered grid. Multiple Lagrangian advection steps may be run, particularly at low Mach number, prior to a remap back to the initial grid. A distinguishing feature of this approach is that the Lagrangian phase is non-dissipative in the absence of shocks, while the dissipation in the remap phase is independent of the Mach number, making it well suited for computing nearly incompressible flows. A direct quantification of the amount of numerical dissipation introduced in the remap phase is also available with this method, which is useful for estimating the level of grid independence obtained when performing DNS [64]. The relative resolving power of each of the codes in the  $\alpha$ -group study was compared by examining the critical wavenumber  $N_{\text{crit}}$ , beyond which the spectra of fluctuating volume fraction depart from the expected Kolmogorov inertial range.

For the  $\theta$ -group study [63], seven compressible codes (and an additional interface reconstruction code) were used to perform simulations of turbulent mixing induced by the multimode, narrowband RM instability. The codes used in the study include the previously discussed ARES, Miranda, FLASH and TURMOIL as well as the conservative finite difference code Triclide [215] and two high-order Godunov methods, Flamenco [216] and NUT3D [217]. As previously discussed, for standard Godunov methods, pressure and density fluctuations scale as  $\mathcal{O}(M)$  in the incompressible limit, contrary to the theoretical  $\mathcal{O}(M^2)$  scaling [218]. This results in a kinetic energy dissipation rate of  $\varepsilon \sim 1/M$  in the standard formulation of these schemes and hence any low-Mach features in the flow are heavily damped. In Flamenco, a correction for this behavior is applied in the reconstruction phase [219], restoring the correct scaling of pressure and density in the incompressible limit and significantly enhancing the fidelity of the numerical method for little additional computational cost. The algorithm has also recently been extended to include a DNS

capability [194], as well as a semi-Lagrangian moving mesh option [220]. This approach maintains the favorable properties of Godunov finite-volume methods, namely robust shock capturing and good resolution of material interfaces, while also improving the ability to resolve fine-scale vortical motions.

Comparisons between the various codes in the  $\theta$ -group collaboration found that there was very good agreement in the representation of the large scales of motion for quantities such as the turbulent kinetic energy spectra and the growth exponent  $\theta$ . The main sources of disagreement between the codes were in general confined to higher wavenumbers and determined to be due to the different dissipative properties of the various numerical methods. The study also gave some insights into the relative advantages and disadvantages of each of the main approaches to modeling compressible turbulent mixing. One such issue is in the definition of initial conditions, with algorithms based on finite-differences requiring that there be a smoothly varying profile across the material interface to avoid oscillations due to Gibbs phenomenon. Other algorithms, such as finite-volume methods, are able to initialize with a sharp profile, provided an appropriate cell-average is specified.

## 7. Effects of material strength on RT instabilities

### 7.1. Preliminary remarks

The classical presentation of RT and RM instabilities in previous sections is indeed useful, as it represents the simplest manifestation of the phenomenon and allows one to develop an intuition regarding the fundamental physics at work. However, as is evident from the myriad of applications discussed in this Special Issue, the RT instability's "real world" manifestations are inevitably complicated by any number of "non-classical" considerations. At first glance, these complications can easily be viewed as an annoyance in which the fundamental physics is obscured by "non-fundamental" details which introduce deviations from the classical behavior. However, if the experimental or observational tools for probing a system are sufficiently precise, these deviations may provide a means of studying, and even quantifying, the complicating physics. One such example is found in the behavior of solid materials under extreme pressures where they exhibit hydrodynamic properties more typical of fluids.

The essential point suggesting the possibility of inferring material strength through RT growth measurements in solids is that material strength tends to suppress this growth [32,221]. Thus, at one extreme is the case of classical RT growth (no strength), while at the other extreme (infinite strength) RT growth is suppressed entirely. Between these extremes lies a wide range in which the RT instability will be more or less suppressed, and the degree of this suppression may be used as a window into the material's strength. Unfortunately, this window is more translucent than transparent, as material properties such as strength are decidedly non-constant as the material evolves from its initial ambient condition to the pressures and temperatures required to generate measurable RT growth in solids.

Material strength is conventionally separated into two regimes, those of elastic and plastic deformation. Elastic deformation is assumed to be reversible up to a certain yield stress, described by the shear or bulk modulus. This assumption is reasonable under dynamic loading conditions, but does not take into account longer term deformation mechanisms such as ductility, creep, brittle failure or fatigue [222–225]. For a typical metal under tensile loading in ambient conditions, irreversible plastic deformation starts once the stress exceeds a yield threshold of  $Y \sim 100$  MPa

$= 1$  kbar. More generally, yield occurs when the von Mises condition is exceeded, i.e.

$$\frac{1}{2}S_{ij}S_{ij} = \frac{Y^2}{3} \quad (58)$$

where

$$\mathbf{s} = \boldsymbol{\tau} - \frac{1}{3}(\text{tr } \boldsymbol{\tau})\mathbf{I} \quad (59)$$

is the stress deviator. Typically, the material is assumed to deform so as to return the stress onto the von Mises yield surface. However, the yield strength increases by an order of magnitude (or more) under the high pressure dynamic conditions required to achieve RT growth in solids [226]. Thus, the strength  $Y$  is no longer a unique value, but is a function of the material's pressure and temperature; in more realistic material models, additional variables are also taken into account, including the strain rate and dislocation density, among others. These models will be described in detail in Section 7.3.

The purpose of this section is to introduce the relatively new field of dynamic RT strength experiments and to provide a general picture of both the complexities and the promises it contains. We begin in Section 7.2 by discussing an experimental platform for RT strength experiments and the diagnostics available for obtaining the relevant data. Next, in Section 7.3 we provide an overview of some common material strength models which, when used in conjunction with hydrodynamic simulations, allow material strength to be inferred from the experimental data. Finally, in Section 7.4 we present an example of the results obtained from this platform as well as the methods for inferring strength estimates.

### 7.2. Experimental Rayleigh–Taylor strength platform

A number of related platforms have been developed to extract strength-relevant RT data from high energy density experiments. In this review, we restrict our consideration to the indirect-drive platform which has been applied at both the National Ignition Facility (NIF) and the Laboratory for Laser Energetics (LLE)'s Omega laser. This method, as depicted in Fig. 9, builds upon the concept first suggested by Barnes, et al. [227] and the development of "indirect" hohlraum-based reservoir-gap ramp drives [228]. In this platform, laser beams enter a hohlraum, which generates an intense X-ray source that in turn is incident upon a multi-layer ablator and foam reservoir. The reservoir is thereby converted into a plasma, which expands across a gap and is incident upon a sample with preformed sinusoidal ripples, generating an RT instability in the solid rippled sample. These ripples grow [1,2], and are characterized at a later time via face-on X-ray radiography [31, 221].

A brief word is in order regarding the platform's primary diagnostic of face-on X-ray radiography. In a traditional analysis of the RT instability the amplitude of the unstable interface provides the metric by which the RT growth is quantified. In the present platform, however, a direct measurement of this interface's amplitude would require side-on radiography (i.e., perpendicular to the plasma drive) with a pulse duration much shorter than is currently achievable. In addition, it would create undesirable sensitivities to the planarity of the drive, as deviations from planarity would generate blurring of the radiographic image, along with corresponding uncertainties in the measured RT growth. As a result, the platform is restricted to using face-on radiography, which probes the integrated opacity through the target package rather than directly measuring the amplitude of the rippled interface [230]. More will be said regarding the corresponding RT growth metric later in this section.

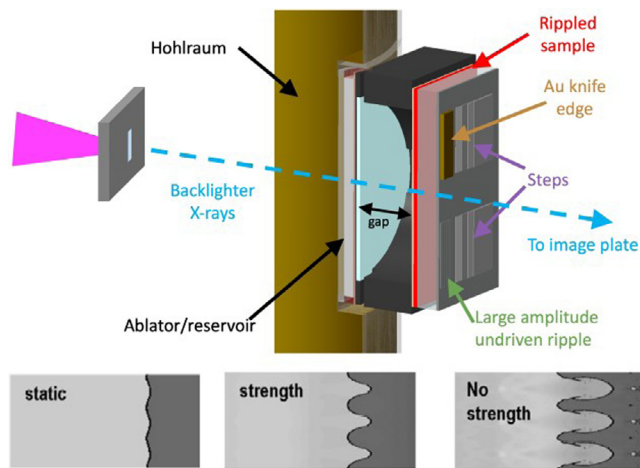


**Fig. 9.** Schematic of the indirect-drive RT strength platform, showing the hohlraum, multi-layer ablator/reservoir, rippled sample target, and backlighter. Soft X-rays from the hohlraum ablate material from the multi-layer ablator and foam reservoir, generating a plasma that expands across a vacuum gap and ramp-compresses the rippled sample. The bottom inset shows the initial ripples and simulated ripple growth, both with and without strength [229]. Reproduced with permission.

As noted in Section 7.1 and discussed in detail in Section 7.3, in order to infer material strength from an RT experiment, it is necessary to compare experimental RT growth to hydrodynamic simulations. Thus, it is necessary to define a metric for quantifying RT growth which both represents the experimentally accessible data (transmission of face-on radiography) and is calculable in a hydrodynamic simulation. To this end, we begin by noting that the absorbed X-ray intensity is proportional to the integrated density<sup>3</sup>:

$$I_{\text{abs}}(r, t) = \xi \int_{z_1(r,t)}^{z_2(t)} \rho(r, z, t) dz, \quad (60)$$

where we take the plasma drive to be incident along the  $z$ -axis,  $z_1(r) = z_{\text{av}}(t) + a \cos(kr)$  is the rippled sample interface with wavelength  $\lambda = 2\pi/k$ , amplitude  $a$ , and mean location  $z_{\text{av}}(t)$ ,  $z_2(t)$  is the sample's flat "back" interface,  $r$  is a radial coordinate perpendicular to  $z$ , and  $\xi$  is a constant of proportionality. The transmitted intensity  $I_{\text{trans}}(r, t) = I_0 - I_{\text{abs}}(r, t)$  will be periodic with the same period as  $z_1(r, t)$ , as the thicker portions of the sample (along ripple maxima) will absorb somewhat more of the X-ray source photons than the thinner portions (along ripple minima). In order to isolate this effect, we Fourier transform to wave-number space,  $\tilde{I}_{\text{trans}}(k)$ , and evaluate at the wave number of the preformed ripple,  $k = 2\pi/\lambda$ . Finally, we define the growth factor,  $GF(t)$ , as the ratio of the  $k$ -component of  $\tilde{I}_{\text{trans}}$  to its  $t = 0$  value:

$$GF(t) = \frac{\tilde{I}_{\text{trans}}(k, t)}{\tilde{I}_{\text{trans}}(k, 0)}. \quad (61)$$

For a constant density sample this expression reduces to the geometric growth of the rippled interface, while in the more general case of a density varying sample, such as is realized in RT strength experiments, it continues to represent the experimentally accessible data obtained via face-on radiography.

<sup>3</sup> Strictly speaking, the absorbed X-ray intensity is actually proportional to the integrated opacity not the density. However, for a given material the opacity is proportional to the density, and in a typical RT strength experiment only the rippled layer of the target has nontrivial opacity. Thus, to a very good approximation the density may serve as a proxy for opacity.

The growth factor defined in Eq. (61) is the primary metric for comparing experimental data and hydrodynamic simulations, a comparison which, when favorable, allows one to infer the material strength by inquiring directly of the simulation. In order to do so, however, the simulation requires a strength *model* be specified, which describes the dependence of the material strength on properties such as the pressure, temperature, and strain rate. Thus, it is the subject of these models to which we now turn.

### 7.3. Material strength models

In material science and engineering there exist a number of "strengths" which characterize different aspects of a material's response to applied stress. In the present review the term *strength* will be synonymous with *yield strength* or *flow stress*, both of which are common terms in the literature. Thus, the strength  $Y$  of a material is the lowest stress which will produce a plastic (permanent) deformation in the material. Meanwhile, the *shear modulus*  $G$ , which will also be relevant in the following discussion, is the ratio of the shear stress to the fractional elongation of the material (the shear strain) resulting from that stress.

As outlined in Section 7.1, the dynamic conditions required to realize the RT instability in solids involve exploring a wide range of pressures and temperatures, over which the material strength varies considerably. As a result, we cannot speak of the strength  $Y$  of a material, but are instead required to specify the strength (function)  $Y(p, T, \dots)$ . Indeed, even experiments designed to probe material strength at a specific pressure (e.g., lead strength at 400 GPa [229]) are in fact integrated experiments that begin at ambient conditions, ramp and/or shock to some peak pressure at or near which data is taken, and eventually decompress as the experiment ends. Thus, the RT growth captured by the experimental diagnostic is a result of the *integrated strength* along the entire history of the experiment prior to data collection, not simply the strength at a specific set of conditions (i.e., pressure, temperature, etc.).

To summarize the above considerations, the ultimate task of an RT strength study might be described as follows: first, obtain some number of RT growth measurements with various "loading" (pressure) and temperature histories; then "invert" this data to obtain the strength function  $Y(p, T, \dots)$ . Of course, this inversion is by no means unique even for large data sets, and, given the practical limitations of obtaining experimental time at the few facilities capable of reaching the necessary conditions, in practice the available data sets will be relatively small, perhaps  $\sim 10$  measurements. The path forward is thus:

1. postulate a functional form of  $Y(p, T, \dots)$  based either on phenomenology or a microscopic model;
2. perform hydrodynamic simulations of the various experiments using the postulated form of  $Y(p, T, \dots)$  along with varied sets of its unknown parameters;
3. identify the parameter sets of  $Y(p, T, \dots)$  consistent with the experimental data;
4. if the "strength at given conditions  $(p_*, T_*)$ " is desired, evaluate  $Y(p_*, T_*, \dots)$  for all consistent parameter sets; the variation in these evaluations gives an estimate of the uncertainty in the material strength under those conditions.

Of course, the variations obtained in step four above will depend on the specific strength model employed (i.e., the functional form chosen for  $Y(p, T, \dots)$ ), so in general this procedure is typically repeated for several model choices and the strength evaluations, and their spreads, are compared across models. To provide some concrete background, we now briefly outline two common material strength models used in the present context.

### 7.3.1. Steinberg–Guinan model

The first and simplest dynamic strength model, which includes the effects of pressure-hardening (the increase in material strength with pressure) and temperature, was developed by Steinberg, Cochran, and Guinan in 1979 [231]. The model begins by expressing the material's *shear modulus* as a modified Taylor series expansion in pressure and temperature:

$$G(p, T) = G_0 \left[ 1 + \left( \frac{G'_p}{G_0} \right) \frac{p}{\eta_c^{1/3}} + \left( \frac{G'_T}{G_0} \right) (T - T_0) \right], \quad (62)$$

where  $\eta_c = \rho/\rho_0$  is the compression (the ratio of the density to its ambient value), and  $G_0$ ,  $G'_p$  and  $G'_T$  are parameters whose value is typically determined via experiments at ambient conditions ( $p = 0$  and  $T_0 \approx 300$  K). The essence of the Steinberg–Guinan (SG) model is the assumption that the material strength's variation with pressure and temperature is identical to that of the shear modulus, with the exception of an additional multiplicative work-hardening function:

$$Y(p, T) = Y_0 (1 + \beta_W \epsilon)^n \times \left[ 1 + \left( \frac{Y'_p}{Y_0} \right) \frac{p}{\eta_c^{1/3}} + \left( \frac{G'_T}{G_0} \right) (T - T_0) \right], \quad (63)$$

where  $\epsilon$  is the material *strain*,  $\beta_W$  and  $n$  are work-hardening parameters, and  $Y_0$  and  $Y'_p$  are additional unknown parameters. Note that it is assumed within the Steinberg–Guinan model that the temperature dependence of the material strength is the same as that of the shear modulus (thus, the coefficient of the temperature-dependent term in Eq. (63) is the same as that in Eq. (62)).

As outlined above, even this “simplest” material strength model has eight parameters which must be determined by fitting to experimental data. Fortunately, given the nature of the Steinberg–Guinan model as a Taylor expansion, the majority of these parameters can be fit by static or low strain-rate experiments (e.g., Hopkinson bar [232], Kolsky bar [233], diamond-anvil cell [234]). Thus, when “inverting” RT strength data to obtain Steinberg–Guinan parameters, the majority of these parameters are typically maintained at their ambient values, with variations of only a few parameters (and often only one:  $Y_0$ ) considered.

### 7.3.2. Steinberg–Guinan–Lund model

An extension of the Steinberg–Guinan model that accounts for strain-rate effects (i.e., the faster a material deforms, the stronger it is) is known as the Steinberg–Guinan–Lund (SGL) model [235]. In this model the shear modulus continues to be given by Eq. (62), while the material strength is of a similar form to Eq. (63), but with the addition of strain-rate term:

$$Y = \left[ Y_0 (1 + \beta_W \epsilon)^n + Y_T(\dot{\epsilon}_p, T) \right] \frac{G(p, T)}{G_0}, \quad (64)$$

where  $Y_T(\dot{\epsilon}, T)$  represents the *thermally activated* part of the material strength. The strain rate is taken to be of the form [236–239]

$$\dot{\epsilon}_p = \frac{1}{C_1} \exp \left[ \frac{2U_K}{k_B T} \left( 1 - \frac{Y_T}{Y_p} \right)^2 \right] + \frac{C_2}{Y_T}, \quad (65)$$

where  $Y_p$  (known as the *Peierls stress*) is the maximum value of  $Y_T$ ,  $2U_K$  is the energy required to form a pair of “kinks” in a dislocation segment of length  $L_p$ , and  $k_B$  is the Boltzmann constant. The constants  $C_1$  and  $C_2$  are typically treated as material-specific parameters in hydrodynamic codes, but can also be related to microscopic model variables. Given an equivalent plastic strain rate, Eq. (65) can be solved numerically for the rate-dependent strength  $Y_T$ , from which the total strength may be computed via Eq. (64).

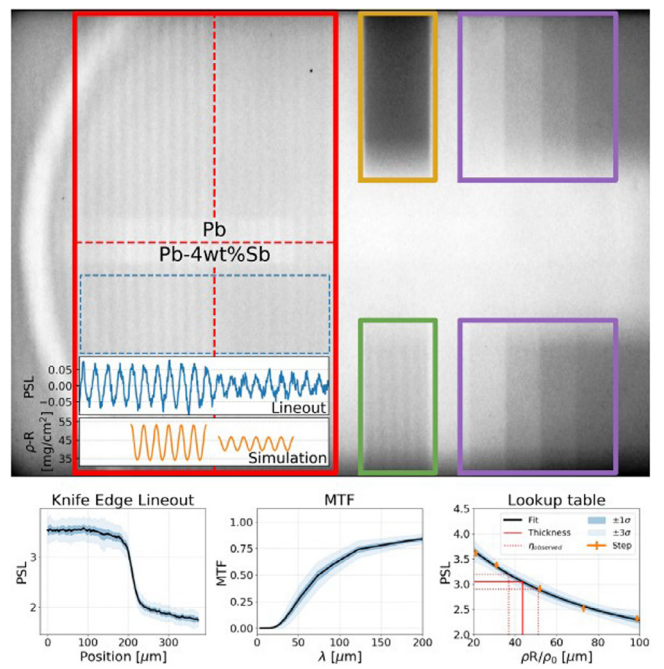


**Fig. 10.** Radiographic data and analysis plots from an RT strength experiment performed on lead at NIF with a  $\sim 400$  GPa peak pressure [229]. The modulated X-ray intensity is clearly visible in the left half of the target, indicating the sinusoidally-varying thickness of the rippled lead sample. The right half contains a knife-edge, undriven ripples and “steps” of various thickness, which provide a means of inferring ripple growth through establishing a *lookup table*, as shown at bottom right.

### 7.3.3. Other material models

Before leaving this section, a word should be said regarding other material models in the literature. One common material strength model of the same general class as the Steinberg–Guinan models, but somewhat more physically motivated, is the Preston–Tonks–Wallace (PTW) model [240]. This model goes beyond the Steinberg–Guinan model by including strain-rate effects, but in a way whose details differ from the simpler Steinberg–Guinan–Lund model. From a computational standpoint, the PTW model is interchangeable with the SG or SGL models, and can be constrained in the same way described above. However, the detailed implementation of this model is somewhat more involved and therefore beyond the scope of this brief review. Models have also been developed which capture the transition from plastic deformation to brittle failure [241].

Besides the phenomenological models discussed thus far, there are also material models based directly on the underlying microscopic physics, such as the Livermore Multiscale (LMS) model [242,243]. The LMS model begins with a quantum mechanical inter-atomic potential and builds up the macroscopic properties of shear modulus and strength through large-scale computational methods. As a result of its microscopic character, the LMS model has somewhat fewer easily tunable parameters than the phenomenological models described above, but a more detailed discussion is beyond the scope of this review.

## 7.4. Inferring material strength through hydrodynamic simulation

Having introduced the experimental RT strength platform and discussed a pair of representative material models, we now proceed to discuss the hydrodynamic simulations that provide the crucial link between experimental data and the hitherto unknown material strength. These simulations allow for the direct

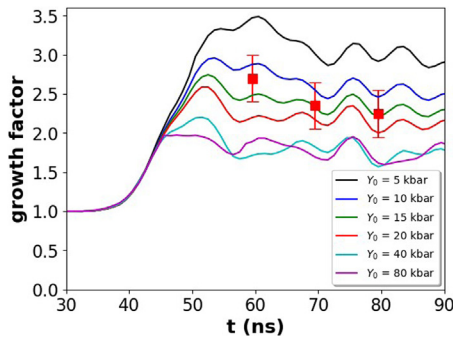


**Fig. 11.** Simulated growth factor curves for a hypothetical RT strength experiment and several variations of the SG strength model parameter  $Y_0$  (with all other parameters held fixed; see, Eq. (63)). Experimental data, which is used to constrain the SG parameter space, is also shown.

calculation of the RT growth factor of Eq. (61) as a function of time, according to the prescription outlined in Section 7.3. The corresponding experimental datapoint can be evaluated in an analogous way from face-on radiographic data, a typical example of which is shown in Fig. 10 [229]. On the left side of the target the sinusoidal modulation of the transmitted X-ray intensity is clearly visible. This intensity is correlated to the material thickness through the presence of both undriven ripples (i.e., ripples not subject to the laser-induced pressure drive) at bottom-center of the target, as well as the “steps” of various unknown thicknesses at bottom-right.

For a given set of material strength model parameters and one or more experimental data points the question is then asked: is the experimental data consistent (within errors) with the simulated growth factor? If not, that portion of parameter space is excluded. As the number of experiments increases, ideally performed under a variety of drive conditions (i.e., pressure and temperature histories), the parameter space consistent with the growing data set is narrowed, reducing the uncertainty in the material model. Finally, the model space consistent with the experimental data can be evaluated for material strength, thereby inferring the strength of the material itself. This procedure can be repeated for a number of strength models, providing not only a specific value of the material strength at the specified conditions, but also an indication of its uncertainty, through the distribution of these evaluations.

Fig. 11 illustrates the procedure for constraining strength models, from which the material strength can be inferred. In this example, a number of simulations with variations in  $Y_0$  are performed, while the remaining Steinberg–Guinan parameters are assumed to be otherwise constrained (i.e., well known) and are therefore held constant. In this case, as indicated by the figure, the RT strength data is consistent with  $15 \text{ kbar} \lesssim Y_0 \lesssim 20 \text{ kbar}$ . Values of  $Y_0$  greater than 20 kbar would suppress RT growth to a greater extent than that observed in the experiments, while values less than 15 kbar would result in excessive growth. Finally, given this range of  $Y_0$  values, the strength of Eq. (63) can be evaluated at the conditions of interest.

Fig. 12 shows the result of the procedure outlined above, which consists of upper and lower bounds for the material strength at any given  $(p, T, \varepsilon)$ . While the temperature is held constant in this plot for the sake of visualization, it is generally the case that as long as the material does not approach its melt surface ( $p, T = T_{\text{melt}}(p)$ ), temperature effects on material strength are typically much smaller than the effects of pressure and strain, as indicated by the fact that  $G'_T/G_0$  is typically an order of magnitude smaller than  $(Y'_p/Y_0)$  (see Eq. (63)) [231,244].

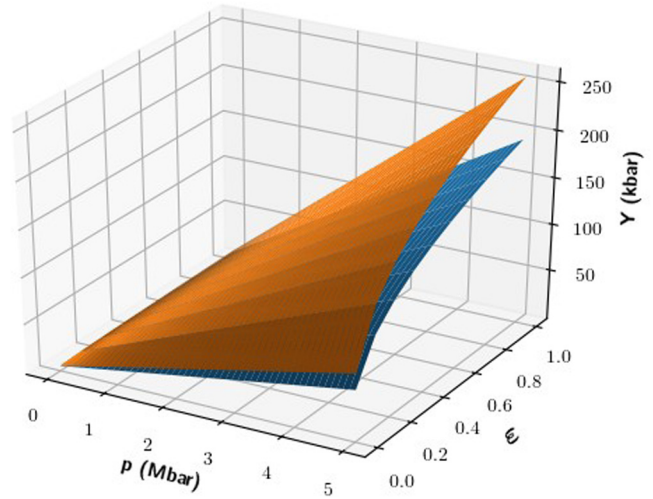


**Fig. 12.** Upper (orange) and lower (blue) bounds on the material strength  $Y(p, T, \varepsilon)$  of a hypothetical material, based upon the data and simulations represented in Fig. 11. The temperature,  $T$ , and compression,  $\eta_c = \rho/\rho_0$ , are held constant in order to represent the result in three dimensions. (For interpretation of the references to color in this figure legend, the reader is referred to the web version of this article.)

There are a variety of methods for defining the upper and lower bounds of this function, depending on whether the experimental errors represent, for example, a  $1\sigma$  standard deviation, an absolute limit on the error, or something else. Regardless of the precise definition, however, as the number of experimental data points increases, the separation of the upper and lower bounds represented in Fig. 12 will be reduced, particularly if experiments are performed under varying drive conditions. It is possible that after a sufficient number of data points are obtained, the parameter space consistent with the data will be reduced to the null set, in which case one is forced to conclude that the model form in question (e.g., Steinberg–Guinan, PTW) is insufficient to describe the material in question over the range of conditions probed.

## 8. Ejecta

Ejecta is a term used in a variety of fields for impulsively generated flows, often laden with particles. Such flows may be generated by a variety of mechanisms: driven externally, for example by the energetic impact of a body such as a bullet or a meteorite onto a surface [245]; or internally as a result of the rapid release of energy by phase change or violent chemical reaction (see for example, Section 9). At the time of writing, another rather timely example is the role of violent respiratory events such as coughs and sneezes in transferring respiratory diseases between infectious and susceptible individuals [246,247]. This pertains directly to the coronavirus disease 2019 (COVID-19) pandemic, in particular regarding the social distancing strategies which are critical to limiting transmission [248–250] (Fig. 13). In each case, the cloud of dense material generated will initially move ballistically, until any diffuse medium through which it passes starts to have an aerodynamic effect. Once particles have swept through a column-density of diffuse material comparable to their own column density, they will start to be subject to significant drag forces, which may even be strong enough to lead to the particles breaking up. The resulting particle-laden flows are often turbulent and subject to internal multiphase instabilities driven by buoyancy differences between their components.

The initial particle creation can result from a variety of processes. When volcanic ejecta form, the primary breakup mechanism is the result of a violent dissolution of gases as the geological

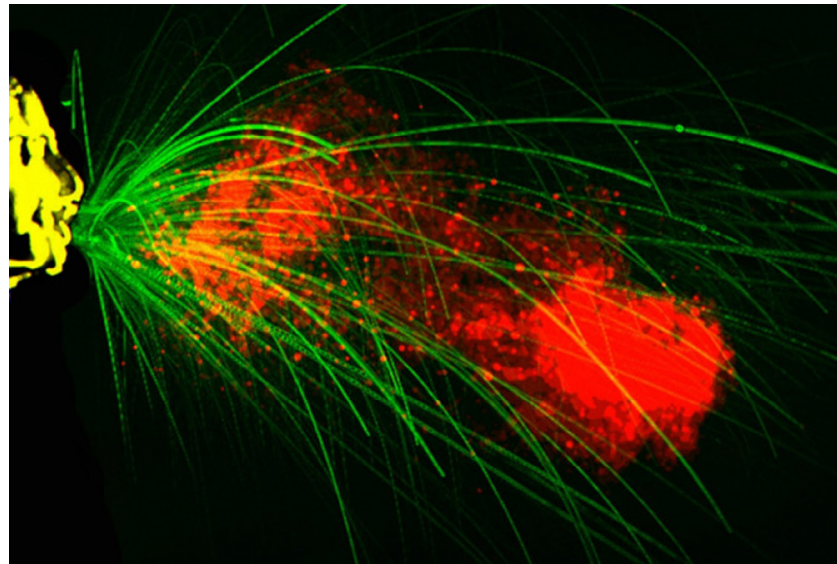


**Fig. 13.** Multiphase turbulent gas cloud from a human sneeze. The fluid dynamics data is relevant for evaluating social distancing strategies during the COVID-19 outbreak. Image reproduction showing the semi-ballistic largest drops, visible to the naked eye, and on the order of mm, which can overshoot the puff at its early stage of emission [251,252]. The puff continues to propagate and entrain ambient air as it moves forward, carrying its payload of a continuum of drops [246], over distances up to 8 meters for violent exhalations such as sneezes [249]. Figure 1 of Balachandar, Zaleski, Soldati, Ahmadi, and Bourouiba, [253]. ©.

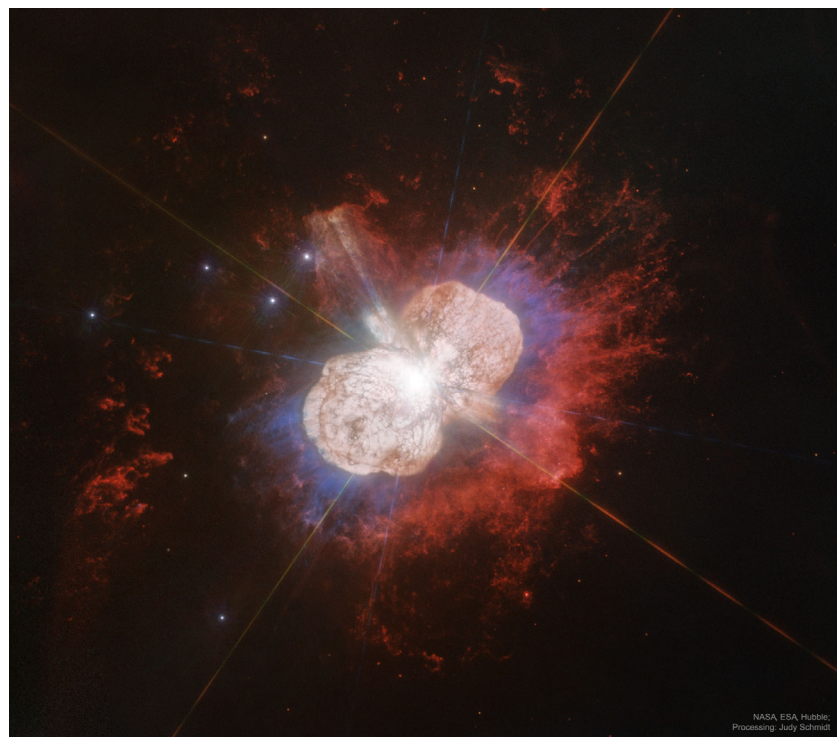


**Fig. 14.** The explosively-driven ejection nebula around Eta Carinae. Image Credit: NASA, ESA, HST; Processing: Judy Schmidt. Reproduced under the Creative Commons Attribution 2.0 Generic License.

pressure confining the lava is released; for impact and shock-driven ejecta, the mechanism is the formation of jets by processes akin to RM instability. For most astrophysical ejecta, the fluid flow becomes clumpy as a result of rapid cooling of material due to expansion and radiative losses, leading to its collapse into a thin sheet, and this thin sheet then fragmenting as it expands further.

The initial ballistic nature of the expansion once the dense ejecta have formed results in a characteristic kinematic signature, where the velocity of the material varies linearly in position with the time of the initial impulsive driving event, the ‘kinematic age’.

being (to a good approximation)  $\tau_{\text{kin}} \simeq 1/(dv/dx)$ . This kinematic signature can be clearly seen in spectroscopic observations in astrophysics, as applied for example to the spectacular explosive ejecta seen around Eta Carinae, Fig. 14 [254].

For the case of shock-driven ejecta, the situation is similar to that considered in the previous section, where the effects of strength on the linear development of RT and RM instabilities, and the corresponding use of the arrest of perturbation growth in the linear and weakly non-linear phases to infer material properties were discussed. If the stress on the interfacial material

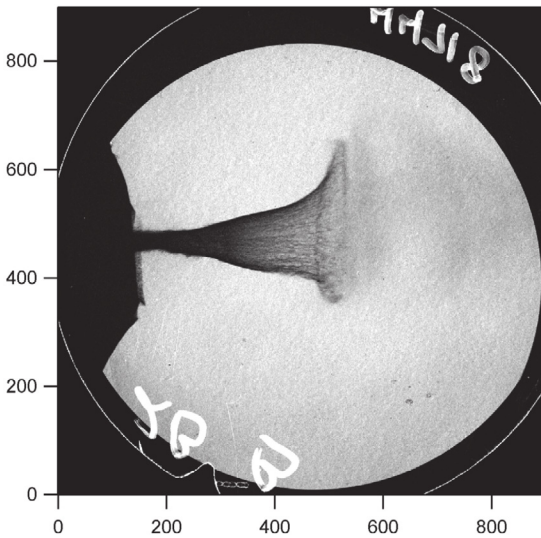


**Fig. 15.** Ejecta jet generated by plane shock incident on the surface of a sample with a cylindrical ‘divot’, expanding into vacuum. This high-resolution backlit radiograph shows the tip of the ejecta plume, which collapses to the jet expected for this perturbation geometry close to its base, and the break-up of a thin sheet at its heads into clear thread-like structures oriented along the jet, and likely then into particles although the particles cannot be individually resolved. Source: From [255], based on previously unpublished data from the experiments of [256].

due to RMI is sufficient to exceed the material’s yield strength in the non-linear phase, then the material will fail and perturbation growth will continue. However, the strength of the material will still play a role reducing the growth rate and preventing the formation of a fully-developed turbulent mixing cascade described in the sections on fluid instabilities. Instead, the flow will tend to take the form of penetration of discrete, dense ejecta particles into the diffuse medium or vacuum beyond the sample.

This surface ejecta process has been the subject of experimental study over a long period, and has been the subject of significant recent progress in modeling and theory, much of which has been summarized in a special issue of *Journal of Dynamic Behavior of Materials* [257,258]. These experiments have been performed using a variety of shock drivers, including gas guns [259,260], high explosives [261,262] and high-power lasers [256,263–266] (see Fig. 15). These different techniques offer distinct capabilities both in the extent to which the drive pressure can be tuned to explore different scenarios, and the diagnostics which can be applied to the resulting ejecta.

Eventually, the ejecta particles will become entrained in the surrounding gaseous flow, a process which results in a variety of complex multi-phase dynamical phenomena. For volcanic ejecta, see e.g. Fig. 16, buoyancy is created by the dissolved gases and the heating of entrained air [267,268], often generating a plume of material which rises high into the atmosphere. This form of volcanic eruption is named after the Roman author Pliny the Younger, who observed the eruption of Vesuvius in A.D. 79, and accurately described the formation of the plume and associated flows in his letters.<sup>4</sup> As the particle-laden plume rises, expands and cools, it eventually loses buoyancy and collapses, often generating pyroclastic surges which move rapidly across the landscape and can deposit the volcanic ejecta in deep layers.

<sup>4</sup> Pliny’s uncle, the author and natural historian Pliny the Elder, used a pillow strapped to his head to protect him from falling pumice ejecta particles. Pliny the Elder sadly died near Pompeii, having sailed there to observe the eruption and rescue friends. See Pliny, “Letters”. Book VI, Letters 16 & 20.

### 8.1. Surface ejecta physics

Particulate ejection from the surface of a dense material as a result of a shock wave driven through the material is now well-recognized as being an extreme limit of the RM instability where the Atwood number  $\mathcal{A}$  tends to  $-1$  [269]. The low density of the material ahead of the shocked interface has a substantial effect on the asymptotic behavior of the growing mixing layer. Rather than evolving to a fully self-similar state at late time in which the growth law is controlled by the evolution of turbulence, jets of dense material propagate away from the surface at close to constant velocity, while the bubbles slow as these quasi-ballistic jets remove the kinetic energy of the fluctuations from the surface.

Indeed, the initial kinetic energy per unit area,  $\mathcal{K}_0 \simeq \rho \lambda \dot{a}_k^2$  for a perturbation of characteristic size scale  $\lambda = 2\pi/k$  is one of the dominant characteristics of ejecta flows. Here the growth rate of the RM instability in the fluid regime  $\dot{a}_k$  can be approximated by the

$$\dot{a}_k = k \Delta u \mathcal{A}^+ (a_0^+ + a_0^-)/2, \quad (66)$$

where the subscript  $-$  and  $+$  denote the pre- and post-shock quantities, respectively. Here, the Meyer-Blewett formula [49] should be used since it is  $\mathcal{A} < 0$ . Note, however, that since the flows are nearly incompressible, the Meyer-Blewett formula will likely give values close to the RM formula (e.g., Eq. (27)).

This process can be strongly affected by material properties such as strength and surface tension. The growth will be suppressed where the yield strength is  $Y \gtrsim \mathcal{K}_0/\lambda$ , i.e. the work done against the yield strength in growing to nonlinear amplitude would be greater than the kinetic energy deposited at the surface by the shock interaction, as discussed in the previous section (see also, e.g., [261,270] for more detailed quantitative criteria). As the movement of material into the spikes leads to loss of kinetic energy in the bulk perturbations, these material property effects can become increasingly important at later times. The late-time growth of the bubbles can also be affected by interactions with layered spall breakup of the substrate material, if the shock which drives the ejecta growth is not supported [271]. Spall is an internal material brittle failure or rupture (cracking) which occurs when the material is placed under tensile loading due to unsteady pressure waves. Cracks initiated due to spall may be sufficiently large to cause a separation from the bulk of the material. This effect is of course amplified if the surface is shocked on multiple occasions [272].

In the remainder of this section, we will discuss the process of ejecta production and breakup in more detail, and describe theoretical approaches to the different stages of the development of the ejecta cloud and experimental and computational evidence of the processes at work. We will also consider examples of analogous processes in other contexts, such as high-velocity impacts, astrophysical jets and diesel injection.

### 8.2. Spike formation

While the dominant mechanism for the formation of ejecta from shocked metal surfaces is believed to be via the formation of jets from microscopic surface imperfections, the planar symmetry of the shock–surface interaction can be broken up by other effects, such as the presence of grain structure or sub-surface inclusions, which can also lead to ejecta formation. However, the impact of such sub-surface perturbations scales inversely with their depth, limiting their overall effect.

While it is possible to estimate RM linear instability growth rates in fluids by taking the asymptotic behavior of impulsively-accelerated, incompressible RT, with minor empirical corrections



**Fig. 16.** The particulate ejecta plume from the eruption of Mount St. Helens, May 18, 1980. Image Credit: USGS.

for compressibility effects, Eq. (66), the details of the jet formation process can become more important in the context of ejecta formation. The direct effect of the interaction of the shock with the perturbed surface is that the reflected rarefaction introduces transverse motions in the material. Due to the relatively low Mach number of transverse motions, these soon result in the formation of jets of material (known as spikes) where they are compressive, or draw-back of the surface (bubbles) where they are expanding. The form of the spikes varies with the topology of the initial perturbation: an initial pit or divot in the surface leads to a localized jet, while a groove will lead to the formation of a sheet of ejecta. A surface with a raised feature will lead to the formation of a divot in the post-shock surface surrounded by an expanding ring of ejected material, a process somewhat analogous to the impact of a droplet on a fluid surface, or on a larger scale to a meteorite impact. A surface with regular machining grooves will generate an array of parallel sheets.

While the underlying equation (66) is based on incompressible flow, Figs. 17 and 18 illustrate clearly that the sub-surface structures in real experiments can in fact have very high-density contrasts. The velocity field below the surface is imprinted by the reflected rarefaction, as usual, but in this case the rarefaction is strong enough that the material breaks up into sharply defined layers, as also observed by [274].

Buttler et al. [261] performed experiments using a variety of initial surfaces to study the effect of strength on the growth rate of the bubble tips over time, as illustrated in Fig. 19, and related these results to a simple and effective theory.

In addition to the change in perturbation amplitude, or peak expansion rate of the ejecta front if the material fails, another important factor is the total mass of material which is ejected from the surface. As with other forms of RMI, the source of dense material into the ejecta sheets is controlled by the dynamics of the bubbles: the process of bubble merger can lead to sheets or

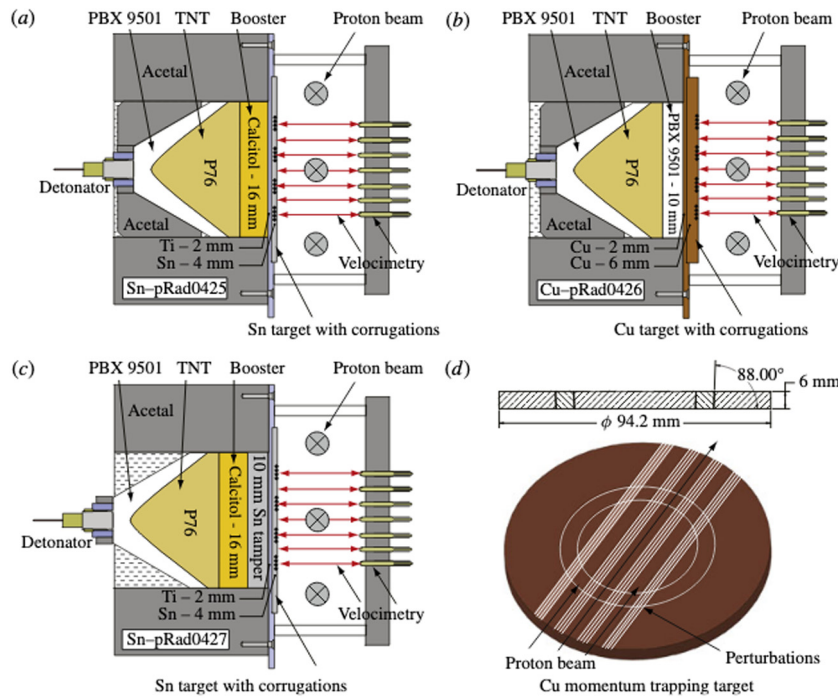


**Fig. 17.** Rad RM experimental package geometries encase in acetal plastic a 76 mm diameter plane-wave HE lens used to uniformly detonate an HE booster cylinder in contact with a buffer plate; the sample/target is mounted onto the buffer plate on top of the acetal plastic as well. The target design incorporates momentum trapping concepts, as illustrated (d) together with the target perturbation schemes. The targets were machined to a diamond turn finish that included four bands of sinusoidal corrugations,  $\lambda = 500 \mu\text{m}$  but with varying amplitudes. Each corrugation band was eight wavelengths wide and separated by flat regions that were 5 mm wide. Over each corrugation band and intervening flat region was positioned a velocimetry probe used to measure jump times and velocity histories over the duration of the experiment. The proton beam is aligned into the page, along the perturbations. Figure 2 of Buttler et al. [261] with permission. ©Cambridge University Press.

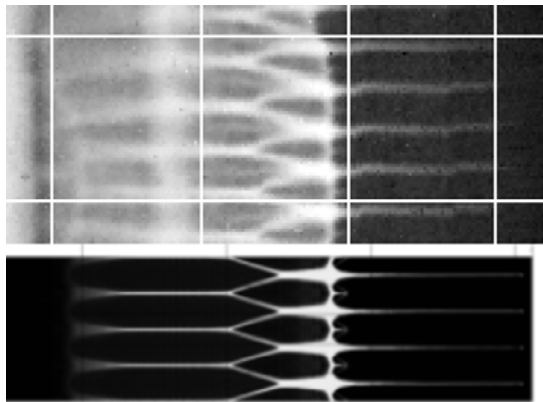


**Fig. 18.** Comparison of experimental pRad data from Buttler et al. [261] (above) with 2D numerical calculations [273]. The experimental data show both the growing spikes and the sub-surface structures which drive them, which in this case has a far sharper structure than expected for an incompressible flow. Reproduced with permission.

jets pinching off, but for a sufficiently regular surface this process of bubble merger will be suppressed.

The form of the grooves on the initial surface can be quite variable, dependent on the details of the surface preparation. However, the form of the bubbles which form is rather weakly dependent on the initial surface profile (e.g. [275]). It is helpful in this context to look at the shock–surface interaction as the introduction of vorticity primarily at the surface, where the sub-surface velocity field is determined – at least primarily – by the Biot–Savart law [53]. From Kelvin’s circulation theorem, this

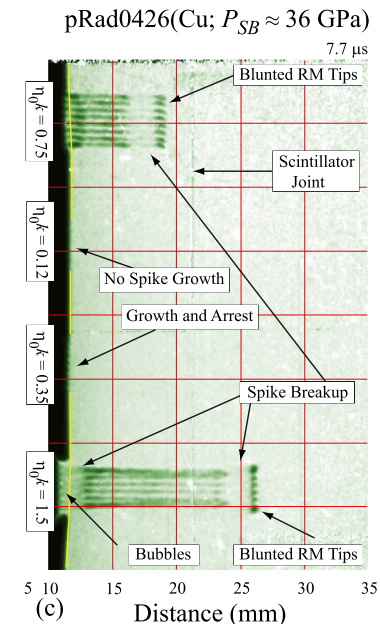


**Fig. 19.** Experimental data (from [261], with permission) illustrating the effect of varying the initial amplitude of the perturbation, and hence the RM instability growth rate, on the growth of ejecta jets. For low initial amplitudes, the post-shock strength of the material can suppress or arrest the spike growth. For higher initial amplitudes, ejecta jets can escape, but discrete clumps of material form at the jet tips, and the effects of strength and surface tension eventually act to cause the supply of material entering the jets to cease. Reproduced with permission.

vorticity remains essentially pinned in the material in which it is initially deposited when there is no barotropic source (i.e. for supported shocks, or when surface spallation has suppressed pull-back). As the surface evolves, the details of the initial surface profile encoded into the vorticity distribution tend to be dragged into the spike of ejecta. As a result, the bubble, as well as the lower-velocity part of the spike, tends to relax toward a self-similar form (e.g.[276,277]).

This self-similar dependence may be derived from the following argument. The perturbation kinetic energy per unit area,  $\mathcal{K}$ , will reduce as a result of loss of material into the jets as

$$\frac{d\mathcal{K}}{dt} \simeq -\frac{v}{\lambda}\mathcal{K}, \quad (67)$$

where  $v \simeq (\mathcal{K}/\rho\lambda)^{1/2}$  is the velocity of material at the base of the jet. Integrating, we find

$$\mathcal{K} \propto \frac{1}{(1+t/\tau)^2}, \quad (68)$$

or

$$v \propto \frac{1}{1+t/\tau} \quad (69)$$

as discussed by [275–277]. Here,  $\tau = \lambda/(3\pi v_0)$  where  $v_0$  is a characteristic velocity roughly equal to the jet tip velocity.

In the region of the spike between the bubble, where the material is still being accelerated by pressure in the bulk, and the tip, where the mass distribution depends in detail on the initial surface, mass conservation then implies that the distribution of mass above a velocity  $v$  over time for the jet as a whole can be described by a function with the general form

$$M(v, t) \propto \ln \left[ \min \left( \frac{v_0}{v}, 1 + \frac{t}{\tau} \right) \right]. \quad (70)$$

### 8.3. Particle formation

In the previous section, we discussed the growth of the bubble and spike structure typical of high density-ratio Richtmyer–Meshkov in pure fluids. For real materials, subject to strength or surface tension, the spikes will tend to break up into discrete particles at late times. It is important to understand the size distribution of particles, as this affects their transport and reactivity. There is extensive literature on the break-up of fluid jets, which has been surveyed for example by Eggers [278], however this tends to concentrate primarily on continuous rather than impulsive jets.

The process of particulate formation typically occurs in two phases. An initial process of rapid primary breakup occurs before there is a significant interaction of the ejecta jets with their environment, as a result of the balance between local kinematic perturbations within the dense fluid and restoring forces such as surface tension and elastic strength. This process is enhanced in importance for the impulsively-driven ejecta jets, compared to the essentially continuous jets of fluid considered in contexts such as fuel injection or inkjet nozzle flows.

Once the interaction of the ejecta with any gas in its environment becomes significant, an additional reservoir of kinetic energy becomes available, due to the relative motion of the ejecta particles through their environment. This leads to an additional secondary breakup process driven by drag on the ejecta particles. Of course, which process dominates the initial breakup depends on the balance between the level of initial perturbations and the density of the gaseous environment: Andrews and Preston [279] consider the case where there is no primary breakup, and the breakup from sheets into filaments and particles is driven entirely by shear instability effects.

#### 8.3.1. Primary breakup

As it moves away from the surface, the motion of the spike material becomes close to kinematical. For a simple initial surface profile and pure fluid physics, this spike can remain entirely smooth. However, in the faster components of the spike which are sensitive to the initial surface profile, the velocity field will typically not be strictly monotonic. Moreover, as kinematical expansion continues, the surface area per unit volume becomes increasingly large and the local strain rate reduces; viscosity and plasticity will also lead to the loss of kinetic energy. Hence, for real materials, further expansion of the jet requires an increasing fraction of the available initial kinetic energy and, unless it is sufficient to retract the jets entirely, the breakup of the jet into discrete particles [276], and the cessation of mass loss into it, becomes inevitable on energetic grounds. This primary breakup process can be enhanced by the effects of non-monotonic expansion velocities, non-uniform mass flux and capillary instability. The effect of the non-monotonic expansion velocity is analogous to the formation of internal working surfaces in high Mach number fluid jets (e.g. [280]), with additional breakup processes resulting from, e.g., caustic formation in ejecta sheets with small lateral motions.

#### 8.3.2. Secondary breakup and atomization

The process of secondary breakup is generally considered to be the result of a balance between aerodynamic forces on the particles, their inertia, and restoring forces such as material strength and surface tension. A variety of breakup models have been developed [281,282], which capture an essentially similar set of physical processes with varying fidelity.

In addition to these dynamical processes driving particle breakup and atomization, high temperatures caused by the shock energy deposition and increased surface areas due to jet growth and particle formation can act to significantly enhance the rate of chemical reaction between flow components [283], leading to another route to eventual break-up.

#### 8.3.3. Experimental particle sizing

A variety of techniques have been applied to the characterization of the particle size distribution in experiments. These techniques have complementary benefits and limitations, in terms of their ability to measure the properties of single particles against the population as a whole, and the completeness of the sampling that is achieved.

Holography [284], shadowgraphy [285] and phase Doppler anemometry [286] allow the properties of single particles to be characterized, but as a result are limited to rather small total numbers of particles, and particular experimental geometries. The Mie scattering diagnostic gives a measure of the ejecta particle population as a whole, by measuring the angle by which light is diverted as a result of diffraction around individual particles [287], while multi-wavelength extinction measures the loss of light along the direct path [288]. In both approaches, valuable additional information may be obtained by measuring at more than one probe wavelength. Such measurements provide statistics for the particle population as a whole, which can be applied to cases where the particle number would overwhelm a tracking diagnostic but adds complexity to the interpretation of the results.

### 8.4. Modeling

#### 8.4.1. Direct simulation

The details of the ejecta production process have been modeled using both continuum flow [265,273,290,291] and molecular dynamic [275,292–298] codes (see Fig. 20). Comparisons between

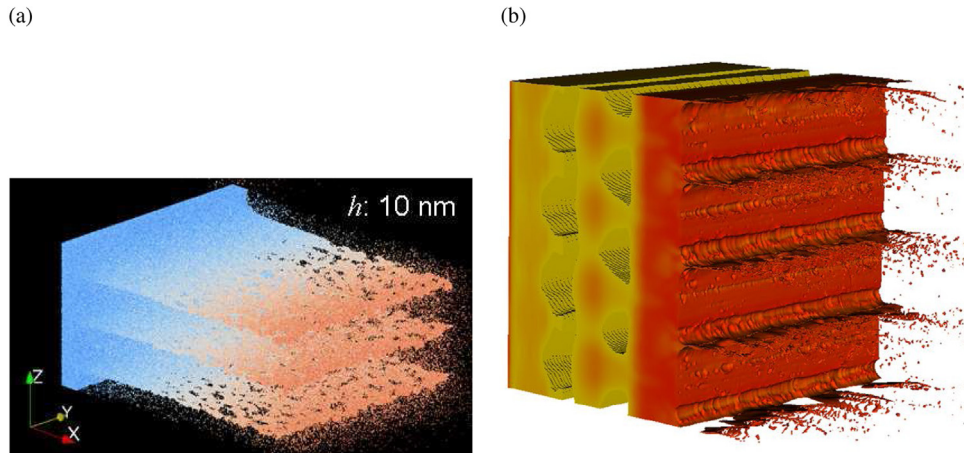


**Fig. 20.** Examples of the results of direct simulation of ejecta production processes. (a) molecular dynamics (from [289]); (b) continuum simulation (from [272]) – here cells below a certain density threshold have not been rendered, to give an impression of the jet break-up and sub-surface spall structures.

these techniques [275,299,300] tend to emphasize their good agreement on the overall properties of the jet formation, but complementary strengths. Molecular dynamical studies include the effects of constitutive properties modeled in an *ab initio* consistent manner (subject to the accuracy of the numerical scheme and the interatomic potential), but to date have been constrained to domain sizes far smaller than the most relevant experimental data. Continuum studies are not limited to small scales, but do require supporting models for constitutive properties such as strength, surface tension and fragmentation. Established models for these properties are not available or well validated at the mesoscopic scales and extreme conditions under which ejecta jet formation and breakup occur.

#### 8.4.2. Particle transport

Once ejecta particles have formed, the trajectories they follow in a vacuum will be determined purely by kinematics. However, in a medium of finite density, they will be subject to the usual hydrodynamical forces of drag and lift, and may also be subject to inter-particle collisions and breakup. Given the number of particles produced from a surface, it is generally impractical to model in detail the propagation of each individual particle, and so some statistical model must be applied to the population. Many computational codes have been developed for the modeling of particle- and droplet-laden flows in a wide variety of applications, such as diesel sprays [281,301], fire suppression [302], fluidized beds [303], pyroclastic flows [304,305], spray irrigation and inkjet printing. These approaches can be categorized broadly as (i) Eulerian-Lagrangian, where the particle populations are modeled using representative Monte-Carlo particles, e.g.[262,306–308], and (ii) Eulerian-Eulerian, where the particle populations are modeled using a smoothed continuum phase field [304,305]. In each case, many choices are available for the completeness with which processes such as drag are modeled, as well as the level of detail with which properties such as the particle size distribution are treated, whether by random sampling, binning at some resolution, or moment-based techniques.

It is often the case that differing approaches suit different applications, with Eulerian-Lagrangian techniques being particularly appropriate for modeling the initial ballistic expansion phase, while Eulerian-Eulerian approaches, similar to the RANS techniques described elsewhere in this tutorial for modeling turbulent mixing flows, can capture cases where drag is dominant, or where particles are compacting into an ejecta bed. The above modeling methods may also be applied to flows where a particle population is already present due to the seeding of the initial flow, as discussed the explosive RT/RM section.

## 9. Reactive flows

### 9.1. Preliminary

In this section, we discuss the occurrence of RT and RM instabilities in flows with chemical or nuclear reactions accompanied by heat release. Typically, the reaction time scales are orders of magnitude shorter than the flow timescales so that the hydrodynamic timescales which are set by the above interfacial instabilities determine the rate and efficiency of the overall process. Reacting RM and RT instabilities occur in a wide array of applications and natural situations including Scramjet combustion, ICF, type Ia supernovae, vapor cloud explosions, multiphase combustion in propulsion applications and gas turbines.<sup>5</sup> However, the flow in all the above applications can be analyzed in the framework of premixed or non-premixed combustion.

In premixed combustion, a homogeneous mixture of fuel and oxidizer is ignited resulting in a self-sustaining flamefront that then separates the burned material from the unburned. The development and propagation of the flamefront is dictated by the balance between chemical reactions, diffusion (of heat and mass) across the reaction front and convective development of the front. Heat conduction across the reaction front results in the combustion of additional unburned gases, so that the flame front propagates forward with a flame speed. RT and RM instabilities often aid the transition of the flamefront to a turbulent state, which is accompanied by an increase in the surface area available for combustion. As a result, the burning velocity for the turbulent flame is higher than the laminar counterpart. Through a sequence of processes initiated by RM or RT, and the transition of the flame brush to turbulence, the flame deflagration may transition to a detonation front, a process termed DDT (deflagration-to-detonation transition). Turbulence generated from hydrodynamic instabilities are thus key to DDT, without which the run-up distances of the corresponding 1D flame would approach lengthscales of kilometers [312,313].

When the fuel and oxidizer are separated by a diffuse interface, the resulting combustion is confined locally to the interface and is rate-limited by the diffusion. This scenario is referred as *non-premixed* combustion, and results in a flame that propagates in neither the fuel nor the oxidizer streams. As a result, non-premixed or diffusion flames are safer, but less efficient since the burning is dictated by the mixing process across the interface. Thus, hydrodynamic instabilities can significantly influence the

<sup>5</sup> See [309–311] for recent studies.

outcomes in diffusion flames through local stretching of the flame surface as well as enhancing the mixing through the deposition of localized vorticity. In the extreme cases, hydrodynamic instability-driven turbulence can improve the mixing between fuel and oxidizer streams through increased entrainment, thereby resulting in higher burning efficiencies.

Based on the above discussion, we may classify reacting RM and RT flows into four distinct categories (i) non-premixed RM, (ii) premixed RM, (iii) non-premixed RT and (iv) premixed RT. In premixed RM/RT, the flame front separates burned and unburned mixtures, so that the density difference across the interface can lead to instability when a suitable acceleration is applied (impulsive or otherwise). In non-premixed RM/RT, a sharp or diffuse interface initially separates fuel from the oxidizer. When accelerated impulsively by a shock or through other means accompanied by heat addition, stirring at the interface brings the fuel and oxidizer streams in direct contact followed by flame formation. While reacting flows occurring in applications are complex and involve multiple physical processes, the above classification allows us to study each component process in detail by isolating it from other physics.

## 9.2. Applications

Early interest in the interaction of a shock with a flame bubble was motivated by a desire to enhance mixing in Scramjet applications. In hypersonic flight, to minimize losses and heat load, the combustion must occur in a supersonic gas stream which reduces the residence times and requires greater and more efficient mixing [314–317]. Marble et al. [315] suggested using shock-induced mixing associated with the RMI to accelerate the mixing process between a cylindrical column of hydrogen fuel and the ambient air. In a typical Scramjet configuration (or a Shramjet: shock-induced combustion ramjet [318]), the fuel jet is supersonic and is intersected by an oblique stationary shock at every cross-section along its length. The authors of [315] applied thin body theory to show that the spatial development of the cross-section of the cylindrical jet is equivalent to the temporal development of a fuel jet that is processed by a moving shock wave. The latter unsteady configuration is simpler to investigate in experiments and can be interrogated with detailed time-dependent diagnostics. A secondary benefit of the baroclinic vorticity deposition is that it can result in jet liftoff away from the wall, avoiding the possibility of excessive wall heating [317]. The use of standing shock waves to enhance mixing and combustion through RMI eliminates the need to use active strategies such as shear layer excitation or intrusive injection features such as struts which would also require additional cooling [319].

RMI-mediated mixing also plays a significant role in multiphase detonation which occurs in propulsion applications with liquid fuels or in dust explosions. Pulse detonation engines (PDEs) or rotating detonation engines (RDEs) rely on detonative combustion which is more efficient, and are expected to outperform engines designed around the Brayton cycle [320]. However, for practical applications these devices must be powered by high-density liquid fuels to maximize the thrust-to-weight ratios. The resulting multiphase detonations involve a complex sequence of events (Fig. 21) including the shock-driven breakup of the fuel particles, evaporation and mixing, and reactions. The timescales for these processes depend strongly on the particle sizes and can overlap, further complicating the analysis. As the fuel particle is processed by the detonation wave, RMI leads to stretching of the interface followed by breakup into child particles. The timescales of breakup, and the details of the particle distribution following breakup will depend on the Weber number among other parameters. Following breakup, the increase in temperature

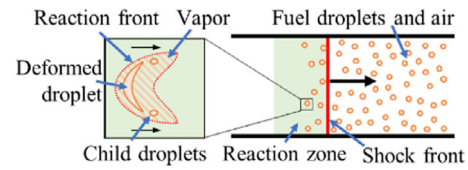


**Fig. 21.** Fuel droplets processed by a shock front in a multiphase detonation application. Inset shows details of the droplet deformation due to shock interaction, breakup of the parent droplet through shock-driven instabilities, and subsequent evaporation.

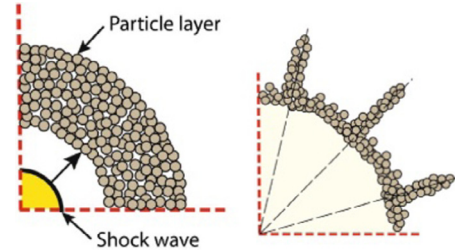


**Fig. 22.** Dispersal of particle layer by an explosive shock wave, and subsequent formation of particle jets resulting from SDMI. Images reproduced from [329] with permission.

will lead to droplet evaporation resulting in a supercritical fuel vapor cloud that will react with the ambient oxidizer after a chemical induction time. Depending on the parameters of the problem, RMI can strongly influence the droplet breakup process as well as the subsequent mixing between the supercritical fuel and the ambient.

Interfacial instabilities in a reactive context also play an influential role in dust cloud explosions, which have been observed in coal mines [321,322], food processing facilities and other industrial facilities [323,324]. A related problem is the augmentation of explosive performance through the addition of reactive particles to a charge [325–329].

In the latter scenario, the interaction of the detonation with the particle layer might be influenced either by the shock driven multiphase instability (SDMI [330–332], a multiphase analog of RMI) or the RT instability. SDMI is observed when a particle layer is dispersed by a shock as shown in Fig. 22, so that the interaction of the shock and the density gradient at the gas/particle interface leads to vorticity formation which culminates in particle jetting.

RT instabilities have also been identified as improving the performance of ultra-compact combustors (UCCs) in gas turbine systems [334,335]. UCC designs under consideration have the potential to greatly reduce the weight of gas turbine engines, thus increasing the thrust to weight ratio. In addition, the compact size allows for the inclusion of a reheat cycle between turbines, thus increasing the efficiency of the system. Most common UCC designs involve the admission of fuel and oxidizer streams tangentially into a circumferential combustor chamber, while the g-loading is provided centrifugally through high-speed rotation. Such a configuration in which a non-premixed fuel and oxidizer interface is subjected to high g-loading ( $\sim 300g_0$ – $3000g_0$ ) is susceptible to the development of the RT instability at the flame site. RT instability is also influential in premixed formulations of the UCC concept, where pressure waves generated from ignition can accelerate the flamefront resulting in an increase in the flamespeed [334].

Similarly, pressure gain combustors using shock-flame interactions have been recently considered as a means to improving the efficiency and specific fuel consumption of gas turbines. A promising approach is to allow shock waves to interact with

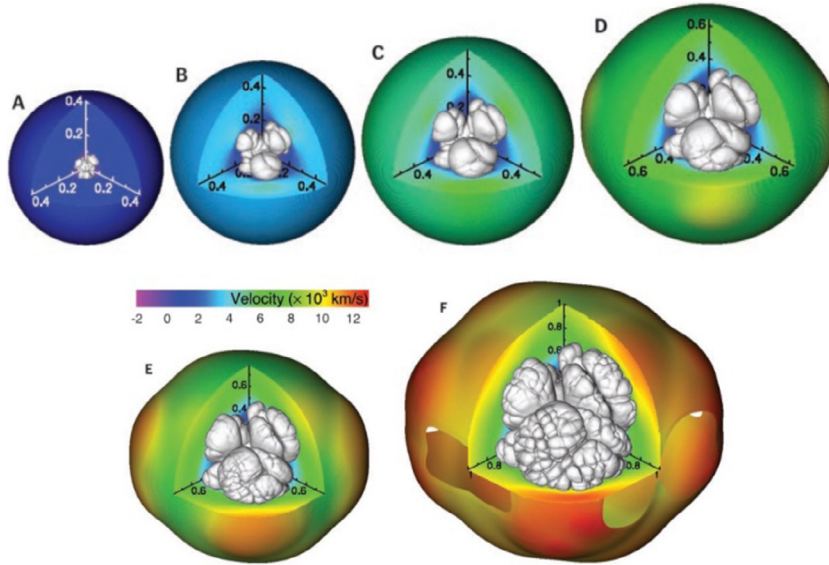


**Fig. 23.** Evolution of a carbon–oxygen white dwarf showing the RT-dominated thermonuclear flame (gray iso-surfaces) as well as the outer extent of the greatly expanded star. Spatial coordinates are scaled by the initial radius of the white dwarf. Panels (A)–(F) correspond to 1.26, 1.49, 1.57, 1.65, 1.76 and 1.9 s after ignition. Images are reproduced from [333] with permission.

the pre-mixed flame within the combustor, so that RM instabilities increase the flame surface area and hence the heat release rate [336]. The enhanced heat release rate can lead to an expansion of the burned gas, accompanied by the formation of additional pressure waves which can in turn drive further instabilities at the flame front. Preliminary experiments have shown a parabolic dependence of the flame heat release rate with the shock Mach number [336].

At the astrophysical scale, RTI has been hypothesized to trigger DDT in type Ia supernovae explosions of white dwarfs in binary systems. The mechanism underlying the supernova explosion in this system is runaway thermonuclear burning in a dense, electron-degenerate carbon–oxygen star which is driven over the Chandrasekhar stability limit by accretion from a binary companion. Recent simulations by [333] summarized in Fig. 23, used high-resolution numerical simulations to investigate the deflagration process. The mass of a stable white dwarf can exceed the Chandrasekhar limit through accretion from a neighboring star, resulting in a sequence of processes (core contraction, compression of core material, accompanying increase in temperature, and acceleration of thermonuclear reactions) that culminates in a runaway process and ignition [333]. The ensuing thermonuclear flame propagates radially outward initially with a laminar flame speed, but soon succumbs to the growth of RT unstable modes. The onset of RT on the flamefront signals a significant spike of the flame speed to a turbulent velocity, while the rising plumes of hot burned gas are interspersed with cold jets of unburned material that descend toward the core as reported in [333]. For a detailed overview of RT flame simulations in the context of SN Ia objects, we point the reader to the references discussed in Hicks [337]. The detailed simulations of [333] show a complex array of processes in which RT instability corrugates the flame surface across an ever-widening range of scales, secondary structures are observed on the flamefront and the counterflow of burned and unburned material triggers the KH instability which further increases the mixing and the flame speed. Comparison of computed spectra of carbon and oxygen from the simulations of [333] with Ia observations [338,339] show a discrepancy in the velocities associated with these elements. The authors of [333] hypothesize the higher velocities in the observational data imply these elements occur in the outer layers of the expanding star, and that the

flame has undergone a transition to a detonation likely instigated by RT. The higher flame velocity of the detonation and the more complete burning would explain the observation of C/O in the outer layers (while the total energy burned from detonation models are in broad agreement with observations [340]).

SN Ia are used as standard candles, since their light curves appear to satisfy a self-similar solution parametrized by the peak luminosity and the rate of decay [341]. However, a significant source of uncertainty in the empirical relations used to collapse the different light curves is the precise explosion mechanism, including whether a DDT is observed and the mechanisms that drive it. A second source of uncertainty arises in the modeling of turbulent, expanding flames in regimes of relevance to type Ia supernovae. Owing to the wide separation in scales, numerical simulations must make use of subgrid models to describe flame behavior. A parameter that governs the subgrid model is the flame speed which could either be the RT flame speed, or the result of the flame interaction with the ambient turbulence [337].

### 9.3. Flame physics

When chemical/nuclear reactions and heat release are present alongside instability-driven mixing, the resulting flow evolution can be very complex governed by multiple scales and parameters. In both premixed and non-premixed flames, ignition is accompanied by generation of pressure waves, the acceleration from which can further enhance (or impede) the growth of the underlying instability. In non-premixed flames, the formation of the reaction zone can sometimes alter the stability of the flow. Often, the initial perturbation seed for RT/RM in premixed flames is the growth of modes due to the Darrieus–Landau (DL) instability [342–344]. The DL instability occurs due to hydrodynamic effects induced by the thermal expansion of the burned gas, and is dependent on the density ratio  $\sigma_r = \rho_u/\rho_b$  between the unburned and burned gases. The thermal expansion induces a jump in the tangential velocities across the perturbed interface, while the resulting vorticity induces perturbation growth at all wavenumbers according to linear stability analysis [343,344]. However, Markstein [345] argued based on observations, that

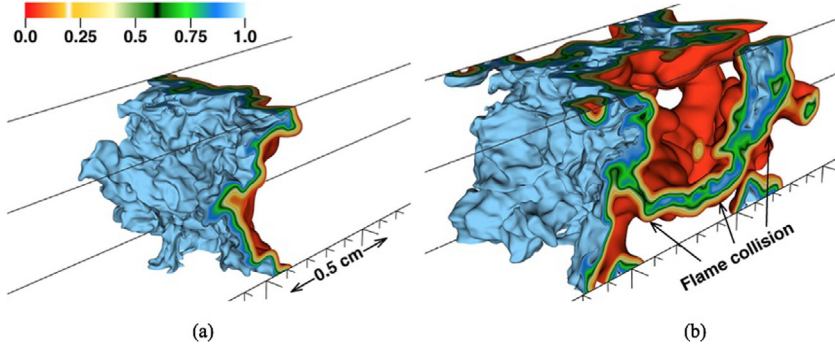


**Fig. 24.** Flame evolution showing mechanism of pulsating behavior from DNS of [346]. Images correspond to fuel mass fractions of 0.05 (red) and 0.95 (blue), and correspond to instances of minimum (a) and maximum (b) flame speeds. In (b), flame collision is visible. Images are reproduced from [346]. Reproduced with permission. (For interpretation of the references to color in this figure legend, the reader is referred to the web version of this article.)

small-scale perturbations must be stabilized due to curvature-dependent local stretching. This effect is captured by modifying the flame speed ( $S_f$ ) according to [342,345].

$$S_f = S_{f,\infty} - \kappa L_M, \quad (71)$$

where  $S_{f,\infty}$  is the laminar flame speed of the unperturbed flame,  $L_M$  is the Markstein length that sets the cutoff for the critical wavelength, and  $\kappa = \nabla \cdot \mathbf{n}$  is the interface curvature. The consequence of Eq. (71) is to differentially modify the flame speeds at the crests and troughs in such a way as to stabilize the DL instability [342,345] for wavelengths shorter than  $\lambda_c = 4\pi\sigma_r L_M / (\sigma_r - 1)$ . Spherically expanding flames such as those occurring in the astrophysical applications [347,348] approach the infinitesimally thin flame limit as their radius increases, and are thus particularly vulnerable to DL instabilities without the stabilizing effect of a diffusion thickness.

Massa and Jha [312] argued for an alternate mechanism for the stabilization of small scales on a flamefront. From a linear analysis of the premixed RM configuration, the authors of [312] showed that small scales on the flame surface are damped by a competition between combustion and baroclinic effects. The suppression of small scales is thus expected to depend adversely on the reactivity of the mixture and is more pronounced for weak shocks. Small-scale perturbations may also be affected by the increased diffusivity as a result of the temperature increase on the flame surface. In many situations, this leads to diffusive broadening of the flame as well as a relaminarization of the flame surface as small-scale features are lost to diffusion. Both RT and RM instability growth rates are compromised when the perturbations are imposed on an initially diffuse interface [65].

In addition to seeding perturbations, the DL instability could also potentially play a role in the self-acceleration of a spherically expanding flame. Akkerman et al. [347] illustrate such a scenario comprised of the following sequence: an initially laminar, smooth and spherical flame is formed as a result of energy deposition; as the flame front expands it is susceptible to the formation of cusps and creases due to the DL instability; the flame surface area increases as a result of the appearance of these features, thereby increasing the consumption rate of the fresh charge; the flame speed then continually increases leading to a sustained self-acceleration of the flame. During the self-acceleration phase, the flame may additionally be unstable to the growth of RT modes. While DDT driven by RT may be possible eventually in a self-accelerating flame, the authors of [347] show the required time and length scales are too large for it to be a concern in terrestrial applications.

An RT-unstable flame front may also exhibit self-regulating behavior [333,337]. The flame speed increases through turbulent

wrinkles generated by RTI. However, a corrective to this trend is that as cusps form on the flame front they might be lost to burning due to their high curvatures (Eq. (71)). As a result, a measure of balance may be achieved between the production of flame surface through RTI and the corresponding losses due to cusp burning [337]. However, it is not clear if this balance will be maintained through late times as the RT-unstable flame front is populated by low wavenumber modes which have low curvatures and are thus likely to survive the burning process with their flame speeds largely unaffected.

From detailed DNS, [346] showed an alternate mechanism for self-acceleration of a turbulent flame brush resulting from a self-generated pulsating instability. Fig. 24 shows the problem setup in which an initially laminar, unstrained flame is passed through an isotropic turbulent flow field with a characteristic velocity scale  $U_t$ . In [346], the authors show that the evolution of the flame surface area is a competition between the turbulent flame growth and the negative contribution due to intermittent flame collisions (Figs. 24). The balance between the continuous flame growth and the intermittent flame collisions results in a pulsating behavior of the flame surface area which leads to great variability in the turbulent flame speeds.

The pulsating behavior described above can establish an alternate pathway to flame acceleration, RM instability and a runaway process ultimately leading to DDT. The pulsations produce progressively stronger pressure waves, which initiate RM as they pass through regions of misaligned density gradients within the flame. The RM instability further intensifies the turbulence within the flame brush, leading to even stronger pressure waves. Thus, the RM instability is self-generated and driven by the pressure waves that stem from the pulsating flame, rather than an external source. Eventually, the overpressures strengthen to a point where the resulting waves reach the detonation CJ velocities as hypothesized and observed in the simulations of [346]. The above sequence of events could explain the DDT mechanism in SN Ia events, where the acceleration effects observed in terrestrial applications due to confinement are not available. Similarly, the configuration studied in [346] of a premixed flame is relevant to SN Ia, where convective turbulence in the core may be present prior to ignition. When the flame is formed, it will then propagate through this pre-ignition core convection field and interact with it [341].

In the following, we provide a brief review of the significant progress that has been made in our understanding of RM and RT flames. Note that this review is not intended to be comprehensive, but our hope is to provide the reader merely with a summary of significant trends in these areas of research and to identify potential opportunities for further progress.

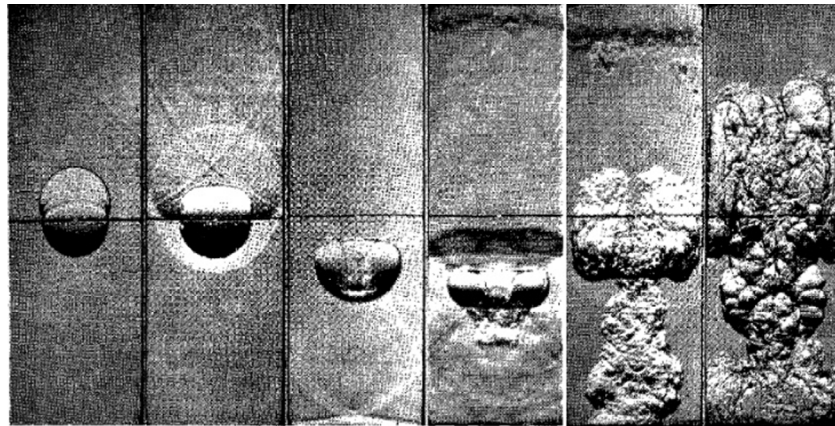


**Fig. 25.** Planar shock interaction with a spherical n-butane-air premixed flame from the experiments of Markstein [349]. Images correspond to timestamps of (from left to right) 0, 0.1, 0.14, 0.7, 2.5 and 3.5 ms. Reproduced from [350] with permission.

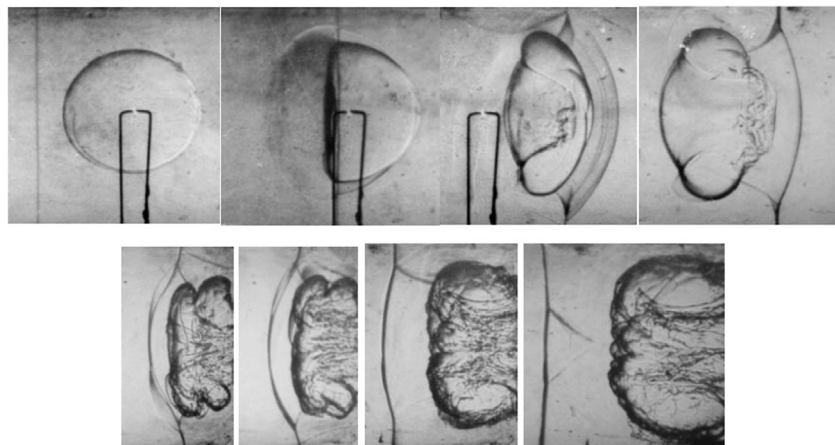


**Fig. 26.** Schlieren images of an ethylene flame bubble processed by an incident shock (traveling rightward), and later by a reflected shock (traveling leftward), from experiments of [351]. The incident shock Mach number was 1.7. Images are reproduced from [351] with permission.

#### 9.4. RM flames

The earliest experimental studies of a shock interaction with a flame were undertaken by Markstein [349,352,353], who examined the passage of a planar shock through a n-butane-air stoichiometric flame. The experiments were conducted in a vertical shock tube, in which a premixture of fuel and air were admitted, while the shock was introduced by rupturing a diaphragm separating compressed and ambient air. From high-speed photography, and pressure tracers, the authors diagnosed multiple interactions, first between the incident shock and the flame, and followed by interactions between reflected shocks and expansion waves. The interactions resulted in funnels (spikes in the RMI context), of cold air penetrating the flamefront, corrugating the flame surface and enhancing burning. The funnel features were correctly attributed to RM (due to shock/flame interaction), and RT (due to subsequent expansion wave interactions with the flame). The experiments were extended to a curved flame surface by Markstein in [349,353], where the effect of shock strength was also studied. In [350], results from experiments by Markstein were summarized for the first time for a spherical flame interacting with a planar shock (Fig. 25). Results were also included for the case in which the flame was perturbed by a fine-grid perturbation. Shortly after shock interaction, the flame surface was dominated by small scales, while larger scales due to RMI asserted themselves at late times.

Recent experiments include the study by Thomas et al. [351] of a shock interaction with a spheroidal ethylene flame bubble.

In the experiments, the flame was distorted by the passage of several reflected shocks, ultimately leading to a turbulent state as well as transitioning to a detonation wave. Fig. 26 shows high-speed Schlieren images from the experiment, including the appearance of RM-created spike strands at late times.

Rudinger [350] presented a wave diagram approach for analytically computing the interaction of a planar (1D) shock with a flame surface approximated using small perturbation theory. Early simulation work was performed by Picone et al. [355] who reported 2D simulations of a cylindrical flame-like region driven by a planar shock under conditions similar to Markstein's experiments [349,352,353]. In their simulations however, the flame was represented without reactive effects as a region of reduced density and higher temperature. A nonlinear theory of vorticity deposition was proposed to explain the simulation results.

In Batley et al. [356], the authors used a 2nd order Godunov solver to compute the shock-flame problem using a 1-step Arrhenius reaction, and a temperature-dependent thermal conductivity, while taking  $\text{Pr} = \text{Le} = 1$ . The simulations corresponded to the experimental configuration of Scarinci and Thomas [357]. More recently, Dong et al. [358] reported results from simulations of an ethylene/oxygen/nitrogen premixed flame subjected to an incident shock with a Mach number of 1.7, followed by repeated reflected shocks. The simulations used a detailed (35-step) mechanism for ethylene combustion, and reproduced the results of the experiments of [351].

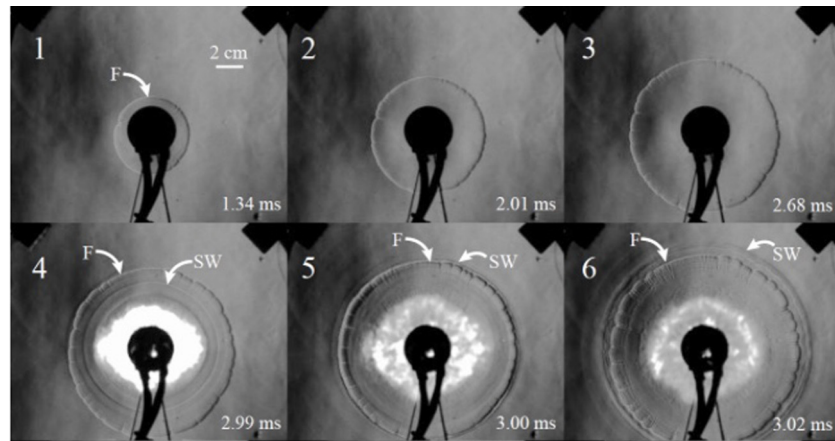


**Fig. 27.** Experimental Schlieren images of the interaction of an expanding shock with a cellular flame [354]. The cellular features on the flame surface provide the initial perturbations for the subsequent RM instability due to shock passage. Images reproduced from [354] with permission.

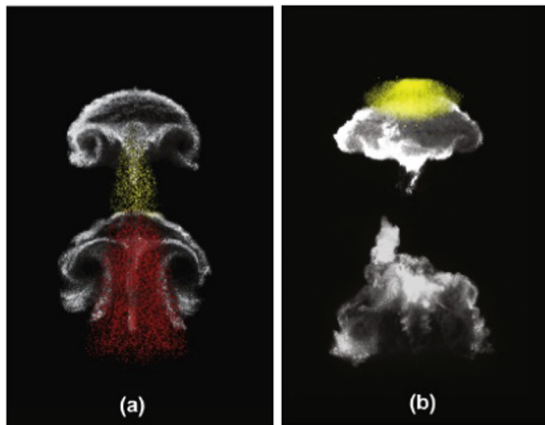


**Fig. 28.** Experimental images from Mie scattering and Chemiluminescence showing the reacting shock–bubble interaction problem at early (top) and late (bottom) times. The images correspond to shock Mach numbers of (a) 1.65 and (b) 2.83. Images are reproduced from [360]. Reproduced with permission.

Khokhlov et al. [359] employed 2D and 3D numerical simulations to investigate the modification of a stoichiometric acetylene-air flame due to shock interaction. They found that the shock induces RMI at the sinusoidally-perturbed flame site, and the associated vorticity deposition sustains the flame to late times against the stabilizing effects described in the Markstein model above. The formation of a “funnel” due to RM instability is evident in their simulations, as it transports fresh unburned material toward the flame. At late times, the mushroom head detaches from the rest of the spike, and proceeds to burn out leaving behind a cusped spike. The simulations of [359] showed an increase in the energy release rate of a factor of 20–30 for the RM flame over the unshocked case. Additionally, the energy release rate per unit area was also found to increase weakly with the shock Mach number, as the increased density at higher shock strengths leads to greater mass flow through the flame.

When a circular flame is repeatedly reshocked [361], the complex shock–flame and shock–shock interactions were observed to eventually lead to DDT. In their 2D simulations, Khokhlov et al. [361] found RM to be the dominant mechanism in the deformation of the flame surface, while the shear-driven KH instability only contributed to a third of the total turbulent kinetic energy at any scale. The transition to detonation occurs at the end of a sequence of processes initiated by the RM instability [361]. As the flame is repeatedly reshocked, a transition to a turbulent

flame brush is observed. The corrugated flame surface creates pressure fluctuations, which lead to localized hot spots. The hot spots represent sharp gradients in the chemical induction time, so that the location of the minimum induction time ignites spontaneously. The accompanying reaction wave propagates in the direction of the gradient of the induction time, and can eventually strengthen to a detonation propagating at the CJ velocity. Houim and Taylor [362] observed similar dynamics in their simulations of a hydrogen flame with detailed chemistry, under multiple shocks. The appearance of hot spots in their simulations precedes the formation of a detonation through the reactivity gradient mechanism. However, in contrast to [361], the authors of [362] found the hot spot formation is not due to flame corrugation, but essentially a 1D process also observed in their unperturbed flame simulations.

Using experiments in a vertical Hele-Shaw cell, La Fleche et al. [354] investigated RMI on a cellular flame. The Hele-Shaw plates had a gap width of 5 mm, and filled with a hydrogen–air mixture at ambient pressure and ignited using spark electrodes. As cellular features develop on the flame (due to thermo-diffusive instabilities), an expanding shock parallel to the flamefront is launched. The shock interacts with the flame, triggering RM seeded by the cellular structures (Fig. 27). Both light-to-heavy and heavy-to-light interactions were studied, with the RM in the latter situation resulting in a phase inversion of the seeded perturbations. More recently, Yang & Radulescu [364] presented a more complete work, whose Figs. 4, 7 or 9 show a similar sequence as the one we just described.

Haehn et al. [360] reported experimental results of RM-driven combustion in a novel configuration of direct relevance to the ICF application. In their experiments, a planar shock is refracted through a spherical bubble containing a stoichiometric premixture of H<sub>2</sub>, O<sub>2</sub> and Xe, so that the shock-focusing at the downstream pole of the bubble raises the temperature beyond the ignition point. The experiments were the first of their kind to extend the widely studied shock–bubble interaction (SBI) problem to the reactive flow scenario. During the shock “implosion”, the transmitted shock becomes curved, and is thus stronger as it reaches the focal point, before reflecting from the downstream implosion center [360].

Fig. 28 is a typical diagnostic image from the experiments of [360], using Mie scattering and chemiluminescence. The Mie scattering reveals the outline of the cloud of droplets resulting from the bubble atomization from shock impact. The chemiluminescence images are time-integrated, and responsive to the OH radical. Thus, a triangular shape is indicative of a reaction front that is propagating outward as the bubble traverses

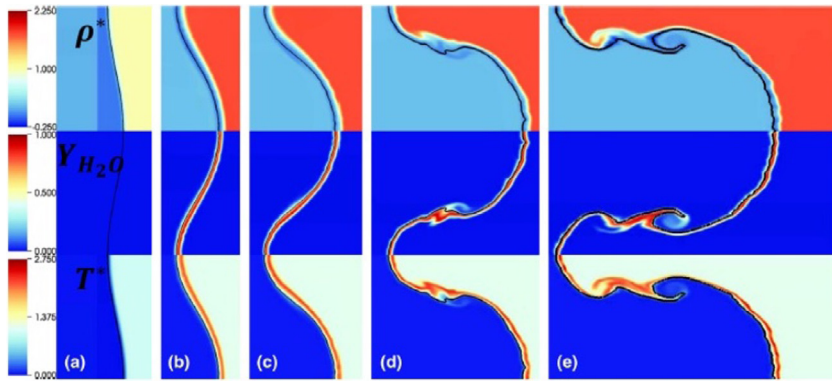


**Fig. 29.** Contours of scaled density,  $H_2O$  mass fraction and scaled temperature from 2D numerical simulations of a sinusoidally perturbed, non-premixed  $H_2$ - $O_2$  flame shocked by a Mach 1.2 planar shock. Images are reproduced from [363].

downward. This behavior was observed at low Mach numbers (Fig. 28(a)) when the reaction timescales were long compared with the bubble deformation timescales. At higher shock Mach numbers (Fig. 28(b)), the greater shock focusing resulted in much faster reaction timescales, so that the combustion process was completed before the bubble was completely deformed. This resulted in an oblate shape for the time-exposed reaction cloud seen in Fig. 28(b). The bottom figure which corresponds to a later time shows no OH signal, suggesting the combustion has proceeded to completion while the bubble is still undergoing deformation. The results from the reacting shock–bubble experiments of [360] were also reproduced numerically by [365] in their 3D simulations, using detailed  $H_2$ - $O_2$  chemical kinetics. The simulations revealed complex vortex dynamics due to secondary instabilities, which were inhibited in the presence of reactions and heat release.

In contrast to the extensive studies of premixed RM summarized above, the corresponding non-premixed problem has received little attention in spite of its significance to applications such as multiphase combustion. In [366], results from a comparative study of premixed and non-premixed combustion were reported at different incident shock Mach numbers. For the conditions of their shock tube experiment, the RMI-induced mixing did not result in the combustion of a pure hydrogen bubble in an oxygen environment. In contrast, premixed bubbles of  $H_2$ / $O_2$  (in  $O_2$  or  $N_2$  surroundings) underwent ignition when shocked at the same Mach numbers. Billet et al. [141] and Attal et al. [367] reported 2D results from simulations of a non-premixed shock–bubble flame interaction problem. In both studies, the effects of detailed chemistry and transport coefficients were included, while the problem setup involved an initially quiescent cylindrical  $H_2$  bubble embedded in air, and shocked by a Mach 2 planar shock. The development of the diffusion flame proceeds through a complex sequence of events, and is fundamentally different from the premixed examples discussed earlier. Ignition was first observed in a thin rib connecting the kidney-shaped vortex features on either side. The thin ridge is flanked on either side by air, and thus constitutes a double-diffusion flame surface. As the vortices develop more small-scale features, increased mixing is observed leading to combustion within the vortex cores. The corresponding sinusoidally perturbed, non-premixed RM problem was studied by Attal et al. [363] using high-resolution numerical simulations with detailed chemistry (Fig. 29). When no initial shock was present, ignition at the interface resulted in the formation of spontaneous combustion waves, which then accelerated the interface through RT and RM instabilities. The resulting growth rates were found to depend on several factors including the thickness of the interface, initial temperatures, degree of non-planarity of the combustion waves, reactivity of the mixture etc.

In addition, when an initial shock passed through the interface, the resulting development depended on the sequence of the shock-interactions. When the interface was first processed by the combustion wave followed by the incident shock, an RM-like growth was observed. In the opposite scenario, a variable- $g$  RT growth was observed, where the initial amplitude for the RT was seeded by RM from the incident shock passage.

### 9.5. RT flames

In the experiments of [368], a combustible mixture of hydrogen and air was pressurized in a cylindrical container and spark ignited. The diagnostics included high speed photography of the flame front, from which the radial trajectory of the expanding flame could be inferred. The authors in [368] concluded from the radial trajectory that the flame was RT unstable, and corroborated by the observation of flame bubbles ascending toward the unburned material. RTI was also found to be influential in the transition of so-called tulip flames (TF) to distorted tulip flames (DTF) in premixed combustion. Xiao et al. [369] performed 2D numerical simulations of a stoichiometric mixture of hydrogen and air confined in a long duct, and found the RTI to be responsible for the flame transition to DTF. The tulip flame is characterized by cusps, which collapse when the flame touches the walls of the duct. This generates strong pressure waves, which in turn provide the destabilizing acceleration for RTI development. The growth of RT modes at the flame front causes further deformation, leading to the formation of the DTF [369].

Hicks [337] performed 3D simulations of a premixed RT flame front to investigate the accuracy of commonly used subgrid models for flame thickness and flame speeds in astrophysical calculations. The simulations were initialized with a multimode perturbation, while reactions were modeled using a bistable reaction term implemented in an advection–diffusion–reaction equation. The simulations revealed the flame widths were thinner than suggested by traditional turbulent combustion models, likely due to stretching by the RT modes. Similarly, the observed flame speeds were in disagreement with traditional models which typically assume  $S_t \sim U_l$ , where  $U_l$  is the laminar flame speed. The authors of [337] attribute the failure of standard turbulence models to the formation of cusps on the flame surface, which are unaccounted for in the models. The likelihood of cusp formation and their prevalence scales with the RT forcing, so that at large values of  $g\mathcal{L}$  (where  $\mathcal{L}$  represents a dominant RT scale and  $g$  is the acceleration) such features are widely present. The cusps increase the flame surface area, as well as creating a focusing effect for the thermal flux [337] enhancing the flame speed beyond the theoretical estimates.

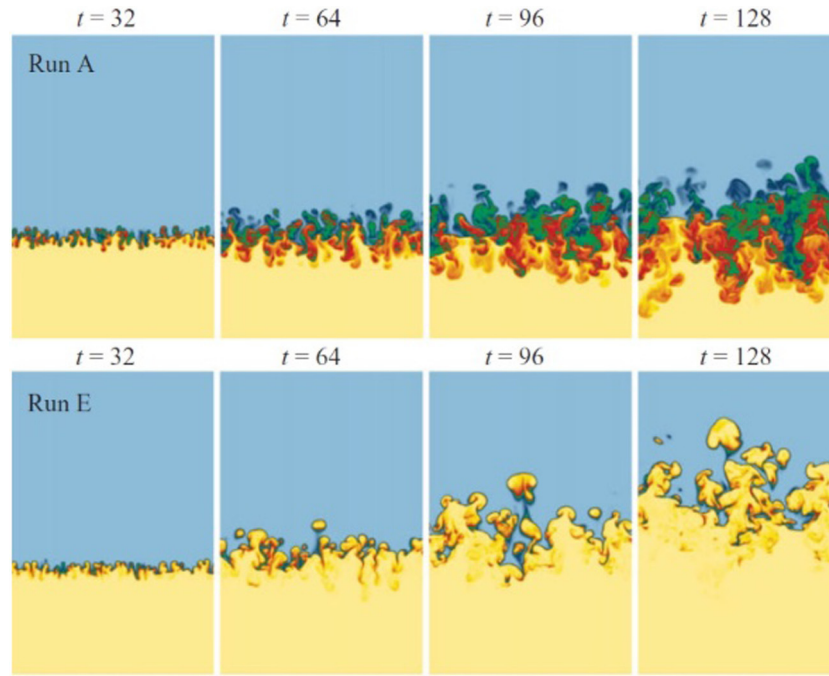


**Fig. 30.** Vertical slices of temperature (or a reaction progress variable) from the reacting RT simulations of [130]. The top row of images correspond to a reaction time  $\tau_r = 1600$ , while the bottom row is obtained for  $\tau_r = 16$ . The simulations depict a transition from a mixed phase ( $t < \tau_r$ ) to a segregated phase ( $t > \tau_r$ ). Images are reproduced from [130] with permission.

Reactive RT driven by reactions with timescales longer than the instability timescales (the so-called slow reaction regime) were investigated numerically by Chertkov et al. [130]. The authors were interested in the Boussinesq limit, with a 1-step reaction implemented in an advection–reaction–diffusion model. The resulting phenomenology is categorized into a mixed phase and a segregated phase. The mixed phase is observed for  $t < \tau_r$ , where  $\tau_r$  is a characteristic reaction timescale, and resembles a non-reacting RT, where the mixing between the cold reactants and hot products dominates the proceedings. For  $t > \tau_r$ , the reactions within the mixing layer dominate as there is a return to the pure phases due to the formation of hot products from the mixed material. This is accompanied by a noticeable shift of the center of the mixing layer toward the reactant stream seen in Fig. 30. The authors point out similarities between reactive RT and immiscible RT, since in both cases mixing is suppressed with a shift toward pure phases.

Finally, Attal and Ramaprabhu [370] reported the dynamics of non-premixed single-mode and multimode [371] RT mixing layers. The problem setup consisted of a sharp, perturbed interface initially separating a fuel and oxidizer, and evolving under the influence of gravity while instability-driven mixing improved burning at the flame site. Heat addition within the mixing layer was observed to modify the stability of the underlying RT flow. For instance, for an initially unstable configuration, heat addition from reactions resulted in the formation of a third, intermediate layer which caused the flame interface near the spikes to stabilize. In contrast, when the initial configuration was stable, reactions within the flame region resulted in subsequent instability.

## 9.6. Concluding remarks

Since Markstein's early experiments [349,352,353], significant progress has been realized in the study of reacting RT and RM instabilities. The vast majority of these studies have investigated the premixed RM problem, likely due to its relevance to the Scramjet application. Similarly, a lot of the activity in the

premixed RT community has revolved around the astrophysical application of type Ia supernovae events. In comparison, the non-premixed RT and RM flame problems have received little attention, in spite of their potential relevance to multiphase combustion applications. Experimental studies of such flow configurations remain challenging due to difficulties associated with achieving the initial ignition (requiring very high initial temperatures or pressures), the ability to sustain the flame, as well as demands placed on the diagnostics. Numerical simulations can play a role here in the design of experiments of non-premixed RT/RM, and in the identification of fruitful regimes for exploration. However, a significant source of uncertainty for simulations is the accuracy of chemical kinetic mechanisms for high pressure conditions. Available detailed chemistry mechanisms need to be validated either using first-principles approaches such as molecular dynamics or experimental techniques at high pressures. To compound the difficulty further, experiments at high pressures are often conducted with diluents such as inert gases for safety considerations. The effect of such added diluents at high pressures must be properly accounted for in constructing and validating reaction mechanisms for such regimes. Finally, we echo the remarks of Oran [341] who called for greater synergy and collaboration between the astrophysical and the chemical combustion research communities.

## 10. Explosively expanding single and multiphase flows

### 10.1. Preliminary remarks

This section hopes to shine some light on the role of RT and RM instabilities that arise in explosively driven flows. In these flows, a highly compressed, high-pressure, high-density region of fluid is suddenly allowed to expand radially and the front between the initially compressed fluid and the ambient undergoes RT and RM instabilities. A range of environmental and engineering applications exhibit features of this explosively driven flows.

This section offers a brief discussion of these instabilities in flows issued from and related to the detonation of an explosive

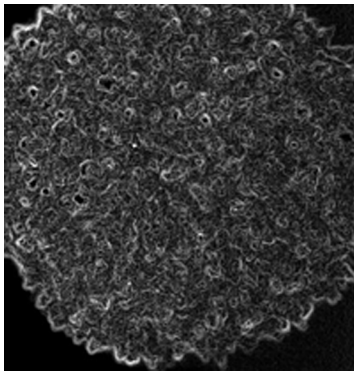


**Fig. 31.** Rapidly expanding turbulent reactive front resulting from a thermobaric test [372]. Reproduced with permission.

charge. The study of RT and RM instabilities in this extreme regime is particularly difficult using experiments due to the challenges of obtaining detailed measurements, while simulations are complicated by the restrictive grid and time-stepping requirements. For homogeneous explosives, i.e. bare explosive charges, these instabilities occur at the material front (or contact discontinuity) between the explosive products and the surrounding medium. In the case of heterogeneous explosives, i.e. explosives in which metal particles are either embedded within the charge or emplaced surrounding the charge, the instabilities take place not only between the explosive products and the surrounding medium, but also at the advancing front of the particle cloud. The RT and RM instabilities in these rapidly expanding flows are substantially more complicated than their classical counterparts.

Explosive flows could be classified into two broad categories: (i) homogeneous explosive driven flows, in which only an energetic reactive substance is involved and the resulting flow is entirely in the gaseous phase; (ii) heterogeneous explosive driven flows, in which the explosively driven flow is a mixture of gaseous products of the detonation process along with the particulate matter that was initially seeded as part of the multiphase explosive. In both cases, the evolution of the pressure and density profiles in the flow is such that RT and RM instabilities occur multiple times within the typical period of interest. In this section, we discuss these hydrodynamic instabilities in the context of homogeneous and heterogeneous explosives where the hydrodynamic instabilities occur at the material front between two gases or at the particulate front.

In subsection 2, we give an overview of the flow following the detonation of explosive charges. Next, we report on the gas-particle counterpart to the classic two-fluid RT and RM instabilities. The final subsection summarizes the state-of-research concerning the characterization of hydrodynamic instabilities in particle laden-flows and the explosive flow regime.

## 10.2. Some examples of explosives flows

We first consider a few examples of explosively expanding flows and the observations of RT and RM instabilities in them. Fig. 31 shows the surface of a very rapidly expanding turbulent reactive material front resulting from a thermobaric test. The effect of RT and RM instabilities is clearly seen in the highly wrinkled nature of the expanding front. The early growth of these instabilities and their later development into a highly turbulent interface is often not easy to observe in such explosively driven flows, due to the rapid evolution of the process and the intense brightness associated with an explosion. The difficulties associated with describing the initial detonation process are avoided if

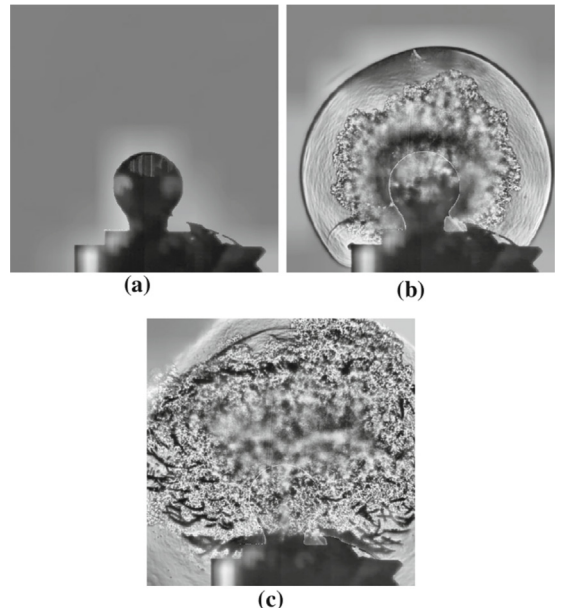


**Fig. 32.** Schlieren images of pressurized glass sphere experiment: (a) before explosion; (b) strong blast wave phase; (c) end of reshock phase. The secondary shock is visible near the top left corner of the picture. [373]. Reproduced with permission.

we consider the problem of a sudden release of a highly pressurized spherical or cylindrical region of gas into an ambient of much lower pressure. In this section, we will refer to these idealized configurations as spherical or cylindrical shock tubes, as they are analogous to the classical planar shock tube problem, and the sudden release is equivalent to bursting of the diaphragm in a conventional shock tube. Fig. 32 shows Schlieren images of flow resulting from sudden release of pressurized gas initially contained within a glass sphere. The outermost sphere, seen in frame (b), is the outward propagating primary shock (PS), which is observed to be stable. In contrast, the material interface (or the contact surface) between the gas initially contained within the sphere and the ambient undergoes instability, which later develops into the highly turbulent interface seen in frame (c).

The presence of particles (or droplets) in the rapidly expanding fluid greatly alters the nature of RT and RM instabilities. In addition to the density jump across the gas-gas interface between the initially pressurized and the ambient fluid, in the multiphase case, we also have a strong density jump across the particle front. The particle front separates the high-density fluid-particle mixture from the lighter, particle-free fluid, and thus can undergo RT and RM instabilities. Two different configurations have been considered in these studies. In the first configuration, the particles are embedded within the explosive and thus at the end of detonation, the region of high-pressure, high-density gas contains the particles and the mixture rapidly expands into the ambient. The time evolution of the interface in this scenario showing the development of RT and RM instabilities can be seen in Fig. 33 for a spherical explosive charge of nitromethane embedded initially with zirconium particles.

The second configuration often considered is a spherical or cylindrical explosive charge surrounded by an annular region packed with particles. Examples of experiments studying this configuration include those by Frost et al. [374] or, more recently, by Hughes et al. [375]. In a weak cylindrical casing, Frost et al. set up an annulus of packed glass particles sandwiched between two thick annuli of packed iron powder in an attempt to enforce quasi-two-dimensionality in the dispersal of the glass

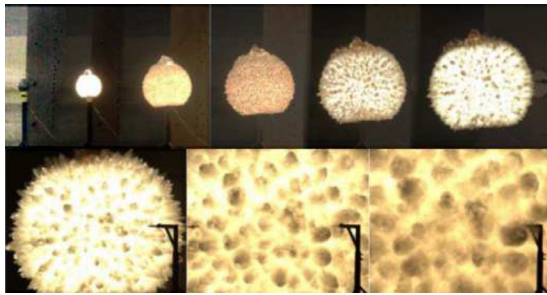


**Fig. 33.** Development of instabilities on fireball surface from detonation of a charge packed with zirconium particles saturated with nitromethane [376]. Reproduced with permission.

particles. A PETN (pentaerythritol tetranitrate) chord ran through the length of the arrangement and was lit at the far end, opposite the camera. The explosive was chosen to limit afterburn, and the cylindrical geometry allowed for better optical access and quantification of instabilities. High-speed recordings of the post-detonation flow showed in detail the formation of late-time aerodynamically stable particle jets. These can be seen in the top row of snapshots in Fig. 34. Interestingly, a substantial difference in the particle jet instabilities is observed in the top row between the dry powder (left frame) versus the water-saturated wet condition (right frame). Hughes et al. [375] furthered the study of this type of configuration through experiments that were instrumented specifically to capture gas, particles and gas-particle flow data. Note that these experiments were significantly more energetic than those studied in Frost et al. [374], using 8.5lbs of Composition B in contrast with the few grams of PETN. However, the particle mass-to-charge ratio remained consistent at around 10–13. The middle and bottom row snapshots of Fig. 34 show axial and transverse views of a tungsten-particle shot (left) and a steel-particle shot (right). Luminescence of the tungsten particles aside, one can clearly distinguish different shapes of instabilities between these shots. The instabilities in the experiments involving steel particles display numerous fine structures leading the particle front, comparable to the observations made by Frost et al. In contrast, the instabilities in the experiments involving steel particles are manifested as bright and dark striations following a bright and dense leading band of particles.

It is thus clear that though the fundamental mechanisms of RT and RM instabilities remain the same, their manifestation in terms of observed evolution of material interfaces in explosively driven flows can show substantial variations. The factors that seem to influence the evolution are (i) the geometry of the problem (spherical versus cylindrical expansion), (ii) instability of rapidly expanding single-phase gas–gas interface versus multiphase particulate front, (iii) particles being initially embedded within the high-pressure, high-density gas versus emplaced outside, and (iv) other factors such as initial pressure and density ratio between the inside and the ambient, size, density and packing volume fraction of the particles, etc.

### 10.3. Phenomenology of explosively driven flows

The wave diagram in Fig. 35 represents the main events that follow the detonation of an explosive charge surrounded by a bed of particles in spherical or cylindrical geometry. Ignoring for the moment the particle cloud, as the explosive charge detonates, at the end of the detonation there exists a spherical or cylindrical region of very high-pressure, high-density gas surrounded by the ambient fluid. What follows next can be approximately thought of as a spherical or cylindrical shock tube problem. An

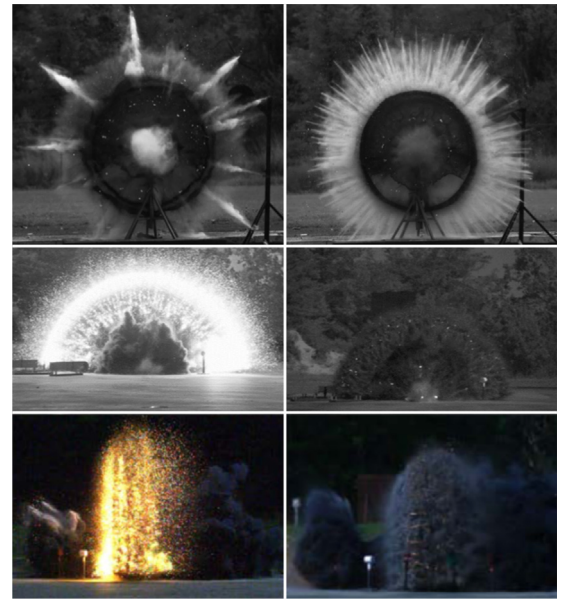


**Fig. 34.** Top row: dispersal of a layer of dry (left) and wet (right) glass particles shown at  $t = 12$  ms. [374]. Middle row: axial view of the dispersal of layers of tungsten particles (left) and steel particles (right) by composition B at  $t = 3.67$  ms. Bottom row: transverse view of the dispersal of layers of tungsten particles (left) and steel particles (right) by composition B at  $t = 3.60$  ms [375]. Reproduced with permission.

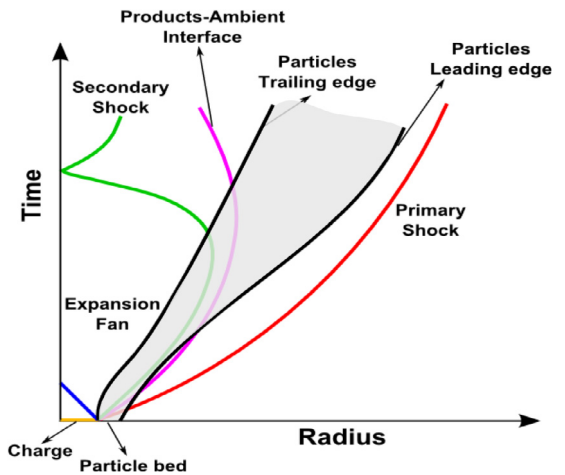


**Fig. 35.** Schematic wave diagram for the detonation of a heterogeneous explosive.

outward propagating blast wave (BW) and an inward propagating expansion wave (EW) are generated. The contact interface (CI) forms as the discontinuous surface between the outward moving detonation products and the shock-heated air and is RT unstable. Due to the over-expansion of the flow near the origin, the tail of the expansion wave typically turns into a secondary shock (SS) wave. The initially weak secondary shock wave starts expanding outward, entrained within the detonation products. As it strengthens, the secondary shock wave turns and implodes [377]. The deceleration of the contact interface during this phase of the flow promotes the growth of RT structures at its interface. Eventually, the secondary shock wave reflects off the origin and propagates out and interacts with the contact interface initiating RM instability. This interaction reverses the direction of travel of the CI which begins to move outward. The SS continues as a transmitted shock and the interaction also generates a weaker,

reflected, tertiary shock that travels inward and reflects off the origin. Meanwhile the CI slows and eventually heads back toward the origin where it encounters the outward moving tertiary shock. This process continues until there is not enough energy left to repeat itself [377].

With the added presence of particles, the interaction of the primary shock, gas contact and the secondary shock with the particle cloud must be considered. When particles are initially distributed within the explosive (and within the high-pressure products of detonation) the process is similar to that of the single-phase limit, especially when the particles are very fine. Fig. 35 depicts the scenario where particles are emplaced initially around the high-pressure gas region. In this case, the particle cloud presents an inner front and an outer front, across which the gas-particle density increases and decreases, respectively. As the primary shock, and later the secondary shock propagate over the particle cloud, both the inner and outer fronts can undergo RM instability. Also, due to the deceleration of the particle bed, after the rapid initial acceleration, the outer front also undergoes RT instability.

The instability of a CI in a detonation problem resulting from a spherically or cylindrically expanding material front is in several ways more complex than those considered in corresponding planar configurations [378–380]. For example, classical studies have considered the simplified problem of an isolated interface with a density jump, with uniform fields on either side of the interface, and with a controlled evolution of the interface. In contrast, in a spherical or cylindrical shock tube, the PS and SS remain very close to the CI, so that the CI cannot be considered to be spatially isolated. At later times, as the secondary shock approaches and interacts with the CI, the evolution of the interface switches from RT instability to RM instability. Since the SS passes from heavy-to-light gas, the CI instability is expected to first decay, change phase, and then grow linearly due to the RM instability. After the passage of the SS, the instability again switches from RM to RT instability. Thus, the time evolution of perturbation at the CI is quite complex. Furthermore, in the detonation problem the compression rate on either side of the CI is not the same, nor is it spatially uniform. These factors make the instability of a detonation-driven material front a non-classical one.

The above non-classical instability of an explosively driven CI was considered by [378–380], who pursued the following steps: (1) Solve the mean flow equations for the detonation products and obtain the base flow solution, (2) linearize the perturbation equations and expand in terms of spherical harmonics or cylindrical modes, (3) solve the linearized perturbation equations as an initial value problem, (4) perform the calculation for different harmonic modes and identify the most amplified mode. The key point to note here is that since the base flow is time-dependent, the stability analysis does not lead to a standard eigenvalue problem. Most interestingly, even in the time-dependent problem, the linear perturbation evolves to a global eigenmode and the growth rate is independent of the details of the initial perturbation. The advantage of such a numerical approach is that except for the assumption of linearity, the analysis considered both the base flow and the perturbation to be fully compressible, while the complex radial structure of the base flow was also retained in the analysis.

In the numerical simulations, an initial half-Gaussian perturbation in density was added to the base flow in the high-pressure region. Immediately, the phase of the density perturbation reversed and began to grow into a Gaussian-like shape as did the temperature perturbation. The radial velocity is also Gaussian-like, while the perturbed transverse velocity and pressure modes near the contact interface appear to be odd functions centered

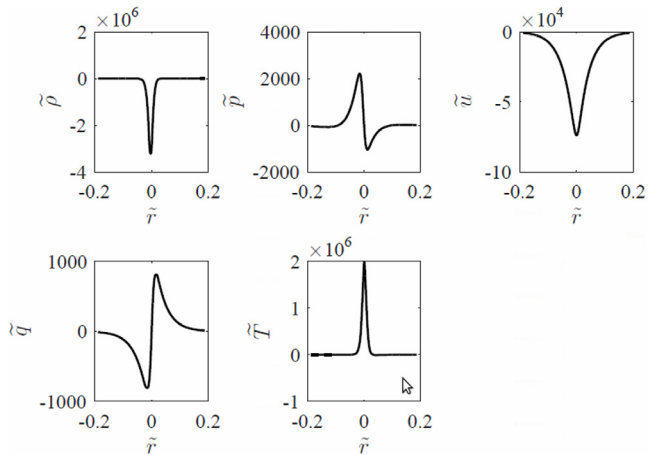


**Fig. 36.** Radial structure of the perturbation modes obtained at nondimensional time  $t = 5$ . The different frames show the structure of density, pressure, radial velocity, transverse velocity and temperature eigenmodes for spherical harmonic mode  $N = 64$ .

Source: Adapted from Crittenden and Balachandar [378], *Phys. Fluids*.

around the contact. In Fig. 36, the radial structure of the perturbation eigenmodes are plotted for the  $n = 64$  spherical harmonic mode.

The results of the stability analysis are presented in Fig. 37 as the integrated perturbation amplitude plotted against time and compared against the theoretical model for perturbation growth by Epstein [381]. The results are for spherical geometry, where the different frames are for different spherical harmonic mode numbers. Note that the spikes in the curves are due to sign-changes that occur during interaction with the SS. Excellent agreement between the theoretical and numerical results for the middle range of wavenumbers (i.e., for  $n = 16, 32, 64$ ) is observed, and is maintained through the collision of the secondary shock and the contact interface. A key finding is that, despite its simplifying assumptions, the instability theory of Epstein predicts the RT instability of the CI during its initial deceleration quite well. Even more remarkably, the theory is able to predict accurately the evolution of the perturbation during the RM instability and during the late-time RT instability.

Similar linear stability results were obtained for much higher pressure ratios that are typical of the detonation problem. Also, cylindrical geometry was considered with similar good agreement between the numerical simulation results and the simple theoretical model of Epstein. These results are presented in [378]. The above results are for the gas-gas contact interface and the corresponding results for a multiphase situation for the instability of the particulate front were discussed in [382,383].

#### 10.4. Simulations of RT and RM instabilities

High-fidelity simulations of explosions are challenging by nature – these flows are broadly multiscale, fully three-dimensional, highly unsteady and turbulent; their characteristic time scales are extremely short; and the pressure and temperature ranges reach extreme values. Therefore, despite the recent expansion of computing power, fully-resolved, multiphysics simulations of explosions are still out of reach, and detailed studies of the embedded RT and RM instabilities remain a difficult task.

##### 10.4.1. Single phase flows

An early study of turbulent mixing in explosions was proposed by Kuhl [384] in 1993. The work consisted of two-dimensional

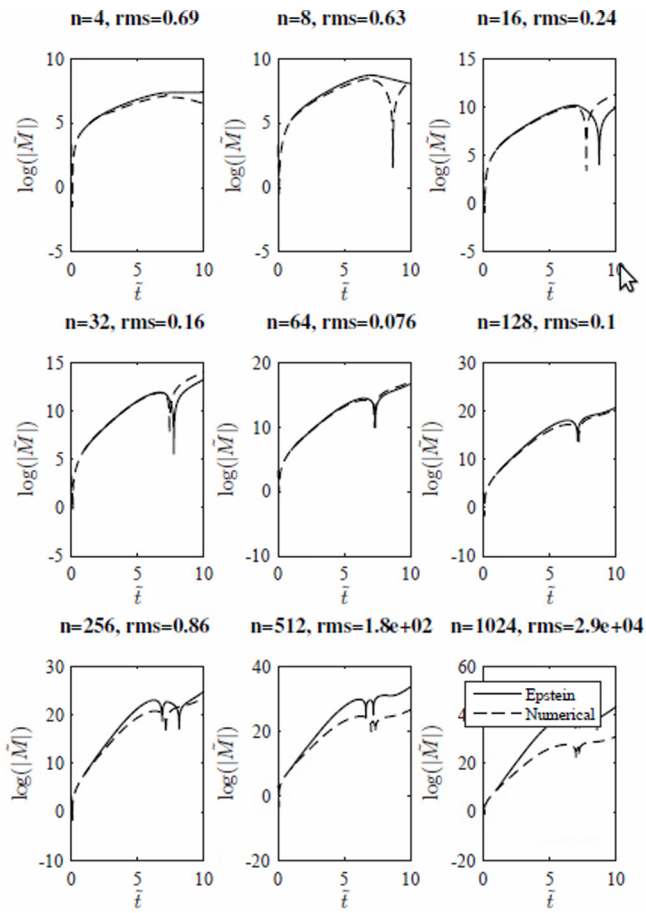


**Fig. 37.** Comparison of numerically evaluated perturbation amplitude in log scale to Epstein's theoretical results for a spherical shock tube with an initial pressure ratio of 22:1.

Source: Adapted from Crittenden and Balachandar [378], *Phys. Fluids*.

simulations of the mixing taking place in the fireball of an HE-driven blast wave, and the author identified four mixing phases [385–387]: (i) a strong blast wave phase, during which the fireball interface is subject to the RM instability when the detonation wave reaches the edge of the charge, causing the mixing width to grow linearly; (ii) an implosion phase where the fireball is subject to RT instability, and the mixing width grows according to a power-law; (iii) a reshock phase when a secondary shock interacts with the density structures in the fireball, causing another RM instability; and finally (iv) an asymptotic mixing phase at late time, during which the mixing layer achieves an asymptotically-constant width. It was found that a small residual of fluctuating kinetic energy driven by the vorticity field remained at late times.

Balakrishnan et al. [388] investigated the flow following the detonation of nitromethane, trinitrotoluene, and High-Melting Explosive. Using three-dimensional simulations, they studied the role of hydrodynamic instabilities on the blast effect of these explosives. To promote instability growth, random density and energy fluctuations were added to the inner edge of the initial explosive charge. The authors reported the four mixing phases and similar mix width timeline as described in [384], resulting in afterburn/combustion between the detonation products and the shocked air. At the onset of the asymptotic phase, structures in the mixing layer begin to merge, leading to a wrinkled appearance and loss of memory of the initial perturbation. Nonetheless, the appearance of the fireball seemingly remained unique. Therefore, the authors suggested that two similar explosive charges

could result in the same energetic characteristics post-detonation while appearing visually distinct. They also observed the secondary shock wave distorts as it passes through the mixing layer. Vortical structures in the mixing layer cause local variations in the level of afterburn, thus affecting the local speed of sound. It follows that the secondary shock wave may become faster or slower locally, leading to its distortion. However, the secondary shock recovers its spherical shape shortly after exiting the mixing layer. The simulations suggested that the mixing and afterburn energy release lead to a stronger and faster secondary shock and to a smaller decay rate of pressure behind the primary shock. Finally, the authors observed that enhanced mixing between the detonation products and shock-compressed air leads to improved impulse characteristics of the explosives that only three-dimensional simulations can predict accurately.

Recently, Courtiaud et al. [373] reported a numerical and experimental study of mixing inside fireballs using the analogous non-reacting pressurized glass sphere experiment illustrated in Fig. 32. Removing the numerical complication associated with the detonation and subsequent combustion/afterburn of a high explosive (HE), they were able to concentrate on mixing. First, their two- and three-dimensional LES confirmed that the glass sphere analog is a good approximation for the flow of a HE fireball as all four characteristic mixing phases discussed earlier [384, 388] were captured. Then, their results suggested that the overall mixing layer development qualitatively parallels the classic RT theory. Indeed, their analysis indicated that the spectral content of the initial perturbations directly influenced the mixing layer growth. Notably, the initial perturbation amplitude dictated the development regime of the RT instability. Finally, they observed that the mixing process scales with the initial energy of the flow, while being susceptible to the initial density contrast between the explosive products and air, reminiscent of the initial Atwood number effect.

Annamalai et al. isolated the RT instability within the explosion context [389]. They performed two- and three-dimensional studies of an outward propagating but decelerating single-mode perturbation around the contact interface, following a finite source cylindrical blast wave. The RT instability in this context contrasts with classical studies, since it involves a cylindrical geometry, time-dependent acceleration, both radially inward and outward displacement of the contact interface causing the wavelength under consideration to change in time, and time-dependent and compressible background flow. The authors narrowed the scope of their study to cases of isolated circumferential modes, isolated axial modes, and isolated circumferential-axial modes. Their simulations show that in the linear regime, the instability's perturbation growth rate is proportional to the exponential of the square-root of the wavenumber. In the nonlinear regime, they reported that the bubble height grows as the inverse of the square root of the wavenumber. They complemented their study with comparisons against three variations of a buoyancy-drag flow model of increasing levels of complexity. Although non-trivial to initialize, the most exhaustive version of the models considered accounted for unsteadiness, compressibility, finite interface thickness, and linear-to-nonlinear transition and offered reasonable predictions of the numerical simulations.

#### 10.4.2. Multiphase flows

The heterogeneous explosive configuration where the particles are embedded in the charge has been explored by Balakrishnan et al. [390]. Using an Eulerian-Lagrangian formulation along with an extended version of LES to handle dense flow fields, the authors studied the role played by a dense cloud of inert metal particles in the mixing layer following the detonation. Their three-dimensional spherical simulations showed that

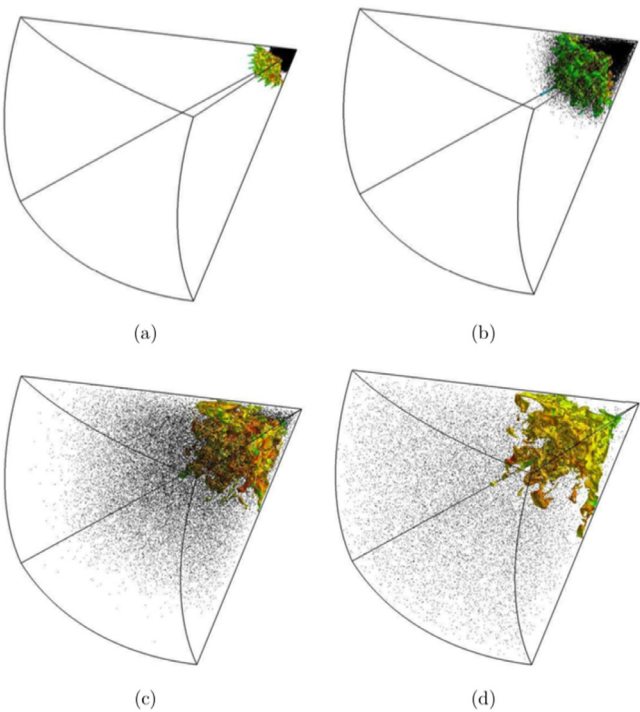


**Fig. 38.** Contact front overtaken by particles in an Eulerian-Lagrangian LES simulation. (a)  $t = 0.13$  ms, (b)  $t = 0.58$  ms, (c)  $t = 1.52$  ms, (d)  $t = 4.02$  ms [390]. Reproduced with permission.

Rayleigh–Taylor structures emerge from the mixing layer prior to its interaction with the particles as seen in Fig. 38a. Interestingly, these are the same particles that initially perturbed the flow-field between the outer edge of the particle cloud and the contact interface. The mixing layer growth is further enhanced soon after as the solid particles overtake the contact surface, Fig. 38b. A familiar sequence of events follows with a stretched RT-unstable mixing layer as the secondary shock moves inwards, Fig. 38c, and then a re-shocked mixing layer after the focusing of the secondary shock. The vorticity deposited further wrinkles the mixing layer, Fig. 38d. In this heterogeneous explosive configuration, the peak rms concentration fluctuations reaches 23%–30% in intensity, indicative of significant mixing. Upon comparison with a homogeneous configuration containing the same quantity of explosive, it is concluded that the turbulence intensity is enhanced by the presence of the solid particles and by the delayed re-shock. The action of the particles on the flow causes the mixing layer to grow non-linearly from early time. The momentum and energy absorption by the particles slow the mixing layer growth during the implosion phase.

The above efforts were also extended to the problem of the propagation of a spherical explosive charge (TNT) surrounded by a dilute cloud of reacting aluminum particles in [391,392]. Results from the simulations indicate that similar to the charge-embedded case, the presence of particles seed the RT instability at the CI, which promotes mixing and afterburn. The four mixing phases characteristic of homogeneous explosive flows are still observed. Particle size appears to play no role in the amount of mixing and afterburn following the blast wave, independent of the initial particle distribution and particle-to-charge mass ratio. The authors report that, due to the energy released by the afterburn, the pressure diminishes relatively slowly behind the main shock wave, while the secondary shock becomes stronger as a result of the hydrodynamic instabilities. The late-time energy

release by the afterburn appears nearly self-similar and independent of the hydrodynamic instabilities. The authors also observed that the radial trajectory of the aluminum particles was deflected by the vortex rings surrounding the growing instability features, thus causing lateral dispersion and clustering. Preferential heating and combustion of particles were observed, in particular in the afterburn regions. The initial particle mass loading appears to promote larger particle clusters in response to the formation of stronger vortex rings. Particle size was conjectured to play a key role in the clustering process during the second interaction with the mixing layer.

An observation widely reported in the explosive dispersal of particles surrounding a HE charge is the formation of late-time aerodynamically-stable particle jets. The mechanism for formation and evolution of these jetting instabilities is still unclear. However, the important role played by hydrodynamic instabilities in HE flows, as illustrated in the discussions above, points to the RT and RM instabilities as natural candidates for contributing toward late-time jetting. Milne et al. [393] numerically studied the processes following the interaction of an explosive with a surrounding layer of liquid or powder. Their multiphase simulations showed that the HE detonation causes a spall layer, and then an accretion layer that can break up, thus seeding the conditions for particle jet formation. These fragments follow a ballistic trajectory while leaving a trail of debris. The authors' analysis of two-dimensional simulations coupled with experimental data lead them to the conclusion that the timescale of the RT instability was too long to successfully initiate the formation of the particle jets. In a comparable study, Ripley et al. [394] conjectured the jet formation follows the shock-particle front interaction near the charge's surface and that the number of jets is a function of shock pressure. In other words, the RM instability is responsible for seeding the particle jets. The subsequent growth of these jets was linked to transverse displacement of particles induced by complex shock interactions, inelastic collisions and particle wake interactions that were qualitatively modeled with a particle attraction force.

Recent efforts in furthering the understanding of the late-time particle jet formation has focused on the effects of initial perturbations present in the explosive charge or in the surrounding bed of particles. Annamalai et al. [328] investigated the effect of a single-mode perturbation on the energetic dispersal of heavy inert particles at low volume fractions. Their point particle simulations indicated that initial perturbations in the explosively expanding detonation products did not have a noticeable impact on either the gas phase or the particles. Conversely, a perturbation imposed on the initial particle bed leaves a clear signature in the particle cloud volume fraction distribution. The innermost front of the cloud shows a fingering instability pattern at the same wavelength as the initial perturbation. Similarly, the mixing layer exhibits instability structures with the same dominant wavelength. Ouellet et al. [395] refined this work by introducing combinations of two-mode perturbations. Their simulations suggested that the bimodal perturbation causes an increase in the width of the dispersed particle cloud. Overall, this dilute initial particle cloud of heavy particles behaved similarly to a bimodal fluid–fluid RT instability. Interestingly, the authors noted that the particle cloud expands faster locally in regions in lower initial volume fraction. Also, the underlying mixing layer structure grew perturbations mirroring the particle cloud perturbations as seen in Fig. 39.

### 10.5. Experiments of RT and RM instabilities

Carefully controlled experiments of explosively expanding flows are difficult to design and hence remain scarce. To date,

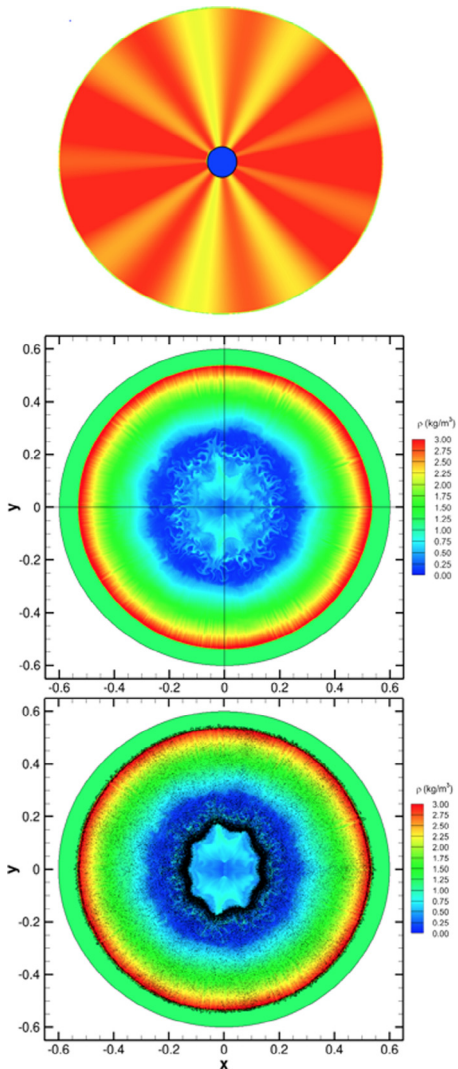


**Fig. 39.** Top: Initial particle volume fraction contour (close up view). A baseline uniform volume fraction of 5% is modified by the addition of perturbation wave numbers 2 and 9. The local maximum particle volume fraction is 7% and local minimum is 3%. Middle: Gas density contours only at  $t = 500 \mu\text{s}$ . Bottom: Gas density contour and computational particles at  $500 \mu\text{s}$  [395]. Reproduced with permission.

few have presented a detailed view of the hydrodynamic mixing that follows the primary blast wave.

Courtiaud et al. [373] exercised the compressed balloon method to study mixing inside a HE explosion by analogy. This experimental setup consists of a pressurized glass sphere sealed to a metallic base with gas inlet enclosed in a steel vessel with optical access. Experiments using this apparatus have been successful at reproducing the characteristic features of blast-driven flows and have provided results consistent with numerical simulation results available in the literature. The authors conducted accompanying numerical simulations that illustrated the impact of the initial perturbations and resemblance of the mixing with the theory of RT instability, as reported in Section 10.4.1.

Recently, a new facility to study blast-driven RT and RM at non-diffuse interfaces has been tested by Musci et al. [396]. This experimental apparatus consists of a  $30^\circ$  diverging chamber, allowing for testing in cylindrical coordinates. The explosive charge is located in a reloadable cylindrical sleeve inserted at the bottom of the chamber. This sleeve is sealed prior to a test to ensure the upward propagation of the blast wave in the test chamber.

The heavy gas is filled from the bottom and the light gas from the top of the test chamber. A vacuum box gently pulls out the gases through a thin slot located at the center of the chamber on the back wall, producing a non-diffuse interface. Finally, a loudspeaker is used to induce small disturbances at the interface. Initial testing of this facility has suggested good repeatability and controllability of the blast wave. In addition, the characteristic mixing phases of a HE-driven blast wave appear to have been observed.

An elegant experimental apparatus was designed by Rodriguez et al. [397] to investigate the mechanisms of the late-time particle jet formation following the explosive dispersal of a particle cloud by a blast wave. In this experiment, a weak blast wave generated in an open shock tube at the center of a packed bed of particles is confined to a Hele-Shaw cell. This allows for clear visualization of the solid particle jet formation in a quasi-two-dimensional geometry as illustrated in Fig. 40(a). Their experiments have shown that the particle jets took shape following the shock-particle bed interaction. It appears that initial disturbances referred to as filaments are seeded at the inner surface of the particle cloud. These filaments continue to migrate to the outer particle cloud front, forming jets at late times. The effects of other key parameters are also reported in [398,399]. Simulations by Osnes et al. [400] concurred with the findings reported by Rodriguez et al. [397–399], with the exception of the trend in the number of jets with the increasing strength of the blast wave. Fig. 40(b) shows the result of a four-way coupled simulation of a blast-induced dispersal of a dense particle cloud in a Hele-Shaw cell (42% mean initial volume fraction) [401]. This study indicates that the deposition of vorticity through a multiphase analog of RM instability plays a key role in channeling the particles into well-defined jets at the outer edge of the particle bed.

#### 10.6. Summary

RT and RM instabilities in explosively expanding flows are challenging to study both using experiments and simulations. However, their important role in the mixing processes that follow the detonation of an HE explosive motivates the continuing efforts to further their detailed understanding. Four stages of mixing at the expanding material fronts have been observed and these underlying linear and nonlinear processes remain qualitative similar for both homogeneous and heterogeneous explosives. The addition of particles to the explosive, as metal inclusions inside as casing, or particle bed outside, introduces small wavelength random initial perturbations, which tend to enhance the mixing between the detonation products and shock-compressed air in each phase. Clustering of particles that form coherent particle jets has been reported under both dilute and dense-packed initial concentrations of particles. The complex interplay of shock-particle interaction, inter-particle collisions and particle-wake interactions has been conjectured to promote this late-time particle jet formation. However, precise quantification and modeling of this jet formation process is still lacking. Most studies have been limited to 2D because of the excessive computing power requirement. Also, for the case of particles surrounding an explosive charge, studies have been limited to modest particle volume fraction. Ingenious experiments have become available in recent years and the increase in computing power has already allowed for further refinement in calculations.

### 11. Magnetohydrodynamics: Governing equations

Magnetohydrodynamics is a fluid-mechanical formulation in which the fluid medium is assumed to be electrically conductive so that it can interact with magnetic fields. In particular, the

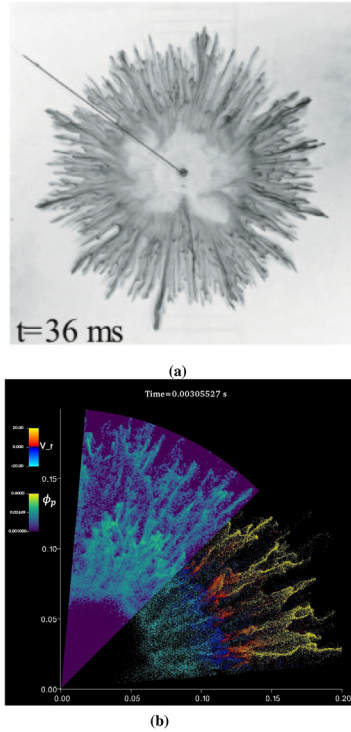


**Fig. 40.** (a) Initially packed bed of flour particle dispersed by a blast wave in a Hele-Shaw cell at late time (experiment) [399]. (b) Four-way coupled point-particle simulation with discrete element method collision model of a blast-driven dense particle bed in a Hele-Shaw cell (42% mean initial volume fraction) [401]. The upper part of the figure displays particle volume fraction, while the lower part shows the particles colored by their radial velocity. Reproduced with permission.

electromagnetic Lorentz force appears as a body force which acts on a fluid parcel, in addition to body forces such as gravity, while the magnetic field itself can change according to Faraday's law of induction, due to the motion of the fluid, which carries charge.

In deriving any of the usual formulations of MHD, several essential assumptions are made about the medium, which can be viewed as a continuum of separated positive and negative electrical charges. First, the fluid is electrically quasineutral. In a given region of the fluid, it may come about that a group of positive charges will separate from a group of negative charges, so that one part of the region has a net positive charge and the other has a net negative charge. This separation causes a large electrical field that will tend to force the charges back toward each other, so that large charge separations cannot be sustained in the plasma. Despite this, however, local thermal effects may cause charge imbalances on smaller scales which are characterized by the Debye length. By assuming a quasineutral plasma with some appropriate flow length scale, we are implicitly assuming the Debye length scale is sufficiently small relative to the flow scales to be neglected. We assume the same with respect to the Larmor radius, which is the radius of the circular trajectory a charged particle travels in a uniform magnetic field. Finally, if we treat the electrons and ions (which are really separate species) as a single unified fluid, we arrive at MHD [18,19,402].

There are several different formulations of MHD, but here we will focus primarily on *ideal* MHD. This is the most idealized model – it neglects viscosity, thermal conduction<sup>6</sup> and electrical

resistivity in the fluid. The resulting equations are:

$$\frac{\partial \rho}{\partial t} + \nabla \cdot (\rho \mathbf{u}) = 0, \quad (72)$$

$$\rho \left( \frac{\partial \mathbf{u}}{\partial t} + \mathbf{u} \cdot \nabla \mathbf{u} \right) + \nabla p - \mathbf{J} \times \mathbf{B} + \rho \mathbf{g} = 0, \quad (73)$$

$$\frac{\partial p}{\partial t} + \mathbf{u} \cdot \nabla p + \gamma p \nabla \cdot \mathbf{u} = 0, \quad (74)$$

$$\frac{\partial \mathbf{B}}{\partial t} - \nabla \times (\mathbf{u} \times \mathbf{B}) = 0, \quad (75)$$

$$\nabla \cdot \mathbf{B} = 0. \quad (76)$$

where the pressure equation (74) is again obtained from an ideal gas equation of state with specific heat ratio  $\gamma$ ,  $\mathbf{J}$  is the electric current,  $\mathbf{B}$  is the magnetic field (formally, the flux density) and  $\mathbf{g}$  is the gravity vector. Eq. (75) is obtained from the induction equation coupled with Ohm's law for a perfect conductor. The electric current  $\mathbf{J}$  is defined as

$$\mathbf{J} = \frac{1}{\mu_0} \nabla \times \mathbf{B}, \quad (77)$$

where  $\mu_0$  is the magnetic permeability in a vacuum. This relation is obtained from Ampere's law (in the limit where relativistic effects are unimportant allowing the displacement current to be neglected). The Gauss law (76) simply states that there are no magnetic monopoles, and serves as a constraint on the other equations.

The key aspect to note about the ideal MHD equations is that the magnetic field influences the velocity field evolution in (73), and vice versa in (75); thus the magnetic field and velocity fields are nonlinearly coupled. This aspect leads to an important property of the magnetic field in ideal MHD, which we present following Goedbloed and Poedts [19]. The induction law (75) can be written in Lagrangian form,

$$\frac{D\mathbf{B}}{Dt} = \mathbf{B} \cdot \nabla \mathbf{u} - \mathbf{B} \nabla \cdot \mathbf{u}, \quad (78)$$

where  $D/Dt = \partial/\partial t + \mathbf{u} \cdot \nabla$  is the Lagrangian derivative. By combining this with continuity (72), also in Lagrangian form, one can write

$$\frac{D}{Dt} \left( \frac{\mathbf{B}}{\rho} \right) = \left( \frac{\mathbf{B}}{\rho} \right) \cdot \nabla \mathbf{u}. \quad (79)$$

But this is exactly the form of the kinematic equation for a line element  $d\mathbf{l}$  embedded in the flow,

$$\frac{D}{Dt} (d\mathbf{l}) = d\mathbf{l} \cdot (\nabla \mathbf{u}), \quad (80)$$

which relates its Lagrangian derivative with the *directional* derivative of the flow gradient. Thus, the field moves locally as if it were a line element with the same orientation embedded in the flow: the magnetic field lines are “frozen” into the fluid! They follow the motion of the plasma. (This property is shared, incidentally, by vorticity in an inviscid fluid.)

The Lorentz force, taking the form  $(\mathbf{J} \times \mathbf{B})$  in Eq. (73), gives a force on the fluid perpendicular to both the magnetic field vector and the current vector ( $\mathbf{J}$ ). This force can be decomposed into two components

$$\mathbf{J} \times \mathbf{B} = \left( \frac{\mathbf{B}}{\mu_0} \cdot \nabla \right) \mathbf{B} - \nabla \left( \frac{B^2}{2\mu_0} \right). \quad (81)$$

The first of these components is called the magnetic tension force, and the second is called the magnetic pressure force. A key parameter for measuring the importance of the magnetic field in an MHD fluid is the plasma  $\beta$ . This is defined as the ratio of gas to magnetic pressure given by

$$\beta = \frac{p}{B^2/(2\mu_0)}. \quad (82)$$

<sup>6</sup> For details on the nature of viscosity and thermal conduction in a magnetic field, the reader is referred to [403].

When  $\beta \gg 1$ , in general the hydrodynamic forces dominate the system, and in contrast when  $\beta \ll 1$  the magnetic forces are expected to dominate the system. It is important to note that because gravity scales differently with length than these other forces, even in a low  $\beta$  system gravity can be important. The magnetic RT instability is just such an example where this can happen.

When magnetic diffusion ( $\eta_D$ ) is included, the magnetic field and the flow are no longer frozen in to each other. Eq. (75) then becomes

$$\frac{\partial \mathbf{B}}{\partial t} - \nabla \times (\mathbf{u} \times \mathbf{B} - \mu_0 \eta_D \mathbf{J}) = 0. \quad (83)$$

Including diffusion in the induction equation also result in the addition of the Ohmic heating term, taking the form  $\mu_0 \eta_D J^2$ . to the RHS of Eq. (74).

Since the diffusion term in Eq. (83) is in effect a second-order differential operator on  $\mathbf{B}$ , it is more effective at smaller scales. The importance of diffusion at a given scale can be understood by calculating the magnetic Reynolds number (the ratio of the diffusion time to the advection time) given by

$$R_m = \frac{VL}{\eta_D}, \quad (84)$$

where  $V$  is a characteristic velocity of the system, and  $L$  a characteristic length scale. In a collisional plasma the magnitude of  $\eta_D$  relates to the level the current is being reduced as a result of the current carriers (normally electrons) colliding with other particles.

Using an ideal MHD system (no viscosity or diffusivity) and taking possibly the simplest situation of an isotropic, homogeneous plasma with density  $\rho$  at rest that is permeated by a uniform, unidirectional magnetic field with no gravity, we simply determine the wave spectra of this system. However, before performing any analysis it is common to absorb the factor of  $1/\sqrt{\mu_0}$  into the  $\mathbf{B}$  term seen in Eq. (73), leading to

$$\rho \left( \frac{\partial \mathbf{u}}{\partial t} + \mathbf{u} \cdot \nabla \mathbf{u} \right) + \nabla p - (\nabla \times \mathbf{B}) \times \mathbf{B} + \rho \mathbf{g} = 0. \quad (85)$$

It is worth noting that if one is using the CGS unit system, absorbing the factor of  $1/\sqrt{4\pi}$  into the  $\mathbf{B}$  results in exactly the same equation.

In the situation we are studying, unlike hydrodynamics where sound waves are the only waves that exist, there are three kinds of waves in the system. Firstly there is the Alfvén wave, which has frequency

$$\omega^2 = k_x^2 \frac{B_{x,0}^2}{\rho} \quad (86)$$

where we have assumed initially we have a uniform magnetic field that is in the  $x$  direction and of magnitude  $B_{x,0}$ , and with  $k_x$  the component of the wave vector along the magnetic field. These waves are incompressible and propagate along the magnetic field at phase speed  $V_A = B_{x,0}/\sqrt{\rho}$ .

Then there are two compressible waves, the slow and fast-mode magnetoacoustic waves, which have frequencies

$$\omega^2 = \frac{1}{2} k^2 (C_s^2 + V_A^2) \left( 1 \pm \sqrt{1 - \frac{4C_s^2 V_A^2 \cos^2 \theta}{(C_s^2 + V_A^2)^2}} \right), \quad (87)$$

where  $\theta$  is the angle between the wave vector  $\mathbf{k}$  and  $\mathbf{B}$ ,  $k$  is the magnitude of  $\mathbf{k}$ , and  $C_s$  is the sound speed. The solution with the  $+$  sign is the fast mode, and that with the  $-$  sign is the slow mode. This means that fast mode waves propagate at the largest speed in the direction across the magnetic field, while slow mode waves propagate most quickly along it. Since  $\omega$  is a linear function of  $k$ , these waves are not dispersive. More information on the MHD wave spectra can be found in [18], for example.

## 12. The magnetic Rayleigh–Taylor instability

The previous section contained a discussion of the coupling of a magnetic field, through the framework of MHD, to the hydrodynamic body forces leading to an additional body force, namely the Lorentz force. In this section, we will explore the effect this additional force, and the requirement to solve for the evolution of the magnetic field under the constraint that the field has zero divergence, has on the Rayleigh–Taylor instability.

### 12.1. Studying the magnetic Rayleigh–Taylor instability in an incompressible 2D model

In this subsection we present some of the key ideas and results needed to understand how the presence of magnetic fields alters RT. Here we will focus on cases where the magnetic field vector is perpendicular to the direction of gravity. This instability was first investigated by Kruskal and Schwarzschild [404]. The case with the magnetic field parallel to gravity, and other interesting examples, are presented in Chandrasekhar [405].

Our main investigation will focus on a simplified setting of the linear stability of a discontinuous density inversion with a uniform, horizontal magnetic field under gravity in 2D. The initial conditions we study in this section are

$$\rho_0 = \begin{cases} \rho_1 & \text{if } z < 0 \\ \rho_2 & \text{if } z > 0, \end{cases} \quad (88)$$

$$u_{x,0} = 0, \quad u_{z,0} = 0, \quad (89)$$

$$B_{x,0} = B_x, \quad B_{z,0} = 0, \quad (90)$$

$$p_0(z) = p_0(0) - \rho_0 g z. \quad (91)$$

We also assume the system is inviscid, ideal and incompressible (i.e. we solve the evolution using Eqs. (72), (75), (76), (85) and  $\nabla \cdot \mathbf{u} = 0$ , the last of which removes the requirement to solve for the evolution of the gas pressure).

These assumptions and initial conditions result in the following linear equations for the perturbed quantities  $\delta\rho$ ,  $\delta\mathbf{u}$  and  $\delta\mathbf{B}$

$$\frac{\partial \delta\rho}{\partial t} = -\delta\mathbf{u} \cdot \nabla \rho_0, \quad (92)$$

$$\rho_0 \frac{\partial \delta\mathbf{u}}{\partial t} = -\nabla \delta p + (\nabla \times \delta\mathbf{B}) \times \mathbf{B}_0 + \delta\rho \mathbf{g}, \quad (93)$$

$$\frac{\partial \delta\mathbf{B}}{\partial t} = \nabla \times (\delta\mathbf{u} \times \mathbf{B}_0), \quad (94)$$

$$\nabla \cdot \delta\mathbf{u} = \nabla \cdot \delta\mathbf{B} = 0. \quad (95)$$

#### 12.1.1. Lagrangian displacements in linear MHD

There are several ways in which the above equations can be manipulated to allow for further investigation of the ideal MHD instabilities. Here, we will apply the use of the Lagrangian displacement vector field, since it is an effective way of reducing the equations to a meaningful form.

The Lagrangian displacement, denoted by the vector  $\xi$ , describes the difference in position of a fluid element at a time  $t$  in two different flows where the fluid element in each flow is at the same position  $\mathbf{a}$  at time  $t = 0$  (see Fig. 41). Taking the two flows to be the initial flows  $\mathbf{u} = \mathbf{u}_0 = \mathbf{0}$  and the perturbed flows  $\mathbf{u} = \mathbf{u}_0 + \delta\mathbf{u} = \delta\mathbf{u}$ , then  $\xi$  describes the manner in which the instability displaces fluid elements. The change of  $\xi$  with time must then be

$$\delta\mathbf{u} = \frac{\partial \xi}{\partial t}. \quad (96)$$

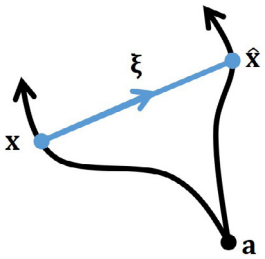


**Fig. 41.** The schematic diagram of the Lagrangian displacement  $\xi$  for two flows; one which takes the fluid parcel from position  $\mathbf{a}$  to position  $\mathbf{x}$  at time  $t$  and one which takes it to  $\hat{\mathbf{x}}$ .

For a more detailed explanation of Lagrangian displacements see, for example, Hillier [406].

We can insert this into Eqs. (92) and (94), and (with the appropriate simplifications and choice of integration constants) find

$$\delta\rho = -\xi \cdot \nabla \rho_0, \quad (97)$$

$$\delta\mathbf{B} = \nabla \times (\xi \times \mathbf{B}_0). \quad (98)$$

This means our linear equations become

$$\rho_0 \frac{\partial^2 \xi}{\partial t^2} = -\nabla \delta p + (\nabla \times \nabla \times (\xi \times \mathbf{B}_0)) \times \mathbf{B}_0 - (\xi \cdot \nabla \rho_0) \mathbf{g}, \quad (99)$$

$$\nabla \cdot \xi = 0, \quad (100)$$

as we also note that due to the form of Eq. (98) the solenoidal condition on the magnetic field is now automatically satisfied. Later, we will use Eq. (100) to remove the pressure from Eq. (99). Once this is done, what we have achieved is writing Eq. (99) in the form

$$\rho_0 \frac{\partial^2 \xi}{\partial t^2} = \mathbf{F}(\xi), \quad (101)$$

i.e. the second derivative of  $\xi$  with respect to time (the acceleration) relates to a force operator  $\mathbf{F}$  that only depends on  $\xi$ . This now gives us quite a general tool to investigate instabilities (though not one we will apply here). If for a given  $\xi$ , we have  $\xi \cdot \mathbf{F}(\xi)$  greater than zero somewhere, then the force in the system is working to increase the displacement (i.e. we have instability). Otherwise, the system is stable.

### 12.1.2. Derivation of the dispersion relation

Because of the initial conditions prescribed above, there is no variation in the equilibrium in the horizontal direction. This means that in these directions, a normal mode decomposition can be used, so that perturbations (both  $\delta p$  and the components of  $\xi$ ) are taken to be of the form

$$\delta f(\mathbf{x}, t) = \tilde{f}(z) \exp(i\mathbf{k} \cdot \mathbf{x} - i\omega t). \quad (102)$$

This results in the Lagrangian displacement given by

$$-i\omega \xi = \delta \mathbf{u}. \quad (103)$$

In addition, this gives the following set of linear equations (dropping the  $\sim$ s from the eigenfunctions)

$$-\rho_0 \omega^2 \xi_x = -ik \delta p, \quad (104)$$

$$-\rho_0 \omega^2 \xi_z = -\frac{\partial}{\partial z} \delta p + B_{x,0} \left( \frac{\partial^2}{\partial z^2} - k^2 \right) \xi_z + \xi_z \frac{\partial}{\partial z} \rho_0 g. \quad (105)$$

We also have the incompressible condition

$$ik \xi_x = -\frac{\partial}{\partial z} \xi_z. \quad (106)$$

Taking the  $x$  derivative of Eq. (104) allows  $\xi_x$  to be eliminated from the equations,

$$-\rho_0 \omega^2 (ik \xi_x) = \rho_0 \omega^2 \frac{\partial}{\partial z} \xi_z = k^2 \delta p. \quad (107)$$

Rearranging Eq. (107) and differentiating with respect to  $z$  gives

$$\frac{\partial}{\partial z} \delta p = \frac{1}{k^2} \frac{\partial}{\partial z} \left( \rho_0 \omega^2 \frac{\partial}{\partial z} \xi_z \right). \quad (108)$$

On substitution into Eq. (105) we obtain

$$\begin{aligned} \rho_0 \omega^2 \xi_z &= \frac{1}{k^2} \frac{\partial}{\partial z} \left( (\rho_0 \omega^2 - (kB_{x,0})^2) \frac{\partial}{\partial z} \xi_z \right) \\ &\quad + (kB_{x,0})^2 \xi_z - \xi_z g \frac{d}{dz} \rho_0. \end{aligned} \quad (109)$$

Using this equation, we will now determine the variation of  $\xi_z$  with  $z$  and the dispersion relation.

Away from  $z = 0$ , Eq. (109) simplifies to

$$(\rho_0 \omega^2 - (kB_{x,0})^2) \left( \frac{\partial^2}{\partial z^2} - k^2 \right) \xi_z = 0. \quad (110)$$

In the following, we will assume the non-trivial case:  $\rho_0 \omega^2 - (kB_{x,0})^2 \neq 0$ . Therefore, Eq. (110) reduces to

$$\left( \frac{\partial^2}{\partial z^2} - k^2 \right) \xi_z = 0, \quad (111)$$

to which the solutions are

$$\xi_z(z) = C_0 \exp(-kz) + C_1 \exp(kz). \quad (112)$$

To maintain a finite energy in the system we require that the as  $z \rightarrow \pm\infty$ ,  $\xi_z(z) \rightarrow 0$ . Combining this condition with the continuity of  $\xi_z$  at  $z = 0$  leads to the solution

$$\xi_z(z) = C_0 \begin{cases} \exp(kz) & \text{if } z < 0, \\ \exp(-kz) & \text{if } z > 0. \end{cases} \quad (113)$$

With the full spatial distribution of  $\xi_z$ ,  $\omega$  can be determined. The next step is to integrate Eq. (109) from  $-\epsilon$  to  $\epsilon$  and take the limit  $\epsilon \rightarrow 0$ . This means that any terms of this equation that are continuous or form a step function at  $z = 0$  will not contribute to the integration in the limit  $\epsilon \rightarrow 0$ . Therefore, we are only interested in terms containing the derivatives of step functions (i.e. the first and third terms of the right-hand-side of Eq. (109)). Upon integration (and evaluation at  $z = 0^\pm$ ) we get

$$\omega^2 k(\rho_2 + \rho_1) - 2k^3 B_0^2 = -(\rho_2 - \rho_1) g k^2. \quad (114)$$

Finally, solving for  $\omega$  gives

$$\begin{aligned} \omega &= \left[ \frac{2k^2 B_0^2}{(\rho_2 + \rho_1)} - g k A \right]^{1/2} \\ &= \left[ \frac{k^2 \rho_1 V_{A1}^2}{\rho_2 + \rho_1} + \frac{k^2 \rho_2 V_{A2}^2}{\rho_2 + \rho_1} - g k A \right]^{1/2}, \end{aligned} \quad (115)$$

where  $V_{A1}$  and  $V_{A2}$  are the Alfvén speeds in the regions below and above the discontinuity respectively.

The term inside the square root can either be positive or negative. The term that can drive the instability is the same term that drives the hydrodynamic RT and can be simply understood as the square of the inverse of the free-fall time over a distance of  $1/k$  with a modified gravity of magnitude  $A g$ . The positive term represents the suppression of instability by magnetic tension and is the square of the frequency of a surface Alfvén wave.

## 12.2. Beyond 2D – the role of 3D effects and additional physics

We can now look at the dispersion relation produced from more complex settings. Extending our previous model to include perturbations that can also be perpendicular to the magnetic field leads to a small change in our dispersion relation. In this more general case, the frequency is given as [405]:

$$\omega = \left[ \frac{2(\mathbf{k} \cdot \mathbf{B})^2}{\rho_2 + \rho_1} - g_A k \right]^{1/2}. \quad (116)$$

The clear difference between this and the 2D case is that since the magnetic field has a direction, and perturbations perpendicular to that direction are allowed, the influence of the magnetic field is anisotropic.

We can understand more about the magnetic RT instability by thinking about two fundamental perturbations that can be applied to the system. These are the interchange mode, where  $\mathbf{k} \cdot \mathbf{B} = 0$  and the undular mode where  $\mathbf{k} \parallel \mathbf{B}$  (which is equivalent to the 2D setting). The interchange mode removes the influence of the magnetic field, resulting in the instability developing with the growth rate of the hydrodynamic instability at the same wavenumber. The undular mode, so called because it makes the magnetic field undulate, behaves differently. As the magnetic field will work to suppress the instability, there is a play-off between how quickly gravity can drive the instability and how quickly magnetic tension can suppress it. For this mode, simply differentiating with respect to  $k$  will reveal the  $k$  associated with the fastest growing mode:

$$k = \frac{(\rho_2 - \rho_1)g}{4B^2}. \quad (117)$$

Therefore the stronger the magnetic field strength, the smaller the wavenumber at which the most unstable undular mode forms.

Due to the fact that the undular mode includes the influence of a suppression term, for the same magnitude of  $k$  the interchange mode will always grow faster than the undular mode. The most common mode to be excited in realistic conditions is the mixed mode, where there is a component of  $k$  both parallel and perpendicular to  $B$ . For more information on the linear stage of this instability see, for example, [407].

### 12.2.1. Variations in the direction of the magnetic field at the interface

A well-known issue with the magnetic RT instability is that certain perturbations (for example, perturbations with  $\mathbf{k} \cdot \mathbf{B} = 0$ ) have a growth rate which is unbounded with  $k$ . Simply put, for certain perturbations, as  $k$  goes to infinity so does the growth rate. This issue also exists for the hydrodynamic problem, where the problem is often regularized by the introduction of a region of finite size over which the density transitions, or the introduction of viscosity or surface tension.

Similarly, MHD terms can also be used to regularize the problem. This can be achieved by allowing for the magnetic field vector to be pointing in different directions above and below the density jump. Assuming a uniform magnetic field strength, the growth-rate of the instability is given by [407,408]:

$$\omega = \left[ \frac{2(k_x B_x)^2 + 2(k_y B_y)^2}{\rho_2 + \rho_1} - g_A k \right]^{1/2}, \quad (118)$$

where it has been assumed, without loss of generality, that the magnetic field is of the form  $\mathbf{B} = [B_x, B_y, 0]$  above the discontinuity and  $\mathbf{B} = [B_x, -B_y, 0]$  below (i.e. the  $y$  component of the magnetic field changes sign but not magnitude across the discontinuity whereas the  $x$  component is the same on both sides).

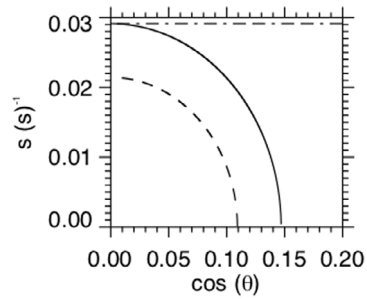


**Fig. 42.** Growth rate  $s = i\omega$  of the uniform field (in the  $x$  direction) magnetic Rayleigh–Taylor instability (solid line), the sheared field case (dashed line) for the same field strength and the hydrodynamic case (dot-dashed line). For this calculation we have  $\rho_1 = 10^{-12} \text{ kg m}^{-3}$  and  $\rho_2 = 10^{-10} \text{ kg m}^{-3}$ . We take a wavelength of  $2 \times 10^6 \text{ m}$  and  $\theta$  giving the angle between the wavevector and the  $x$  direction. In both magnetic cases, the magnitude of  $B$  is  $\sqrt{\mu_0}|\mathbf{B}| = 5 \times 10^{-4} \text{ T}$ , for the sheared field case  $B_y = 0.1B_x$ . For the uniform field case, only modes close to the interchange mode grow. The inclusion of the sheared field, in this case only a small amount of shear, noticeably reduces the growth rate.

It is clear from Eq. (118) that there is no longer any wavevector that can be applied to the system that removes the influence of the magnetic field. Therefore, we know that when there is magnetic shear at the density jump, magnetic tension will always work to suppress the instability, with the higher wavenumbers experiencing greater suppression. Fig. 42 shows the variation of the growth rate of the instability with the inclusion of magnetic shear, highlighting the reduction in the growth rate as a result of magnetic shear and the anisotropic influence of the magnetic field overall.

The most unstable mode is calculated by maximizing the gravitational term which drives the instability whilst minimizing the suppressive terms from the magnetic field. This can be done simply by determining which of  $B_x^2$  or  $B_y^2$  is smaller. Without loss of generality, we can assume that  $B_x^2$  is the smaller. Therefore, to minimize the second term it is necessary to set  $k_y$  to be zero. Therefore, the  $k_x$  that satisfies the following equation

$$g_A - \frac{4k_x B_x^2}{\rho_2 + \rho_1} = 0 \quad (119)$$

is the  $k_x$  that gives the fastest growing mode in this system [407]. This result is the same as that of the fastest growing undular mode for a uniform magnetic field of strength  $|B_x|$ .

### 12.2.2. Role of magnetic diffusion

The inclusion of diffusion has a few key effects on the dispersion relation and its derivation. To solve these systems, unfortunately the Lagrangian displacement method is not applicable, so other methods have to be employed. An example is the approach by Chandrasekhar [405] for the viscous Rayleigh–Taylor instability.

The presence of the higher order derivative in the induction equation results in there being more solutions for the spatial dependence of the eigenfunction. It can be shown that the equivalent of Eq. (111) for the diffusive case (i.e. for 2D) is

$$\left( \frac{\partial^2}{\partial z^2} - F^2 \right) \left( \frac{\partial^2}{\partial z^2} - k^2 \right) \delta B_z = 0, \quad (120)$$

where

$$F^2 = k^2 + \frac{i\omega}{\eta_D} - \frac{i\omega_A^2}{\eta_D \omega}, \quad (121)$$

and  $\omega_A^2 = k^2 B_{x,0}^2 / \rho_0$ . This has solutions of the form

$$\delta B_z = C_0 \exp(-kz) + C_1 \exp(kz) \quad (122)$$

$$+ C_2 \exp(-Fz) + C_3 \exp(Fz).$$

Applying  $\delta B_z \rightarrow 0$  as  $|z| \rightarrow \infty$  gives the solutions in each layer. We can see, because of the form of  $F^2$ , that for large  $\eta_D$ , the eigenfunction behaves in exactly the same way as the ideal eigenfunction, and that in cases where  $\omega$  has a real part  $F$  is complex.

The role of magnetic diffusion on the growth of the instability is that it works to remove current from the system. For a plane-wave perturbation, the larger the wavenumber along the magnetic field of the perturbation the larger the current, which means the larger the diffusive term in the induction equation. Therefore, perturbations with sufficiently large  $k$  will lose their Lorentz force, which works to suppress the instability, as diffusion will have removed all the current. The magnetic fields no longer suppress the instability at high-wavenumbers, on the contrary the fluid will no longer feel the Lorentz force and the instability can grow at the same rate as the hydrodynamic instability. However, at small  $k$  where the diffusive term is unimportant, the result will be approximately the same as the ideal MHD situation. This effect can be seen in the calculations of Díaz et al. [409], though note the diffusion used in their calculations is modified from the simple diffusion discussed here. Finally, any wave solution to the system will be subject to diffusion, so the wave should damp implying we have complex solutions giving damped waves instead of purely real frequencies as in the ideal MHD case.

### 12.2.3. Compressibility

An important consideration is that the investigation of the growth rate presented here has only been derived for incompressible systems. In cases where the growth rate  $s = i\omega$  is such that  $|s| > |\omega_{\text{comp}}|$  where  $\omega_{\text{comp}}$  is the frequency of a compressible wave mode (either the slow or fast-mode in MHD), then it is likely to result in compressible effects becoming important. The result will be that work has to be done to compress the fluid instead of driving the instability, reducing its growth rate.

A simple estimate of the conditions for which compressible effects become important can be given by taking the ratio of the growth rate of the instability to the frequency of a sound wave. In situations where this ratio approaches or becomes greater than one, compressible effects are likely to become important. Taking the RTI growth rate in the incompressible limit we can calculate this ratio

$$\frac{s^2}{k^2 C_s^2} = \frac{1}{H_p k} \frac{\mathcal{A}}{\gamma}, \quad (123)$$

where  $H_p$  is the pressure scale height defined by  $H_p = k_B T / \mu_m M_p g$  with  $k_B$  the Boltzmann constant,  $T$  the temperature,  $\mu_m$  the mean molecular mass and  $M_p$  is the mass of a proton. This implies that hydrodynamic RTI wavenumbers of scale  $k \lesssim \mathcal{A}/H_p$  will naturally evoke compressible effects, whereas much larger wavenumbers will be approximately incompressible.

There are two reasons why the inclusion of magnetic fields further complicates this picture. Firstly, there are two compressible wave speeds being maximized either parallel or perpendicular to the magnetic field, i.e. the slow and fast mode waves. Secondly, the growth rate of the instability depends on the angle of the wave vector to the magnetic field direction.

We can extend these considerations on hydrodynamic compressibility to that of MHD quite easily. We first note that compressible wave speeds will be smaller in the region at higher densities (which gives smaller  $V_A$  and  $C_s$  for the same magnetic field strength and gas pressure). As such, it is this layer that is most likely to be influenced by compressible effects. Therefore, the influence of compressibility is reduced for wavevectors associated with larger compressible wave speeds. For low- $\beta$  plasmas this implies that wavevectors perpendicular to the magnetic field

(associated with the MHD fast-mode) will be less compressible and potentially grow faster. So compressibility is likely to create new favored directions in the system.

This was observed in the investigation by Ruderman [410], who performed a compressible extension to the incompressible study of Ruderman et al. [408]. Their study showed that compressibility does not change the critical wavevector for the instability. This can be understood as the growth rate of the instability is 0 for this perturbation, so the compressible effects modifying the instability are also 0. They also found a new favored direction in the system for instability growth, as explained above, something that does not appear in the incompressible growth rate, e.g. see Eq. (118).

### 12.3. The nonlinear phase of the magnetic Rayleigh–Taylor instability

Having covered some key aspects of the linear stability of the magnetic RT, we now turn our attention to the effect of the magnetic field on the nonlinear regime of RT instability.

Here, we discuss the different terms of the momentum equation that can lead to the nonlinear saturation of a magnetic RTI. Our starting point is the linear eigenfunction for the vertical Lagrangian displacement  $\xi_z$ , i.e.

$$\xi_z(\mathbf{x}, t) = \xi_z(\mathbf{0}, 0) \exp(i\mathbf{k} \cdot \mathbf{x} - k|z| - i\omega t), \quad (124)$$

where  $\xi_z(\mathbf{0}, 0)$  is the value of  $\xi_z$  at  $x = y = z = t = 0$ . The scaling in the vertical ( $z$ ) direction is  $1/k$ , highlighting an inherent spatial scale for the vertical displacement of the linear instability. That is to say, once the density jump has undergone a vertical deformation of distance  $|\xi_z| > 1/k$ , then the instability has driven the system beyond the linear regime.

We can further this argument by investigating a simple model of nonlinear development. From the equation of motion, Eq. (73), nonlinear terms exist for both the velocity and the Lorentz force. Therefore, we can expect that saturation of the instability could be caused by either of these terms. Here, we follow some of the arguments laid out in Refs. [407] and [406].

Nonlinearities in hydrodynamic systems can result in the occurrence of large shear flows that allow parasitic instabilities, e.g. the Kelvin–Helmholtz instability, to develop. In MHD systems, these saturation mechanisms are still present. If we balance the temporal derivative of the velocity with the advective derivative, we have the following scaling,

$$\frac{\partial^2 \xi}{\partial t^2} = s^2 \xi \propto s^2 \xi \cdot \nabla \xi \sim s^2 k \xi^2 \quad (125)$$

$$\implies \xi \sim \frac{1}{k}. \quad (126)$$

Therefore, it can be predicted that velocity shear created by the growth of the instability will saturate the linear stage of the instability when the boundary has been perturbed through a distance of approximately  $1/k$ .

Alternatively, the role of magnetic forces in halting the further evolution of the instability can be given by,

$$s^2 \xi = \frac{\partial^2 \xi}{\partial t^2} = \frac{1}{\rho_0} \nabla \times \delta \mathbf{B} \times \delta \mathbf{B} \sim \frac{k_x^2 B_0^2}{\rho_0} \xi^2, \quad (127)$$

$$\implies \xi \sim \frac{1}{k} \frac{s^2}{\omega_A^2}, \quad (128)$$

where  $\omega_A$  is the frequency of a surface Alfvén wave. Therefore, when  $|\omega_A| \gtrsim |s|$  we would expect that magnetic forces will be important in the nonlinear saturation of the instability.

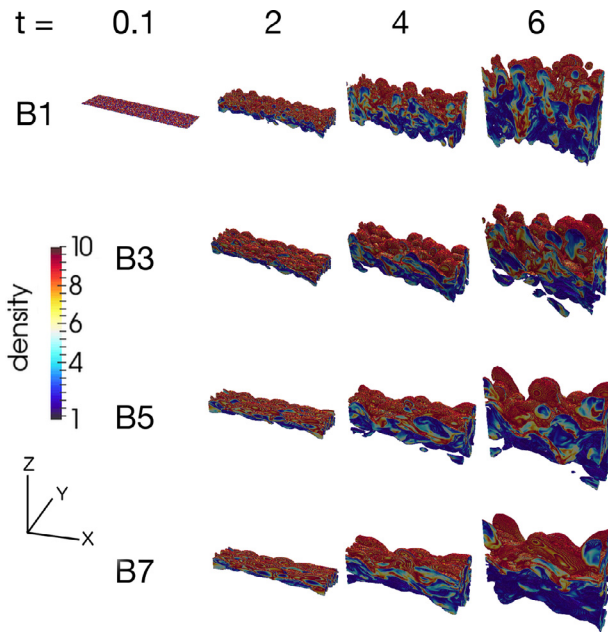


**Fig. 43.** Images of the development of magnetic RTI mixing layers over time for different field strengths, going from weak at the top to strong at the bottom. Fig. 2 of [411], with permission.

#### 12.4. MHD extensions to the self-similar mixing model

In previous sections of this paper, and in many other articles (see, for example, [3]), the nonlinear evolution of the hydrodynamic Rayleigh-Taylor instability has been discussed. A key property of the nonlinear regime is that the thickness of the mixing layer grows at late time following Eq. (38), e.g.  $h \approx \alpha A g t^2$ . Therefore, when considering the magnetic RT instability, we are interested in (i) whether the thickness of the mixing layer grows at the late-time still scales  $t^2$ , and (ii) whether the value of the  $\alpha$  parameter will be different from that of the fluid turbulence cases.

To study the nonlinear magnetic RT instability, numerical simulations are generally employed. The particular case of nonlinear mixing has thus far been addressed by few groups, with studies by Stone & Gardiner [412,413], and Carlyle et al. [414]. A set of simulations of the mixing process is shown in Fig. 43, taken from [411], where the effect of increasing the field strength on the development of the mixing layer is investigated. The simulation with the weakest field strength is shown at the top with progressively stronger fields further in the images below. It is clear that the increase in field strength results in the creation of elongated structures along the magnetic field due to the increasing significance of magnetic tension.

Using these simulations, the value of  $\alpha$  as it depended on the strength of the magnetic field (in this case the non-dimensional parameter  $J_0$ , defined as  $J_0 \equiv V_A^2/gL$ , was used) has been calculated. The  $\alpha$  values found in these simulations ( $\sim 0.04$ ) [412–414] are larger than the hydrodynamic value of  $\alpha \sim 0.025$  found in comparable simulations [412,413]. At the lower  $J_0$  values ( $J_0 \sim 0.03$ ), a suggestion for the increase in  $\alpha$  compared to hydrodynamic mixing is the suppression of secondary Kelvin-Helmholtz instability by the magnetic field. This increases the efficiency with which the boundary can be distorted as suggested by Stone & Gardiner [412,413]. However, increasing the field strength further results in a decrease in the  $\alpha$  value, but it is unclear if  $\alpha$  ever approaches the hydrodynamic value. It is clear that there are many open questions in this area.

One question that needs to be answered still is if mixing in MHD flows has a self-similar phase or if the changing importance of gravity against the magnetic field over lengthscale (as seen in the linear dispersion relation) means that the mixing is fundamentally a function of system size? If a broadband perturbation were imposed on the system, large wavelengths along the magnetic field would grow, and would be likely to be associated with the thicker mixing layers. This would imply that the  $J_0$  parameter varied with layer width, so that  $\alpha$  could also be expected to vary with the width. Also, the corresponding evolution when narrowband perturbations are imposed is a question that still remains to be investigated.

In this section we have looked at a case when a coherent horizontal magnetic field influences the mixing evolution. Another possible case is where a very weak magnetic field is enhanced through the turbulence driven by the RT instability (this would be in a regime where the instability behaved in a fluid like way). This possibility is discussed in Section 13.3

### 13. The magnetic Richtmyer-Meshkov instability

#### 13.1. Shock waves

Like gases, plasmas support shock waves. The conditions on the shock waves can be determined in a manner similar to the corresponding gas dynamic case. For a surface of discontinuity in MHD, the conservation properties of (72)–(76) (neglecting gravity) yield [19],

$$\begin{aligned} \llbracket \rho u_n \rrbracket &= 0, \quad \llbracket B_n \rrbracket = 0, \\ \rho u_n \llbracket \mathbf{u}_t \rrbracket &= B_n \llbracket \mathbf{B}_t \rrbracket, \quad \left[ \llbracket \rho u_n^2 + p + \frac{1}{2} B_t^2 \rrbracket \right] = 0, \\ \rho u_n \llbracket \frac{1}{2}(u_n^2 + u_t^2) + \frac{p}{(\gamma - 1)\rho} + \frac{p}{\rho} + \frac{B_t^2}{\rho} \rrbracket &= B_n \llbracket \mathbf{u}_t \cdot \mathbf{B}_t \rrbracket. \end{aligned} \quad (129)$$

In order, these state conditions for conservation of mass, solenoidal magnetic field, and conservation of tangential momentum, tangential magnetic flux, normal momentum, and energy.

While the character of MHD shock waves is thus derived in a similar way to that of their gas dynamic counterparts, the situation here is much richer. This is because in non-conducting gases, information is transmitted throughout the fluid only through sound waves, and the shock Mach number which is defined in terms of the sound speed characterizes the shock jump conditions. That is, the jumps (A.2) are controlled by only one parameter, which we usually define as the Mach number. By contrast, there are three types of waves that can travel through MHD fluids; these are the Alfvén wave, and the fast and slow magnetosonic waves (see Section 11 for more details), each traveling at a different characteristic speed; thus there are three parameters that control the jump conditions (129). Hence, we can define three different Mach numbers for the MHD shock in terms of each speed, say  $M_f$ ,  $M_I$ ,  $M_s$  respectively, the  $I$  representing the intermediate wave speed. We thus encounter a situation where, in the shock frame, six different configurations are permitted by the jump conditions. Assuming the characteristic speeds are distinct, these configurations are shown in Table 1, where F, S and I designate the fast magnetosonic, slow magnetosonic, and intermediate shock types respectively, and the numbering indicates where in the ordering of characteristic speeds the upstream and downstream velocities in the shock frame are placed.

Each of these shocks has its own unique character. The intermediate shocks in particular are controversial in the literature,

**Table 1**

Types of MHD shocks.

Type	Upstream	Downstream
F(1-2)	$M_s > M_l > M_f > 1$	$M_s > M_l > 1 > M_f$
I(1-3)	$M_s > M_l > M_f > 1$	$M_s > 1 > M_l > M_f$
I(1-4)	$M_s > M_l > M_f > 1$	$1 > M_s > M_l > M_f$
I(2-3)	$M_s > M_l > 1 > M_f$	$M_s > 1 > M_l > M_f$
I(2-4)	$M_s > M_l > 1 > M_f$	$1 > M_s > M_l > M_f$
S(3-4)	$M_s > 1 > M_l > M_f$	$1 > M_s > M_l > M_f$

and it is a subject of debate whether they can develop physically [415–418]. Bypassing this important but rather complicated discussion for the moment, it will suffice for us to discuss the first type (fast shocks). As can be seen from the first line of Table 1 the shock jump for this type of shock crosses only the fast magnetosonic speed (and is generally uncontroversial). For the other five shock types, they do not cross the fast magnetosonic speed, but may cross one or both of the other characteristic speeds. In the case of a vanishing field, the gas dynamic conditions (A.2) are reproduced. In fact, as the field strength approaches zero, the Alfvén and slow magnetosonic speeds also approach zero, and in this limit, the only remaining shock type is the fast magnetosonic, which degenerates to the familiar gas dynamic shock. Of the MHD shocks, the fast magnetosonic type is then the most similar to the gas dynamic counterpart.

However, regardless of the shock type, it is clear from the third and fourth relations in (129) that in contrast to gas dynamic shocks, the presence of a magnetic field will generally require a jump in both the tangential field components  $\mathbf{B}_t$  and the tangential velocity components  $\mathbf{u}_t$ , and that these jumps tend to occur together. So, unlike gas dynamic shocks, MHD shocks can support tangential velocity jumps (hence vorticity).

In the case of zero mass flux, we again get density interfaces as in gas dynamics. Arbitrary jumps in tangential velocity, however, are only supported in the case where the magnetic field does not penetrate the interface, that is  $B_n = 0$ . In this case, a pressure jump is supported provided the total pressure  $p + B_t^2/2$  remains continuous. This is the MHD tangential discontinuity. However with a finite  $B_n$ , all quantities except density must remain continuous on the interface, which is classified as an MHD *contact discontinuity*; that is, MHD contact discontinuities do not support vorticity.

The resulting situation is in general exactly the opposite of the gas dynamic case: while gas dynamic shocks cannot carry vorticity and tangential discontinuities can, MHD shocks can carry vorticity and contact discontinuities cannot. This has a fundamental impact on the RT and RM instabilities in MHD.

### 13.2. The RM instability in MHD

We are now equipped to discuss the two main features of RM in magnetohydrodynamics: suppression of the instability, and amplification of magnetic fields.

#### 13.2.1. Suppression of the instability

As with the RT instability, the RM instability can be suppressed by a magnetic field in MHD. This was in fact shown for RT by Chandrasekhar [405] in his monograph on hydrodynamic stability, in a linear stability analysis (see also the details of the previous section).

It was only much more recently that RM suppression was discovered by Samtaney [419], who showed numerically, under the vorticity paradigm, that an oblique interface with an applied magnetic field in MHD did not exhibit the instability. Fig. 44 depicts this situation. After the initial passage of the shock, the interface remains coherent unlike the gas dynamic (that is, unmagnetized)

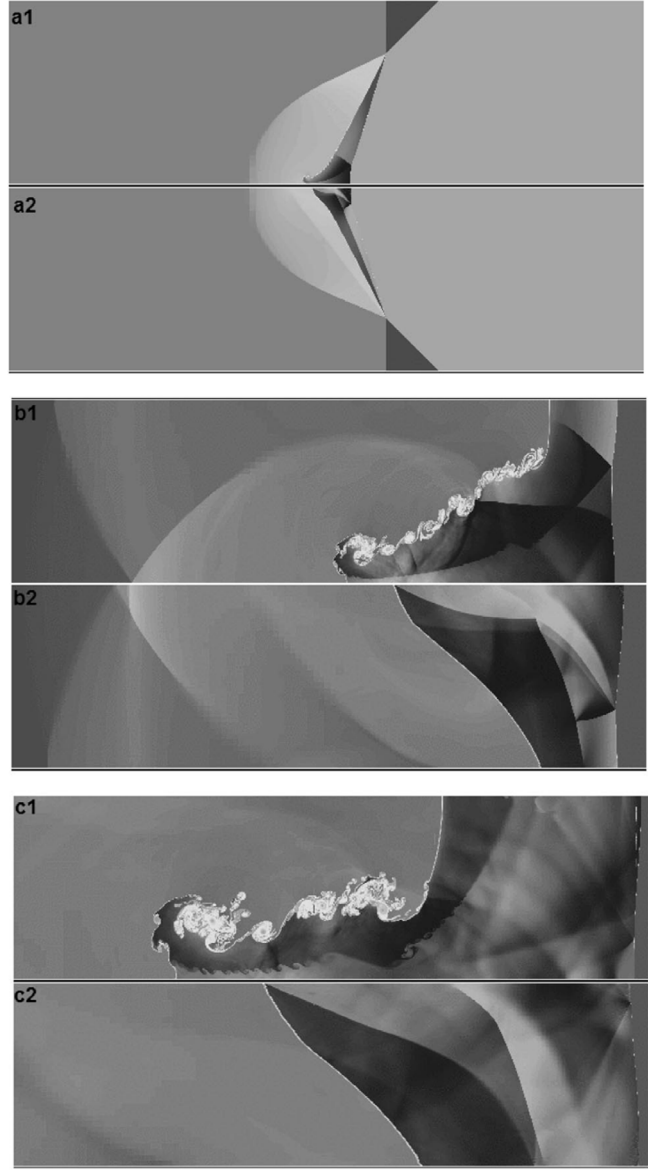


**Fig. 44.** Development of the shock-accelerated interface, with zero magnetic field (a1, b1, c1) and a finite-strength, horizontally oriented applied magnetic field (a2, b2, c2) with  $\beta = 2$  and a Mach number  $M = 2$  (see text for  $\beta$  definition). After the shock initially traverses the interface (a1, a2), the RM instability develops in the unmagnetized case (b1, c1) but remains suppressed in the presence of the magnetic field (b2, c2) [419]. Reproduced with permission.

case which is indeed unstable. The magnetized case is suppressed even though the total generated circulation is similar between the two cases.

How then is the RMI suppressed? In the gas dynamic case, the incident shock hits the interface and produces, via *shock refraction*, a transmitted shock and a reflected shock. Neither of these shocks carries vorticity, unlike the interface, which is accordingly unstable as discussed previously. In MHD, the interaction produces four waves: transmitted fast and sub-fast slow shocks, and reflected fast and sub-fast shocks (see Fig. 45). Each of these shocks can carry vorticity, but the interface itself cannot. Hence, even though the incident shock deposits baroclinic vorticity on the interface, this vorticity is immediately transported away from the interface by the transmitted and reflected MHD waves. With the vorticity removed from the interface, the growth agent has disappeared, and the interface is stable.

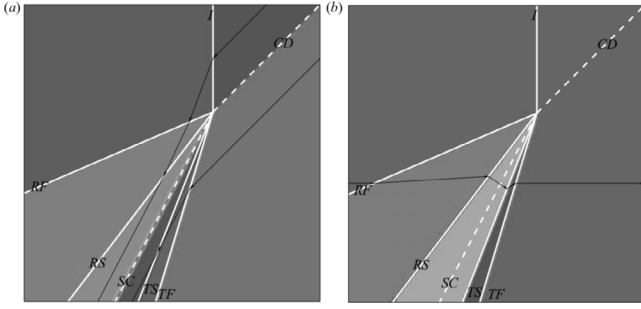


**Fig. 45.** MHD shock refraction diagram [417] for the magnetized configuration described in Fig. 44 showing contours of (a) density and (b) transverse (vertical) magnetic field component. As the incident shock (I) traverses the interface (contact discontinuity, CD), then refracts into a system of waves including the transmitted fast and sub-fast waves (TF, TS), the shocked interface (SC), and reflected fast and sub-fast waves (RF, RS). Vorticity not shown. Reproduced with permission.

As the Mach number  $M$  in one sense determines the severity of the RM instability, so the strength of the magnetic field influences the extent of suppression observed in MHD. This is usually quantified using the parameter  $\beta = 2p_0/B_0^2$  (see Eq. (82)), which measures the reference magnetic pressure (with the permeability constant scaled out) compared to the thermodynamic pressure. Thus, gas dynamic behavior is reproduced in the limit  $\beta \rightarrow \infty$ , while small values of  $\beta$  correspond to strong magnetic fields. The MHD shocks arising from the interaction, particularly the sub-fast waves, tend to travel with higher velocities in relatively stronger fields (lower  $\beta$ ), since the corresponding characteristic speeds are faster.

In general, the precise nature of the sub-fast shocks depends on the relative magnetic field strength, and can be quite complex in certain cases, as determined by Wheatley et al. [417]. A large part of this discussion again involves the consideration of which shocks can be considered physically admissible. While the instability is suppressed, the interface itself does also grow to an extent, since intuitively, the vorticity is removed from the interface at only a finite speed by the refracted waves and hence has some limited effect [420,421].

The extent of the instability suppression was also quantified in a solution to the *incompressible* linear problem with impulsive acceleration, in the form of an initial value problem solved with Laplace transform techniques (that is, without using the method of normal modes), by Wheatley et al. [420]. In the incompressible model, only the Alfvén waves arise, and these are the agents by which vorticity is transported away from the interface. In this case, the initial growth rate of the interface is identical to the hydrodynamic case; however, at asymptotically large time  $t \rightarrow \infty$ , they found that the interface  $a$  extended to its asymptotic value,

$$a_\infty = a_0 \left[ 1 + V \left( \frac{1}{V_{A1}} - \frac{1}{V_{A2}} \right) \right], \quad (130)$$

where  $a_0$  is the initial amplitude,  $V$  is the impulsive velocity increment, and  $V_{A1}, V_{A2}$  are the Alfvén speeds in the two media separated by the interface. This result, and the solution otherwise obtained to the initial value problem, compared well at early times with the fully nonlinear, compressible problem solved numerically.

Generally, the mechanism requires that the vorticity is transported away from the interface more quickly than the interface grows; Sano et al. [422] point out that this constitutes a critical condition for the instability to be suppressed. If  $v_{lin}$  indicates the linear perturbation amplitude growth rate in the hydrodynamic

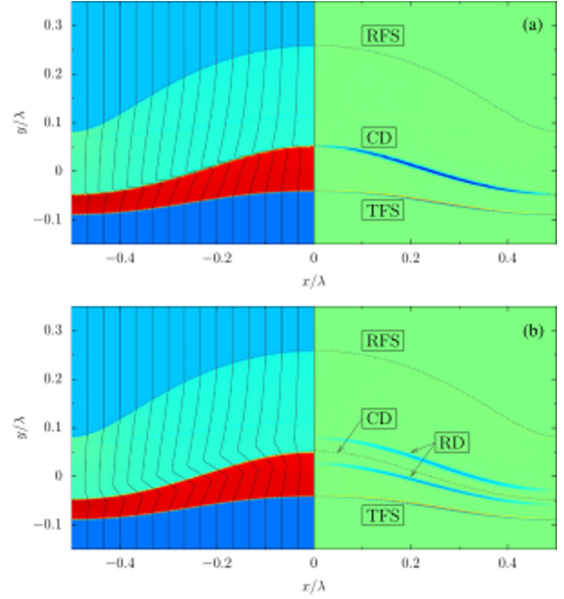


**Fig. 46.** Numerical results of Sano et al. [422] showing the importance of critical field strength for RM suppression, after passage of the shock. Contours show density distribution on the left and vorticity on the right. Magnetic fields lines are shown on the left. Shock refraction process produces a transmitted (TFS) and reflected (RFS) fast shock, and the contact discontinuity (CD). (a) For a weak magnetic field, the vorticity remains on the CD as the RM growth rate outstrips the Alfvén speed, so that RM is not suppressed. (b) For magnetic field above the critical strength, for the parameters chosen in the study, the vorticity is transported off the interface by rotational discontinuities (RD), which are a type of intermediate shock, suppressing RM. Note the deflection of the field lines at the vortex sheets. Reproduced with permission.

case, then the authors introduce the condition that the Alfvén velocity must be greater than some factor of this speed,

$$V_{A2} \geq C_\alpha v_{lin}, \quad (131)$$

where they estimate  $C_\alpha \simeq 0.1$  based on numerical results. Since the Alfvén speed is determined by the field strength, the critical magnetic field strength is,

$$B_{crit} = \sqrt{\rho_2^+ C_\alpha v_{lin}}, \quad (132)$$

where  $\rho_2^+$  is the postshocked density in the dense fluid. (In the study of Sano et al. a normalization of the MHD equations based on Gaussian units is used, and hence includes a factor of  $4\pi$ ; here, we remain consistent with the SI-normalization used in the rest of the article.) Since  $v_{lin}$  can be estimated directly [423, 424], a critical  $\beta$  can thus be computed for a particular plasma configuration (see Fig. 46).

The above discussion is pertinent to magnetic fields oriented normal to the mean interface profile. The description of the above mechanism can be generalized to the situation when the field is oblique to the interface, so that the vorticity is transported roughly in the direction of the field lines [426]. In the case where the field is transverse to the interface, the vorticity never leaves the interface, but self-interferes in a way that causes the interface amplitude to oscillate [427]. Cao et al. [428] considered an alternative transverse-field case where the field is also perturbed along with the interface, so that no field lines cross it; in this case, the RMI is also suppressed, but the mechanism is attributed to the Lorentz force directly rather than vorticity transport. In fact, the interface oscillates due to this effect even in the absence of shock acceleration.

MHD suppression of RT and RM is important because it suggests that inertial fusion techniques, such as ICF or pinch techniques, which feature cylindrical and spherical geometries, could

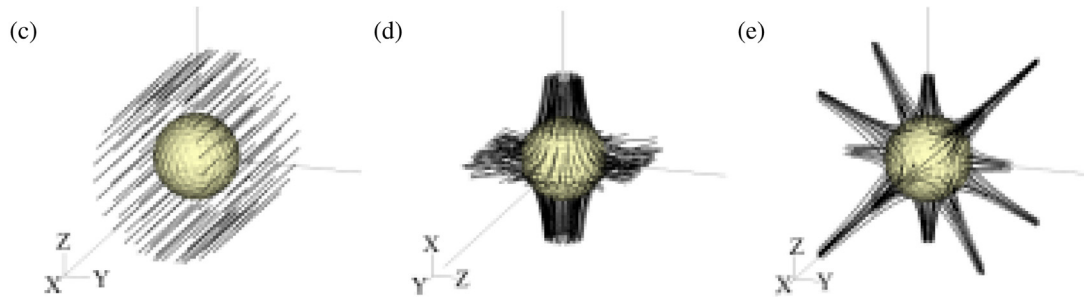


**Fig. 47.** Example field configurations for converging flows showing density interface and magnetic field lines in three dimensions from [425]. (a) Three-dimensional uniform unidirectional field; (b) Three-dimensional “two-loop” field, notionally generated by two current loops placed above and below the target; (c) Three-dimensional “six-loop” field with octahedral symmetry, notionally generated by six current loops placed on the principal axes around the target.

be stabilized by applying a magnetic field (see Fig 6 of [37] that indicates suppression of RT instability in ICF with an imposed magnetic field). The above planar results might be interpreted as applying to a differential element of a cylindrical interface with vanishing curvature. A linear stability analysis and numerical solution for such a cylindrical configuration was carried out by Bakhsh et al. [429], who found that the RMI indeed remained suppressed during the cylindrical implosion. Now, fields that are simply extended from a planar context to a cylindrical or spherical context, however, would require magnetic monopoles at the origin of the cylinder or sphere. These are forbidden by the Gauss law and have never been observed in nature, and they certainly are not produced in fusion reactors. Therefore, plausible magnetic field geometries must be devised that satisfy physical and engineering constraints while continuing to suppress RM.

The first step in such a study is to properly understand the base MHD flow. Since the magnetic field is generally not radially symmetric, there will be variations of field orientation to both the density interface and the direction of shock propagation. Mostert et al. [425,430] investigated a set of plausible field configurations in two and three dimensions, the latter of which are shown in Fig. 47, focusing on the symmetry of the shock structure during the implosion process, and concluded that more symmetrical choices in the field configuration result in similarly symmetrical shock structures. This is important since the inertial fusion technique relies on symmetry of the imploding shock to generate the hot spot.

Symmetry is not the only consideration, however. In other two-dimensional (that is, cylindrical) cases, a rotationally symmetric azimuthal field configuration, which could be generated by a current-carrying wire aligned with the cylinder's axis, exhibits a magnetic field which becomes singularly strong on the axis. This implies that the ambient fast magnetosonic characteristic speed increases to infinity approaching the axis. Since Mach number depends on the local ambient characteristic speed and is a measure of the shock strength (and hence its ability to heat and compress fuel), it was found that the imploding MHD shock actually weakens as it implodes [431] which defeats the purpose of the endeavor. This effect could be mitigated by tuning the electrical current on the wire to decay to zero sufficiently quickly during the implosion, thereby limiting the characteristic speed at the position of the shock [432]. Studies such as these show that given the pervasive and often counterintuitive effect of magnetic fields on such systems, there is a risk of destroying the efficacy of the process by choosing the field symmetries injudiciously even before RM considerations are introduced.

RM is itself indeed suppressed in many plausible magnetic field configurations [434]. The suppression mechanism is locally unchanged from the planar case, as shown in Fig. 48, while the key global qualitative features of the suppression are shown in Fig. 49 for the candidate configurations in three dimensions [432].

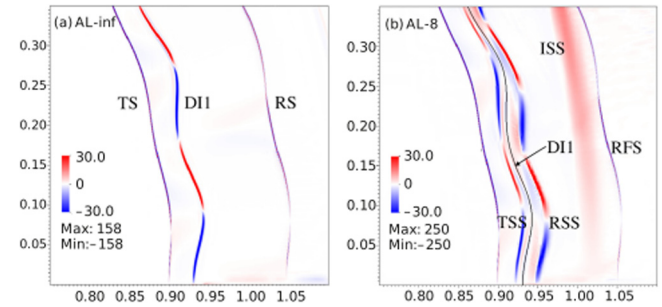


**Fig. 48.** Vorticity contour of shock refraction for (left) unmagnetized, and (right) MHD flow with a field penetrating the interface from a portion of a converging MHD RM problem [433]. In the unmagnetized case, shock refraction on the density interface (DI1) produces a transmitted (TS) and reflected (RS) shock with vorticity remaining on the interface. In MHD, the transmitted and reflected subfast shocks (TSS, RSS) carry vorticity off the interface. The incident slow shock (ISS) results from details of the initialization. Reproduced with permission.

The suppression mechanism, determined theoretically in the planar cases, is clearly visible in these converging geometries when visualizing vorticity, as in Fig. 49d,e; it is transported away from the interface, roughly along magnetic field lines. Where the field lines are parallel to the interface, the vorticity moves along the interface in a way that allows the perturbations to oscillate around zero without growth. The RT instability, while not the main focus of these studies, is also suppressed; at late times in the simulations, there is a gradual formation and transport of vorticity away from the interface. Again, the symmetry of the field configuration is reflected in the RM suppression patterns, suggesting that the best and most consistent performance might be obtained by maximizing the symmetry planes of the field configurations.

There are many additional aspects of the MHD RMI in cylindrical and spherical geometries that deserve interest, and subsequent studies have investigated some of these. Mostert et al. [425] found that a field configuration with an octahedral symmetry group better maintains symmetry in the base flow, without compromising the extent of RM suppression. Li et al. [433] found that using a double density interface also shows suppression, but that the separation distance between the interfaces affects the quality of the suppression. In one context featuring explosions, possibly applicable to supernovae or other chemically reacting gas eruptions, RM is affected by the field according to local orientation as in the imploding cases, with Lin et al. [435] numerically showing orientation-dependent suppression in exploding cylindrical and spherical SF<sub>6</sub> gas clouds, as shown in Fig. 50. The RM suppression effect was also observed by Black et al. [436] with simulations of a cylindrical gas cylinder being shocked by a planar incident wave. One particular feature of the configuration of Black et al. is the ease of eventual experimental comparison, for example in shock tubes.

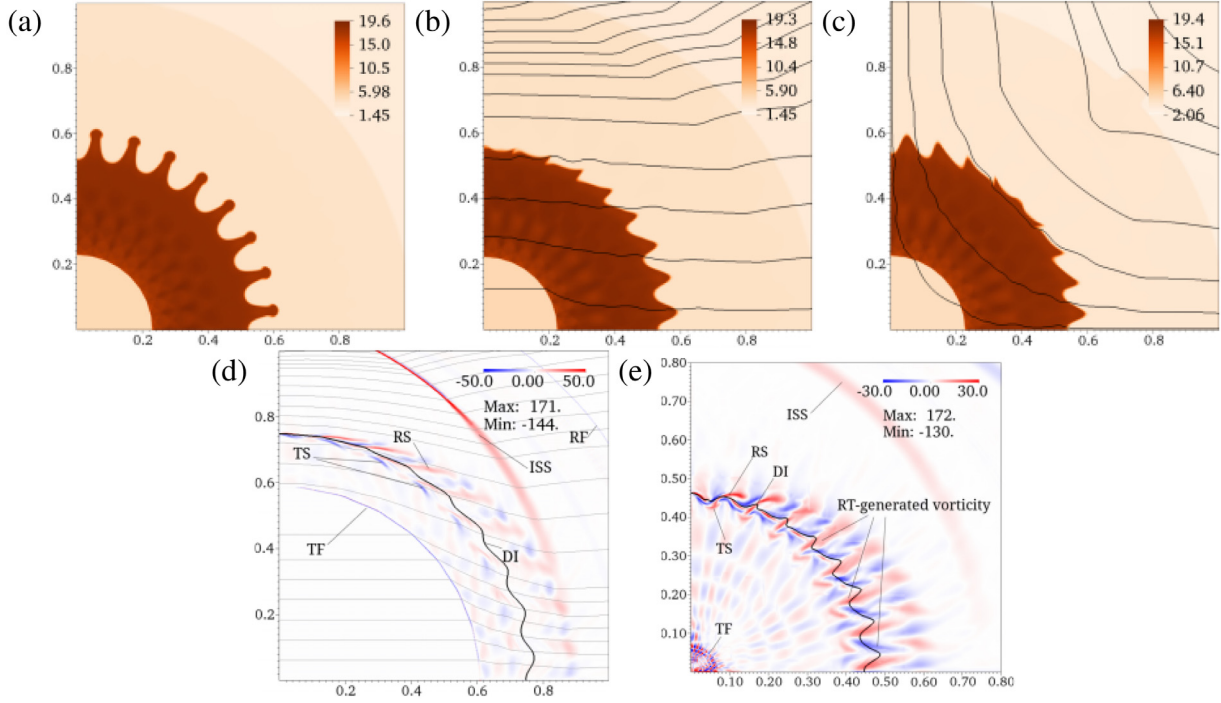


**Fig. 49.** RM suppression in two-dimensional converging flows [434]. (a) Density contour showing unsuppressed RM after passage of a converging cylindrical shock. (b) Density contour of MHD RM suppression with a two-dimensional field analogous to Fig. 47a. (c) Density contour of MHD RM suppression with field analogous to Fig. 47b. (d) Vorticity contour and density isoline for a uniform initial field,  $\beta_0 = 4$ , showing the transmitted fast (TF), transmitted sub-fast (TS), reflected sub-fast (RS) and reflected fast (RF) waves, and the incident slow shock (ISS) resulting from the initialization and not directly related to the initial shock-interface interaction. (e) Vorticity contour for a uniform field  $\beta_0 = 32$  but otherwise similar to (d) after appearance of RT instability. RT vorticity is generated on the interface, but continually advected away from it. In all cases, the initial sonic shock Mach number  $\approx 2$ .

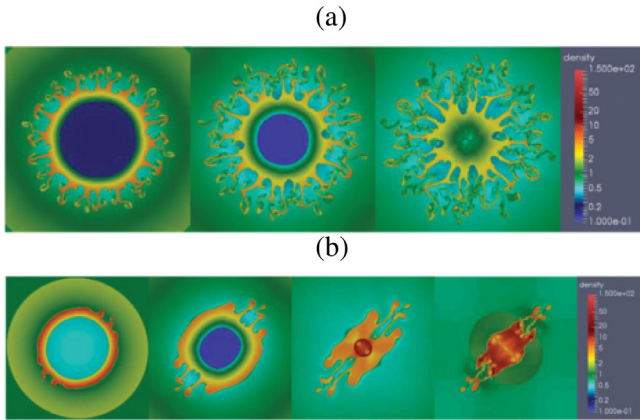


**Fig. 50.** Density contours for an explosion of a cylindrical SF<sub>6</sub> cloud of diameter 0.1 m in air (a) without a magnetic field, (b) in the presence of a forward-diagonally oriented magnetic field of strength 0.1 T. Initial air ambient pressure and density are 101.3 kPa, 1.205 kg/m<sup>3</sup> respectively [435]. Reproduced with permission.

### 13.3. Magnetic field amplification in the MHD RM and RT

As we have shown previously, in both RM and RT, the magnetic field must be sufficiently strong to suppress the instability, and for field strengths below some critical value the suppression effects are muted or absent [422]. In this circumstance, the magnetic field can be *amplified* by RT- or RM-induced mixing. Moving away from the inertial fusion context, this phenomenon has been

used to explain some large magnetic fields in supernova remnants (SNRs).

The essential mechanism for magnetic field amplification for both RM and RT follows from the same property of magnetic flux conservation in MHD, and is related to the magnetic dynamo effect [437]. Figs. 51 and 52 show the development of the RM instability for the cases where the field is oriented horizontally (Fig. 51) and obliquely (Fig. 52) [14]. The shock travels vertically from top to bottom. After the shock passage, the unstable interface develops into its characteristic mushroom shape and eventually leads to turbulent mixing. As this develops, magnetic field lines which are embedded in the fluid close to the interface on one side are dragged along with the interface. As the complexity of the interface grows, the field lines are stretched and compacted next to each other, which increases the flux density locally. Clusters of field lines thus take on a filamentary character, which is strikingly shown in the right of Fig. 52. These strong-field filaments are structured along the mushroom-shaped density interface, and the magnetic fields inside can be magnified by orders of magnitude, up to the point where the (initially very weak) magnetic pressure balances the thermal pressure. The field strength may be locally greater than the critical value identified by Sano et al. [422] in which case further development of secondary Kelvin-Helmholtz instability may be inhibited. The discussion for RT instability is essentially similar, as described in the extensive earlier study by Jun et al. [438], except that the RT system typically persists within an acceleration field such as gravity. Both studies, among others, suggest that this amplification phenomenon may explain the high magnetic fields observed in the filamentary structures of SNRs. Sano et al. [14] note however that in the presence of plasma resistivity, the amplification property cannot continue indefinitely as magnetic dissipation will counteract the very high field gradients.

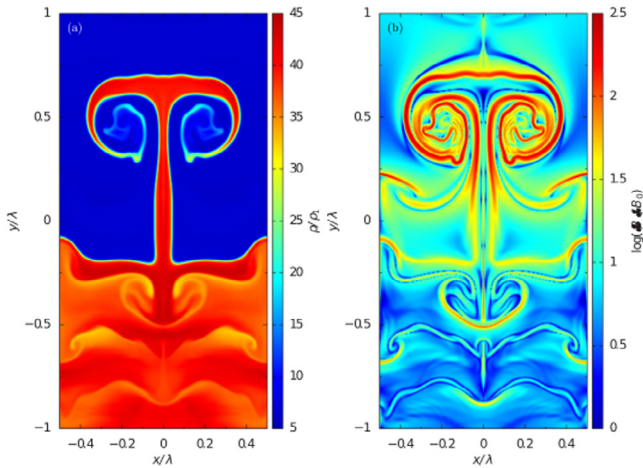


**Fig. 51.** Density (left) and magnetic field (right) contours of the MHD RM instability [14]. The initial weak magnetic field is oriented horizontally, but is swept up in the nonlinear evolution of the RM instability and amplifies in filamentary structures. Reproduced with permission.

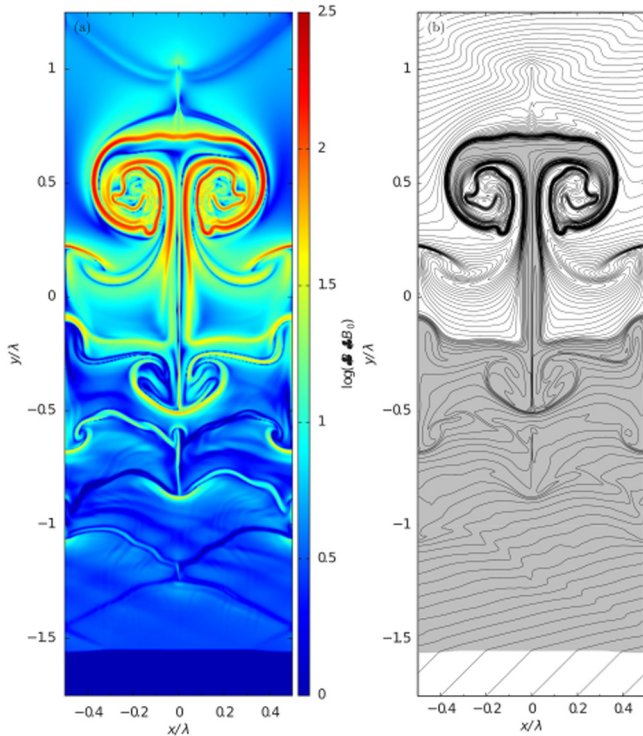


**Fig. 52.** Magnetic field strength contour (left) and magnetic field lines (right) of the MHD RM instability [14]. The initial weak magnetic field is oriented obliquely to the interface. Reproduced with permission.

Generally, MHD turbulence tends to lead to local field amplification by this same mechanism [439,440], particularly in the presence of shocks [441,442], but the particular role played by RT and RM instabilities in these processes is also an active research topic and their field amplification properties have been used in subsequent studies concerned especially with SNRs. For example, a study on the development of vortical structures downstream of the shocked interface described the magnetic field amplification analytically [443], and Inoue et al. [444] used the MHD RM amplification property to describe why magnetic fields are oriented radially in young SNRs.

Some of the similarities between vortex dynamics and magnetic fields in MHD have been exploited in the further study of vortex sheets which arise in models of RM as well as KH instability. Matsuoka et al. developed a model for two-dimensional vortex dynamics in MHD [445], reminiscent of the classic Birkhoff-Rott equation, and which was subsequently used to model the nonlinear evolution of these two instabilities for the case where the field does not penetrate the interface [446].

### 13.4. Beyond ideal MHD

While the ideal MHD results discussed thus far are promising with regard to understanding the RM and RT instabilities in plasmas, they are limited in their physical application by the assumptions underlying the MHD model, particularly the assumption that the various plasma length scales are much smaller than the smallest lengths of interest in the MHD problem. However, at least one ICF experiment has featured a plasma with at least one of these length scales *larger* than the hot spot radius at the implosion center [447]. Moreover, self-generated magnetic fields, which are not accounted for by ideal MHD models, can arise in inertial implosions [448]. Observations like these lead to more sophisticated MHD models, such as Hall MHD [449] and especially *two-fluid* models, in which the ions and electrons are considered as separate fluid species which interact with each other and with the electromagnetic environment. This increased complexity brings with it significant theoretical and numerical challenges, such as the explicit appearance of the speed of light in the resulting calculations. The wave environment is also much expanded in this framework and the picture of shocks and interface jump conditions in the previous discussion, complicated as it was, again needs revision [132]. Nonetheless, it is possible to make direct comparisons between two-fluid and MHD models regarding the suppression mechanisms discussed above [450] and more fundamentally, to investigate where the various MHD models sit mathematically, with respect to the two-fluid models [451]. We briefly discuss two recent results of interest, both of which involve self-generated magnetic fields in plasmas.

One key effect introduced by the use of a two-fluid model is that the scales on which charge separation (for example, between ion and electron species) occurs are explicitly modeled. This is done by the introduction of finite values for the Larmor and Debye lengths  $d_L$  and  $d_D$ , which are reference plasma length scales, the vanishing limit of which contains the single-fluid MHD equations. In two-fluid models, since the sound speed for electron species is considerably higher than for typical ion species, electron shocks will typically outrun ion shocks. In a study of the two-fluid RM instability without an applied magnetic field, [132] shows numerically using a Riemann problem initialization that this effect leads to rapid charge separation between species along with a corresponding counteracting Lorentz-force acceleration on both species. This acceleration leads to oscillatory motion on the species and can result in RT instability on ion and electron interfaces, including the shocked interface. The complex nonlinear interplay between electron and ion species can even destabilize the (ion) shock surfaces themselves. The overall effect can be seen in Fig. 53, noting particularly the faceted appearance of the ion shock at late times and the fine structure induced in the ion and electron species number densities. The complexity of the physics and the mathematical structure of the model make the two-fluid RM instability a challenging research area. Nevertheless, for now it appears that RM suppression is retained in the presence of an applied magnetic field, and the MHD behavior is approached in the limit of vanishing  $d_L, d_D$ , providing confidence in the use of MHD to model the phenomenon [450,452–454].

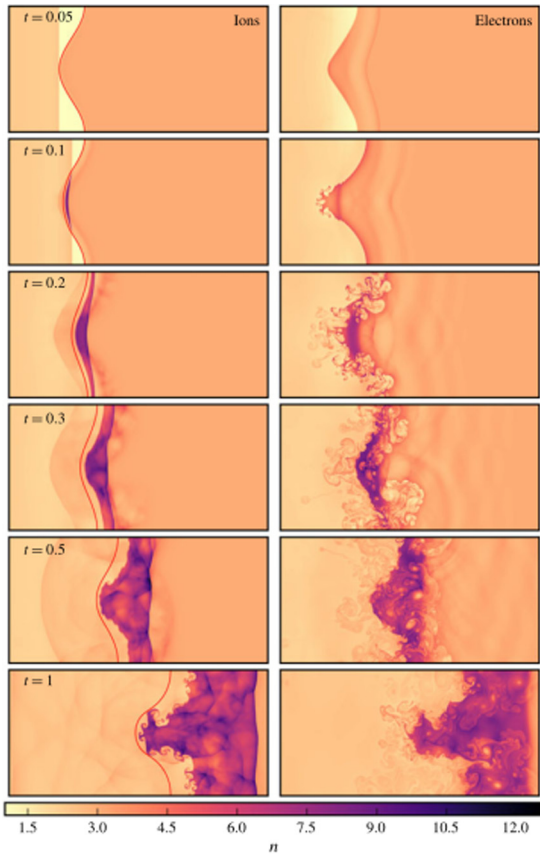


**Fig. 53.** Ion and electron species number densities in two-fluid RM problem without an applied magnetic field, with hydrodynamic interface position overlaid, for reference Larmor and Debye lengths  $d_L = d_D = 0.1$  relative to the flow length scales [132]. Reproduced with permission.

Another effect not observable in ideal or resistive MHD models is the appearance of self-generated magnetic fields via the Biermann battery effect, which appears through the inclusion of electron physics in some measure [449]. The generated field arises from density and pressure (or temperature) gradient misalignment in the flow [132,449,455], typically entering into Hall-MHD or two-fluid formulations. This is a baroclinic generation term and can thus be linked to vorticity generation in the flow [455], and has been seen to arise in plasmas featuring the RTI [448,449]. This has possible implications with respect to electron thermal conductivity inhibition, which has been observed in magnetized inertial flows [447], and may affect transport processes in z-pinches [456]. The extent of effects beyond MHD, for example Hall effect and the Biermann battery, in astrophysical flows is also of ongoing interest [457]. While we do not attempt a review of the rich literature on this topic here, the appearance of this effect in these models commends their usefulness in modeling plasma flows beyond RM and RT contexts.

Finally, the increased physical resolution afforded by such models is also likely to complicate the vorticity paradigm picture outlined in the previous section; for example, the mechanism of MHD waves carrying vorticity away from the density interface may need to be revised. Hence, to understand the RM and RT instabilities fully in plasma flows – not merely ideal MHD flows – further investigation into these models is necessary.

#### 14. RT instability in solar prominences

Having detailed the effect of magnetic fields on the development of the RTI and RMI, we now turn our focus to “real-world”

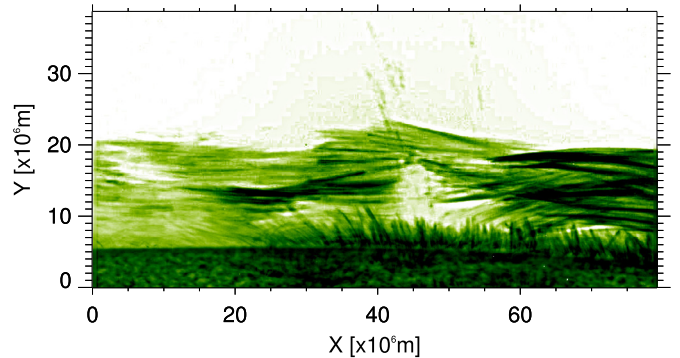


**Fig. 54.** An example of an active region of prominence (panel a) observed on the 8th Feb. 2007 at 17:24UT (observations performed using Hinode Solar Optical Telescope).

examples where magnetic fields influence the development of these instabilities. Our first example is the development of RTI plumes in solar prominences.

The high density material that constitutes solar prominences is suspended against gravity by the magnetic field of the solar atmosphere. When buoyant bubbles of magnetic field rise beneath prominences, the high-density material of the prominence finds itself situated above material of much lower density. Recent observations have shown that, unsurprisingly, RTI develops in this situation. In this section the information required to understand these observations, and the quirks of RTI in this context, will be presented.

#### 14.1. Prominences and their dynamics

Prominences, an example of which is shown in Fig. 54, are one of the most striking features of the solar atmosphere. Seen clearly when the light from the Sun’s disk is obscured during solar eclipses, prominences appear as colorful clouds in the solar corona. These “clouds” are composed of, what is relatively speaking, cool and dense plasma (in fact prominences are composed of neutral atoms, ions and electrons dominated by the neutral hydrogen component) surrounded by the hot and tenuous solar corona. To give a more precise statement of these quantities, the characteristic temperature and density of the solar corona are  $\sim 10^6$  K and  $\sim 10^{-12} \text{ kg m}^{-3}$ , while for prominences we have  $\sim 10^4$  K and  $\sim 10^{-10} \text{ kg m}^{-3}$  [458,459] (note that these values can vary depending on where exactly in the solar atmosphere they are being measured).

The density and temperature of the prominence mean that the black-body radiation from prominences is negligible compared to their total radiation, therefore they are generally observed as a result of absorption or emission of photons in specific atomic spectral lines. In emission (how prominences are seen during eclipses), these include the hydrogen Lyman (transitions from higher levels to the ground energy level of the atom) and the Balmer (transitions from higher levels to the second level) lines including H-alpha as well as lines emitted at prominence temperatures and densities by magnesium, calcium and helium atoms and ions, for example. The fact that many of the spectral lines produced by these elements are at wavelengths that appear in the visible light spectrum gives prominences their colorful tinge when seen during an eclipse.

Though prominences are observed at the solar limb, as the Sun rotates, they will rotate around from the solar limb onto the solar disk. On disk, the material that forms the prominence absorbs some of the light radiated from the solar surface below. As a result in the spectral lines where prominences can be observed, on disk

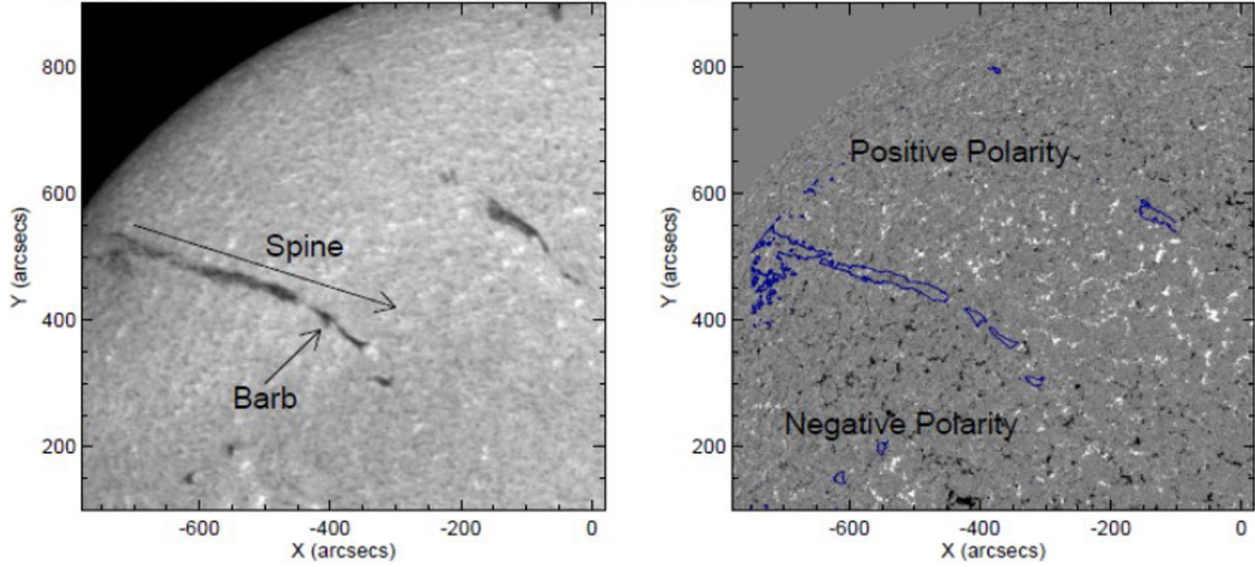


**Fig. 55.** H-alpha filaments on the solar disk (left) with the spine (central axis of the filament) and a bard (a prong that protrudes from this axis) for a particular filament (observed on 21 Dec. 2010 using SMART T1, Hida Observatory, Kyoto University). Also shown is its position in relation to the photospheric magnetic field (right) with the positive polarities shown in white and the negative shown in black. The outline of the H-alpha filaments are shown in blue, showing they form on the polarity inversion lines observed with the HMI instrument onboard SDO. Axes units are in arcseconds, with one arcsecond  $\sim 730$  km at the Sun-Earth distance. (For interpretation of the references to color in this figure legend, the reader is referred to the web version of this article.)

they can be seen as dark features known as filaments (see Fig. 55). This multi-angle view of prominences means that characteristic dimensions can be measured, which are (note that there can be large variances depending on the prominence measured): length of  $6 \times 10^4$  to  $6 \times 10^5$  km, height of  $1.5 \times 10^4$  to  $10^5$  km and thickness  $5 \times 10^3$  to  $1.5 \times 10^4$  km [458].

The positions on the solar surface where the filaments, and obviously with that the prominences, form strongly depend on the distribution of the magnetic field at the solar surface (see right panel of Fig. 55). When the magnetic field at the photosphere (the base of the solar atmosphere) is measured, the positions where prominences have formed strongly correlate with the positions of what are known as polarity inversion lines (the strips on the solar surface where the radial component of the magnetic field at the changes its polarity). It may be the case that the polarity inversion line is found in a group of sunspots associated with a shorter, low-lying active region of prominence, or with the polar-crown type quiescent prominences that form at the large-scale polarity inversion lines that occur when the magnetic polarity of the solar poles changes as a result of the solar cycle.

As well as its position on the solar surface, the height of a prominence in the solar atmosphere is also determined by the magnetic field. The height of a prominence is large compared to its pressure scale height (as defined in Section 12.2.3)  $H_p \sim 300$  km. Therefore, there has to be a force beyond gas pressure gradients to levitate the material. The low plasma  $\beta$  (defined in Eq. (82), and is  $\lesssim 0.2$  in the solar corona) means that the Lorentz force in particular the magnetic tension component, see Eq. (81) and related discussion, becomes crucial for supporting the prominence material. The combination of magnetic tension being crucial for prominence support and the position a prominence may form being dictated by the magnetic field of the photosphere provide important constraints for global prominence models. The basic understanding now is that prominence material collects in dipped regions of the coronal magnetic field, e.g. [460], so that the tension force can work upwards to support the material. The implication of this is that the magnetic field in prominences is measured to be close to horizontal (strengths of this horizontal field are regularly found to be between 3 and 30 G

or 0.0003 to 0.003 T), as confirmed by measurements, e.g. [461, 462]. For a review of prominence models see, for example, [459].

There are a number of different classifications of prominences, and one of the most informative ways of making this classification is based on their proximity to the active regions (the regions in the solar atmosphere surrounding sunspots that are filled with strong magnetic fields). Based on this classification, there are quiescent (see Fig. 56), intermediate and active region prominences (see Fig. 54). A key aspect of this classification is the strength of the photospheric magnetic field. Active region prominences are associated with the polarity inversion lines of the strong magnetic fields that manifest as sunspots and active regions. This type of prominence is often short-lived and can undergo the violent eruptions that produce strong flares and coronal mass ejections. For regions where the photospheric magnetic field is weak, i.e. far from active regions, the visible characteristics of the prominence change, and as their eruptions are less frequent and less violent – these are known as quiescent prominences. On smaller scales ( $O(10^3)$  km) these prominences display a wide range of flow dynamics [463], with strong motions both in and against the direction of gravity, e.g. [464, 465], as well as flow instabilities and turbulence, e.g. [466–469]. Many of the flows in prominences reach speeds of  $O(10 \text{ km s}^{-1})$ , close to the sound speed in the prominence material (8 to 10  $\text{km s}^{-1}$ ), but lower than the Alfvén speed (the characteristic speed of magnetic waves) which for a  $\beta = 0.1$  prominence becomes  $\sim 30 \text{ km s}^{-1}$ .

To understand the difference in dynamics, it is important to look at the relative importance of the key forces in the system. For a magnetohydrostatic balance, we would look for gravity ( $F_G$ ), where

$$F_G = \rho g, \quad (133)$$

to be balanced by magnetic tension ( $F_T$ ), where (from Eq. (81))

$$F_T = \frac{B_x}{\mu_0} \frac{\partial B_z}{\partial x} \sim \frac{B^2}{\mu_0 L}, \quad (134)$$

with  $L$  the radius of curvature of the magnetic field. Taking the ratio of these two, and assuming an ideal gas ( $p = \rho k_B T / \mu_m M_p$ ),

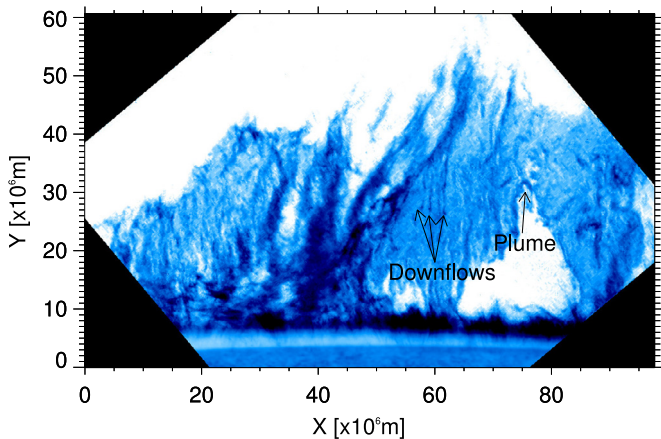


**Fig. 56.** A quiescent prominence observed by Hinode SOT on 29th Sept. 2008 at 10:02UT showing the intensity in the CaIIH broadband filter, a plume and three downflowing knots are marked on the figure.

gives:

$$\frac{F_G}{F_T} \sim \rho g \frac{\mu_0 L}{B^2} = \frac{p}{B^2/2\mu_0} \frac{g\mu_m M_p}{k_B T} \frac{L}{2} = \frac{\beta}{2} \frac{L}{H_p}. \quad (135)$$

This highlights that even for  $\beta < 1$ , gravity can be an important force if the system size is much larger than the pressure scale height (as is possible in prominences). The  $L$  value required to set this ratio to unity, given the pressure scale height of the prominence material is  $H_p \sim 300$  km, is  $L \sim 3 \times 10^5$  km for an active region prominence (which is much bigger than the scale of an active region) but shrinks to  $\sim 3 \times 10^3$  km for a quiescent prominence (which is much smaller than the prominence global scale). This implies gravity can be dynamically important in quiescent prominences.

#### 14.2. Prominence plumes as observational evidence of the magnetic RTI

Now that the arguments behind the importance of gravity in the quiescent prominence system have been laid out, we move to the main focus of this part of the paper, i.e. the observations of the magnetic Rayleigh–Taylor instability in quiescent prominences. These features are observed as dark plumes that rise upward through the prominence. An example of plumes in a prominence is shown in Fig. 56 (note this is a negative image so the dark plumes appear light).

The first observations of plumes were presented by Stellmacher and Wiehr [470]. In these observations a large bubble (22,000 km in size) that was dark in the cool spectral lines in which a prominence can be observed formed beneath the prominence. From this bubble, a plume broke off and then rose at approximately  $12 \text{ km s}^{-1}$  through the prominence before fragmenting. By analyzing the spectra, the authors observed that the lack of cool emission in the plume was a result of a dearth of cool, prominence material, and argued that the observed dynamics were created by an instability. These observations did not garner much attention at the time of publication, and interest in them grew only when the plumes were rediscovered by two research groups in 2008 [471,472].

In [472], the authors presented as an example, a prominence from 30 November 2006 that underwent the formation of multiple plumes of width  $\sim 800$  km which formed from a bubble that developed at the base of the prominence and buoyantly rose through the prominence. The plumes propagated a large way

through the body of the prominence before breaking up and mixing into the prominence. The authors also noted the brightenings that formed at the plume head and their connection to downflows of prominence material. Further investigations into the bright material at the plume head showed that it represented a Doppler-shift variation along the head of the plume [473,474] which is expected when the plumes push the prominence material out of the way as they rise [475].

Berger et al. [476] performed observational analysis of three different prominences to determine some more general characteristics of the plumes. They found that for most of its lifetime, the plume rose through the prominence material at a constant velocity with mean speeds of approximately  $16 \text{ km s}^{-1}$  (note that these are supersonic speeds, but are sub-Alfvénic). Following the period of constant rise, the plumes were often found to breakup coincident with a deceleration of the structure. Plumes were found to have a wide range of widths from 500 km to 5000 km. Some of the observations show not only the rising plumes, but falling spikes of the dense prominence material between two rising plumes [476].

The majority of the plumes are observed to develop from large bubbles (as with the plumes, the bubbles are dark in the cool spectral lines used to observe prominences [470]) that form beneath the prominence, and are also called voids and cavities in the literature. It is from the boundary between the prominence and the bubble that the plumes develop and then rise up through the prominence. This has made the nature of the bubbles one of the key issues for understanding how the plumes are formed. Measurements show there is significantly less cool material in the bubbles than in the prominences e.g. [477], though the presence of any excess hot material compared to the corona is still a matter of dispute [473,478]. Thus, the possibility that this material may be observed is likely to vary based on various conditions in and around the bubble. It is generally accepted that the bubbles are formed by the emergence of magnetic field underneath the prominence from beneath the solar surface [473,479].

These observations can be summarized as follows: We have relatively dense material of the prominence supported above a low density bubble. The boundary between these two systems can become unstable to the formation of rising plumes and falling spikes. As the prominence system is threaded with a magnetic field, and the magnetic field is understood to be generally horizontal where the prominence material is found [462], the classic scenario for magnetic RTI is realized, e.g. [404,405]. It was Ryutova et al. [480] who was the first to realize that this instability could be key to plume formation, with Berger et al. [476] developing this idea further.

#### 14.3. Linear and nonlinear modeling of prominence plumes

For plumes formed by the magnetic Rayleigh–Taylor instability, both linear and nonlinear theory can be used to understand the dynamics of prominences, while observations of prominences can in turn be used to advance our understanding of the theory of magnetic RT instability. In this section, we introduce some of the key theoretical results that have been developed to understand the plumes, and the physics that underpins these results.

##### 14.3.1. Linear behavior

There have been numerous attempts to use the linear dispersion relation of the magnetic RTI to investigate prominence plumes. In general, simple models for the linear stability assuming an incompressible plane-parallel system have been applied [476,480,481]. These models use a classical dispersion relation similar to those found in e.g. [405] (see also, Eq. (115)).

By assuming a fixed angle between the magnetic field and the wave vector, [480] used Eq. (115) to estimate the strength

of the magnetic field of the prominence. By using observations to measure the growth rate of the instability as  $\sim 8 \times 10^{-3} \text{ s}^{-1}$  and a wavelength in the plane-of-sky of  $\sim 1.2 \times 10^6 \text{ m}$  observed in a prominence on 30 November 2006, the authors of Ryutova et al. [480] determined the magnetic field strength to be 6 G. This value is consistent with those measured for quiescent prominences [461]. These ideas were further developed by [481], and applied to a case where there was also a shear flow at the boundary (used as a potential additional source of instability). Again, a similar magnetic field strength was inferred.

#### 14.3.2. Theoretical developments connected to prominence plume observations

Though the dispersion relations directly applied to prominence dynamics to make estimates of the prominence magnetic field strength are relatively simple, the observations of prominence plumes have inspired further development of the theory behind the instability. There have been a number of developments in understanding the role of shear in the magnetic field (the change in direction of the magnetic field around the density jump) on the stability of the prominence bubble boundary [407,408]. The general conclusion from these studies is that the presence of this magnetic shear implies there is no longer a wave vector  $\mathbf{k}$  such that the tension force can be reduced to zero, so that growth rates are reduced. There have also been developments in including compressible effects [410], which are important at the length scales that the instability develops in prominences.

Since the lengthscales over which the instability develops are generally greater than the pressure scale height of the prominence material, compressibility may become important in the development of the instability. Furthermore, as the boundary between the prominence and the bubble beneath it is created by the interaction of two different magnetic systems, it is likely that the direction of the magnetic field above the boundary is different from that below. As such, we would also expect this shear of the magnetic field across the prominence-bubble boundary to be an important factor in determining the stability of the boundary.

An area of development we will highlight is the modeling of the effect of the predominantly neutral material (which is not directly affected by the magnetic forces) that makes up prominences on the stability of the system. One of the standard methods of accounting for this physics into a MHD model is by using a generalized Ohm's law, which includes the ambipolar diffusion term in the induction equation, i.e.:

$$\frac{\partial \mathbf{B}}{\partial t} = \nabla \times \left( \mathbf{u} \times \mathbf{B} + \eta_A \frac{\mathbf{J} \times \mathbf{B} \times \mathbf{B}}{|B|^2} \right), \quad (136)$$

where  $\eta_A = \xi_n^2 |B| / v_{n,i} \rho_n$ .  $\xi_n$  is the neutral fraction,  $\rho_n$  is the density of the neutrals and  $v_{n,i}$  is the collision frequency between the neutrals and the ions (i.e. the number of collisions per second between a neutral particle and an ion). It is worth noting that in some fields they use Cowling resistivity or Pedersen conductivity which are conceptually similar but take slightly different forms to the ambipolar diffusion presented here. Also note the name ambipolar diffusion has a different meaning in other branches of plasma physics.

In the small wavenumber limit, the growth rate of the RT instability was found to be similar to the ideal MHD limit. However, at larger wavenumbers where the magnetic field could suppress the instability in the ideal MHD case, instability was still observed [409]. In this case the growth rate  $s$  was found to be complex (i.e., an over-stable wave) instead of purely real (direct instability).

This result can be easily understood from a simple thought experiment. In a hot bubble region, there are no neutrals and

only a low-density plasma, but the dense prominence material is roughly made up of only 5% ionized species. Therefore, we can say we have a neutral fluid that has an Atwood number of unity, and will always be unstable. Whereas thinking of only the ionized species as a fluid, we can expect that it may be stable because of the reduced density contrast that exists when only considering this component of the fluid. Therefore, the neutral component of the fluid is always unstable, meaning that even though the collisions between the species will slow down the instability the neutrals will always be able to slip across the magnetic field.

There have been studies that look at the full problem (i.e. treating the two fluids separately, but coupling them through collisions) [482], and nonlinear simulations of the magnetic Rayleigh-Taylor instability including ambipolar diffusion which show that the neutral and ion flows can have large (order of a few  $\text{km s}^{-1}$ ) differences in the velocities between them [483]. Details of the formulation behind ambipolar diffusion and multi-fluid modeling can be found in [484].

#### 14.3.3. Nonlinear modeling

The basic level at which it is necessary to model the nonlinear phase of this phenomenon is by the compressible, ideal MHD equations with gravity included (see Section 11). In general, because the diffusive and viscous scales are many orders of magnitude smaller than the dynamic scales, they can be assumed to be negligible as a starting point for modeling (i.e. the Reynolds and magnetic Reynolds numbers become infinite).

There are a number of key components a nonlinear model of the instability occurring in prominences would have to include. The most basic of these is that there needs to be dense material supported against gravity by the Lorentz force, preferably the magnetic tension component of that force. These models must also include a low density bubble beneath the prominence material. Since this observed phenomenon occurs in the solar corona, it should be expected that the plasma  $\beta$  of the model is less than unity, with reasonable values ranging between 0.01 to 0.2. We can divide the nonlinear modeling approaches of the plume dynamics into roughly three categories: local models, simple global models and "realistic" global models.

The first attempt at plume modeling was based on a local model [485,486]. They used the Kippenhahn-Schlüter (KS) model as the starting point, which provides an analytic solution for mass collecting in the dips of the magnetic field, so that it can be supported against gravity. For these calculations, a buoyant bubble was created by extracting mass from a localized volume. The plasma  $\beta$  used for this model is  $< 0.5$ . On perturbing the system, RT plumes rose from the bubble through the simulated prominence. Due to the strong, predominantly horizontal magnetic field, the plumes are forced to align with the direction of the magnetic field (see Fig. 57), so that when we observe the plumes in the prominence we are looking approximately along the direction of the magnetic field. This happens because the instability grows while working to minimize the bending of the magnetic field (as can be understood from the linear growth rate, i.e. see Eq. (115)). The plumes rose at speeds of  $\sim 8 \text{ km/s}$  through the prominence body. One reason that explains the smaller rise speed compared to the observations is that the maximum density contrast used in these simulations is only one order of magnitude, whereas the contrast between the prominence and corona is about two orders of magnitude. Fig. 57 shows a 3D rendering of the density, with magnetic field lines included, of the initial conditions (showing the buoyant bubble beneath the prominence) and at late times when rising plumes and falling spikes of dense prominence material had developed.

Before addressing the details of more complex numerical simulations of plume formation, it is worthwhile to look at

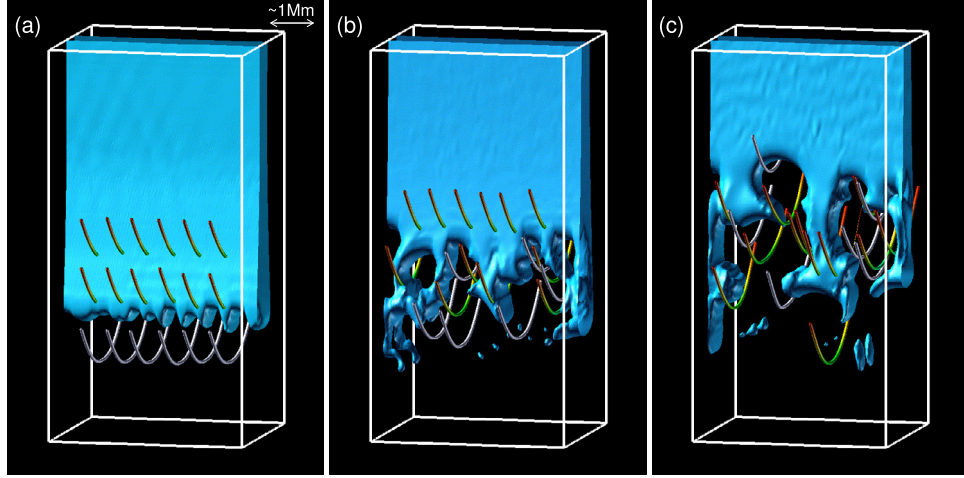


**Fig. 57.** Evolution of plumes driven by the magnetic Rayleigh–Taylor instability in the KS prominence model presented in [486]. Reproduced with permission.

some simple nonlinear modeling of plume rise to understand the particular flow speeds observed. Based on simulation results showing the plume heads can be approximated by cylindrical structures aligned with the magnetic field [486] the plume is modeled as a circular cylinder rising through the prominence. By matching the buoyancy with aerodynamic drag, we find the rise speed of the plume ( $v_{\text{rise}}$ ) should be:

$$v_{\text{rise}} = \sqrt{\frac{2r_{\text{plume}}g}{c_D} \frac{\Delta\rho}{\rho_{\text{prom}}}} \approx 23 \text{ km s}^{-1}, \quad (137)$$

where  $r_{\text{plume}}$  is the radius of the plume head,  $g$  is the solar gravity,  $c_D$  is the drag coefficient (here taken to be 0.5),  $\Delta\rho$  is the density contrast between the plume and the prominence and  $\rho_{\text{prom}}$  is the prominence density. The ratio of the density contrast to the prominence density is taken to be  $\sim 1$ . Note that this estimate, crude as it may be since it does not include the effects of magnetic tension or compression, does appear to nicely match the higher values in the range of observed the plume rise velocities, providing further evidence that these plumes can be driven by buoyancy.

So-called global models, which represent the next level of complexity in modeling prominence plumes, can be seen as reproducing the plume dynamics. These models include the prominence plume dynamics by embedding the prominence in a hot, tenuous corona with the height and width (but not necessarily the length) of the prominence contained within the calculation domain. As seen in the simulations presented in [487] and [488] the plume dynamics produced are similar to the local models.

An important extension to these models was given in [489], where the magnetic field of the prominence model was rooted in the solar photosphere, mimicking the solar atmosphere, where the high density of the photosphere can act like a fixed boundary for the coronal magnetic field when studying dynamics that are fast compared to the evolutionary timescales of the photosphere. In these calculations, the magnetic RT instability developed, although the instability was suppressed as the angle between the magnetic field of the prominence and the direction of the spine of the prominence/filament system was reduced. One way in which this suppression could be understood is through the ratio of gravity to magnetic tension shown in Eq. (135). In the model of [489] the magnetic field strength was increased as the angle was increased, so that even though changing this angle of the magnetic field effectively increased the length “L” of the system, the plasma  $\beta$  became smaller at a faster rate making the system more dominated by the magnetic tension force that is trying to

suppress the instability. Since a prominence size that was about a factor of 5 smaller than those observed was used in this study, the relative importance of the magnetic field of the full scale of the system was modeled (through the increase in L) reducing the role of instability dynamics in their model.

To go beyond these “simple” global models, extra physics should be included to model the physical conditions of the solar corona where a prominence might form. These include a (artificially determined) heating source, energy losses from the atmosphere via radiation, and thermal conduction that is dominated by the conduction of heat along the magnetic field (as this is the direction in which the electrons have the greatest freedom to transport heat). The inclusion of these processes will allow for material to be evaporated from the dense layers of the lower atmosphere into the corona, and if the situation becomes favorable, the cooling of this material can then overpower the heating, resulting in run-away cooling of coronal material, forming the cool prominence material inside the corona, e.g. [488].

The work of Kaneko and Yokoyama [490] can be viewed as the most complete modeling of the instability in a prominence setting to date, as it was able to reproduce magnetic RT dynamics as a result of the formation of the prominence. In this model material condensed in the corona to form a prominence. However, due to mass of the material that condensed, the magnetic RTI developed driving highly turbulent motions in the prominence (as shown in Fig. 58). This closely mimics many of the observations of quiescent prominences which show the material is highly dynamic and turbulent. The authors found the mass loss from the prominence to be balanced by fresh material condensing to reform the prominence.

#### 14.4. Discussion and outlook

To summarize what has been learnt from these studies, the conditions for the magnetic RT instability are satisfied in solar prominences creating plumes that rise through the prominence body. Given the high resolution and temporal cadence of plume observations, these observations are quite possibly the highest quality observations of the magnetic RT instability in any astrophysical system. Note that observations of the RT instability in prominences are not only restricted to prominence plumes: there have been some clear observations of the instability in erupting prominences, e.g. [414], which show the breakup of the dense prominence material as it falls back to the solar surface. These observations have also driven new areas of study, both for linear instability analysis and for nonlinear modeling. If the reader is

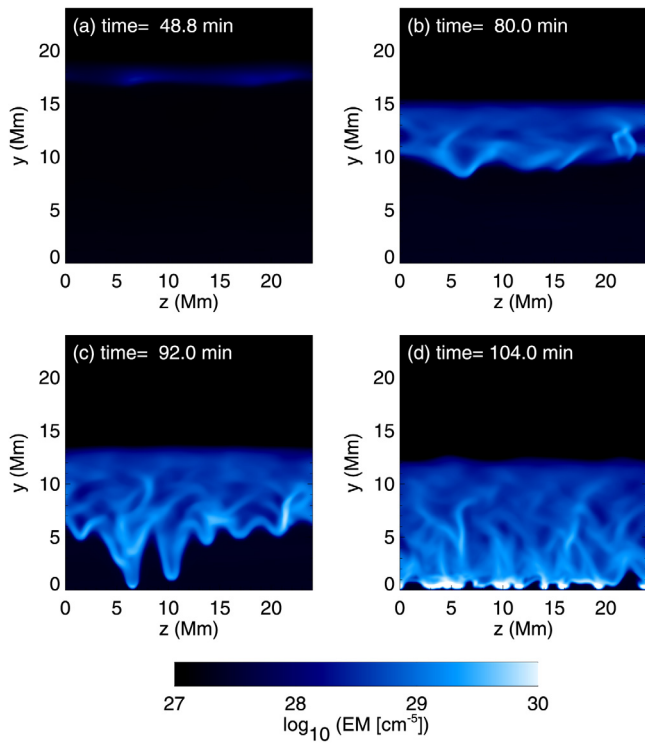


**Fig. 58.** Development of the RTI in a global prominence model [490]. Reproduced with permission.

interested in additional details of the phenomenon of prominence plumes and our current understanding of them, they are directed to [491].

Though there has been significant progress in both modeling the plumes by the magnetic RTI and developing RTI theory to describe the physical environment of a prominence in the solar corona, there are still areas where development and further investigation is required. The vast majority of the linear stability models used are highly simplified, so more advanced models will allow for the possibility of the RT instability to be used to accurately characterize the prominence system. Numerically, the nonlinear simulations are becoming very advanced. However, a clear area to investigate further is the effect the inclusion of the separate dynamics of the ions and neutrals has on the physical process under study. Finally, observationally there is still the necessity for a wide-ranging statistical study of the plumes to determine the relation between key instability characteristics – for example, the dependence of the growth rate on the wavenumber. An additional case of interest is one in which the magnetic field, and with it the plume structure, is perpendicular to the line of sight.

## 15. Space physics: Ionospheric flows

Space physics encompasses the study and monitoring of Earth's space environment and solar-terrestrial relationships. The field is critical to advancing and protecting the nation's economic, defense, and scientific interests. Its strategic importance has led to the creation of the National Space Weather Program (academia-industry-government partnership [492]) and the publication of The National Space Weather Strategy and Action Plan [493]. Multi-scale physics-based predictive modeling, data assimilation and computation of ionospheric dynamics and turbulence are major frontiers of space sciences and space

weather research. A range of scales, from mesoscale to ionospheric microscale, needs to be included in a three-dimensional modeling framework to capture physical mechanisms associated with RT instabilities and turbulence in ionospheric flows.

The ionosphere is a dynamic mixture of ions, electrons and neutral gases surrounding the Earth in the altitude range from approximately 90 km to beyond 1000 km. The ionosphere can also be viewed as a transition region from the earth's lower atmospheric regions (i.e., troposphere, stratosphere, mesosphere) to the outer space environment (i.e., the magnetosphere). As such, the ionosphere acts to mediate and transmit external forces and drivers from below and from above (Fig. 59a).

The ionosphere involves interactions between phenomena of varying scale sizes. Large-scale variations, like solar cycle, seasonal and tidal effects, drive large-scale changes in global structure. Such changes define the mean state (climate) of the ionospheric system. These processes have characteristic spatial scales greater than a thousand kilometers and time scales from several hours to a few years. General circulation models have been developed to simulate these large-scale structures (e.g., [495–498]). These global models, together with the large observational datasets that have been accumulated over the years, have led to a much greater understanding of large-scale structures in the ionosphere and the response of these structures to variations in geophysical inputs.

Space weather is the perturbation of the ionosphere and thermosphere from its long-term global mean state. These perturbations involve not only large-scale variations, but also mesoscale and small-scale processes that occur locally and may have short periods. Mesoscale and small-scale processes, such as RT instabilities and turbulence, affect not only local plasma and neutral distributions, but also large-scale structures through dynamical and energetic coupling. Such coupling between processes of different scales occurs in the equatorial region, mid- and high latitudes. Dynamics of large and mesoscale winds is often characterized by the presence of zonal jets, layers and anisotropic turbulence (i.e., [499–512]). Improving our understanding of neutral/plasma interactions and RT physical processes at ionospheric meso/microscales is a challenge for ionospheric science studies.

### 15.1. Equatorial spread F

The F region is the terrestrial plasma environment between an altitude of 120 and 800 km. The F region is bounded by the E region below and the exosphere above, and together these three regions form the terrestrial ionosphere [513].<sup>7</sup> The RTI was first proposed in [514] as the process driving Convective Equatorial Ionospheric Storms (Equatorial Spread F, or ESF). Using analogy with the hydrodynamic RT instability when a light fluid supports a heavier fluid against gravity, it was suggested that lower (higher) density ionospheric plasma is advected upward (downward), creating a larger perturbation, and the system is unstable. In the ionospheric case, the 'light fluid' is the low-density plasma, which carries a gravity-driven current that provides the  $\mathbf{J} \times \mathbf{B}$  force, preventing the plasma from freely falling. The system is unstable when the vectors  $\mathbf{g}$  and  $\nabla n$  are oppositely directed. Here  $n$  is the electron number density of plasma [494]. See the illustration in Fig. 60.

Plasma irregularities and inhomogeneities in the F region caused by RT plasma instabilities manifest as spread F echoes. The scale sizes of the density irregularities range from a few

<sup>7</sup> These rather pedantic names have a curious history, according to Kelley [494]. The E region received its name from the electric field in the radio wave reflected by the "Heavyside" layer (the first name for the ionosphere). The other layers were simply alphabetical extensions.

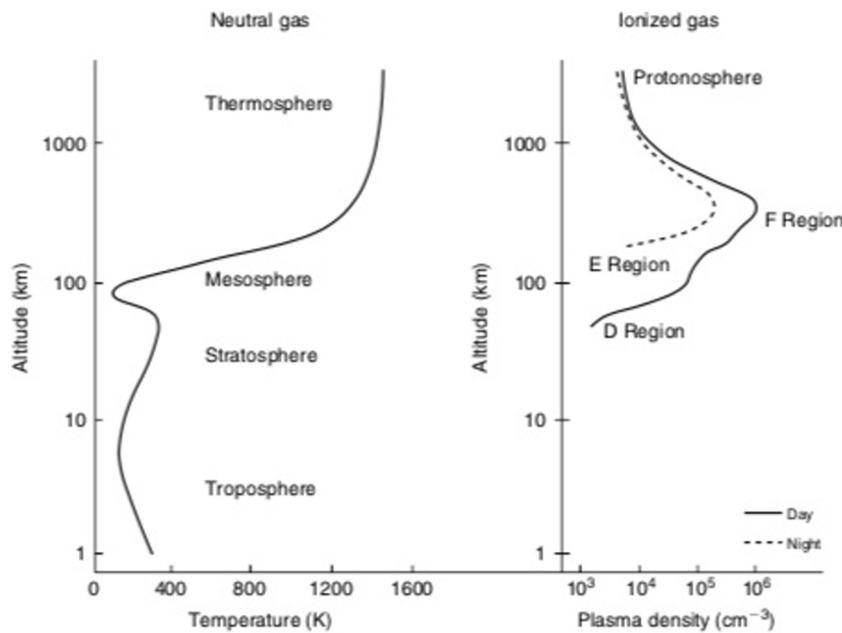


**Fig. 59.** Typical profiles of neutral atmospheric temperature and ionospheric plasma density with the various layers designated [494]. Reproduced with permission. ©Elsevier.

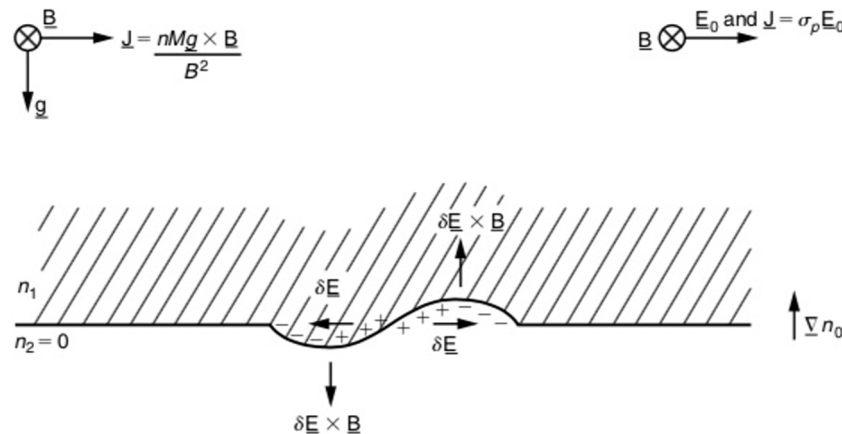


**Fig. 60.** Schematic diagram of the plasma analog of the Rayleigh-Taylor instability in the equatorial geometry. [494]. Reproduced with permission. ©Elsevier.

meters to a few hundred kilometers, and the irregularities can appear at all latitudes. However, spread F in the equatorial region can be particularly severe. At night, fully developed spread F is characterized by plasma bubbles, which are vertically elongated wedges of depleted plasma that drift upward from beneath the bottomside F layer (Fig. 59b). A density perturbation can trigger the RT instability on the bottomside of the F layer under certain conditions. Once triggered, density irregularities develop, and the field-aligned depletions then bubble up through the F layer. The east–west extent of a disturbed region can be several thousand kilometers, with the horizontal distance between separate depleted regions being tens to hundreds of kilometers. The plasma density in the bubbles can be up to two orders of magnitude lower than that in the surrounding medium. When spread F ends, the upward drift ceases and the bubbles become fossilized. Equatorial plasma bubbles (EPBs) are irregular plasma density depletions in the post-sunset ionosphere that degrade communication and navigation signals.

## 15.2. Spacecraft and general circulation model data

The electron density in the ionosphere varies diurnally, geographically and seasonally with sunspot number, and other solar phenomena. The total electron content (TEC) can vary by two orders of magnitude depending on the time and location of observations. Apart from the variation with altitude, the electron density varies with the activity level of the sun, time of the year, time of the day, and geographical position.

As an example, Gentile et al. [515] have established a statistical database of more than 14,400 equatorial plasma bubble (EPB) observations after inspecting evening sector plasma density measurements from polar-orbiting Defense Meteorological Satellite Program (DMSP) spacecraft for 1989–2004. DMSP spacecraft fly in circular, Sun-synchronous polar orbits at an altitude of 840 km and an inclination of 98.7°. Solar cycle, seasonal, and longitudinal effects are evident in the data (Figs. 61–62).

Using the National Center for Atmospheric Research Thermosphere Ionosphere Electrodynamics General Circulation Model (TIEGCM) [516], Fig. 63 shows the RT growth rate at 270 km altitude for different longitudes and local time for different seasons [517]. The large growth rate occurs near 18:00 local time

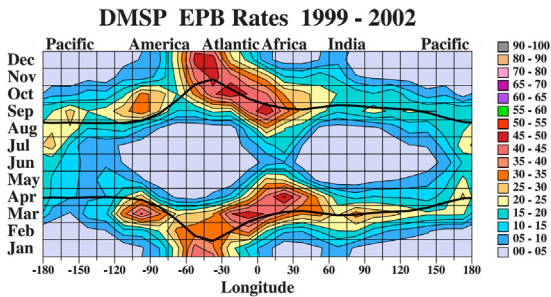


**Fig. 61.** Contour plot of equatorial plasma bubble (EPB) rates for solar maximum 1999–2002 on a month versus longitude grid. EPB rates are fairly symmetric, high in the America–Atlantic–Africa sector both early and late in the year. [515]. Reproduced with permission. ©AGU.

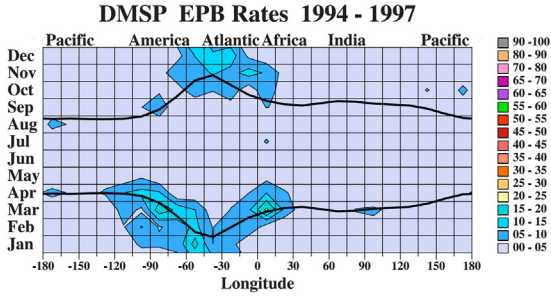


**Fig. 62.** Contour plot of EPB rates for solar minimum 1994–1997 in the same format as Fig. 61. EPB rates were generally 5%. Highest rate (21%) occurred in the Africa sector in March. [515]. Reproduced with permission. ©AGU.

(LT), which can be attributed to the large upward ion drift related to the vertical ion drift pre-reversal enhancement (PRE) near dusk [518]. The upward ion drift is directly related to the RTI growth rate. To illustrate the solar effect, the RT growth rates at 18:00 LT. Fig. 64a, b illustrated the RTI growth rate for the cases of the solar minimum year (2009) and maximum (2003), respectively [519]. The RT growth rates during the solar maximum (2003) are much larger compared to those of the solar minimum case. The TIEGCM model utilizes the field line integrated growth rate with both neutral wind and ion drift [520]. The model calculation, in general, agrees with observations.

The evolution of ESF is a strongly nonlinear phenomenon with multiscale interactions for ionospheric dynamics. The large-scale primary RT mode can promote a hierarchy of smaller scale plasma instability processes that give rise to a wide spectrum of irregularities. The presence of these small-scale irregularities was evidenced from observations that showed the coexistence of kilometer and meter scale disturbances in the nighttime equatorial F region [521,522]. In addition, a number of stochastic effects and scintillations play an important role in the influence of the ionosphere on electromagnetic wave propagation. At low latitude, an important scintillation source is F-spread. F-spread is caused by rod-shaped magnetic field-aligned plasma bubbles, which are formed in the F-layer just after sunset and have lifetime of 2–3 h. The edges of the bubbles of F-spread are highly unstable and can be the source of intensity scintillations. F-spread is more prevalent during equinoxes and summers, occurs preferentially during magnetically quiet periods, and increases with sun activity.

### 15.3. Nested simulation studies

Since the discovery of the plasma instability phenomenon that occurs in the nighttime equatorial F-region ionosphere, and which is revealed by rising plumes identified as large-scale depletions or bubbles, considerable efforts have been made in the

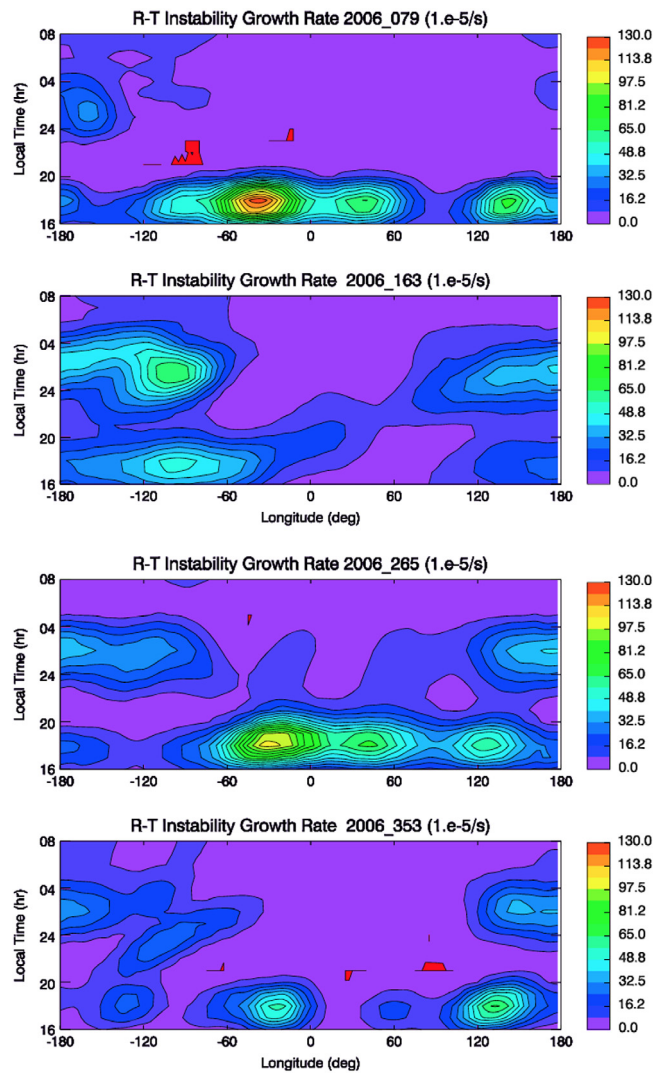


**Fig. 63.** Local time and longitudinal variations of the Rayleigh–Taylor instability growth rate ( $10^{-5} \text{ s}^{-1}$ ) during the March equinox, solstice, September equinox, and December solstice (from top to bottom). [517]. Reproduced with permission. ©AGU.

development of computer models that simulate the generation and evolution of the Equatorial Spread F (ESF) dynamics [521, 523–541]. Here, analyses and simulations of primary and secondary RT instabilities in the equatorial spread F (ESF) triggered by the response of plasma density to neutral turbulent dynamics and wave breaking in the lower region of ionosphere are discussed for coupled systems (ions, electrons, neutral winds), thus enabling studies of mesoscale/microscale dynamics for a range of altitudes encompassing ionospheric E and F layers. Thus, simulations using coarse and fixed resolutions cannot resolve the small-scale disturbances. Poor resolution of these scales can in turn affect the accuracy of the larger scales due to nonlinearity. Obviously, one can design a computer model with a very high spatial resolution everywhere. But then, the simulations will be prohibitively expensive, particularly in three dimensions.

In this subsection, nested numerical simulations of ionospheric plasma density structures associated with nonlinear evolution of the primary and secondary RT instabilities in ESF are discussed [542–544]. For the limited domain and nested simulations, the lateral boundary conditions are treated via implicit relaxation techniques applied in buffer zones where the density of charged

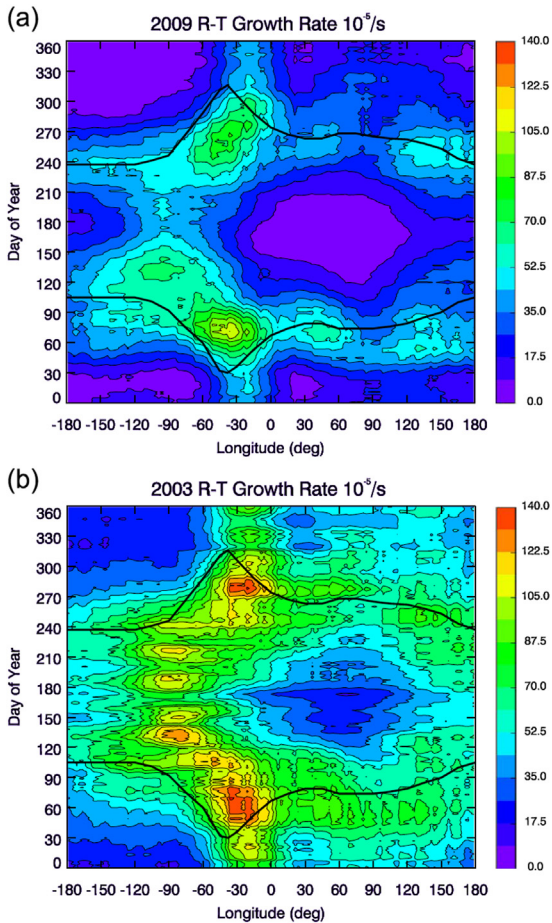


**Fig. 64.** Seasonal and longitudinal variations of the field line-integrated Rayleigh–Taylor instability growth rate ( $10^{-5} \text{ s}^{-1}$ ) at 18:00 LT simulated with non-migrating tides for solar minimum year 2009 (a) and maximum 2003 (b). The peak height for the field lines is at pressure level 1.75, which is 264 (298) km during solar minimum (maximum). The black lines are days and longitudes that match the Tsunoda condition [519]. Reproduced with permission. ©Elsevier.

particles for each nest is relaxed to that obtained from the parent domain. The high resolution in targeted regions offered by the nested model is able to resolve scintillation producing ionospheric irregularities associated with secondary RT instabilities characterized by sharp gradients of the refractive index at the edges of mixed regions. The scintillation effects induced by trapping of electromagnetic (EM) waves in parabolic cavities created by the refractive index gradients along propagation paths were analyzed [522,545–548].

The three-dimensional equations for ionospheric dynamics include coupling of neutral fluid, ion gas, electron gas, and electromagnetic equations. For brevity, these equations will not be presented here, but they are documented in standard books on Earth's Ionosphere [494,549]. The extent of the nested domain simulation is [-200 km; 200 km] in the horizontal and [300 km; 550 km] in the vertical, with a grid spacing of 4 km, and 2.5 km in horizontal directions and vertical respectively. Fig. 65 shows 3D, large-domain simulation of ESF. The neutral wind is  $125 \text{ m s}^{-1}$ , and the imposed external electric field is given by  $E_0/B = 100$ , where  $B$  is the magnetic field. The horizontal axis represents the east–west range (a) and (b); the north–south range (c) and (d). The solid curves represent the iso-density contours after 2000 s. The simulation is initialized with a small 3D density perturbation superimposed to the background density profile. The  $x$ - $z$  cross-sections are at (a)  $y = 0 \text{ km}$ , (b)  $y = 109 \text{ km}$ . The  $y$ - $z$

cross-sections are at (c) at  $x = 0$ , (d)  $x = 31 \text{ km}$ . The development of the ESF as a large scale bubble is evident. The top of this bubble reaches a high altitude and is located below 500 km.

Fig. 66 shows the field of iso-density contours simulated by the nested model at a later time. The results show that in addition to the main spread F bubble, there is a generation of secondary Rayleigh–Taylor instabilities or secondary bubbles. In addition, the primary (the large scale) disturbance is more developed and reaches higher altitudes. We note that by increasing the resolution of the parent model, the secondary instability is resolved in the nested simulation (Fig. 66). Also, the primary disturbance is more developed and reaches higher altitude above 500 km. Thus, the high resolution in targeted regions offered by the nested model is found to be critical for the resolution of ionospheric plasma density structures and the large-scale bubble associated with the evolution of primary and secondary Rayleigh–Taylor instabilities in the Equatorial Spread F.

In summary, analyses and simulations of primary and secondary RT instabilities in the equatorial spread F (ESF) triggered by the response of plasma density to neutral turbulent dynamics and wave breaking in the lower region of ionosphere are discussed for coupled systems (ions, electrons, neutral winds), thus enabling studies of mesoscale/microscale dynamics for a range of altitudes encompassing ionospheric E and F layers. New research efforts focus on combining data-driven and physics-predictive modeling techniques with applications to ionospheric dynamics including studies of extreme space weather events such as geomagnetic storms and turbulence driven by RT instabilities.

#### 15.4. Challenges

The ionosphere plays a major role in space sciences due to its important influence on the propagation of electromagnetic (EM) waves (radio waves, microwaves, lasers). The ionospheric environments can significantly impact communication, navigation and imaging systems primarily through the development of electron density irregularities and plasma turbulence, often in the vicinity of large electron density gradients created by RT instabilities and turbulence. Associated irregularities and inhomogeneous, anisotropic, non-Kolmogorov and patchy ionospheric dynamics can have a spatial range from tens of kilometers through meter scales. A wide variety of physical processes occur on these disparate scales, and this has posed a considerable challenge to the goal of a truly self-consistent, comprehensive model-based understanding of irregularity dynamics and morphology.

Recent studies have demonstrated the importance of a full 3D, high-resolution nested approach for local studies of limited area ionospheric environments and for understanding the impact of mesoscale and small-scale ionospheric processes on EM propagation. New research efforts focus on combining data-driven and physics-predictive modeling techniques with applications to ionospheric dynamics and space weather including studies of extreme events such as geomagnetic storms [530]. The lower ionospheric altitudes are challenging to model, because they are too low for orbiters and too high for radiosondes to take direct measurements. In recent years, computer simulations of the earth's ionosphere have become a prevailing tool to obtain properties of plasma flows in the ionosphere, especially at low altitudes. Numerical models have been developed to study RT instabilities in equatorial spread F and ionospheric responses to neutral atmospheric motions in the mid-latitude. In these studies, the neutral dynamics are prescribed as idealized velocity fields such as a constant drift flow or empirical shear flow models; specifically for mid-latitude simulations, linear models of inertial gravity waves (IGW) or data sets from other atmospheric models are influenced by many dynamical processes associated with ionospheric layers.

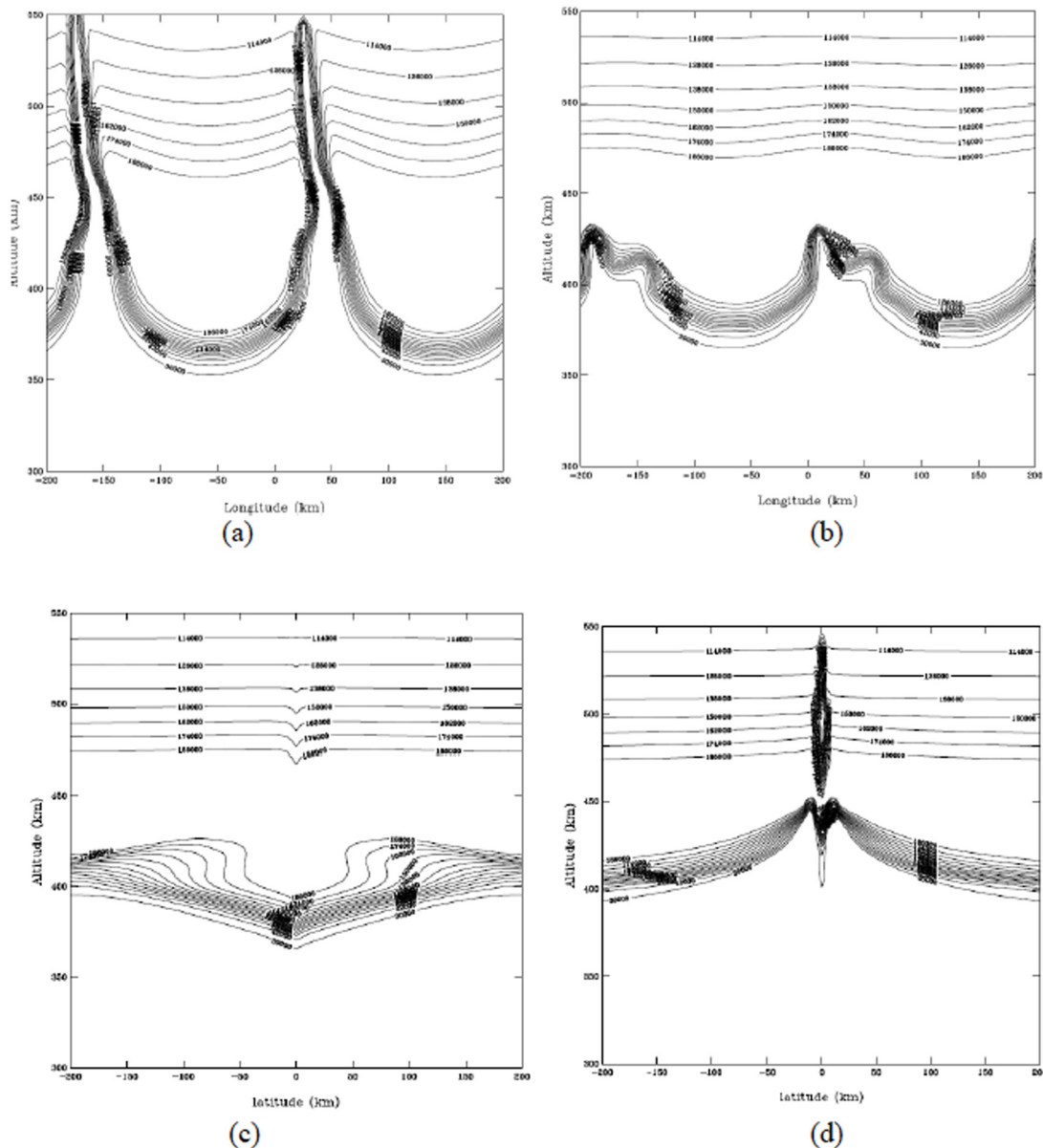


**Fig. 65.** 3D-Large domain simulation of ESF. The neutral wind is 125 m/s, and the imposed external electric field is given by  $E_0/B = 100$ , where  $B$  is the magnetic field. The horizontal axis represents the east–west range (a) and (b); the north–south range (c) and (d). The solid curves represent the iso-density contours after 2000 s. The simulation is initialized with a small 3D density perturbation superimposed on the background density profile. The x-z cross-sections are at (a)  $y = 0$  km, (b)  $y = 109$  km. The y-z cross-sections are at (c) at  $x = 0$ , (d)  $x = 31$  km.

Sporadic E layers are ionization enhancements in the E region at altitudes between 90 and 120 km. The layers tend to occur intermittently and can be seen at all latitudes. Sporadic E layers at mid-latitudes are primarily a result of wind shears but they can also be created by diurnal and semi-diurnal tides. The layers are formed when the vertical ion drift changes direction with altitude, occurring at the altitudes where the ion drift converges. In the E region, the zonal neutral wind is primarily responsible for inducing vertical ion drifts which result from a dynamo action. A reversal of the zonal neutral wind with altitude results in ion convergence and divergence regions.

In contrast to sporadic E layers, intermediate layers are broad (10–20 km wide), and occur in the altitude range of 120–180 km. They frequently appear at night in the valley between the E and F regions, but they can also appear during the day. They tend to form on the bottomside of the F region and then slowly descend throughout the night toward the E region. As with sporadic E

layers, intermediate layers can occur at all latitudes, can have a large horizontal extent, and an order of magnitude density enhancement relative to background densities. Intermediate layers are primarily a result of wind shears connected with the semi-diurnal tide. In the E–F region valley (130–180 km), the meridional neutral wind is mainly responsible for inducing the upward and downward ion drifts. When the wind blows toward the poles, a downward ion drift is induced, whereas when it blows toward the equator, an upward ion drift is induced. If the wind changes direction with altitude (a helical wind shear), the plasma will either diverge and decrease its density or converge and increase its density (layer formation). When a null in the wind shear moves down in altitude, the ion convergence region, and hence intermediate layer, also descends.

Many “active experiments” have been conducted to excite plasma instabilities by creating artificial plasma density gradients and observing the resulting layered structures and their nonequilibrium dynamics. The active technique is to inject large amounts

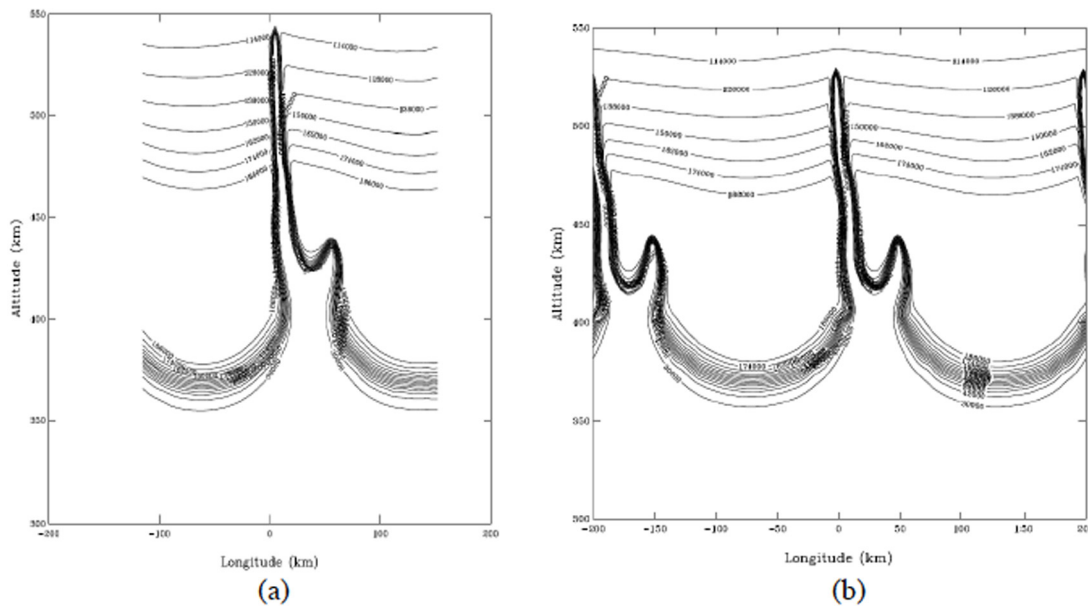


**Fig. 66.** (a) Nested domain simulation of ESF. The lateral boundary conditions use the implicit relaxation applied in buffer zones where the density of charged particles is relaxed to that interpolated from the parent domain. The neutral wind magnitude is 125 m/s, and the imposed external electric field is given by  $E_0/B=100$ , where  $B$  is the magnetic field. The horizontal axis represents the east-west range. The cross-section is taken at  $y=0$ . The curves represent the isodensity contours after 2000s. The simulation is initialized with a small density perturbation superimposed on the background density profile. Note that the nested simulation resolves secondary RT instabilities. (b) Large domain simulation shows several secondary RT instabilities (bubbles) resolved by the nested simulations.

of tracer (barium gas) into the ionosphere from a rocket. The barium is ionized by sunlight and, if released at sunset or sunrise, results in a long-lived plasma made visible by resonant scattering of sunlight. Figure 6.17 from [494] shows visualization of F-layer Rayleigh-Taylor plasma instabilities using Lagrangian tracer techniques. The ionosphere flow pattern is seldom laminar but rather is usually turbulent. The effect of this turbulence is to mix any existing density gradient due to solar production or particle impact ionization. It was noticed that the spectra of turbulent electric field show evidence for slopes encompassing -3 and  $-5/3$  power laws [494]. Unfortunately, very few turbulent field data exist in the literature due to technical challenges and expenses in ionospheric data collection campaigns. Turbulent mixing induced by the RT instabilities in ionospheric flows is an important area of current research.

## 16. Z-pinch, pulsed-power experiments and other applications

### 16.1. Z-pinch

If a current is passed through a cylindrical column of conducting material, then the resulting Lorentz force perpendicular to the current stream acts to constrict the column in a cylindrical collapse. This configuration, called a *z-pinch*, was considered and analyzed before the development of such concepts as ICF (for example see Bennett [550] and Tonks [551] for early analyses of the z-pinch). Its potential for controlled fusion, by constricting the interior plasma to the required temperature and pressure, was developed in the 1950s [552].

Z-pinches are important in certain classes of fusion schemes and, as we will see below, in the reproduction of astrophysical phenomena in the laboratory. They do however feature an interesting array of challenges. The traditional z-pinch is formed into an equilibrium where the plasma column is sustained by a balance between thermodynamic and magnetic pressures. This equilibrium is susceptible to various instabilities, most famously the *sausage* and *kink* instabilities. The kink instability, for example, arises from the amplification of helical perturbations, caused

by an unbalanced increase of magnetic pressure on the perturbations and resulting in a runaway growth and disruption of the pinch. The growth rates of these instabilities are such that the use of z-pinches for magnetically confined fusion is impractical, and this is a major reason for the relative lack of interest in z-pinches until recently [456].<sup>8</sup>

In an alternate configuration enabled by more recent developments in pulsed-power technology, the current pulse may be rapid so that an equilibrium of the above type is never reached. If the timescales of the process are sufficiently short, it may be able to run to completion before these instabilities, whose growth rates are known, can spoil the effort [19]. These are called *fast z-pinches* [456]. There is some further variation on the essential concept, including quasi-spherical wire arrays or even X-shaped wire crossings [556].

Fast z-pinches are however susceptible to the RT instability, which is a particularly pernicious destabilizing influence on the cylindrical collapse, featuring a free acceleration across a nonuniform density plasma. In this context, it is sometimes called the *magnetic Rayleigh-Taylor* instability (MRT) given the integral role of the magnetic field generated by the z-pinch. A simple linear analysis for an imploding shell configuration, in the planar approximation, [456] shows that a perturbation of wavenumber  $k$  on the z-pinch shell thickness  $h$  (which is small), aligned at an angle of  $\varphi$  to the magnetic field, is unstable if  $k$  is smaller than the critical value,

$$k_0 = \frac{1}{2h \cos^2 \varphi}. \quad (138)$$

Hence, long wavelengths (small  $k$ ) are unstable and small wavelengths (large  $k$ ) are stable. However, in the case where the perturbations are aligned with the axis (hence perpendicular to the magnetic field)  $c_z = \pi/2$  and  $k_0$  is not defined: all wavenumbers are unstable. Perturbations at this orientation are sometimes called *flute modes* [456]. On the other hand, the longest stable wavelengths are permitted when the perturbations are aligned

<sup>8</sup> For recent publications, see Refs. [553–555].

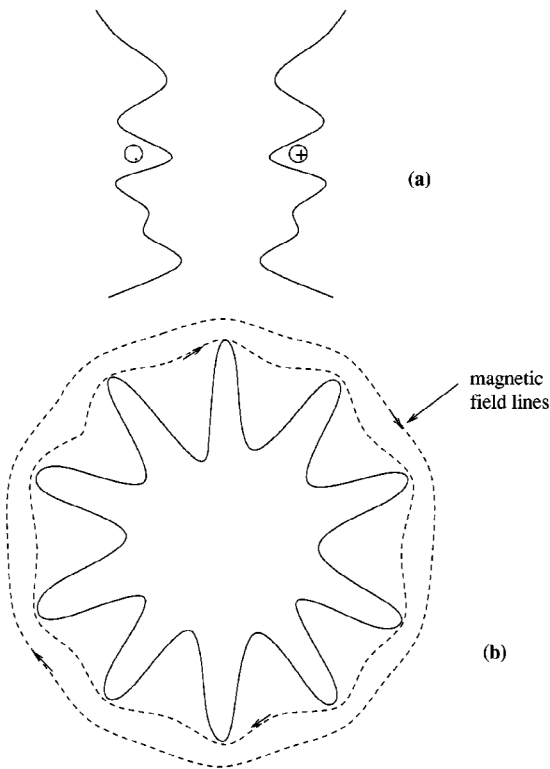


**Fig. 67.** Taken from [456]. Unstable flute modes (a; z-pinch axis runs vertically through center) and more stable, small-wavelength modes (b; z-pinch axis runs normal to page) of the RT instability in z-pinches. Reproduced with permission.

with the field ( $\phi \simeq 0$ ). Fig. 67 shows an interpretation of the cylindrical, nonlinear instability. At the top, a longitudinal cross section of the perturbed cylindrical shell is shown. In the perturbation “valleys”, the magnetic field is stronger and reinforces perturbation growth. At the bottom, an axial cross-section suggests the magnetic field does not necessarily “fall into” the valleys of the perturbations, so that their amplitudes do not grow, provided their wavelengths are not too long. This description, while being simplistic, indicates the stability of perturbations in this case depends on their wavelengths and orientations relative to the axis of the pinch.

Nevertheless, some ideas have been suggested to attempt to stabilize the RT instability appearing in these pinches, including introducing a velocity shear, a rotation around the pinch axis, or an axial magnetic field in addition to the existing azimuthal field [456]. The latter idea in particular, of applying an additional magnetic field to a z-pinch configuration, has led to the development of magnetized liner inertial fusion (MagLIF) [557] and magnetized target fusion (MTF) [558], although with the stated aim of inhibiting electron heat transport rather than hydrodynamic stabilization. However, the unstable flute modes associated with the MRT instability were found in one series of MagLIF studies to recede in favor of another helical instability [559], which has since been identified as yet another manifestation of MRT [560]. Understanding and perhaps conquering RT in z-pinch contexts remain a challenge.

Pulsed-power facilities have also proved useful for reproducing aspects of astrophysical phenomena in a laboratory setting by moving beyond the most basic z-pinch configurations. The plasmas generated by z-pinches can often be modeled by ideal MHD if care is taken in the setting of the various pinch parameters [556], and may also resemble the plasmas in these astrophysical contexts. By an appropriate arrangement of wire arrays in conical,

spherical, or planar settings, it has been possible to investigate jets emitted from young stellar objects (a review of which is given by Reipurth and Bally [561]), jet interactions with interstellar plasma “winds” [562], astrophysical shock waves, and even to some extent, the accretion disks which form around celestial objects [563]. A review of experimental efforts in this regard is given by Lebedev et al. [457]. Many of these astrophysical phenomena can be investigated in terms of resistive or ideal MHD, and likewise feature hydrodynamic instabilities such as RTI. Examples of the RT instability in particular can be found in the linear, highly collimated plasma-jets mentioned above [564], and in arch-shaped jets strongly guided by magnetic field [565]. The experiments generated using pulsed-power facilities can in turn be used to validate numerical models, particularly in MHD, of these phenomena, providing a powerful investigative tool for understanding astrophysical flows often in the absence of direct observational data [457].

## 16.2. Supernovae

The motion of material surfaces and interfaces in supernovae has been a topic of interest for a long time. Supernova dynamics has seen much intense research from the astrophysics community across a broad spectrum of topics (see for example studies by Arnett et al. [566–568] regarding Supernova 1987A, a well-known Type-II core-collapse supernova), so that a full survey of the results cannot be given here (see [3,13]). However, we can discuss briefly the role that RM and RT has in these flows, and the role of MHD in the modeling of the shock and wave dynamics. Two particular examples are the role of hydrodynamic mixing in the stellar model during the supernova explosion, and the subsequent dynamics of stellar material (supernova remnants, or SNRs) long after the initial explosion.

Numerical modeling of the early stages of supernova explosion hydrodynamics, particularly core-collapse supernovae, has often been hydrodynamic with radiative effects; that is, without magnetic field contributions (there are many studies, but a discussion is provided in Hammer et al. [569]). Core-collapse supernovae form following the successive fusion of heavier elements up to silicon (into iron and nickel) by very large stars. Eventually, the huge gravitational pressure on the resulting nickel–iron core is large enough to overcome the electron degeneracy pressure, causing in turn the core to collapse into itself and resulting in electron capture, thereby emitting an enormous quantity of neutrinos. The core continues to collapse into itself away from the outer layers of the stars. Subsequent to this – and the precise mechanism is debated – a shock wave is formed which explodes out from the star. The brightness of this event has a particular luminosity evolution over time called a light curve. From the particular smoothness of these light curves, especially from SN 1987 A, it has become evident that some kind of hydrodynamic mixing occurs inside the star during the core collapse and subsequent explosion [568]. Indeed, it was found that at least two-dimensional models were required to capture the mixing that occur inside a star prior to supernova, with three-dimensional models properly required to capture the correct physics [569]. Large-scale convection effects inside the star cause large perturbations on density interfaces within the star, which in turn act as triggers for RT [569], while the importance of RM during this process remains a topic of discussion [569–571]. Incorporating flame physics complicates the physics further [333,572].

Supernova explosions exist in complex electromagnetic environments, and fully understanding them requires among other things a proper accounting of the electromagnetic effects [12]. The magnetorotational mechanism [573], is one candidate to explain the core-collapse supernova explosion. While the magnetic field inside the star is amplified to a great extent during

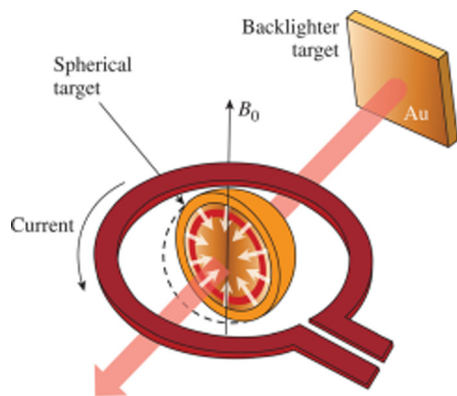


**Fig. 68.** Magnetic field application to an ICF-type target at the University of Rochester, with an aim to improve performance by magnetic flux compression. Taken from [447]. Reproduced with permission.

gravitational collapse, this amplification alone is not enough to allow it to appreciably affect the hydrodynamics of the star. However, as the star collapses and loses gravitational energy, its rotational energy increases due to conservation of angular momentum. This increased rotation rate can boost the magnetic energy density further by “wrapping” the lines around the core in an increased number of windings [574,575]. MHD models have also been used, for example, in the study of type Ia supernovae (featuring white dwarves which undergo catastrophic runaway thermonuclear fusion), to develop propagation models of nuclear combustion fronts [576,577].

RT, RM and MHD effects really combine together in the dynamics of supernova remnants. The uneven shape of SNRs is due to RT and RM resulting from perturbations in the stellar structure during the initial explosion (for example [578]). The SNRs move within a magnetic field, which significantly affect their dynamics [579]. Moreover, SNRs are known to greatly accelerate cosmic rays which pass through them, resulting from MHD waves produced by these rays [580], but this phenomenon may be best understood in terms of the magnetic field amplification which can occur precisely in the MHD RM and RT instabilities [14,438].

### 16.3. Inertial fusion

In inertial confinement fusion (ICF), a small, millimeter-scale capsule containing a deuterium-tritium fuel mixture is irradiated with high-intensity laser energy, causing the shell material to vaporize abruptly, which in turn forces a shock wave to implode radially into the fuel mixture. As the shock travels through the mixture and reaches the center, it heats and compresses the mixture to hundreds of millions of Kelvin and billions of atmospheres pressure, causing the fuel to ignite in a nuclear fusion reaction. The surrounding fuel, having been accelerated inward by the shock, is confined close to the ignition point by its own inertia – hence the name – and can thus maintain the fusion burn. However, since the density of the fuel mixture is not uniform, RT and RM instabilities are excited and can promote mixing between the different layers, disrupting the spherical symmetry of the system and inhibiting confinement and fusion burn. These instabilities are two of the primary culprits for ICF not having been able to produce net positive energy in the laboratory, despite significant sophisticated efforts [17]. A detailed discussion can be found in Zhou et al. [3].

In inertial fusion, the fluids are in fact plasmas, which interact with magnetic fields, and there is the prospect of using this

fact in some way to control or otherwise influence the development of the RT and RM instabilities. One idea is to use the implosion to amplify the magnetic field, in a process called *flux compression*, to inhibit electron transport near the hot spot at the center, increasing its ability to retain heat (see Fig. 68). Using the OMEGA laser at the University of Rochester, it has been shown experimentally that embedding a strong magnetic field in an ICF-type capsule could yield an increase in ion temperature by 15% and neutron yield by 30%, a greater increase than even predicted by a parallel one-dimensional numerical code [447, 581]. This discrepancy was attributed to the inability of the code to capture higher-dimensional effects. The magnetic field may also affect performance in other aspects. However, the reduced electron conductivity afforded by field line electron confinement may also be detrimental to performance because of a reduced coupling between drive laser energy and the capsule [448]. Another line of research, relevant to our discussion, has focused on the hydrodynamic aspects of the plasma motion using magnetohydrodynamics (MHD); this idea is based on the observation that RM can be suppressed altogether in MHD [419], along with the long-known similar observation regarding RT [405]. As we have seen, fundamental numerical investigations in MHD along these lines have been promising for the possibility of instability suppression in these problems. Along with the property of flux compression [447,581], RM and RT instabilities can also amplify the magnetic field during their development [14,438], which can further inhibit electron transport [582]. While not all physical effects in ICF can be captured by ideal MHD, some of its essential aspects are necessary to understand the principles that allow these strategies to work. We have discussed these aspects in the sections above.

## 17. Conclusion

Each year, over a thousand publications that focus on either the physics or applications of Rayleigh–Taylor (RT) and Richtmyer–Meshkov (RM) instabilities are published.<sup>9</sup> Often, these works are motivated by seeking to understand the physical processes at play in supernovae detonations or inertial confinement fusion (ICF). While these fascinating scientific and technological applications are indeed significant (the interested reader is referred to a comprehensive description in recent comprehensive reviews [1–3]), the RT and RM instabilities also play key roles in several other interesting engineering applications and natural phenomena, which are rarely considered in the literature.

Given the vast diversity of fields in which these applications occur, the individual researcher may not be aware of the entire gamut of rapidly evolving applications in which RT and RM flows are relevant: astrophysics, space physics, geophysics, inertial confinement fusion, high-energy-density physics, combustion, turbulent mixing, and many engineering processes. Thus, the goal of this work is to bring attention to the interdisciplinary nature of the field and to illustrate the underlying physical principles that can be applied to a far wider range of problems, with length scales ranging from microns to hundreds of kilometers and time scales ranging from nanoseconds to seconds. This pedagogical review is written to make these applications accessible to a broad and heterogeneous audience.

Specifically, we illustrate the different phases of time-dependent development these instabilities share in common,

<sup>9</sup> A sample of interesting articles which have appeared very recently can be found here [583–706]. The reader may also be interested in a special issue of *Physica D* entitled “Hydrodynamic Instability Driven Flows” (<https://www.sciencedirect.com/journal/physica-d-nonlinearity-physics/special-issue/100VVJ0T0QN>) [58,125,370,707–732].

starting from the linear and advancing to nonlinear, transition, and turbulent states. We also review the various numerical methods designed specifically to tackle these challenging problems in order to allow the sharp interface separating the fluids to be captured with fidelity. Along the way, we present the multi-faceted approaches that have been taken, using numerical simulations, theories, observations, or laboratory and laser experiments.

We further show how these instabilities have revealed themselves in chemically reactive and explosively expanding flows, with important applications in pulsed detonation engines, Type 1a supernovae, and Scramjets. RT and RM instabilities have also been utilized to investigate the properties of material strength. The effects of RM instability can also be seen in the production of particulate ejecta in many contexts. We also stress the role of magnetic fields and their role in the development of the instability growth in solar prominences, supernovae, and pulsed-power experiments. We conclude the paper by discussing the instrumental role the RT instability plays in the plasma environment of ionospheric flows in space.

## Declaration of competing interest

The authors declare that they have no known competing financial interests or personal relationships that could have appeared to influence the work reported in this paper.

## Acknowledgments

The authors wish to acknowledge Profs. Steven Armfield, Guido Boffetta, Daniel Chung, David Youngs and Dr. Andrew Cook for valuable discussions and feedback in the preparation of this manuscript. They would like to thank Drs. William T. Buttler, Brian Grieves, and Jacob McFarland for help in obtaining supporting figures and Drs. David Frost, Takafumi Kaneko, Suresh Menon, Matei Radulescu and Takayoshi Sano for granting them permissions to use figures from their publications. The first author is also grateful to Drs. S. Gail Glendinning, L. John Perkins, Anna Rosen, Alison Rust, and Edmund Yu for helpful conversations and correspondences.

BT would like to acknowledge the computational resources at the National Computational Infrastructure provided through the National Computational Merit Allocation Scheme. A.H. is supported by his STFC Ernest Rutherford Fellowship, UK grant number ST/L00397X/2 and STFC, UK research grant ST/R000891/1. HMI is an instrument on board SDO, a mission for NASA's Living With a Star program. Hinode is a Japanese mission developed and launched by ISAS/JAXA, with NAOJ as domestic partner and NASA and STFC (UK) as international partners. It is operated by these agencies in co-operation with ESA and NSC (Norway). A.H. also acknowledges the use of data from Astronomical Observatory, Graduate School of Science, Kyoto University. A.M. is supported in part by the AFOSR, USA Grant No. FA9550-19-1-0064. The work of B.R. and S.B. is supported in part by the U.S. Department of Energy, National Nuclear Security Administration, Advanced Simulation and Computing Program, as a Cooperative Agreement under the Predictive Science Academic Alliance Program, under Contract No. DE-NA0002378. This work was performed under the auspices of the Lawrence Livermore National Security, USA, LLC under Contract No. DE-AC52-07NA27344.

## Appendix A. Surfaces of discontinuity

We discuss shocks and discontinuous surfaces in additional detail. Shock waves are nearly discontinuous surfaces in space which move faster than the speed of sound in the medium, and carry jumps in pressure, density, and velocity. In gas dynamics,

they are derived from the Euler equations, which express conservation of mass, momentum, and energy, where in the latter case the ideal gas law was used to write the evolution equation for pressure. Unfortunately, shock waves are, in the ideal limit, *discontinuous* surfaces of the flow variables featuring jumps in density, pressure, etc. Across shocks and material discontinuities, the Euler equations fail to satisfy existence properties, since they involve derivatives of discontinuous functions. However, when written in *conservation form*,

$$\frac{\partial}{\partial t} \mathbf{U} + \nabla \cdot \mathbf{F}(\mathbf{U}) = 0, \quad (\text{A.1})$$

for the appropriate conserved quantities signified by  $\mathbf{U}$  and with flux functions  $\mathbf{F}$ , it is straightforward to integrate them over an infinitesimally small region in space covering the discontinuous surface. Effectively, the differential system (A.1) is transformed to an integral (weak) form over a control volume that contains the discontinuities. Thus, the integral form can be interpreted as an algebraic description for the magnitudes of the jump discontinuities. These relations lead to the *Rankine–Hugoniot* conditions when applied to shock waves, but in their basic form are really conservation law statements for any discontinuous surfaces,

$$\begin{aligned} \llbracket \rho u_n \rrbracket &= 0, \quad \llbracket \rho u_n \llbracket \mathbf{u}_t \rrbracket \rrbracket = 0, \quad \llbracket \llbracket \rho u_n^2 + p \rrbracket \rrbracket = 0, \\ \rho u_n \left[ \left[ \frac{1}{2}(u_n^2 + u_r^2) + \frac{p}{(\gamma - 1)\rho} + \frac{p}{\rho} \right] \right] &= 0, \end{aligned} \quad (\text{A.2})$$

where  $\llbracket \Phi \rrbracket$  indicates the difference between the upstream and downstream values of  $\Phi$ . The subscript  $n$  indicates the component normal to the shock,  $r$  tangential to the shock. All variables are taken in the reference frame in which the shock is stationary. These conditions assert that some quantities remain continuous even across a discontinuous surface. For example, a jump in the shock-normal velocity component across the shock requires corresponding jumps in density and pressure such that the bracketed quantities in (A.2) remain continuous. The magnitude of these jumps is controlled by the *Mach number*. Provided  $\rho u_n$  is nonzero, the second condition states that *gas dynamic shocks do not support jumps in tangential velocity*. In particular, they cannot act as vortex sheets. Now, in a coordinate frame moving with a gas dynamic shock, the upstream is supersonic and the downstream subsonic. In this sense, a gas dynamic shock “crosses” the sonic speed. This is what is expressed by the Mach number: in the shock frame, the upstream (normal component of velocity) is supersonic ( $M > 1$ ), and downstream is subsonic ( $M < 1$ ). This is the only type of shock wave in gas dynamics.

In the special case where there is no mass flux across the discontinuity, the first condition of (A.2) is trivially satisfied and the remaining conditions reduce to  $\llbracket p \rrbracket = 0$ , with discontinuities allowed in density and tangential velocity. This interface is called a *tangential discontinuity* if the tangential velocity jump is not zero, and for constant velocities is highly unstable as a result of Kelvin–Helmholtz instability. In the case of RM and RT instabilities, a perturbed density interface is subjected to a shock or a non-impulsive acceleration. Baroclinic generation will then generate a tangential velocity jump at the interface, but here the tangential velocity will be non-uniform away from the interface. In particular, when a shock and tangential discontinuity collide, as in RM, instability arises at the contact discontinuity because it can carry a tangential velocity jump, which the transmitted and reflected shock waves cannot.

## Appendix B. Definitions

### B.1. Abbreviations

ALE	Arbitrary Lagrangian–Eulerian (fluid dynamics code methodology)
BC	Boundary Condition
BW	Blast Wave
CFL	Courant–Friedrichs–Lewy (computational fluid dynamics timestep limit)
CD	Contact discontinuity
CI	Contact interface
CJ	Chapman–Jouguet (detonation wave state)
DDT	Deflagration-to-detonation transition
DL	Darrieus–Landau (flame instability)
DMSP	Defense Meteorological Satellite Program
DNS	Growth rate Simulation
DTF	Distorted tulip flames
EM	Electromagnetic
ESF	Equatorial Spread F
EPB	Equatorial Plasma Bubble in ionosphere
EW	Expansion wave
HE	High explosive
I	Incident shock
ICF	Inertial Confinement Fusion
IGW	Inertial Gravity Waves
ILES	Implicit Large Eddy Simulation
ISS	Incident Slow Shock
KHI	Kelvin–Helmholtz Instability
KS	Kippenhahn–Schlüter
LES	Large Eddy Simulation
LMS	Livermore Multiscale (strength model)
LT	Local time in ionosphere measurements
MHD	Magnetohydrodynamics
MRT	Magnetic Rayleigh–Taylor
MagLIF	Magnetized Linear Inertial Fusion
MTF	Magnetized Target Fusion
PAWCM	Parallel Adaptive Wavelet Collocation Method (fluid dynamics code methodology)
PDF	Probability Density Function
PETN	Pentaerythritol tetranitrate (explosive)
PPM	Piecewise Parabolic Method (fluid dynamics code methodology)
PS	Primary shock
PTW	Preston–Tonks–Wallace (strength model)
RD	Rotational Discontinuity
RF	Reflected Fast wave
RFS	Reflected Fast Shock
RM	Richtmyer–Meshkov
RMI	Richtmyer–Meshkov Instability
RS	Reflected Shock
RS	Reflected Sub-fast wave
RSS	Reflected Sub-fast Shock
RT	Rayleigh–Taylor
RTI	Rayleigh–Taylor Instability
SBI	shock–bubble interaction
SDMI	Shock-driven multiphase instability
SG	Steinberg–Guinan (strength model)
SGL	Steinberg–Guinan–Lund (strength model)
SN	Supernova
SNR	Supernova Remnant
SS	Secondary shock

TCD	Tuned Centered-Difference (fluid dynamics code methodology)
TF	Transmitted Fast wave
TFS	Transmitted Fast Shock
TIEGCM	Thermosphere Ionosphere Electrodynamics General Circulation Model
TS	Transmitted Sub-fast wave
TSS	Transmitted Sub-fast Shock
UCC	Ultra-compact combustor
WENO	Weighted Essentially Non-Oscillatory (fluid dynamics code methodology)

### B.2. Notations

$\hat{\mathbf{x}}$	Unit vector
$\hat{\zeta}$	Value at interface
$[\cdot]$	Change across interface
$\tilde{f}$	Spatial Fourier transform of function $f$
$\langle \cdot \rangle$	Plane average in homogeneous direction
$\bar{f}$	Result of applying LES low-pass filter to function $f$
$\delta\phi$	Value of $\phi$ perturbed from steady solution
$\phi'$	Fluctuation in $\phi$ , i.e. difference from ensemble mean
$\phi^+$	Post-shock value of $\phi$

### B.3. Symbols

Throughout this manuscript, we use the following definitions for common symbols.

$\alpha$	Linear amplitude growth rate scaling factor
$\alpha_b, \alpha_s$	Scaling constants for growth of RT bubbles, spikes
$\alpha_{RM}$	Scaling constant in RM layer growth
$\alpha_{RT}$	Scaling constant in RT layer growth
$\beta$	Plasma parameter, $\beta = 2p/B^2$
$\beta_B$	Scaling between density and concentration fluctuations, $\rho' = \beta_B \phi'$
$\beta_W$	Work hardening parameter
$\gamma$	Adiabatic index of equation of state
$\overline{\gamma}$	Mean adiabatic index of equation of state
$\delta\rho$	Density perturbation
$\Delta\rho$	Density difference, $\rho_2 - \rho_1$
$\Delta$	LES filter width
$\delta p$	Pressure perturbation
$\Delta u$	Shock velocity jump
$\Delta x, \Delta y, \Delta z$	Grid spacing
$\epsilon$	Material strain
$\epsilon_\delta$	Small scaling parameter
$\varepsilon$	Penalty function on the divergence of the velocity field [164]
$\zeta$	Bulk viscosity
$\eta$	Kolmogorov scale
$\eta_c$	Compression factor, $\eta_c = \rho/\rho_0$
$\eta_\infty$	Late-time asymptotic interface amplitude
$\eta_A$	Ambipolar diffusivity
$\eta_D$	Magnetic diffusivity
$\theta$	RM power law exponent

$\theta$	Angle between $\mathbf{B}$ and $\mathbf{k}$	$c_p$	Constant pressure specific heat capacity
$\theta_b, \theta_s$	RM power law exponent for bubble and spike	$c_{RT}$	Constant in a RTI mixing layer equation from a mass flux and energy balance argument [77]
$\Theta$	Molecular mixing fraction	$c_v$	Constant volume specific heat capacity
$\kappa$	Interface curvature, $\kappa = \nabla \cdot \mathbf{n}$	$C$	Color function (volume fraction of reference fluid)
$\kappa_T$	Thermal conductivity	$C_\alpha$	Constant in the condition for the growth of interface perturbation where the Alfvén velocity must be greater than some factor of this speed
$\lambda$	Wavelength	$\wp$	Angle between perturbation of wavenumber $k$ on the z-pinch shell thickness $h$ and magnetic field
$\lambda_c$	Stabilization length scale for DL instability	$C_s$	Sound speed
$\lambda_v$	Inner viscous scale	$C_0, C_1$	Integration constants for Lagrangian displacement
$\lambda_D$	Diffusion layer scale	$C_0, C_1$	Integration constants for magnetic field
$\lambda_h$	Analogous diffusion length for the mixing region	$\mathcal{D}$	Material diffusivity
$\lambda_{LT}$	Leipmann–Taylor scale	$\mathcal{D}_T$	Thermal diffusivity, $\mathcal{D}_T = \kappa_T / (\rho c_p)$
$\lambda_T$	Taylor microscale	$\frac{D}{Dt}$	Advection or material derivative, $\frac{\partial}{\partial t} + \mathbf{u} \cdot \nabla$
$\lambda_{\min}$	Minimum perturbation wavelength	$d\mathbf{l}$	Path element
$\mu$	Shear viscosity	$d_D$	Debye length
$\mu_m$	Mean molecular mass	$d_L$	Larmor length
$\mu_0$	Magnetic permeability in a vacuum	$e$	Specific internal energy
$\nu$	Kinematic viscosity	$E$	Specific total energy
$\nu_{n,i}$	Neutral-ion collision frequency	$\mathcal{E}$	Rate of dissipation of turbulent kinetic energy
$\xi$	Lagrangian displacement	$E_0$	Imposed electric field
$\xi$	Interface position when the magnetic field is present	$\mathbf{f}_b$	External body force
$\xi_n$	Fraction of a fluid that is composed of neutral particles	$f_1, f_2$	Volume fractions of materials 1 and 2
$\rho$	Density	$\mathbf{F}$	Force operator (MHD)
$\rho'$	Density fluctuation	$F$	Wavenumber factor in resistive MHD
$\rho_0$	Unperturbed density	$F_G$	Gravitational force
$\rho_0$	Mean density, $(\rho_1 + \rho_2)/2$	$F_T$	Magnetic tension
$\rho_1, \rho_2$	Unperturbed density either side of an interface	$g$	Gravity
$\rho_1^+, \rho_2^+$	Post-shock density either side of an interface	$g(t)$	Time-varying acceleration
$\rho_u, \rho_b$	Unburnt and burnt densities	$g_0$	Standard gravity, $g_0 \simeq 9.8 \text{ m s}^{-2}$
$\rho_n$	Neutral density	$\mathcal{G}$	the number of wavelength doublings or “generations”
$\rho_{\text{plume}}, \rho_{\text{prom}}$	Plume and prominence density	$G$	Shear modulus
$\sigma$	Cauchy stress tensor	$G(\mathbf{r}, \mathbf{x})$	LES filter kernel
$\sigma$	Standard deviation	$GF$	Perturbation growth factor
$\sigma_r$	Unburned-to-burned density ratio	$h$	Mixing layer width
$\chi$	Coefficient of thermal expansion	$h$	Mesh spacing
$\zeta$	Constant of proportionality in absorbed X-ray intensity	$h_b, h_s$	z-pinch shell thickness
$\tau$	Deviatoric stress tensor	$h_k$	Bubble and spike heights
$\tau_h$	Analogous diffusion time scale for the mixing region	$H_p$	Specific enthalpy of species $k$
$\tau_r$	Characteristic reaction timescale	$\mathbf{I}$	Pressure scale height
$\phi$	Velocity potential, $\mathbf{u} = \nabla \phi$	$I_0$	Identity tensor
$\phi$	Generic conserved scalar	$I_{\text{abs}}$	Incident X-ray intensity
$\phi_0$	Unperturbed generic conserved scalar	$I_{\text{trans}}$	Absorbed X-ray intensity
$\phi'$	Generic conserved scalar fluctuation	$\mathbf{J}_k$	Transmitted X-ray intensity
$\phi$	Level set function	$\mathbf{J}$	Flux of material $k$
$\Phi$	Generic flux function	$\mathbf{j}$	Electric current
$\omega$	Angular frequency, perturbations vary as $\exp(i\omega t)$ (or $\exp(-i\omega t)$ for MHD)	$J_0$	Perturbed electric current
$\omega_A$	Alfvén wave frequency	$k_r$	Magnetization parameter, $J_0 = V_A^2/gL$
$a$	Interface perturbation amplitude	$k_x, k_y, k_z$	Span-wise wavenumber, $k_r^2 = k_x^2 + k_y^2$ , $k_r = 2\pi/\lambda$
$a_0$	Initial interface perturbation amplitude	$k$	Components of wavenumber
$a_k$	Mode amplitude	$k_B$	Total wavenumber (Kolmogorov spectrum)
$a_0^+$	Post-shock amplitude	$k_0$	Boltzmann constant
$\mathcal{A}$	Atwood number, $(\rho_2 - \rho_1)/(\rho_2 + \rho_1)$	$k_c$	Maximum wavenumber for shell instability
$\mathcal{A}^+$	Post-shock Atwood number	$\tilde{k}$	Cutoff wavenumber
$\mathbf{B}$	Magnetic field	$k_{\min}$	Span-wise wavenumber, $\tilde{k} \equiv k_r$
$\mathbf{B}_0$	Initial magnetic field	$k_{\max}$	Minimum perturbation wavenumber
$B_n$	Normal component of magnetic field	$K$	Maximum perturbation wavenumber
$B_{\text{crit}}$	Critical magnetic field for RM suppression		PrE-Formed ripple wavenumber
$\mathbf{B}_t$	Tangential component of magnetic field		
$c$	Speed of light		
$c_D$	Drag coefficient		

$\mathcal{L}$	Characteristic length scale	$Y$	Material (yield) strength
$L$	Radius of curvature of the magnetic field	$Y_0$	Material (yield) strength at standard conditions
$L_{11}$	Integral length scale	$Y_P$	Peierls stress
$Le$	Lewis number	$Y_T$	Thermally activated material strength
$L_M$	Markstein scale length	$Y_1, Y_2$	Mass fractions of materials 1, 2
$L_p$	Dislocation segment length	$z$	Perpendicular direction Section 2
$M$	Mach number	$z_1, z_2$	Position of interfaces 1, 2
$M_e$	Electron mass	$z_{rmav}$	Mean interface position
$M_f$	Fast Mach number		
$M_i$	Ion mass		
$M_I$	Intermediate Mach number		
$M_p$	Proton mass		
$M_s$	Slow Mach number		
$M_S$	Shock Mach number		
$n$	Timestep index		
$n$	Work hardening parameter		
$n$	Electron number density		
$n$	Wavenumber (explosively-driven expansion)		
$N$	Wavenumber (explosively-driven expansion)		
$\mathbf{n}$	Interface normal		
$p$	Pressure		
$p_0$	Unperturbed pressure		
$Pr$	Prandtl number, $Pr = \nu/D_T$		
$\mathbf{q}_c$	Diffusive thermal flux		
$\mathbf{q}_d$	Enthalpy diffusion flux		
$r_{\text{plume}}$	Plume radius		
$R_m$	Magnetic Reynolds number, $R_m = VL/\eta_D$		
$Re$	Reynolds number, $Re = \mathcal{L}U/\nu$		
$Re^*$	Critical Reynolds number for scale decoupling		
$r$	Radial coordinate		
$s$	Growth rate, $s = i\omega$		
$\mathbf{s}$	Symmetric strain rate tensor		
$Sc$	Schmidt number, $Sc = \nu/D$		
$S_f$	Flame speed		
$S_{f,\infty}$	Laminar flame speed		
$S_t$	(RT flames)		
$t$	Time		
$t_c$	Characteristic timescale for the prominence system		
$T$	Temperature		
$T_0$	Initial temperature		
$\mathbf{u}$	Fluid velocity		
$u_n$	Normal component of velocity		
$u_r$	Tangential component of velocity		
$u_{z0}$	constant from the solution of a linearized equation for the normal component of velocity		
$\mathcal{U}$	Characteristic velocity scale		
$U_l$	laminar flame speed		
$U_s$	Incident shock speed		
$\mathbf{v}$	Velocity of individual fluid particles		
$\mathbf{V}_k$	Diffusion velocity of species $k$		
$V$	Characteristic velocity scale		
$V_A$	Alfvén wave speed		
$v_{\text{rise}}$	Plume rise speed		
$v_{\text{lin}}$	Linear amplitude growth rate		
$v$	Impulse, $v = \int f(t)dt$		
$W$	Mixing layer integral width		
$W_b, W_s$	Mixing layer integral bubble and spike widths		
$\mathbf{w}$	Vorticity, $\mathbf{w} = \nabla \times \mathbf{u}$		
$x$	Spanwise direction Section 2		
$\mathbf{x}$	Position vector		
$x$	Perpendicular direction Section 4.2		
$x_c$	Mixing layer position Section 4.2		
$x_n$	Neutral fraction		
$y$	Spanwise direction Section 2		

## References

- [1] Y. Zhou, Rayleigh–Taylor and Richtmyer–Meshkov instability induced flow, turbulence, and mixing. I, Phys. Rep. 720–722 (2017) 1.
- [2] Y. Zhou, Rayleigh–Taylor and Richtmyer–Meshkov instability induced flow, turbulence, and mixing. II, Phys. Rep. 723–725 (2017b) 1.
- [3] Y. Zhou, T.T. Clark, D.S. Clark, S.G. Glendinning, M.A. Skinner, C.M. Huntington, O.A. Hurricane, A.M. Dimits, B.A. Remington, Turbulent mixing and transition criteria of flows induced by hydrodynamic instabilities, Phys. Plasmas 26 (2019) 080901.
- [4] Lord Rayleigh (John William Strutt), Investigation of the character of the equilibrium of an incompressible heavy fluid of variable density, Lord. Proc. London Math. Soc. 14 (1883) 170.
- [5] G.I. Taylor, The instability of liquid surfaces when accelerated in a direction perpendicular to their planes, I, Proc. R. Soc. Lond. Ser. A Math. Phys. Eng. Sci. 201 (1950) 192.
- [6] R.D. Richtmyer, Taylor instability in shock acceleration of compressible fluids, Commun. Pure Appl. Math. 13 (1960) 297.
- [7] E.E. Meshkov, Instability of the interface of two gases accelerated by a shock wave, Fluid Dyn. 4 (1969) 101.
- [8] G. Jourdan, L. Houas, High-amplitude single-mode perturbation evolution at the Richtmyer–Meshkov instability, Phys. Rev. Lett. 95 (2005) 204502.
- [9] D. Arnett, The role of mixing in astrophysics, Astrophys. J. Suppl. Ser. 127 (2000) 213.
- [10] A. Burrows, Supernova explosions in the universe, Nature 403 (2000) 727.
- [11] S.F. Gull, M.S. Longair, A numerical model of the structure and evolution of young supernova remnants, Mon. Not. R. Astron. Soc. 161 (1973) 47.
- [12] H.T. Janka, Explosion mechanisms of core-collapse supernovae, Annu. Rev. Nucl. Part. Sci. 62 (2012) 407.
- [13] B. Müller, Hydrodynamics of core-collapse supernovae and their progenitors, Living Rev. Comput. Astrophys. 6 (2020) 3.
- [14] T. Sano, K. Nishihara, C. Matsuoka, T. Inoue, Magnetic field amplification associated with the Richtmyer–Meshkov instability, Astrophys. J. 758 (2012) 126.
- [15] S. Atzeni, J. Meyer-ter-Vehn, The Physics of Inertial Fusion: BeamPlasma Interaction, Hydrodynamics, Hot Dense Matter, vol. 125, OUP Oxford, 2004.
- [16] J.D. Lindl, Inertial confinement fusion: the quest for ignition and energy gain using indirect drive, 1998, American Institute of Physics.
- [17] J. Lindl, O. Landen, J. Edwards, E. Moses, N.I.C. Team, Review of the National Ignition Campaign 2009–2012, Phys. Plasmas 21 (2014) 020501.
- [18] J.P. Goedbloed, R. Keppens, Principles of Magnetohydrodynamics, Cambridge University Press, Cambridge, U.K., 2004.
- [19] J.P. Goedbloed, R. Keppens, S. S. Poedts, Advanced Magnetohydrodynamics, Cambridge University Press, 2010.
- [20] G.A. Houseman, P. Molnar, Gravitational (Rayleigh–Taylor) instability of a layer with non-linear viscosity and convective thinning of continental lithosphere, Geophys. J. Int. 128 (1997) 125.
- [21] G. Seropian, A.C. Rust, R.S.J. Sparks, The gravitational stability of lenses in magma mushes: Confined Rayleigh–Taylor instabilities, J. Geophys. Res.: Solid Earth 123 (2018) 3593.
- [22] H. von Helmholtz, On the discontinuous movements of fluids, Monder Königlichen Preussische Akademie der Wissenschaften zu Berlin 23 (1868) 215.
- [23] Lord Kelvin (William Thomson), Hydrokinetic solutions and observations, Phil. Mag. 42 (1871) 362.
- [24] M.S. Plesset, C.G. Whipple, Viscous effects in Rayleigh–Taylor instability, Phys. Fluids 17 (1974) 1.
- [25] K.O. Mikaelian, Exact, approximate, and hybrid treatments of viscous Rayleigh–Taylor and Richtmyer–Meshkov instabilities, Phys. Rev. E 99 (2019) 023112.
- [26] K.O. Mikaelian, Effect of viscosity on Rayleigh–Taylor and Richtmyer–Meshkov instabilities, Phys. Rev. E 47 (1993) 375.
- [27] Y.G. Cao, H.Z. Guo, Z.F. Zhang, Z.H. Sun, W.K. Chow, Effects of viscosity on the growth of Rayleigh–Taylor instability, J. Phys. A 44 (2011) 275501.
- [28] K.O. Mikaelian, Rayleigh–Taylor instability in finite-thickness fluids with viscosity and surface tension, Phys. Rev. E 54 (1996) 3676.

- [29] Y.N. Young, F.E. Ham, Surface tension in incompressible Rayleigh–Taylor mixing flow, *J. Turbul.* 7 (2006) 1.
- [30] S.-I. Sohn, S. Baek, Bubble merger and scaling law of the Rayleigh–Taylor instability with surface tension, *Phys. Lett. A* 381 (2017) 3812.
- [31] H.S. Park, R.E. Rudd, R.M. Cavallo, N.R. Barton, A. Arsenlis, J.L. Belof, K.J.M. Blobaum, B.S. El-dasher, J.N. Florando, C.M. Huntington, B.R. Maddox, Grain-size-independent plastic flow at ultrahigh pressures and strain rates, *Phys. Rev. Lett.* 114 (2015) 065502.
- [32] B.A. Remington, G. Bazan, J. Belak, E. Bringa, J.D. Colvin, M.J. Edwards, S.G. Glendinning, D.H. Kalantar, M. Kumar, B.F. Lasinski, K.T. Lorenz, et al., Materials science under extreme conditions of pressure and strain rate, *Metall. Mater. Trans. A* 35 (2004) 2587.
- [33] G.F. Carnevale, P. Orlandi, Y. Zhou, R.C. Kloosterziel, Rotational suppression of Rayleigh–Taylor instability, *J. Fluid Mech.* 457 (2002) 181.
- [34] M.M. Scase, K.A. Baldwin, R.J. Hill, Rotating Rayleigh–Taylor instability, *Phys. Rev. Fluids* 2 (2017) 024801.
- [35] M.M. Scase, K.A. Baldwin, R.J.A. Hill, Magnetically induced Rayleigh–Taylor instability under rotation: comparison of experimental and theoretical results, *Phys. Rev. E* 102 (2020) 043101.
- [36] M.M. Scase, S. Sengupta, Cylindrical rotating Rayleigh–Taylor instability, *J. Fluid Mech.* 907 (2021) A33.
- [37] L.J. Perkins, D.M. Ho, B.G. Logan, G.B. Zimmerman, M.A. Rhodes, D.J. Strozzia, D.T. Blackfield, S.A. Hawkins, The potential of imposed magnetic fields for enhancing ignition probability and fusion energy yield in indirect-drive inertial confinement fusion, *Phys. Plasmas* 24 (2017) 062708.
- [38] B.A. Remington, R.P. Drake, D.D. Ryutov, Experimental astrophysics with high power lasers and z pinches, *Rev. Modern Phys.* 78 (2006) 755.
- [39] R. Betti, O.A. Hurricane, Inertial-confinement fusion with lasers, *Nat. Phys.* 12 (2016) 435.
- [40] D.J. Tritton, *Physical Fluid Dynamics*, Van Nostrand Reinhold, Wokingham, Berkshire, England, 1977.
- [41] C.L. Navier, Sur les lois des mouvements des fluides, en ayant égard à l'adhésion des molécules, *Annal. Chimie Phys.* 19 (1822) 244.
- [42] C.L. Navier, *Mém. Acad. Sci. Institut France* 6 (1827) 389.
- [43] G.G. Stokes, *Mathematical and Physical Papers By George Gabriel Stokes*, Cambridge University Press, Cambridge, U.K., 1880.
- [44] H. Lamb, *Hydrodynamics*, sixth ed., Dover, New York, 1945.
- [45] L. Euler, Mémoires de l'Académie des sciences de Berlin, 11, 1757, p. 274.
- [46] B.S. Hosseini, S. Turek, M. Möller, C. Palms, Isogeometric Analysis of the Navier–Stokes–Cahn–Hilliard equations with application to incompressible two-phase flows, *J. Comput. Phys.* 348 (2017) 171.
- [47] A.R. Piriz, O.D. Cortazar, J.J. Lopez Cela, N.A. Tahir, The Rayleigh–Taylor instability, *Amer. J. Phys.* 74 (2006) 1095.
- [48] S. Gauthier, Compressible Rayleigh–Taylor turbulent mixing layer between Newtonian miscible fluids, *J. Fluid Mech.* 830 (2017) 211.
- [49] K.A. Meyer, P.J. Blewett, Numerical investigation of the stability of a shock-accelerated interface between two fluids, *Phys. Fluids* 15 (1972) 753.
- [50] M. Vandenboomgaerde, C. Mügler, S. Gauthier, Impulsive model for the Richtmyer–Meshkov instability, *Phys. Rev. E* 58 (1998) 2.
- [51] R. Aure, J.W. Jacobs, Particle image velocimetry study of the shock-induced single mode Richtmyer–Meshkov instability, *Shock Waves* 18 (2008) 161.
- [52] E. Schülein, A.A. Zheltovodov, E.A. Pimonov, M.S. Loginov, Experimental and numerical modeling of the bow shock interaction with pulse-heated air bubbles, *Int. J. Aerosp. Innov.* 2 (2010) 165.
- [53] J.F. Hawley, N.J. Zabusky, Vortex paradigm for shock-accelerated density stratified interfaces, *Phys. Rev. Lett.* 63 (1989) 1241.
- [54] C. Truesdell, *The Kinematics of Vorticity*, Indiana University Press, Bloomington, Indiana, 1954.
- [55] N.J. Zabusky, Vortex paradigm for accelerated inhomogeneous flows: Visiometrics for the Rayleigh–Taylor and Richtmyer–Meshkov environments, *Annu. Rev. Fluid Mech.* 31 (1999) 495.
- [56] O. Schilling, M. Latini, W.S. Don, Physics of reshock and mixing in single-mode Richtmyer–Meshkov instability, *Phys. Rev. E* 76 (2007) 026319.
- [57] O. Schilling, M. Latini, High-order WENO simulations of three-dimensional reshocked Richtmyer–Meshkov instability to late times: dynamics, dependence on initial conditions, and comparisons to experimental data, *Acta Math. Sci.* 30 (2010) 595.
- [58] M. Latini, O. Schilling, A comparison of two-and three-dimensional single-mode reshocked Richtmyer–Meshkov instability growth, *Physica D* 401 (2020) 132201.
- [59] P.G. Drazin, W.H. Reid, *Hydrodynamic Stability*, Cambridge University Press, Cambridge, U.K., 1981.
- [60] P.R. Chapman, J.W. Jacobs, Experiments on the three-dimensional incompressible Richtmyer–Meshkov instability, *Phys. Fluids* 18 (2006) 074101.
- [61] J.P. Wilkinson, J.W. Jacobs, Experimental study of the single-mode three-dimensional Rayleigh–Taylor instability, *Phys. Fluids* 19 (2007) 124102.
- [62] M. Brouillette, The Richtmyer–Meshkov instability, *Annu. Rev. Fluid Mech.* 34 (2002) 445.
- [63] B. Thornber, J. Griffond, O. Poujade, N. Attal, H. Varshochi, P. Bigdelou, P. Ramaprabhu, B. Olson, J. Greenough, Y. Zhou, O. Schilling, K.A. Garside, R.J.R. Williams, C.A. Batha, P.A. Kuchugov, M.E. Ladonkina, V.F. Tishkin, N.V. Zmitrenko, V.B. Rozanov, D.L. Youngs, Late-time growth rate, mixing, and anisotropy in the multimode narrowband Richtmyer–Meshkov instability: The  $\theta$ -group collaboration, *Phys. Fluids* 29 (2017) 105107.
- [64] D.L. Youngs, Rayleigh–Taylor mixing: Direct numerical simulation and implicit large eddy simulation, *Phys. Scr.* 92 (2017) 74006.
- [65] R.E. Duff, F.H. Harlow, C.W. Hirt, Effects of diffusion on interface instability between gases, *Phys. Fluids* 5 (1962) 417.
- [66] M. Latini, O. Schilling, W.S. Don, High-resolution simulations and modeling of reshocked single-mode Richtmyer–Meshkov instability: comparison to experimental data and to amplitude growth model predictions, *Phys. Fluids* 19 (2007) 024104.
- [67] B. Walchli, B. Thornber, Reynolds number effects on the single-mode Richtmyer–Meshkov instability, *Phys. Rev. E* 95 (2017) 013104.
- [68] Y. Zhou, W.H. Cabot, Time-dependent study of anisotropy in Rayleigh–Taylor instability induced turbulent flows with a variety of density ratios, *Phys. Fluids* 31 (2019) 084106.
- [69] G. Dimonte, D.L. Youngs, A. Dimits, S. Weber, M. Marinak, S. Wunsch, C. Garasi, A. Robinson, M.J. Andrews, P. Ramaprabhu, A.C. Calder, A comparative study of the turbulent Rayleigh–Taylor instability using high-resolution three-dimensional numerical simulations: the Alpha-Group collaboration, *Phys. Fluids* 16 (2004) 1668.
- [70] V.K. Tritschler, B.J. Olson, S.K. Lele, S. Hickel, X.Y. Hu, N.A. Adams, On the Richtmyer–Meshkov instability evolving from a deterministic multimode planar interface, *J. Fluid Mech.* 755 (2014) 429.
- [71] P. Ramaprabhu, G. Dimonte, P. Woodward, C. Fryer, G. Rockefeller, K. Muthuraman, P.H. Lin, J. Jayaraj, The late-time dynamics of the single-mode Rayleigh–Taylor instability, *Phys. Fluids* 24 (2012) 074107.
- [72] V.V. Krivets, K. Ferguson, Turbulent mixing, induced by the Richtmyer–Meshkov instability, *AIP Conf. Proc.* 1793 (2017) 150003.
- [73] M.J. Andrews, D.B. Spalding, A simple experiment to investigate two-dimensional mixing by Rayleigh–Taylor instability, *Phys. Fluids A* 2 (1990) 922.
- [74] D.L. Youngs, Numerical simulation of mixing by Rayleigh–Taylor and Richtmyer–Meshkov instabilities, *Laser Part. Beams* 12 (1994) 725.
- [75] A.W. Cook, P.E. Dimotakis, Transition stages of Rayleigh–Taylor instability between miscible fluids, *J. Fluid Mech.* 443 (2001) 69.
- [76] D.L. Youngs, Three-dimensional numerical simulation of turbulent mixing by Rayleigh–Taylor instability, *Phys. Fluids A* 3 (1991) 1312.
- [77] W.H. Cabot, A.W. Cook, Reynolds number effects on Rayleigh–Taylor instability with possible implications for type-Ia supernovae, *Nat. Phys.* 2 (2006) 562.
- [78] A.W. Cook, W. Cabot, P.L. Miller, The mixing transition in Rayleigh–Taylor instability, *J. Fluid Mech.* 511 (2004) 333–362.
- [79] Y. Zhou, W.H. Cabot, B. Thornber, Asymptotic behavior of the mixed mass in Rayleigh–Taylor and Richtmyer–Meshkov instability induced flows, *Phys. Plasmas* 23 (2016) 052712.
- [80] D. Livescu, J.R. Ristorcelli, Buoyancy-driven variable-density turbulence, *J. Fluid Mech.* 591 (2007) 43.
- [81] T. Ma, P.K. Patel, N. Izumi, P.T. Springer, M.H. Key, L.J. Atherton, L.R. Benedetti, D.K. Bradley, D.A. Callahan, P.M. Celliers, C.J. Cerjan, Onset of hydrodynamic mix in high-velocity, highly compressed inertial confinement fusion implosions, *Phys. Rev. Lett.* 111 (2013) 085004.
- [82] T. Poinsot, D. Veynante, *Theoretical and Numerical Combustion*, second ed., R.T. Edwards, Philadelphia, PA, 2005.
- [83] J. Hirschfelder, C.F. Curtiss, R. Byrd, *Molecular Theory of Gases and Liquids*, John Wiley & Sons, New York, 1969.
- [84] P.E. Dimotakis, The mixing transition in turbulent flows, *J. Fluid Mech.* 409 (2000) 69.
- [85] Y. Zhou, H.F. Robey, A.C. Buckingham, Onset of turbulence in accelerated high-Reynolds-number flow, *Phys. Rev. E* 67 (2003) 56305.
- [86] Y. Zhou, B.A. Remington, H.F. Robey, A.W. Cook, S.G. Glendinning, A. Dimits, A.C. Buckingham, G.B. Zimmerman, E.W. Burke, T.A. Peyster, W. Cabot, Progress in understanding turbulent mixing induced by Rayleigh–Taylor and Richtmyer–Meshkov instabilities, *Phys. Plasmas* 10 (2003) 1883.
- [87] H.F. Robey, Y. Zhou, A.C. Buckingham, P. Keiter, B.A. Remington, R.P. Drake, The time scale for the transition to turbulence in a high Reynolds number, accelerated flow, *Phys. Plasmas* 10 (2003) 614.
- [88] R.P. Drake, E.C. Harding, C.C. Kuranz, Approaches to turbulence in high-energy-density experiments, *Phys. Scr. T132* (2008) 014022.

- [89] Y. Zhou, Unification and extension of the similarity scaling criteria and mixing transition for studying astrophysics using high energy density laboratory experiments or numerical simulations, *Phys. Plasmas* 14 (2007) 82701.
- [90] M.M. Mansoor, S.M. Dalton, A.A. Martinez, T. Desjardins, J.J. Charonko, K.P. Prestridge, The effect of initial conditions on mixing transition of the Richtmyer–Meshkov instability, *J. Fluid Mech.* 904 (2020) A3.
- [91] H.A. Rose, P.L. Sulem, Fully developed turbulence and statistical mechanics, *J. Physique* 39 (1978) 441.
- [92] D.L. Youngs, Effect of initial conditions on self-similar turbulent mixing, in: Proceedings of the 9th International Workshop on the Physics of Compressible Turbulent Mixing, 2004.
- [93] P. Ramaprabhu, M.J. Andrews, On the initialization of Rayleigh–Taylor simulations, *Phys. Fluids* 16 (2004) L59.
- [94] A. Banerjee, M.J. Andrews, 3D simulations to investigate initial condition effects on the growth of Rayleigh–Taylor mixing, *Int. J. Heat Mass Transfer* 52 (2009) 3906.
- [95] B. Thornber, D. Drikakis, D.L. Youngs, R.J.R. Williams, The influence of initial conditions on turbulent mixing due to Richtmyer–Meshkov instability, *J. Fluid Mech.* 654 (2010) 99.
- [96] N.N. Anuchina, V.I. Volkov, V.A. Gordeychuk, N.S. Es'kov, O.S. Iiyutina, O.M. Kozyrev, 3D numerical simulation of Rayleigh–Taylor instability using MAH-3 code, *Laser Part. Beams* 18 (2000) 175.
- [97] G. Dimonte, P. Ramaprabhu, D.L. Youngs, M.J. Andrews, R. Rosner, Recent advances in the turbulent Rayleigh–Taylor instability, *Phys. Plasmas* 12 (2005) 056301.
- [98] N.A. Inogamov, A.M. Oparin, A.Y. Dem'yanov, L.N. Dembitskii, V.A. Khokhlov, On stochastic mixing caused by the Rayleigh–Taylor instability, *J. Exp. Theor. Phys.* 92 (2001) 715.
- [99] P.F. Linden, J.M. Redondo, D.L. Youngs, Molecular mixing in Rayleigh–Taylor instability, *J. Fluid Mech.* 265 (1994) 97.
- [100] D.L. Youngs, Numerical simulation of turbulent mixing by Rayleigh–Taylor instability, *Physica D* 12 (1984) 32.
- [101] D.L. Youngs, Rayleigh–Taylor instability: numerical simulation and experiment, *Plasma Phys. Control. Fusion* 34 (1992) 2071.
- [102] T.T. Clark, Y. Zhou, Self-similarity of two flows induced by instabilities, *Phys. Rev. E* 68 (2003) 066305.
- [103] T.T. Clark, Y. Zhou, Growth rate exponents of Richtmyer–Meshkov mixing layers, *J. Appl. Mech.* 73 (2006) 461.
- [104] J.R. Ristorcelli, T.T. Clark, Rayleigh–Taylor turbulence: self-similar analysis and direct numerical simulations, *J. Fluid Mech.* 507 (2004) 213.
- [105] G. Dimonte, Dependence of turbulent Rayleigh–Taylor instability on initial perturbations, *Phys. Rev. E* 69 (2004) 056305.
- [106] S.B. Dalziel, P.F. Linden, D.L. Youngs, Self-similarity and internal structure of turbulence induced by Rayleigh–Taylor instability, *J. Fluid Mech.* 399 (1999) 48.
- [107] P. Ramaprabhu, G. Dimonte, M.J. Andrews, A numerical study of the influence of initial perturbations on the turbulent Rayleigh–Taylor instability, *J. Fluid Mech.* 536 (2005) 285.
- [108] U. Alon, J. Hecht, D. Ofer, D. Shvarts, Power laws and similarity of Rayleigh–Taylor and Richtmyer–Meshkov mixing fronts at all density ratios, *Phys. Rev. Lett.* 74 (1995) 534.
- [109] B.L. Cheng, J. Glimm, D.H. Sharp, A three-dimensional renormalization group bubble merger model for Rayleigh–Taylor mixing, *Chaos* 12 (2002) 267.
- [110] J. Glimm, X.L. Li, Validation of the sharp-wheeler bubble merger model from experimental and computational data, *Phys. Fluids* 31 (1988) 2077.
- [111] J. Glimm, X.L. Li, R. Menikoff, D.H. Sharp, Q. Zhang, A numerical study of bubble interactions in Rayleigh–Taylor instability for compressible fluids, *Phys. Fluids A* 2 (1990) 2046.
- [112] J. Glimm, D.H. Sharp, Chaotic mixing as a renormalization-group fixed-point, *Phys. Rev. Lett.* 64 (1990) 2137.
- [113] D. Oron, L. Arazi, D. Kartoon, A. Rikanati, U. Alon, D. Shvarts, Dimensionality dependence of the Rayleigh–Taylor and Richtmyer–Meshkov instability late-time scaling laws, *Phys. Plasmas* 8 (2001) 2883.
- [114] D. Shvarts, U. Alon, D. Ofer, R.L. McCrory, C.P. Verdon, Nonlinear evolution of multimode Rayleigh–Taylor instability in 2 and 3 dimensions, *Phys. Plasmas* 2 (1995) 2465.
- [115] E. George, J. Glimm, X.L. Li, A. Marchese, Z.L. Xu, A comparison of experimental, theoretical, and numerical simulation Rayleigh–Taylor mixing rates, *Proc. Natl. Acad. Sci. USA* 99 (2002) 2587.
- [116] Y. Elbaz, D. Shvarts, Modal model mean field self-similar solutions to the asymptotic evolution of Rayleigh–Taylor and Richtmyer–Meshkov instabilities and its dependence on the initial conditions, *Phys. Plasmas* 25 (2018) 062126.
- [117] G.C. Burton, Study of ultrahigh Atwood-number Rayleigh–Taylor mixing dynamics using the nonlinear large-eddy simulation method, *Phys. Fluids* 23 (2011) 045106.
- [118] W. Cabot, Y. Zhou, Statistical measurements of scaling and anisotropy of turbulent flows induced by Rayleigh–Taylor instability, *Phys. Fluids* 25 (2013) 015107.
- [119] D. Livescu, Numerical simulations of two-fluid turbulent mixing at large density ratios and applications to the Rayleigh–Taylor instability, *Phil. Trans. Ser. A* 371 (2003) 20120185.
- [120] D.L. Youngs, The density ratio dependence of self-similar Rayleigh–Taylor mixing, *Phil. Trans. R. Soc. A* 371 (2013) 20120173.
- [121] I. Yilmaz, Analysis of Rayleigh–Taylor instability at high Atwood numbers using fully implicit, non-dissipative, energy-conserving large eddy simulation algorithm, *Phys. Fluids* 32 (2020) 054101.
- [122] J. Glimm, D.H. Sharp, T. Kaman, H. Lim, New directions for Rayleigh–Taylor mixing, *Phil. Trans. R. Soc. A* 371 (2013) 20120183.
- [123] O. Soulard, F. Guillois, J. Griffond, V. Sabelnikov, S. Simoëns, Permanence of large eddies in Richtmyer–Meshkov turbulence with a small Atwood number, *Phys. Rev. Fluids* 3 (2018) 104603.
- [124] G. Dimonte, M. Schneider, Density ratio dependence of Rayleigh–Taylor mixing for sustained and impulsive acceleration histories, *Phys. Fluids* 12 (2000) 304.
- [125] D.L. Youngs, B. Thornber, Buoyancy-drag modelling of bubble and spike distances for single-shock Richtmyer–Meshkov mixing, *Physica D* 410 (2020) 132517.
- [126] A. Aspden, N. Nikiforakis, S. Dalziel, J.B. Bell, Analysis of implicit les methods, *Commun. Appl. Math. Comput. Sci.* 3 (2008) 103.
- [127] Y. Zhou, F.F. Grinstein, A.J. Wachtor, B.M. Haines, Estimating the effective Reynolds number in implicit large-eddy simulation, *Phys. Rev. E* 89 (2014) 013303.
- [128] Y. Zhou, B. Thornber, A comparison of three approaches to compute the effective Reynolds number of the implicit large-eddy simulations, *J. Fluids Eng.* 138 (2016) 70905.
- [129] F.S. Schranner, J.A. Domaradzki, S. Hickel, N.A. Adams, Assessing the numerical dissipation rate and viscosity in numerical simulations of fluid flows, *Comput. & Fluids* 114 (2015) 84.
- [130] M. Chertkov, V. Lebedev, N. Vladimirova, Reactive Rayleigh–Taylor turbulence, *J. Fluid Mech.* 633 (2009) 1.
- [131] W.J. Black, N.A. Denissen, J.A. McFarland, Evaporation effects in shock-driven multiphase instabilities, *J. Fluids Eng.* 139 (2017) 071204.
- [132] D. Bond, V. Wheatley, R. Samtaney, D.I. Pullin, Richtmyer–Meshkov instability of a thermal interface in a two-fluid plasma, *J. Fluid Mech.* 833 (2017) 332.
- [133] L. Biferale, F. Mantovani, M. Sbragaglia, A. Scagliarini, F. Toschi, R. Tripiccione, High resolution numerical study of Rayleigh–Taylor turbulence using a thermal lattice Boltzmann scheme, *Phys. Fluids* 22 (2010) 115112.
- [134] A. Banerjee, Rayleigh–Taylor Instability: a status review of experimental designs and measurement diagnostics, *J. Fluids Eng.* 142 (2020) 120801.
- [135] M.J. Andrews, S.B. Dalziel, Small atwood number Rayleigh–Taylor experiments, *Philos. Trans. R. Soc. A* 368 (2010) 1663.
- [136] O. Schilling, Progress on understanding Rayleigh–Taylor flow and mixing using synergy between simulation, modeling, and experiment, *J. Fluids Eng.* 142 (2020) 120802.
- [137] K. Prestridge, Experimental adventures in variable-density mixing, *Phys. Rev. Fluids* 3 (2018) 110501.
- [138] F. Williams, Combustion Theory, Perseus, Cambridge, MA, 1985.
- [139] B. Larrouture, How to Preserve the Mass Fractions Positivity when Computing Compressible Multi-Component Flows, INRIA Rapports de Recherche No. 1080, 1989.
- [140] R. Abgrall, How to prevent pressure oscillations in multicomponent flow calculations: a quasi conservative approach, *J. Comput. Phys.* 125 (1996) 150.
- [141] G. Billet, V. Giovangigli, G. De Gassowski, Impact of volume viscosity on a shock-hydrogen-bubble interaction, *Combust. Theory Model.* 12 (2008) 221.
- [142] J. Massoni, R. Saurel, B. Nkonga, R. Abgrall, Proposition de méthodes et modèles eulériens pour les problèmes à interfaces entre fluides compressibles en présence de transfert de chaleur: Some models and Eulerian methods for interface problems between compressible fluids with heat transfer, *Int. J. Heat Mass Transfer* 45 (2002) 1287.
- [143] G. Allaire, S. Clerc, S. Kokh, A five-equation model for the simulation of interfaces between compressible fluids, *J. Comput. Phys.* 181 (2002) 577.
- [144] B. Thornber, M. Groom, D. Youngs, A five-equation model for the simulation of miscible and viscous compressible fluids, *J. Comput. Phys.* 372 (2018) 256.
- [145] E. Johnsen, F. Ham, Preventing numerical errors generated by interface-capturing schemes in compressible multi-material flows, *J. Comput. Phys.* 231 (2012) 5705–5717.
- [146] R.J.R. Williams, Fully-conservative contact-capturing schemes for multi-material advection, *J. Comput. Phys.* 398 (2019) 108809.
- [147] L.D. Landau, E.M. Lifshitz, Fluid Mechanics, second ed., Pergamon Press, Oxford, U.K., 1987.
- [148] B.J. Olson, J. Greenough, Large eddy simulation requirements for the richtmyer–meshkov instability, *Phys. Fluids* 26 (2014) 044103.
- [149] T.J. Rehagen, J.A. Greenough, B.J. Olson, A validation study of the compressible Rayleigh–Taylor instability comparing the ares and miranda codes, *J. Fluids Eng.* 139 (2017) 061204.

- [150] D.J. Hill, C. Pantano, D.I. Pullin, Large-eddy simulation and multiscale modelling of a Richtmyer–Meshkov instability with reshock, *J. Fluid Mech.* 557 (2006) 29.
- [151] E. Johnsen, J. Larsson, A.V. Bhagatwala, W.H. Cabot, P. Moin, B.J. Olson, P.S. Rawat, S.K. Shankar, B. Sjögren, H.C. Yee, X. Zhong, Assessment of high-resolution methods for numerical simulations of compressible turbulence with shock waves, *J. Comput. Phys.* 229 (2010) 1213.
- [152] X. Liu, E. George, W. Bo, J. Glimm, Turbulent mixing with physical mass diffusion, *Phys. Rev. E* 73 (2006) 056301.
- [153] J. Glimm, D.H. Sharp, H. Lim, R. Kaufman, W. Hu, Euler equation existence, non-uniqueness and mesh converged statistics, *Phil. Trans. R. Soc. A* 373 (2015) 20140282.
- [154] N.J. Mueschke, M.J. Andrews, Experimental characterization of initial conditions and spatio-temporal evolution of a small-Atwood-number Rayleigh–Taylor mixing layer, 2006, <http://dx.doi.org/10.1017/S0022112006001959>, 567.
- [155] T. Poinsot, Boundary conditions for direct simulations of compressible viscous flows, *J. Comput. Phys.* 101 (1992) 104.
- [156] D. Sandoval, The dynamics of variable-density turbulence, (Ph.D. thesis), University of Washington, 1995.
- [157] D. Livescu, Turbulence with large thermal and compositional density variations, *Annu. Rev. Fluid Mech.* 52 (2020) 309.
- [158] H.C. Ku, T.D. Taylor, R.S. Hirsh, Pseudospectral methods for solution of the incompressible Navier–Stokes equations, *Comput. & Fluids* 15 (1987) 195.
- [159] D. Chung, D.I. Pullin, Direct numerical simulation and large-eddy simulation of stationary buoyancy-driven turbulence, *J. Fluid Mech.* 643 (2010) 279.
- [160] I. Gat, G. Matheou, D. Chung, P.E. Dimotakis, Incompressible variable-density turbulence in an external acceleration field, *J. Fluid Mech.* 827 (2017) 506.
- [161] D. Livescu, T. Wei, M.R. Petersen, Direct numerical simulations of Rayleigh–Taylor instability, *J. Phys. Conf. Ser.* 318 (2011) 082007.
- [162] J.R. Baltzer, D. Livescu, Low-speed turbulent shear-driven mixing layers with large thermal and compositional density variations, in: D. Livescu, F. Battaglia, P. Givi (Eds.), *Modeling and Simulation of Turbulent Mixing and Reaction: For Power, Energy, and Flight*, Springer Nature, Singapore, 2019.
- [163] M.S. Dodd, A. Ferrante, A fast pressure-correction method for incompressible two-fluid flows, *J. Comput. Phys.* 273 (2014) 416.
- [164] J.L. Guermond, A. Salgado, A splitting method for incompressible flows with variable density based on a pressure Poisson equation, *J. Comput. Phys.* 228 (2009) 2834.
- [165] G.K. Batchelor, V.M. Canuto, J.R. Chasnov, Homogeneous buoyancy-generated turbulence, *J. Fluid Mech.* 235 (1992) 349.
- [166] F. Bertolotti, T. Herbert, P.R. Spalart, Linear and nonlinear stability of the blasius boundary layer, *J. Fluid Mech.* 242 (1992) 441.
- [167] N.J. Mueschke, O. Schilling, Investigation of Rayleigh–Taylor turbulence and mixing using direct numerical simulation with experimentally measured initial conditions. I. Comparison to experimental data, *Phys. Fluids* 21 (2009) 014106.
- [168] N.J. Mueschke, O. Schilling, Investigation of Rayleigh–Taylor turbulence and mixing using direct numerical simulation with experimentally measured initial conditions. II. Dynamics of transitional flow and mixing statistics, *Phys. Fluids* 21 (2009) 014107.
- [169] J. Anderson, *Fundamentals of Aerodynamics*, fourth ed., McGraw- Hill, NY, 2007.
- [170] T. Oggian, D. Drikakis, D.L. Youngs, R.J.R. Williams, Computing multi-mode shock-induced compressible turbulent mixing at late times, *J. Fluid Mech.* 779 (2015) 411.
- [171] B. Thornber, D. Drikakis, D.L. Youngs, R.J.R. Williams, Growth of a Richtmyer–Meshkov turbulent layer after reshock, *Phys. Fluids* 23 (2011) 95107.
- [172] G. Boffetta, A. Mazzino, Incompressible Rayleigh–Taylor turbulence, *Annu. Rev. Fluid Mech.* 49 (2017) 119.
- [173] R.S. Rogallo, Numerical experiments in homogeneous turbulence, in: *NASA Tech. Rep.* 81835, 1981.
- [174] P. Moin, K. Mahesh, Direct numerical simulation: a tool in turbulence research, *Annu. Rev. Fluid Mech.* 30 (1998) 1, <http://dx.doi.org/10.1146/annurev.fluid.30.1.539>.
- [175] Y.N. Young, A. Tufo, R. Dubey, H. Rosner, On the miscible Rayleigh–Taylor instability: Two and three dimensions, *J. Fluid Mech.* 447 (2001) 377–408.
- [176] N. Vladimirova, M. Chertkov, Self-similarity and universality in Rayleigh–Taylor, Boussinesq turbulence, *Phys. Fluids* 21 (2009) 015102.
- [177] G. Boffetta, A. Mazzino, S. Musacchio, L. Vozella, Statistics of mixing in three-dimensional Rayleigh–Taylor turbulence at low Atwood number and Prandtl number one, *Phys. Fluids* 22 (2010) 035109.
- [178] T. Matsumoto, Anomalous scaling of three-dimensional Rayleigh–Taylor turbulence, *Phys. Rev. E* 79 (2009) 055301.
- [179] N. Schneider, S. Gauthier, Vorticity and mixing in Rayleigh–Taylor Boussinesq turbulence, *J. Fluid Mech.* 802 (2016) 395.
- [180] D.D. Gray, A. Giorgini, The validity of the Boussinesq approximation for liquids and gases, *Int. J. Heat Mass Transfer* 19 (1976) 545.
- [181] K.O. Mikaelian, Boussinesq approximation for Rayleigh–Taylor and Richtmyer–Meshkov instabilities, *Phys. Fluids* 26 (2014) 054103.
- [182] J.A. Sethian, P. Smereka, Level set methods for fluid interfaces, *Annu. Rev. Fluid Mech.* 35 (2003) 341.
- [183] J. Glimm, J.W. Grove, X.L. Li, W. Oh, D.H. Sharp, A critical analysis of Rayleigh–Taylor growth rates, *J. Comput. Phys.* 169 (2001) 652.
- [184] D. Gueyffier, J. Li, A. Nadim, R. Scardovelli, S. Zaleski, Volume-of-fluid interface tracking with smoothed surface stress methods for three-dimensional flows, *J. Comput. Phys.* 152 (1999) 423.
- [185] J. Du, B. Fix, J. Glimm, X. Jia, X. Li, Y. Li, L. Wu, A simple package for front tracking, *J. Comput. Phys.* 213 (2006) 613.
- [186] R. Scardovelli, S. Zaleski, Direct numerical simulation of free-surface and interfacial flow, *Annu. Rev. Fluid Mech.* 31 (1999) 567.
- [187] E. George, J. Glimm, X. Li, Y. Li, X. Liu, Influence of scale-breaking phenomena on turbulent mixing rates, *Phys. Rev. E* 73 (2006) 016304.
- [188] A. Shimony, G. Malamud, D. Shvarts, Density ratio and entrainment effects on asymptotic Rayleigh–Taylor instability, *J. Fluids Eng.* 140 (2018) 050906.
- [189] P.A. Davidson, *Turbulence – An Introduction for Scientists and Engineers*, Oxford University Press, Oxford, U.K, 2004.
- [190] B. Thornber, Impact of domain size and statistical errors in simulations of homogeneous decaying turbulence and the Richtmyer–Meshkov instability, *Phys. Fluids* 28 (2016) 045106.
- [191] F. Sherman, A low-density wind-tunnel study of shock-wave structure and relaxation phenomena in gases, *Tech. Note 3298*, National Advisory Committee for Aeronautics, Washington D.C, 1955.
- [192] L.G. Margolin, J.M. Reisner, Fully compressible solutions for early stage Richtmyer–Meshkov instability, *Comput. & Fluids* 151 (2017) 46–57.
- [193] J. Ryu, D. Livescu, Turbulence structure behind the shock in canonical shock-vortical turbulence interaction, *J. Fluid Mech.* 756 (2014) R1.
- [194] M. Groom, B. Thornber, Direct numerical simulation of the multimode narrowband Richtmyer–Meshkov instability, *Comput. & Fluids* 194 (2019) 104309.
- [195] Y. Zhou, Renormalization group theory for fluid and plasma turbulence, *Phys. Rep.* 488 (2010) 1.
- [196] S.B. Pope, Ten questions concerning the large-eddy simulation of turbulent flows, *New J. Phys.* 6 (2004) 35.
- [197] S.B. Pope, *Turbulent Flows*, Cambridge University Press, Cambridge, U.K, 2000.
- [198] F.K. Chow, P. Moin, A further study of numerical errors in large-eddy simulations, *J. Comput. Phys.* 184 (2003) 366.
- [199] B. Kosović, D.I. Pullin, R. Samtaney, Subgrid-scale modeling for large-eddy simulations of compressible turbulence, *Phys. Fluids* 14 (2002) 1511.
- [200] A.W. Cook, Artificial fluid properties for large-eddy simulation of compressible turbulent mixing, *Phys. Fluids* 19 (2007) 055103.
- [201] M. Lesieur, O. Metais, New trends in large-eddy simulations of turbulence, *Annu. Rev. Fluid Mech.* 28 (1996) 45.
- [202] C. Meneveau, J. Katz, Scale-invariance and turbulence models for large-eddy simulation, *Annu. Rev. Fluid Mech.* 32 (2000) 1.
- [203] P. Sagaut, *Large Eddy Simulation for Incompressible Flows: An Introduction*, Springer Science & Business Media, 2006.
- [204] N.O. Braun, D.I. Pullin, D.I. Meiron, Large eddy simulation investigation of the canonical shock-turbulence interaction, *J. Fluid Mech.* 858 (2019) 500.
- [205] B. Vreman, B. Geurts, H. Kuerten, Subgrid-modelling in LES of compressible flow, *Appl. Sci. Res.* 54 (1995) 191.
- [206] E. Garnier, P. Sagaut, M. Deville, Large eddy simulation of shock/homogeneous turbulence interaction, *Comput. Fluids* 31 (2002) 245.
- [207] G.C. Burton, W.J. Dahm, Multifractal subgrid-scale modeling for large-eddy simulation. I. Model development and a priori testing, *Phys. Fluids* 17 (2005) 075111.
- [208] A. Misra, D.I. Pullin, A vortex-based subgrid stress model for large-eddy simulation, *Phys. Fluids* 9 (1997) 2443.
- [209] D.I. Pullin, P.G. Saffman, Reynolds Stresses and one-dimensional spectra for a vortex model of homogeneous anisotropic turbulence, *Phys. Fluids* 6 (1994) 1787.
- [210] J.P. Boris, F.F. Grinstein, E.S. Oran, R.L. Kolbe, New insights into large eddy simulation, *Fluid Dyn. Res.* 10 (1992) 199.
- [211] D. Drikakis, Advances in turbulent flow computations using high-resolution methods, *Prog. Aerosp. Sci.* 39 (2003) 405.
- [212] F.F. Grinstein, L.G. Margolin, W.J. Rider (Eds.), *Implicit Large Eddy Simulation: Computing Turbulent Fluid Dynamics*, Cambridge University Press, Cambridge, U.K.
- [213] B. Thornber, J. Griffond, P. Bigdelou, I. Boureima, P. Ramaprabhu, O. Schilling, R.J.R. Williams, Turbulent transport and mixing in the multi-mode narrowband Richtmyer–Meshkov instability, *Phys. Fluids* 31 (2019) 096105.

- [214] B. Thornber, R.W. Bilger, A.R. Masri, E.R. Hawkes, An algorithm for LES of premixed compressible flows using the conditional moment closure model, *J. Comput. Phys.* 230 (2011) 7687.
- [215] S. Shanmuganathan, D.L. Youngs, J. Griffond, B. Thornber, R.J.R. Williams, Accuracy of high-order density-based compressible methods in low Mach vortical flows, *Internat. J. Numer. Methods Fluids* 74 (2014) 335.
- [216] A. Garcia-Uceda Juarez, A. Raimo, E. Shapiro, B. Thornber, Steady turbulent flow computations using a low Mach fully compressible scheme, *AIAA J.* 52 (2014) 2559.
- [217] V.F. Tishkin, V.V. Nikishin, I.V. Popov, A.P. Favorski, Finite difference schemes of three-dimensional gas dynamics for the study of Richtmyer–Meshkov instability, *Matemat. Modelirovanie* 7 (1995) 15.
- [218] B. Thornber, D. Drikakis, R.J.R. Williams, D.L. Youngs, On entropy generation and dissipation of kinetic energy in high-resolution shock-capturing schemes, *J. Comput. Phys.* 227 (2008) 4853.
- [219] B. Thornber, A. Mosedale, D. Drikakis, D.L. Youngs, R.J.R. Williams, An improved reconstruction method for compressible flows with low Mach number features, *J. Comput. Phys.* 227 (2008) 4873.
- [220] M. Probyn, B. Thornber, D. Drikakis, D.L. Youngs, R.J.R. Williams, An investigation into nonlinear growth rate of two-dimensional and three-dimensional single-mode Richtmyer–Meshkov instability using an arbitrary-Lagrangian–Eulerian algorithm, *J. Fluids Eng.* 136 (2014) 91208.
- [221] H.S. Park, K.T. Lorenz, R.M. Cavallo, S.M. Pollaine, S.T. Prisbrey, R.E. Rudd, R.C. Becker, J.V. Bernier, B.A. Remington, Viscous Rayleigh–Taylor instability experiments at high pressure and strain rate, *Phys. Rev. Lett.* 104 (2010) 135504.
- [222] R.L. Coble, A model for boundary diffusion controlled creep in polycrystalline materials, *J. Appl. Phys.* 34 (1963) 1679.
- [223] S. Ellis, B. Stöckhert, Elevated stresses and creep rates beneath the brittle–ductile transition caused by seismic faulting in the upper crust, *J. Geophys. Res.: Solid Earth* 109 (2004) B05407.
- [224] T.J. Marrow, J.Y. Buffiere, P.J. Withers, G. Johnson, D. Engelberg, High resolution X-ray tomography of short fatigue crack nucleation in austempered ductile cast iron, *Int. J. Fatigue* 26 (2004) 717.
- [225] C.E. Renshaw, E.M. Schulson, Universal behaviour in compressive failure of brittle materials, *Nature* 412 (2001) 897.
- [226] H.S. Park, B.A. Remington, R.C. Becker, J.V. Bernier, R.M. Cavallo, K.T. Lorenz, S.M. Pollaine, S.T. Prisbrey, R.E. Rudd, N.R. Barton, Strong stabilization of the Rayleigh–Taylor instability by material strength at megabar pressures, *Phys. Plasmas* 17 (2010) 056314.
- [227] J.F. Barnes, P.J. Blewett, R.G. McQueen, K.A. Meyer, D. Venable, Taylor instability in solids, *J. Appl. Phys.* 45 (1974) 727.
- [228] J. Edwards, K.T. Lorenz, B.A. Remington, S. Pollaine, J. Colvin, D. Braun, B.F. Lasinski, D. Reisman, J.M. McNaney, J.A. Greenough, R. Wallace, Laser-driven plasma loader for shockless compression and acceleration of samples in the solid state, *Phys. Rev. Lett.* 92 (2004) 075002.
- [229] A. Krygier, P.D. Powell, J.M. McNaney, C.M. Huntington, S.T. Prisbrey, B.A. Remington, R.E. Rudd, D.C. Swift, C.E. Wehrenberg, A. Arsenlis, H.S. Park, Extreme hardening of Pb at high pressure and strain rate, *Phys. Rev. Lett.* 123 (2019) 205701.
- [230] G.B. Rybicki, A.P. Lightman, *Radiative Processes in Astrophysics*, John Wiley & Sons, 2008.
- [231] D.J. Steinberg, S.G. Cochran, M.W. Guinan, A constitutive model for metals applicable at high-strain rate, *J. Appl. Phys.* 51 (1980) 1498.
- [232] B. Hopkinson, A method of measuring the pressure produced in the detonation of high explosives or by the impact of bullets, *Philos. Trans. R. Soc. Lond. Ser. A* 213 (1914) 437.
- [233] H. Kolsky, An investigation of the mechanical properties of materials at very high rates of loading, *Proc. Phys. Soc. Lond. B* 62 (II-B) (1949) 676.
- [234] C. Meade, R. Jeanloz, Yield strength of mgo to 40 GPa, *J. Geophys. Res.: Solid Earth* 93 (1988) 3261.
- [235] D.J. Steinberg, C.M. Lund, A constitutive model for strain rates from  $10^{-4}$  to  $10^6 \text{ s}^{-1}$ , *J. Appl. Phys.* 65 (1989) 1528.
- [236] K.G. Hoge, A.K. Mukherjee, The temperature and strain rate dependence of the flow stress of tantalum, *J. Mater. Sci.* 12 (1977) 1666.
- [237] J.E. Dorn, S. Rajnak, Nucleation of kink pairs and the Peierls' mechanism of plastic deformation, *Trans. Metall. Soc. AIME* 230 (1964) 1052.
- [238] P. Guyot, J.E. Dorn, A critical review of the Peierls mechanism, *Can. J. Phys.* 45 (1967) 983.
- [239] D. Klahn, A.K. Mukherhee, J.E. Dorn, Proc. 2nd Intl. Conf. on Strength of Metals and Alloys, Pacific Grove, CA, vol. 3, 1970, p. 951.
- [240] D.L. Preston, D.L. Tonks, D.C. Wallace, Model of plastic deformation for extreme loading conditions, *J. Appl. Phys.* 93 (2003) 211.
- [241] M.W. Schraad, The TEPLA framework and the physics, mathematics, and numerics of damage modeling (no. LA-ur-11-05846; LA-ur-11-5846), 2011, Los Alamos National Lab.(LANL), Los Alamos, NM (United States).
- [242] N.R. Barton, J.V. Bernier, R. Becker, A. Arsenlis, R. Cavallo, J. Marian, M. Rhee, H.S. Park, B.A. Remington, R.T. Olson, A multiscale strength model for extreme loading conditions, *J. Appl. Phys.* 109 (2011) 073501.
- [243] N.R. Barton, M. Rhee, A multiscale strength model for tantalum over an extended range of strain rates, *J. Appl. Phys.* 114 (2013) 123507.
- [244] J.L. Belof, R.M. Cavallo, R.T. Olson, R.S. King, G.T. Gray III, D. Holtkamp, S.R. Chen, R.E. Rudd, N. Barton, A. Arsenlis, B. Remington, Rayleigh–Taylor strength experiments of the pressure-induced  $\alpha \rightarrow \epsilon \rightarrow \alpha'$  phase transition in iron, *AIP Conf. Proc.* 1426 (2012) 1521.
- [245] G.S. Collins, H.J. Melosh, R.A. Marcus, Earth impact effects program: A web-based computer program for calculating the regional environmental consequences of a meteoroid impact on earth, *Meteorit. Planet. Sci.* 40 (2005) 817.
- [246] L. Bourouiba, E. Dehandschoewercker, J.W. Bush, Violent expiratory events: on coughing and sneezing, *J. Fluid Mech.* 745 (2014) 537.
- [247] B.E. Scharfman, A.H. Techet, J.W.M. Bush, L. Bourouiba, Visualization of sneeze ejecta: steps of fluid fragmentation leading to respiratory droplets, *Exp. Fluids* 57 (2016) 24.
- [248] P. Bahl, C. Doolan, C. de Silva, A.A. Chughtai, L. Bourouiba, C.R. MacIntyre, Airborne or droplet precautions for health workers treating COVID-19? *J. Infect. Dis.* (2020) jiaa189, <https://doi.org/10.1093/infdis/jiaa189>.
- [249] L. Bourouiba, Turbulent gas clouds and respiratory pathogen emissions: potential implications for reducing transmission of COVID-19, *JAMA: J. Am. Med. Assoc.* 323 (2020) 1837.
- [250] D.K. Chu, E.A. Akl, S. Duda, K. Solo, S. Yaacoub, H.J. Schünemann, A. El-harakeh, A. Bognanni, T. Lotfi, M. Loeb, A. Hajizadeh, Physical distancing, face masks, and eye protection to prevent person-to-person transmission of SARS-CoV-2 and COVID-19: a systematic review and meta-analysis, *Lancet* 395 (2020) 1973.
- [251] L. Bourouiba, Anatomy of a Sneeze, Howard Hughes Medical Institute Image of The Week, 2016, <https://www.biointeractive.org/classroom-resources/anatomy-sneeze>.
- [252] L. Bourouiba, A sneeze, *New England J. Med.* 357 (8) (2016) e15.
- [253] S. Balachandar, Z. Zaleski, A. Soldati, G. Ahmadi, L. Bourouiba, Host-to-host airborne transmission as a multiphase flow problem for science-based social distance guidelines, *Int. J. Multiphase Flow* 4 (2020) 103439, <https://doi.org/10.1016/j.ijmultiphaseflow.2020.103439>. Epub ahead of print. PMID: PMC7471834.
- [254] J. Meaburn, P. Boumis, J.R. Walsh, W. Steffen, A.J. Holloway, R.J.R. Williams, M. Bryce, Highly supersonic motions within the outer features of the  $\eta$  Carinae nebulosity, *Mon. Not. R. Astron. Soc.* 282 (1996) 1313.
- [255] R.J.R. Williams, Ejecta sources and scalings, *AIP Conf. Proc.* 1979 (2018) 080015.
- [256] P. Hartigan, J.M. Foster, B.H. Wilde, R.F. Coker, P.A. Rosen, J.F. Hansen, B.E. Blue, R.J.R. Williams, R. Carver, A. Frank, Laboratory experiments, numerical simulations, and astronomical observations of deflected supersonic jets: Application to HH 110, *Astrophys. J.* 705 (2009) 1073.
- [257] W.T. Buttler, R.J. Williams, F.M. Najjar (Eds.), The special issue on ejecta, *J. Dyn. Behav. Mater.* 3 (2017) 151–345.
- [258] W.T. Buttler, R.J. Williams, F.M. Najjar, Foreword to the special issue on ejecta, *J. Dyn. Behav. Mater.* 3 (2017) 151.
- [259] P.A. Rigg, W.W. Anderson, R.T. Olson, W.T. Buttler, R.S. Hixson, Investigation of ejecta production in tin using plate impact experiments, *AIP Conf. Proc.* 845 (2006) 1283.
- [260] D.J. Bell, N.R. Routley, J.C.F. Millett, G. Whiteman, M.A. Collinson, P.T. Keightley, Investigation of ejecta production from tin at an elevated temperature and the eutectic alloy Lead–Bismuth, *J. Dyn. Behav. Mater.* 3 (2017) 208.
- [261] W.T. Buttler, D.M. Oró, D.L. Preston, K.O. Mikaelian, F.J. Cherne, R.S. Hixson, F.G. Mariam, C. Morris, J.B. Stone, G. Terrones, D. Tupa, Unstable Richtmyer–Meshkov growth of solid and liquid metals in vacuum, *J. Fluid Mech.* 703 (2012) 60.
- [262] A.L. Mikhailov, V.A. Ogorodnikov, V.S. Sasik, V.A. Raevskii, A.I. Lebedev, D.E. Zotov, S.V. Erunov, M.A. Syrunin, V.D. Sadunov, N.V. Nevmerzhitskii, S.A. Lobastov, Experimental–calculation simulation of the ejection of particles from a shock-loaded surface, *J. Exp. Theor. Phys.* 118 (2014) 785.
- [263] J.M. Foster, B.H. Wilde, P.A. Rosen, R.J.R. Williams, B.E. Blue, R.F. Coker, R.P. Drake, A. Frank, P.A. Keiter, A.M. Khokhlov, J.P. Knauer, High-energy-density laboratory astrophysics studies of jets and bow shocks, *Astrophys. J. Lett.* 634 (2005) L77.
- [264] L. Signor, G. Roy, P.Y. Chanal, P.L. Héreil, F. Buy, C. Voltz, F. Llorca, T. de Rességuier, A. Dragon, Debris cloud ejection from shock-loaded tin melted on release or on compression, *AIP Conf. Proc.* 1195 (2009) 1065.
- [265] C. Roland, T. de Rességuier, A. Sollier, E. Lescoute, D. Tandiang, M. Toulinet, L. Soulard, Ballistic properties of ejecta from a laser shock-loaded groove: SPH versus experiments, *AIP Conf. Proc.* (2018) 080012.
- [266] A. Sollier, E. Lescoute, Characterization of the ballistic properties of ejecta from laser shock-loaded samples using high resolution picosecond laser imaging, *Int. J. Impact Eng.* 136 (2020) 103429.
- [267] R.V. Fisher, Models for pyroclastic surges and pyroclastic flows, *J. Volcanol. Geotherm. Res.* 6 (1979) 305.
- [268] A.W. Woods, The dynamics of explosive volcanic eruptions, *Rev. Geophys.* 33 (1995) 495.

- [269] G. Dimonte, G. Terrones, F.J. Cherne, P. Ramaprabhu, Ejecta source model based on the nonlinear Richtmyer–Meshkov instability, *J. Appl. Phys.* 113 (2013) 024905.
- [270] A.R. Piriz, J.L. Cela, N.A. Tahir, D.H. Hoffmann, Richtmyer–Meshkov Instability in elastic–plastic media, *Phys. Rev. E* 78 (2008) 056401.
- [271] W.T. Buttler, D. Renner, C. Morris, R. Manzanares, E.K. Anderson, J.J. Goett III, J. Heidemann, R.M. Kalas, A. Llobet, J.I. Martinez, P.V. Medina Jr., Cavitation bubble interacting with a Richtmyer–Meshkov unstable sheet and spike, *AIP Conf. Proc.* 1979 (2018) 080003.
- [272] R.J.R. Williams, C.C. Grapes, Simulation of double-shock ejecta production, *J. Dynam. Behav. Mater.* 3 (2017) 291.
- [273] B. Grieves, 2D direct numerical simulation of ejecta production, in: Proceedings of the 10th International Workshop on the Physics of Compressible Turbulent Mixing, 2007, p. 95.
- [274] W.B. Liu, D.J. Ma, A.M. He, P. Wang, Ejecta from periodic grooved Sn surface under unsupported shocks, *Chin. Phys. B* 27 (2018) 016202.
- [275] F.J. Cherne, J.E. Hammerberg, M.J. Andrews, V. Karkhanis, P. Ramaprabhu, On shock driven jetting of liquid from non-sinusoidal surfaces into a vacuum, *J. Appl. Phys.* 118 (2015) 185901.
- [276] A. Georgievskaya, V.A. Raevsky, Estimation of spectral characteristics of particles ejected from the free surfaces of metals and liquids under a shock wave effect, *AIP Conf. Proc.* 1426 (2012) 1007.
- [277] R.J.R. Williams, The late time structure of high density contrast, single mode Richtmyer–Meshkov flow, *Phys. Fluids* 28 (2016) 074108.
- [278] J. Eggers, Nonlinear dynamics and breakup of free-surface flows, *Rev. Modern Phys.* 69 (1997) 865.
- [279] M.J. Andrews, D.L. and Preston, TAB Models for Liquid Sheet and Ligament Breakup (No. LA-UR-14-26937), Los Alamos National Lab.(LANL), Los Alamos, NM (United States), 2014.
- [280] A.C. Raga, J. Cantó, L. Binette, N. Calvet, Stellar jets with intrinsically variable sources, *Astrophys. J.* 364 (1990) 601.
- [281] P.J. O'Rourke, Amsden, The TAB method for numerical calculation of spray droplet breakup, 1987, SAE Technical Paper.
- [282] M.R. Turner, S.S. Sazhin, J.J. Healey, C. Crua, S.B. Martynov, A breakup model for transient diesel fuel sprays, *Fuel* 97 (2012) 288.
- [283] W.T. Buttler, S.K. Lamoreaux, R.K. Schulze, J.D. Schwarzkopf, J.C. Cooley, M. Grover, J.E. Hammerberg, B.M. La Lone, A. Llobet, R. Manzanares, J.I. Martinez, Ejecta transport, breakup and conversion, *J. Dyn. Behav. Mater.* 3 (2017) 334.
- [284] D.S. Sorenson, G.A. Capelle, M. Grover, R.P. Johnson, M.I. Kaufman, B.M. LaLone, R.M. Malone, B.F. Marshall, R.W. Minich, P.D. Pazuchanics, D.D. Smalley, Measurements of Sn ejecta particle-size distributions using ultraviolet in-line Fraunhofer holography, *J. Dynam. Behav. Mater.* 3 (2017) 233.
- [285] C. Roland, T. de Rességuier, A. Sollier, E. Lescoute, D. Loison, L. Soulard, Ejection of micron-scale fragments from triangular grooves in laser shock-loaded copper samples, *J. Dynam. Behav. Mater.* 3 (2017) 156.
- [286] D.J. Bell, D.J. Chapman, Phase doppler anemometry as an ejecta diagnostic, *AIP Conf. Proc.* 1793 (2017) 060011.
- [287] M.M. Schauer, W.T. Buttler, D.K. Frayer, M. Grover, B.M. Lalone, S.K. Monfared, D.S. Sorenson, G.D. Stevens, W.D. Turley, Ejected particle size distributions from shocked metal surfaces, *J. Dynam. Behav. Mater.* 3 (2017) 217.
- [288] P.T. Steele, B.A. Jacoby, S.M. Compton, J.O. Sinibaldi, Advances in ejecta diagnostics at LLNL, *J. Dynam. Behav. Mater.* 3 (2) (2017) 253–264.
- [289] O. Durand, L. Soulard, Power law and exponential ejecta size distributions from the dynamic fragmentation of shock-loaded Cu and Sn metals under melt conditions, *J. Appl. Phys.* 114 (2013) 194902.
- [290] Y. Liu, B. Grieves, Ejecta production and transport from a shocked Sn coupon, *J. Fluids Eng.* 136 (2014) 091202.
- [291] V. Karkhanis, P. Ramaprabhu, F.J. Cherne, J.E. Hammerberg, M.J. Andrews, A numerical study of bubble and spike velocities in shock-driven liquid metals, *J. Appl. Phys.* 123 (2018) 025902.
- [292] V.V. Zhakhovskii, S.V. Zybin, S.I. Abarzhik, K. Nishihara, Atomistic dynamics of the Richtmyer–Meshkov instability in cylindrical and planar geometries, *AIP Conf. Proc.* 845 (2006) 433.
- [293] T.C. Germann, G. Dimonte, J.E. Hammerberg, K. Kadau, J. Quenneville, M.B. Zellner, Large-scale molecular dynamics simulations of particulate ejection and Richtmyer–Meshkov instability development in shocked copper, in: DYMAT2009 (EDP Sciences, 2009), 2009, p. 1499.
- [294] F.J. Cherne, G. Dimonte, T.C. Germann, Richtmyer–Meshkov instability examined with large-scale molecular dynamics simulations, *AIP Conf. Proc.* 1426 (2012) 1307.
- [295] O. Durand, L. Soulard, Large-scale molecular dynamics study of jet breakup and ejecta production from shock-loaded copper with a hybrid method, *J. Appl. Phys.* 111 (2012) 044901.
- [296] J.L. Shao, P. Wang, A.M. He, Microjetting from a grooved Al surface under supported and unsupported shocks, *J. Appl. Phys.* 116 (2014) 073501.
- [297] O. Durand, L. Soulard, Mass-velocity and size-velocity distributions of ejecta cloud from shock-loaded tin surface using atomistic simulations, *J. Appl. Phys.* 117 (2015) 165903.
- [298] B. Wu, F. Wu, Y. Zhu, P. Wang, A. He, H. Wu, Molecular dynamics simulations of ejecta production from sinusoidal tin surfaces under supported and unsupported shocks, *AIP Adv.* 8 (2018) 045002.
- [299] O. Durand, S. Jaouen, L. Soulard, O. Heuze, L. Colombet, Comparative simulations of microjetting using atomistic and continuous approaches in the presence of viscosity and surface tension, *J. Appl. Phys.* 122 (2017) 135107.
- [300] S. Dyachkov, A. Parshikov, V. Zhakhovsky, Ejecta from shocked metals: Comparative simulations using molecular dynamics and smoothed particle hydrodynamics, *AIP Conf. Proc.* 1793 (2017) 100024.
- [301] A.D. Gosman, D. Clerides, Diesel spray modelling: a review, in: Proceedings of ILASS-Europe, Florence, Italy.
- [302] G. Grant, J. Brenton, D. Drysdale, Fire suppression by water sprays, *Prog. Energy Combust. Sci.* 26 (2000) 79.
- [303] M. Chiesa, V. Mathiesen, J.A. Melheim, B. Halvorsen, Numerical simulation of particulate flow by the Eulerian–Lagrangian and the Eulerian–Eulerian approach with application to a fluidized bed, *Comput. Chem. Eng.* 29 (2005) 291.
- [304] G.A. Valentine, K.H. Wohletz, Numerical models of Plinian eruption columns and pyroclastic flows, *J. Geophys. Res.: Solid Earth* 94 (1989) 1867.
- [305] F. Dobran, A. Neri, G. Macedonio, Numerical simulation of collapsing volcanic columns, *J. Geophys. Res.: Solid Earth* 98 (1993) 4231.
- [306] L.D. Cloutman, A Numerical Model of Particulate Transport, Lawrence Livermore National Lab. Report, CA (USA), 1991.
- [307] J. Fung, A.K. Harrison, S. Chitanvis, J. Margulies, Ejecta source and transport modeling in the FLAG hydrocode, *Comput. & Fluids* 83 (2013) 177.
- [308] J.A. McFarland, W.J. Black, J. Dahal, B.E. Morgan, Computational study of the shock driven instability of a multiphase particle-gas system, *Phys. Fluids* 28 (2016) 024105.
- [309] M. Bambauer, J. Hasslberger, M. Klein, Direct numerical simulation of the Richtmyer–Meshkov instability in reactive and nonreactive flows, *Combust. Sci. Technol.* (2020) <http://dx.doi.org/10.1080/00102202.2020.1763325>.
- [310] S.A. Coronel, J.C. Veilleux, J.E. Shepherd, Ignition of stoichiometric hydrogen–oxygen by water hammer, *Proc. Combust. Inst.* 38 (2021) 3537–3545.
- [311] J.P. Sykes, T.P. Gallagher, B.A. Rankin, Effects of Rayleigh–Taylor instabilities on turbulent premixed flames in a curved rectangular duct, *Proc. Combust. Instit.* 38 (2021) 6059–6066.
- [312] L. Massa, P. Jha, Linear analysis of the Richtmyer–Meshkov instability in shock–flame interactions, *Phys. Fluids* 24 (2012) 056101.
- [313] C.K. Law, *Combustion Physics*, Cambridge University Press, Cambridge, UK, 2006.
- [314] J. Yang, T. Kubota, E.E. Zukoski, Applications of shock-induced mixing to supersonic combustion, *AIAA J.* 31 (1993) 854.
- [315] F.E. Marble, G.J. Hendricks, E.E. Zukoski, Progress toward shock enhancement of supersonic combustion processes, in: R. Borghi, S.N.B. Murthy (Eds.), *Turbulent Reactive Flows*, in: *Lecture Notes in Engineering*, vol. 40, Springer, New York, NY, 1989.
- [316] F.E. Marble, E.E. Zukoski, J. Jacobs, G. Hendricks, Shock enhancement and control of hypersonic mixing and combustion, *AIAA paper* (1990) 90–1981.
- [317] I.A. Waitz, F.E. Marble, E.E. Zukoski, An investigation of a contoured wall injector for hypervelocity mixing augmentation, *AIAA Paper* 9 (1991) 1–2265.
- [318] R.G. Veraar, et al., Proof-of-principle experiment of a shock-induced combustion ramjet, in: 16th AIAA/DLR/DGLR Int. Space Planes Hypersonic Sys. Technol. Conf. (Bremen, Germany), 2009, p. 8.
- [319] Q. Yang, J. Chang, W. Bao, Richtmyer–Meshkov instability induced mixing enhancement in the Scramjet combustor with a central strut, *Adv. Mech. Eng.* 6 (2014) 614189.
- [320] K. Kailasanath, Review of propulsion applications of detonation waves, *AIAA J.* 38 (2000) 1698.
- [321] K.L. Cashdollar, Coal dust explosibility, *J. Loss Prev. Process Ind.* 9 (1996) 65.
- [322] A.G. Dastidar, P.R. Amyotte, M.J. Pegg, Factors influencing the suppression of coal dust explosions, *Fuel* 76 (1997) 663.
- [323] R.K. Eckhoff, Current status and expected future trends in dust explosion research, *J. Loss Prevent. Proc. Ind.* 18 (2005) 225.
- [324] T. Irving, Deadly Dust: Changes in Both Technology and Culture are Needed to Reduce the Risks of Dust Explosions, The Chemical Institute of Canada, 2013.
- [325] A.K. Kapila, R. Menikoff, J.B. Bdil, S.F. Son, D.S. Stewart, Two-phase modeling of deflagration-to-detonation transition in granular materials: Reduced equations, *Phys. Fluids* 13 (2001) 3002.
- [326] R.W. Houim, E.S. Oran, A multiphase model for compressible granular-gaseous flows: formulation and initial tests, *J. Fluid Mech.* 789 (2016) 166.

- [327] Y. Ling, J.L. Wagner, S.J. Beresh, S.P. Kearney, S. Balachandar, Interaction of a planar shock wave with a dense particle curtain: Modeling and experiments, *Phys. Fluids* 24 (2012) 113301.
- [328] S. Annamalai, B. Rollin, F. Ouellet, C. Neal, T.L. Jackson, S. Balachandar, Effects of initial perturbations in the early moments of an explosive dispersal of particles, *J. Fluids Eng.* 138 (2016) 070903.
- [329] D.L. Frost, Heterogeneous/particle-laden blast waves, *Shock Waves* 28 (2018) 439.
- [330] M. Paudel, J. Dahal, J. McFarland, Particle evaporation and hydrodynamics in a shock driven multiphase instability, *Int. J. Multiph. Flow.* 101 (2018) 137.
- [331] P. Vorobieff, M. Anderson, J. Conroy, R. White, C.R. Truman, S. Kumar, Vortex formation in a shock-accelerated gas induced by particle seeding, *Phys. Rev. Lett.* 106 (2011) 184503.
- [332] M. Anderson, P. Vorobieff, C.R. Truman, C. Corbin, G. Kuehner, P. Wayne, J. Conroy, R. White, S. Kumar, An experimental and numerical study of shock interaction with a gas column seeded with droplets, *Shock Waves* 25 (2015) 107.
- [333] V.N. Gamezo, A.M. Khokhlov, E.S. Oran, A.Y. Chtchelkanova, R.O. Rosenberg, Thermonuclear supernovae: Simulations of the deflagration stage and their implications, *Science* 299 (2003) 77.
- [334] A.E. Cottle, M.D. Polanka, Numerical and experimental results from a common-source high-g ultra-compact combustor, in: ASME Turbo Expo 2016: Turbomachinery Technical Conference and Exposition, American Society of Mechanical Engineers, 2016, pp. V04AT04A013-V04AT04A013.
- [335] J. Zelina, D.T. Shouse, R.D. Hancock, Ultra-compact combustors for advanced gas turbine engines, in: ASME Turbo Expo 2004: Power for Land, Sea, and Air, American Society of Mechanical Engineers, 2004, pp. 53–62.
- [336] E. Lutoschkin, Pressure-gain combustion for gas turbines based on shock-flame interaction, (PhD dissertation), Univ. Stuttgart, 2013.
- [337] E.P. Hicks, Rayleigh–Taylor unstable flames—fast or faster? *Astrophys. J.* 803 (2015) 72.
- [338] D.J. Jeffery, B. Leibundgut, R.P. Kirshner, S. Benetti, D. Branch, G. Sonnenborn, Analysis of the photospheric epoch spectra of type Ia supernovae SN 1990N and SN 1991T, *Astrophys. J.* 397 (1992) 304–328.
- [339] A. Fisher, D. Branch, P. Nugent, E. Baron, Evidence for a high-velocity carbon-rich layer in the Type Ia SN 1990N, *Astrophys. J. Lett.* 481 (1997) L89.
- [340] J.C. Wheeler, R.P. Harkness, A.M. Khokhlov, P. Höflich, Stirling's supernovae: a survey of the field, *Phys. Rep.* 256 (1995) 211.
- [341] E.S. Oran, Astrophysical combustion, *Proc. Comb. Inst.* 30 (2005) 1823.
- [342] M. Matalon, The Darrieus-Landau instability of premixed flames, *Fluid Dyn. Res.* 50 (2018) 051412.
- [343] G. Darrieus, Propagation d'un front de flamme La Technique Moderne (Paris) and in 1945 at Congres de Mecanique Appliquee, Unpublished work.
- [344] L.D. Landau, On the theory of slow combustion, *Acta Phys. USSR* 19 (1944) 77.
- [345] G.H. Markstein, Experimental and theoretical studies of flame-front stability, *J. Aeronaut. Sci.* 18 (1951) 199.
- [346] A.Y. Poludnenko, Pulsating instability and self-acceleration of fast turbulent flames, *Phys. Fluids* 27 (2015) 014106.
- [347] V.Y. Akkerman, C.K. Law, V. Bychkov, Self-similar accelerative propagation of expanding wrinkled flames and explosion triggering, *Phys. Rev. E* 83 (2011) 026305.
- [348] V.Y. Akkerman, C.K. Law, Flame dynamics and consideration of deflagration-to-detonation transition in central gravitational field, *Proc. Combust. Inst.* 34 (2013) 1921.
- [349] G.H. Markstein, A shock-tube study of flame front-pressure wave interaction, in: Symposium (International) on Combustion, Vol. 6(1), Elsevier, 1957, pp. 387–398.
- [350] G. Rudinger, Shock wave and flame interactions, in: Third AGARD Coll., Pergamon, London, 1958.
- [351] G. Thomas, R. Bambrey, C. Brown, Experimental observations of flame acceleration and transition to detonation following shock-flame interaction, *Combust. Theory Model.* 5 (2001) 573.
- [352] G.H. Markstein, D. Schwartz, Interaction between pressure waves and flame fronts, *Jet Propulsion* 24 (1955) 173.
- [353] G.H. Markstein, Flow disturbances induced near a slightly wavy contact surface, or flame front, traversed by a shock wave, *J. Aerosp. Sci.* 24 (1957) 238.
- [354] M. La Fleche, Q. Xiao, Y. Wang, M. Radulescu, Experimental study of the head-on interaction of a shock wave with a cellular flame, in: 26th ICDERS, Boston.
- [355] J.M. Picone, E.S. Oran, J.P. Boris, T.R. Young, Theory of vorticity generation by shock wave and flame interactions, in: Dynamics of Shock Waves, Explosions, and Detonations, American Institute of Aeronautics and Astronautics, 1985, pp. 429–448.
- [356] G.A. Batley, A.C. McIntosh, J. Brindley, S.A.E.G. Falle, A numerical study of the vorticity field generated by the baroclinic effect due to the propagation of a planar pressure wave through a cylindrical premixed laminar flame, *J. Fluid Mech.* 279 (1994) 217.
- [357] T. Scarcini, G.O. Thomas, Some experiments on shock-flame interaction, in: Aberystwyth, Rep. DET, University College of Wales, 1992, p. 905.
- [358] G. Dong, B. Fan, J. Ye, Numerical investigation of ethylene flame bubble instability induced by shock waves, *Shock Waves* 17 (2008) 409.
- [359] A.M. Khokhlov, E.S. Oran, A.Y. Chtchelkanova, J.C. Wheeler, Interaction of a shock with a sinusoidally perturbed flame, *Combust. Flame* 117 (1999) 99.
- [360] N. Haehn, D. Ranjan, C. Weber, J. Oakley, D. Rothamer, R. Bonazza, Reacting shock bubble interaction, *Combust. Flame* 159 (2012) 1339.
- [361] A.M. Khokhlov, E.S. Oran, G.O. Thomas, Numerical simulation of deflagration-to-detonation transition: the role of shock-flame interactions in turbulent flames, *Combust. Flame* 117 (1999) 323.
- [362] R.W. Houim, B.D. Taylor, Detonation initiation from shock and material interface interactions in hydrogen-air mixtures, *Proc. Combust. Inst.* 37 (2019) 3513.
- [363] N. Attal, P. Ramaprabhu, Numerical investigation of a single-mode chemically reacting Richtmyer–Meshkov instability, *Shock Waves* 25 (2015) 307.
- [364] H. Yang, M.I. Radulescu, Dynamics of cellular flame deformation after a head-on interaction with a shock wave: reactive Richtmyer–Meshkov instability, arXiv preprint [arXiv:2009.02546](https://arxiv.org/abs/2009.02546), submitted for publication.
- [365] F. Diegelmann, S. Hickel, N.A. Adams, Three-dimensional reacting shock–bubble interaction, *Combust. Flame* 181 (2017) 300.
- [366] M. Valentino, C. Kauffman, M. Sichel, Experiments on shock induced combustion of isolated regions of hydrogen–oxygen mixtures, *AIAA* (1999) 99-16669.
- [367] N. Attal, P. Ramaprabhu, J. Hossain, V. Karkhanis, M. Uddin, J.R. Gord, S. Roy, Development and validation of a chemical reaction solver coupled to the FLASH code for combustion applications, *Comput. & Fluids* 107 (2015) 59.
- [368] A. Elyanov, V. Golub, V. Volodin, Conditions for the development of Rayleigh–Taylor instability on the spherical flame front, *J. Phys. Conf. Ser.* 1129 (2018) 012011.
- [369] H. Xiao, R.W. Houim, E.S. Oran, Effects of pressure waves on the stability of flames propagating in tubes, *Proc. Combust. Inst.* 36 (2017) 1577.
- [370] N. Attal, P. Ramaprabhu, The stability of reacting single-mode Rayleigh–Taylor flames, *Physica D* 404 (2020) 132353.
- [371] N. Attal, Interfacial Instabilities in Reacting Flows (Ph.D. Dissertation), The University of North Carolina at Charlotte, 2016.
- [372] M.R. Baer, private communication, 2012.
- [373] S. Courtiaud, N. Lecysyn, G. Damamme, T. Poinsot, S. L, Analysis of mixing in high-explosive fireballs using small-scale pressurised spheres, *Shock Waves* 29 (2018) 339.
- [374] D.L. Frost, Y. Gregoire, O. Petel, S. Goroshin, F. Zhang, Particle jet formation during explosive dispersal of solid particles, *Phys. Fluids* 24 (2012) 1109.
- [375] K.T. Hughes, A. Diggs, C. Park, D. Littrell, R.T. Haftka, N.H. Kim, S. Balachandar, Simulation driven experiments of macroscale explosive dispersal of particles, in: 2018 AIAA Aerospace Sciences Meeting, 2018, p. 1545.
- [376] D.L. Frost, Z. Zarei, F. Zhang, Instability of combustion products interface from detonation of heterogeneous explosives, in: 20th International Colloquium on the Dynamics of Explosions and Reactive Systems, Montreal, Canada.
- [377] H.L. Brode, Blast wave from a spherical charge, *Phys. Fluids* 2 (1959) 217.
- [378] P.E. Crittenden, S. Balachandar, The stability of the contact interface of cylindrical and spherical shock tubes, *Phys. Fluids* 30 (2018) 064101.
- [379] M.R. Mankbadi, S. Balachandar, Compressible inviscid instability of rapidly expanding spherical material interfaces, *Phys. Fluids* 24 (2012) 034106.
- [380] M. Mankbadi, S. Balachandar, Viscous effects on the non-classical Rayleigh–Taylor instability of spherical material interfaces, *Shock Waves* 23 (2013) 603.
- [381] R. Epstein, On the Bell-Plesset effects: the effects of uniform compression and geometrical convergence on the classical Rayleigh–Taylor instability, *Phys. Plasmas* 11 (2004) 5114.
- [382] P.E. Crittenden, Numerical Methods for Single and Two-Phase Flow Developed to Determine the Stability of Rapidly Expanding Contact and Particle Interfaces (Ph.D. dissertation), University of Florida, 2017.
- [383] M.R. Mankbadi, S. Balachandar, Multiphase effects on spherical Rayleigh–Taylor interfacial instability, *Phys. Fluids* 26 (2014) 023301.
- [384] A. Kuhl, Mixing in Explosions, Tech. Rep., Lawrence Livermore National Lab., El Segundo, CA (United States), 1993.
- [385] S.I. Anisimov, Y.B. Zeldovich, Rayleigh–Taylor instability of boundary between detonation products and gas in spherical explosion, *Pis' ma Zh. Eksp. Teor. Fiz.* 3 (1977) 5.

- [386] S. Anisimov, Y. Zeldovich, M. Inogamov, M. Ivanov, The Taylor instability of contact boundary between expanding detonation products and a surrounding gas, in: Shock Waves, Explosions, and Detonations, in: Progress in Astronautics and Aeronautics, vol. 87, 1977, p. 218.
- [387] A. Kuhl, R. Ferguson, F. Priolo, K. Chien, J. Collins, Baroclinic Mixing in He Fireballs, Technical Report. UCRL-JC-114982, 1993.
- [388] K. Balakrishnan, F. Genin, D.V. Nance, S. Menon, Numerical study of blast characteristics from detonation of homogeneous explosives, *Shock Waves* 20 (2010) 147.
- [389] S. Annamalai, M.K. Parmar, Y. Ling, S. Balachandar, Nonlinear Rayleigh–Taylor instability of a cylindrical interface in explosion flows, *J. Fluids Eng.* 136 (2014) 060910.
- [390] K. Balakrishnan, S. Menon, Mixing layer characterization due to the impulsive dispersion of dense solid particle clouds, in: 45th AIAA/ASME/SAE/ASEE Joint Propulsion Conference & Exhibit, p. 5056.
- [391] K. Balakrishnan, S. Menon, On the role of ambient reactive particles in the mixing and afterburn behind explosive blast waves, *Combust. Sci. Technol.* 182 (2010) 186.
- [392] K. Balakrishnan, S. Ukai, S. Menon, Clustering and combustion of dilute aluminum particle clouds in a post-detonation flow field, *Proc. Combust. Inst.* 33 (2011) 2255.
- [393] A. Milne, C. Parrish, I. Worland, Dynamic fragmentation of blast mitigants, *Shock Waves* 20 (2010) 41.
- [394] R. Ripley, L. Donahue, F. Zhang, Jetting instabilities of particles from explosive dispersals, *AIP Conf. Proc.* 1426 (2012) 1615.
- [395] F. Ouellet, S. Annamalai, B. Rollin, Effect of a bimodal initial particle volume fraction perturbation in an explosive dispersal of particles, *AIP Conf. Proc.* 1793 (2017) 150011.
- [396] B. Musci, S. Petter, G. Pathikonda, D. Ranjan, N. Denissen, An experimental study of the blast driven Rayleigh–Taylor and Richtmyer–Meshkov instabilities: Preliminary results, in: Proceedings of the 16th International Workshop on the Physics of Compressible Turbulent Mixing, 2018, p. 202.
- [397] V. Rodriguez, R. Saurel, G. Jourdan, L. Houas, Impulsive dispersion of a granular layer by a weak blast wave, *Shock Waves* 27 (2017) 187.
- [398] V. Rodriguez, R. Saurel, G. Jourdan, L. Houas, Solid-particle jet formation under shock-wave acceleration, *Phys. Rev. E* 88 (2013) 063011.
- [399] V. Rodriguez, R. Saurel, G. Jourdan, L. Houas, External front instabilities induced by a shocked particle ring, *Phys. Rev. E* 90 (2014) 043013.
- [400] A.N. Osnès, M. Varddal, B.P. Reif, Numerical simulation of particle jet formation induced by shock wave acceleration in a Hele–Shaw cell, *Shock Waves* 28 (2018) 451.
- [401] R.B. Koneru, B. Rollin, B. Durant, F. Ouellet, S. Balachandar, A numerical study of particle jetting in a dense particle bed driven by an air-blast, *Phys. Fluids* 32 (2020) 093301.
- [402] Y. Zhou, W.H. Matthaeus, P. Dmitruk, Colloquium: Magnetohydrodynamic turbulence and time scales in astrophysical and space plasmas, *Rev. Modern Phys.* 76 (2004) 1015.
- [403] S.I. Braginskii, Transport processes in a plasma, *Rev. Plasma Phys.* 1 (1965).
- [404] M.D. Kruskal, M. Schwarzschild, Some instabilities of a completely ionized plasma, *Proc. R. Soc. Lond. Ser. A* 223 (1954) 348.
- [405] S. Chandrasekhar, *Hydrodynamic and Hydromagnetic Stability*, Oxford University Press, London, 1961.
- [406] A. Hillier, Ideal MHD instabilities, with a focus on the Rayleigh–Taylor and Kelvin–Helmholtz instabilities, in: D. MacTaggart, A. Hillier (Eds.), *Topics in Magnetohydrodynamic Topology, Reconnection and Stability Theory*, Springer, 2019.
- [407] A.S. Hillier, On the nature of the magnetic Rayleigh–Taylor instability in astrophysical plasma: the case of uniform magnetic field strength, *Mon. Not. R. Astron. Soc.* 462 (2016) 2256.
- [408] M.S. Ruderman, J. Terradas, J.L. Ballester, Rayleigh–Taylor Instabilities with sheared magnetic fields, *Astrophys. J.* 785 (2014) 110.
- [409] A.J. Díaz, E. Khomenko, M. Collados, Rayleigh–Taylor instability in partially ionized compressible plasmas: One fluid approach, *Astron. Astrophys.* 564 (2014) A97.
- [410] M.S. Ruderman, Compressibility effect on the Rayleigh–Taylor instability with sheared magnetic fields, *Sol. Phys.* 292 (2017) 47.
- [411] J. Carlyle, A. Hillier, The non-linear growth of the magnetic Rayleigh–Taylor instability, *Astron. Astrophys.* 605 (2017) A101.
- [412] J.M. Stone, T. Gardiner, Nonlinear evolution of the magnetohydrodynamic Rayleigh–Taylor instability, *Phys. Fluids* 19 (2007) 9.
- [413] J.M. Stone, T. Gardiner, The magnetic Rayleigh–Taylor instability in three dimensions, *Astrophys. J.* 671 (2007) 1726.
- [414] J. Carlyle, D.R. Williams, L. van Driel-Gesztesy, D. Innes, A. Hillier, S. Matthews, Investigating the dynamics and density evolution of returning plasma blobs from the 2011 June 7 eruption, *Astrophys. J.* 782 (2014) 87.
- [415] C.C. Wu, On MHD intermediate shocks, *Geophys. Res. Lett.* 14 (1987) 668.
- [416] C.C. Wu, Formation, structure, and stability of MHD intermediate shocks, *J. Geophys. Res.: Space Phys.* 95 (1990) 8149.
- [417] V. Wheatley, D.I. Pullin, R. Samtaney, Regular shock refraction at an oblique planar density interface in magnetohydrodynamics, *J. Fluid Mech.* 522 (2005) 179.
- [418] S.A. Falle, S.S. Komissarov, On the inadmissibility of non-evolutionary shocks, *J. Plasma Phys.* 65 (2001) 29.
- [419] R. Samtaney, Suppression of the Richtmyer–Meshkov instability in the presence of a magnetic field, *Phys. Fluids* 15 (2003) L53.
- [420] V. Wheatley, D.I. Pullin, R. Samtaney, Stability of an impulsively accelerated density interface in magnetohydrodynamics, *Phys. Rev. Lett.* 95 (2005) 125002.
- [421] V. Wheatley, R. Samtaney, D.I. Pullin, The Richtmyer–Meshkov instability in magnetohydrodynamics, *Phys. Fluids* 21 (2009) 082102.
- [422] T. Sano, T. Inoue, K. Nishihara, Critical magnetic field strength for suppression of the Richtmyer–Meshkov instability in plasmas, *Phys. Rev. Lett.* 111 (2013) 205001.
- [423] J.G. Wouchuk, K. Nishihara, Linear perturbation growth at a shocked interface, *Phys. Plasmas* 3 (1996) 3761.
- [424] J.G. Wouchuk, K. Nishihara, Asymptotic growth in the linear Richtmyer–Meshkov instability, *Phys. Plasmas* 4 (1997) 1028.
- [425] W. Mostert, D.I. Pullin, V. Wheatley, R. Samtaney, Magnetohydrodynamic implosion symmetry and suppression of Richtmyer–Meshkov instability in an octahedrally symmetric field, *Phys. Rev. Fluids* 2 (2017) 013701.
- [426] V. Wheatley, R. Samtaney, D.I. Pullin, R.M. Gehre, The transverse field Richtmyer–Meshkov instability in magnetohydrodynamics, *Phys. Fluids* 26 (2014) 016102.
- [427] V. Wheatley, R.M. Gehre, R. Samtaney, D.I. Pullin, The magnetohydrodynamic Richtmyer–Meshkov instability: The oblique field case, in: *International Symposium on Shock Waves*, Springer, Cham, 2013, pp. 1107–1112.
- [428] J. Cao, Z. Wu, H. Ren, D. Li, Effects of shear flow and transverse magnetic field on Richtmyer–Meshkov instability, *Phys. Plasmas* 15 (2008) 042102.
- [429] A. Bakhsh, S. Gao, R. Samtaney, V. Wheatley, Linear simulations of the cylindrical Richtmyer–Meshkov instability in magnetohydrodynamics, *Phys. Fluids* 28 (2016) 034106.
- [430] W. Mostert, V. Wheatley, R. Samtaney, D.I. Pullin, Effects of seed magnetic fields on magnetohydrodynamic implosion structure and dynamics, *Phys. Fluids* 26 (2014) 126102.
- [431] D.I. Pullin, W. Mostert, V. Wheatley, R. Samtaney, Converging cylindrical shocks in ideal magnetohydrodynamics, *Phys. Fluids* 26 (2014) 097103.
- [432] W. Mostert, D.I. Pullin, R. Samtaney, V. Wheatley, Converging cylindrical magnetohydrodynamic shock collapse onto a power-law-varying line current, *J. Fluid Mech.* 793 (2016) 414.
- [433] Y. Li, R. Samtaney, V. Wheatley, The Richtmyer–Meshkov instability of a double-layer interface in convergent geometry with magnetohydrodynamics, *Matter Radiat. Extremes* 3 (2018) 207.
- [434] W. Mostert, V. Wheatley, R. Samtaney, D.I. Pullin, Effects of magnetic fields on magnetohydrodynamic cylindrical and spherical Richtmyer–Meshkov instability, *Phys. Fluids* 27 (2015) 104102.
- [435] Z. Lin, H. Zhang, Z. Chen, Y. Liu, Y. Hong, The influence of magnetic field on the physical explosion of a heavy gas cloud, *Int. J. Comput. Fluid Dyn.* 31 (2017) 21.
- [436] W.J. Black, R.C. Allen, W.C. Maxon, N. Denissen, J.A. McFarland, Magnetohydrodynamic effects in a shock-accelerated gas cylinder, *Phys. Rev. Fluids* 4 (2019) 043901.
- [437] R.M. Kulsrud, *Plasma Physics for Astrophysics*, Princeton University Press, 2005.
- [438] B.I. Jun, M.L. Norman, J.M. Stone, A numerical study of Rayleigh–Taylor instability in magnetic fluids, *Astrophys. J.* 453 (1995) 332.
- [439] J. Giacalone, J.R. Jokipii, Magnetic field amplification by shocks in turbulent fluids, *Astrophys. J. Lett.* 663 (2007) L41.
- [440] F. Guo, S. Li, H. Li, J. Giacalone, J.R. Jokipii, D. Li, On the amplification of magnetic field by a supernova blast shock wave in a turbulent medium, *Astrophys. J.* 747 (2012) 98.
- [441] Y. Mizuno, M. Pohl, J. Niemiec, B. Zhang, K.I. Nishikawa, P.E. Hardee, Magnetic-field amplification by turbulence in a relativistic shock propagating through an inhomogeneous medium, *Astrophys. J.* 726 (2010) 62.
- [442] Y. Mizuno, M. Pohl, J. Niemiec, B. Zhang, K.I. Nishikawa, P.E. Hardee, Magnetic field amplification and saturation in turbulence behind a relativistic shock, *Mon. Not. R. Astron. Soc.* 439 (2014) 3490.
- [443] F. Fraschetti, Turbulent amplification of a magnetic field driven by the dynamo effect at rippled shocks, *Astrophys. J.* 770 (2013) 84.
- [444] T. Inoue, J. Shimoda, Y. Ohira, R. Yamazaki, The origin of radially aligned magnetic fields in young supernova remnants, *Astrophys. J. Lett.* 772 (2013) L20.
- [445] C. Matsuoka, K. Nishihara, T. Sano, Nonlinear motion of a current-vortex sheet in MHD Richtmyer–Meshkov instability, *J. Phys. Conf. Ser.* 688 (2016) 012063.
- [446] C. Matsuoka, K. Nishihara, T. Sano, Nonlinear interfacial motion in magnetohydrodynamic flows, *High Energy Density Phys.* 31 (2019) 19.

- [447] M. Hohenberger, P.Y. Chang, G. Fiksel, J.P. Knauer, R. Betti, F.J. Marshall, D.D. Meyerhofer, F.H. Séguin, R.D. Petrasso, Inertial confinement fusion implosions with imposed magnetic field compression using the OMEGA laser, *Phys. Plasmas* 19 (2012) 056306.
- [448] M.E. Manuel, C.K. Li, F.H. Séguin, J. Frenje, D.T. Casey, R.D. Petrasso, S.X. Hu, R. Betti, J.D. Hager, D.D. Meyerhofer, V.A. Smalyuk, First measurements of Rayleigh–Taylor-induced magnetic fields in laser-produced plasmas, *Phys. Rev. Lett.* 108 (2012) 255006.
- [449] B. Srinivasan, X.Z. Tang, Mechanism for magnetic field generation and growth in Rayleigh–Taylor unstable inertial confinement fusion plasmas, *Phys. Plasmas* 19 (2012) 082703.
- [450] D. Bond, V. Wheatley, S. Imran, R. Samtaney, D. Pullin, Y. Li, Shock interactions in multi-fluid plasmas, *Shock* 10 (2018) 13.
- [451] N. Shen, Y. Li, D.I. Pullin, R. Samtaney, V. Wheatley, On the magnetohydrodynamic limits of the ideal two-fluid plasma equations, *Phys. Plasmas* 25 (2018) 122113.
- [452] D. Bond, V. Wheatley, Y. Li, R. Samtaney, D.I. Pullin, The magnetised Richtmyer–Meshkov instability in two-fluid plasmas, *J. Fluid Mech.* 903 (2020) A41.
- [453] N. Shen, D.I. Pullin, V. Wheatley, R. Samtaney, Impulse-driven Richtmyer–Meshkov instability in Hall-magnetohydrodynamics, *Phys. Rev. Fluids* 4 (2019) 103902.
- [454] N. Shen, V. Wheatley, D.I. Pullin, R. Samtaney, Magnetohydrodynamic Richtmyer–Meshkov instability under an arbitrarily oriented magnetic field, *Phys. Plasmas* 27 (2020) 062101.
- [455] R.G. Evans, The influence of self-generated magnetic fields on the Rayleigh–Taylor instability, *Plasma Phys. Control. Fusion* 28 (1986) 1021.
- [456] D.D. Ryutov, M.S. Derzon, M.K. Matzen, The physics of fast Z pinches, *Rev. Modern Phys.* 72 (2000) 167.
- [457] S.V. Lebedev, A. Frank, D.D. Ryutov, Exploring astrophysics-relevant magnetohydrodynamics with pulsed-power laboratory facilities, *Rev. Modern Phys.* 91 (2019) 025002.
- [458] E. Tandberg-Hanssen, *The Nature of Solar Prominences*, Springer Science & Business Media, 2013.
- [459] D.H. Mackay, J.T. Karpen, J.L. Ballester, B. Schmieder, G. Aulanier, Physics of solar prominences: II—Magnetic structure and dynamics, *Space Sci. Rev.* 151 (2010) 333.
- [460] G. Aulanier, Démoulin, 3-D magnetic configurations supporting prominences. I. The natural presence of lateral feet, *Astron. Astrophys.* 329 (1998) 1125.
- [461] J.L. Leroy, Observation of prominence magnetic fields, in: E.R. Priest (Ed.), *Dynamics and Structure of Quiescent Solar Prominences*, Springer, Dordrecht, 1988, pp. 77–113.
- [462] P.J. Levens, B. Schmieder, A. LópezAriste, N. Labrosse, K. Dalmasse, B. Gelly, Magnetic field in atypical prominence structures: Bubble, tornado, and eruption, *Astrophys. J.* 826 (2016) 164.
- [463] Hinode Review Team, K. Al-Janabi, P. Antolin, D. Baker, L.R. Bellot Rubio, L. Bradley, D.H. Brooks, R. Centeno, J.L. Culhane, G. DelZanna, G.A. Doschek, L. Fletcher, H. Hara, L.K. Harra, A. Hillier, et al., Achievements of Hinode in the first eleven years, *Publ. Astron. Soc. Japan* 71 (2019) R1.
- [464] J.C. Chae, Dynamics of vertical threads and descending knots in a hedgerow prominence, *Astrophys. J.* 714 (2010) 618.
- [465] A. Hillier, H. Isobe, H. Watanabe, Observations of plasma blob ejection from a quiescent prominence by Hinode solar optical telescope, *Publ. Astron. Soc. Japan* 63 (2011) L19.
- [466] E. Leonardis, S.C. Chapman, C. Foullon, Turbulent characteristics in the intensity fluctuations of a solar quiescent prominence observed by the Hinode Solar Optical Telescope, *Astrophys. J.* 745 (2012) 185.
- [467] M.S. Freed, D.E. McKenzie, D.W. Longcope, M. Wilburn, Analysis of flows inside quiescent prominences as captured by Hinode/Solar Optical Telescope, *Astrophys. J.* 818 (2016) 57.
- [468] A. Hillier, T. Matsumoto, K. Ichimoto, Investigating prominence turbulence with Hinode SOT dopplergrams, *Astron. Astrophys.* 597 (2017) A111.
- [469] A. Hillier, V. Polito, Observations of the Kelvin–Helmholtz instability driven by dynamic motions in a solar prominence, *Astrophys. J. Lett.* 864 (2018) L10.
- [470] G. Stellmacher, E. Wiehr, Observation of an instability in a quiescent prominence, *Astron. Astrophys.* 24 (1973) 321.
- [471] G. de Toma, R. Casini, J.T. Burkepile, B.C. Low, Rise of a dark bubble through a quiescent prominence, *Astrophys. J. Lett.* 687 (2008) L123.
- [472] T.E. Berger, R.A. Shine, G.L. Slater, T.D. Tarbell, T.J. Okamoto, K. Ichimoto, Y. Katsukawa, Y. Suematsu, S. Tsuneta, B.W. Lites, T. Shimizu, Hinode SOT observations of solar quiescent prominence dynamics, *Astrophys. J. Lett.* 676 (2008) L89.
- [473] T. Berger, P. Testa, A. Hillier, P. Boerner, B.C. Low, K. Shibata, C. Schrijver, T. Tarbell, A. Title, Magneto-thermal convection in solar prominences, *Nature* 472 (2011) 197.
- [474] D.O. Suárez, A.J. Díaz, A.A. Ramos, J.T. Bueno, Time evolution of plasma parameters during the rise of a solar prominence instability, *Astrophys. J. Lett.* 785 (2014).
- [475] A. Hillier, R. Hillier, D. Tripathi, Determination of prominence plasma  $\beta$  from the dynamics of rising plumes, *Astrophys. J.* 761 (2012) 106.
- [476] T.E. Berger, G. Slater, N. Hurlburt, R. Shine, T. Tarbell, B.W. Lites, T.J. Okamoto, K. Ichimoto, Y. Katsukawa, T. Magara, Y. Suematsu, Quiescent prominence dynamics observed with the Hinode Solar Optical Telescope. I. Turbulent upflow plumes, *Astrophys. J.* 716 (2010) 1288.
- [477] P. Heinzel, B. Schmieder, F. Fárník, P. Schwartz, N. Labrosse, P. Kotrč, U. Anzer, G. Molodij, A. Berlicki, E.E. DeLuca, L. Golub, Hinode, TRACE, SOHO, and ground-based observations of a quiescent prominence, *Astrophys. J.* 686 (2008) 1383.
- [478] S. Gunár, P. Schwartz, J. Dudík, B. Schmieder, P. Heinzel, J. Jurčák, Magnetic field and radiative transfer modelling of a quiescent prominence, *Astron. Astrophys.* 567 (2014) A123.
- [479] J. Dudík, G. Aulanier, B. Schmieder, M. Zapiór, P. Heinzel, Magnetic topology of bubbles in quiescent prominences, *Astrophys. J.* 761 (2012) 9.
- [480] M. Ryutova, T. Berger, Z. Frank, T. Tarbell, Observation of plasma instabilities in quiescent prominences, *Sol. Phys.* 267 (2010) 75.
- [481] T. Berger, A. Hillier, W. Liu, Quiescent prominence dynamics observed with the Hinode Solar Optical Telescope. II. Prominence bubble boundary layer characteristics and the onset of a coupled Kelvin–Helmholtz Rayleigh–Taylor instability, *Astrophys. J.* 850 (2017) 60.
- [482] A.J. Díaz, R. Soler, J.L. Ballester, Rayleigh–Taylor instability in partially ionized compressible plasmas, *Astrophys. J.* 754 (2012) 41.
- [483] E. Khomenko, A. Díaz, A. De Vicente, M. Collados, M. Luna, Rayleigh–Taylor instability in prominences from numerical simulations including partial ionization effects, *Astron. Astrophys.* 565 (2014) A45.
- [484] E. Khomenko, Multi-fluid extensions of MHD and their implications on waves and instabilities, in: D. MacTaggart, A. Hillier (Eds.), *Topics in Magnetohydrodynamic Topology, Reconnection and Stability Theory*, Springer, Cham, 2020, pp. 69–116.
- [485] A. Hillier, H. Isobe, K. Shibata, T. Berger, Numerical simulations of the magnetic Rayleigh–Taylor instability in the Kippenhahn–Schlüter prominence model, *Astrophys. J. Lett.* 736 (2011) L1.
- [486] A. Hillier, T. Berger, H. Isobe, K. Shibata, Numerical simulations of the magnetic Rayleigh–Taylor instability in the Kippenhahn–Schlüter prominence model. I. Formation of upflows, *Astrophys. J.* 746 (2012) 120.
- [487] R. Keppens, C. Xia, O. Porth, Solar prominences: Double, Double...Boil and Bubble, *Astrophys. J. Lett.* 806 (2015) L13.
- [488] C. Xia, R. Keppens, Internal dynamics of a twin-layer solar prominence, *Astrophys. J. Lett.* 825 (2016) L29.
- [489] J. Terradas, R. Soler, M. Luna, R. Oliver, J.L. Ballester, Morphology and dynamics of solar prominences from 3D MHD simulations, *Astrophys. J.* 799 (2015) 94.
- [490] T. Kaneko, T. Yokoyama, Impact of dynamic state on the mass condensation rate of solar prominences, *Astrophys. J.* 869 (2018) 136.
- [491] A. Hillier, The magnetic Rayleigh–Taylor instability in solar prominences, *Rev. Modern Plasma Phys.* 2 (2018) 1.
- [492] National Research Council, *Solar and Space Physics: A Science for a Technological Society*, The National Academies Press., Washington, DC, 2013, <https://doi.org/10.17226/13060>.
- [493] National space weather strategy and action plan, space weather operations, research, and mitigation working group space weather, security, and hazards subcommittee committee on homeland and national security of the National Science & Technology Council. <https://www.whitehouse.gov/wp-content/uploads/2019/03/National-Space-Weather-Strategy-and-Action-Plan-2019.pdf>.
- [494] M.C. Kelley, *Earth's Ionosphere, Plasma Physics and Electrodynamics*, second ed., Elsevier, Amsterdam, 2009.
- [495] R.E. Dickinson, E.C. Ridley, R.G. Roble, A three-dimensional general circulation model of the thermosphere, *J. Geophys. Res.: Space Phys.* 86 (1981) 1499.
- [496] T.J. Fuller-Rowell, D.A. Rees, A three dimensional time dependent global model of the thermosphere, *J. Atmos. Sci.* 37 (1980) 2545.
- [497] T.J. Fuller-Rowell, D. Rees, S. Quegan, R.J. Moffett, G.J. Bailey, Interactions between neutral thermospheric composition and the polar ionosphere using a coupled ionosphere–thermosphere model, *J. Geophys. Res.* 92 (1987) 7744.
- [498] R.G. Roble, E.C. Ridley, A thermosphere-ionosphere-mesosphere-electrodynamics general circulation model (TIME-GCM): Equinox solar cycle minimum simulations (30–500 km), *Geophys. Res. Lett.* 21 (1994) 417.
- [499] J.D. DeBoer, J. Noël, J.P. St-Maurice, The effects of mesoscale regions of precipitation on the ionospheric dynamics, electrodynamics and electron density in the presence of strong ambient electric field, *Ann. Geophys.* 28 (2010) 1345.
- [500] M. Gilman, E. Smith, S. Tsynkov, *Transionospheric Synthetic Aperture Imaging*, Birkhäuser/Springer, Cham, Switzerland, 2017.
- [501] R.A. Heelis, J.K. Lowell, R.W. Spiro, A model of the high-latitude ionospheric convection pattern, *J. Geophys. Res.* 87 (1982) 6339.

- [502] D.L. Hysell, M.F. Larsen, Q.H. Zhou, Common volume coherent and incoherent scatter radar observations of midlatitude sporadic E layers and QP echoes, *Ann. Geophys.* 22 (2004) 3277.
- [503] J. Park, K.W. Min, V.P. Kim, H. Kil, S.Y. Su, C.K. Chao, J.J. Lee, Equatorial plasma bubbles with enhanced ion and electron temperatures, *J. Geophys. Res.: Space Phys.* 113 (2008) A09318.
- [504] R. Raghavarao, R. Sekar, R. Suhasini, Nonlinear numerical simulation of equatorial spread-F—Effects of winds and electric fields, *Adv. Space Res.* 12 (1992) 227.
- [505] J.M. Reiterer, Forecasting low-latitude radio scintillation with 3-D ionospheric plume models: 1. Plume model, *J. Geophys. Res.* 115 (2010) A03306.
- [506] J.M. Reiterer, Forecasting low-latitude radio scintillation with 3-D ionospheric plume models: 2. Scintillation calculation, *J. Geophys. Res.* 115 (2010) A03307.
- [507] R. Sekar, R. Suhasini, R. Raghavarao, Effects of vertical winds and electric fields in the nonlinear evolution of equatorial spread F, *J. Geophys. Res.: Space Phys.* 99 (1994) 2205.
- [508] R. Sekar, E.A. Kherani, Effects of molecular ions on the collisional Rayleigh–Taylor instability: Nonlinear evolution, *J. Geophys. Res.* 107 (2002) 1.
- [509] R.A. Steenburgh, C.G. Smithtro, K.M. Groves, Ionospheric scintillation effects on single frequency GPS, *Space Weather* 6 (2008) 1.
- [510] R.F. Woodman, C. La Hoz, Radar observations of F region equatorial irregularities, *J. Geophys. Res.* 81 (1976) 5447.
- [511] Z.P. Sun, R.P. Turco, R.L. Walterscheid, S.V. Venkateswaran, P.W. Jones, Thermospheric response to morningside diffuse aurora: High-resolution three-dimensional simulations, *J. Geophys. Res.: Space Phys.* 100 (1995) 23779.
- [512] Z.W. Xu, J. Wu, Z.S. Wu, A survey of ionospheric effects on space-based radar, *Waves Random Complex Media* 14 (2004) S189.
- [513] J.J. Sojka, Global scale, physical models of the F-region ionosphere, *Rev. Geophys.* 27 (1989) 371.
- [514] J.W. Dungey, Convective diffusion in the equatorial F region, *J. Atmos. Terr. Phys.* 9 (1956) 304.
- [515] L.C. Gentile, W.J. Burke, F.J. Rich, A climatology of equatorial plasma bubbles from DMSP 1989–2004, *Radio Sci.* 41 (2006) RS5S21.
- [516] A.D. Richmond, E.C. Ridley, R.G. Roble, A thermosphere/ionosphere general circulation model with coupled electrodynamics, *Geophys. Res. Lett.* 19 (1992) 601.
- [517] Q. Wu, Longitudinal and seasonal variation of the equatorial flux tube integrated Rayleigh–Taylor instability growth rate, *J. Geophys. Res. Space Phys.* 120 (2015) <http://dx.doi.org/10.1002/2015JA021553-T>.
- [518] B.G. Fejer, L. Scherliess, E.R. de Paula, Effects of the vertical plasma drift velocity on the generation and evolution of equatorial spread F, *J. Geophys. Res.* 104 (19) (1999) 859.
- [519] Q. Wu, Solar effect on the Rayleigh–Taylor instability growth rate as simulated by the NCAR TIEGCM, *J. Atmos. Sol.-Terr. Phys.* 156 (2017) 97.
- [520] P.J. Sultan, Linear theory and modeling of the Rayleigh–Taylor instability leading to the occurrence of equatorial spread F, *J. Geophys. Res.: Space Phys.* 101 (1996) 26875.
- [521] S. Basu, S. Basu, J. Arons, J.P. McClure, M.D. Cousins, On the coexistence of kilometer-and meter-scale irregularities in the nighttime equatorial F region, *J. Geophys. Res.: Space Phys.* 83 (1978) 4219.
- [522] A. Mahalov, Multiscale modeling and nested simulations of three-dimensional ionospheric plasmas: Rayleigh–Taylor turbulence and nonequilibrium layer dynamics at fine scales, *Phys. Scr.* 89 (2014) 098001.
- [523] E. Alam Kherani, E.R. De Paula, F.C. Bertoni, Effects of the fringe field of Rayleigh–Taylor instability in the equatorial E and valley regions, *J. Geophys. Res.: Space Phys.* 109 (2004) 12310.
- [524] O. de La Beaujardiere, the C/NOFS Science Definition Team, C/NOFS: a mission to forecast scintillations, *J. Atmos. Sol.-Terr. Phys.* 66 (2004) 1573.
- [525] C.S. Huang, M.C. Kelley, Nonlinear evolution of equatorial spread F: 2. Gravity wave seeding of Rayleigh–Taylor instability, *J. Geophys. Res.: Space Phys.* 101 (1996) 293.
- [526] C.S. Huang, M.C. Kelley, Nonlinear evolution of equatorial spread F: 4. Gravity waves, velocity shear, and day-to-day variability, *J. Geophys. Res.: Space Phys.* 101 (1996) 24521.
- [527] J.D. Huba, S.L. Ossakow, G. Joyce, J. Krall, S.L. England, Three-dimensional equatorial spread F modeling: zonal neutral wind effects, *Geophys. Res. Lett.* 36 (2009) L19106.
- [528] B. Cheng, A. Mahalov, General results on zonation in rotating systems with a  $\beta$  effect and the electromagnetic force, in: B. Galperin, P.L. Read (Eds.), *Zonal Jets: Phenomenology, Genesis and Physics*, Cambridge University Press, Cambridge, U.K., 2019.
- [529] J. Durazo, E. Kostelich, A. Mahalov, W. Tang, Observing system experiments with an ionospheric electrodynamics model, *Phys. Scr.* 91 (2016) 044001.
- [530] J.A. Durazo, E.J. Kostelich, A. Mahalov, Local ensemble transform Kalman filter for ionospheric data assimilation: Observation influence analysis during a geomagnetic storm event, *J. Geophys. Res.: Space Phys.* 122 (2017) 9652.
- [531] M.C. Kelley, M.F. Larsen, C. LaHoz, J.P. McClure, Gravity wave initiation of equatorial spread F: A case study, *J. Geophys. Res.: Space Phys.* 86 (1981) 9087.
- [532] J. Krall, J.D. Huba, G. Joyce, S.T. Zalesak, Three-dimensional simulation of equatorial spread-F with meridional wind effects, *Ann. Geophys.* 27 (2009) 1821.
- [533] J. Krall, J.D. Huba, G. Joyce, T. Yokoyama, Density enhancements associated with equatorial spread F, *Ann. Geophys.* 28 (2010) 327.
- [534] A. Mahalov, M. Moustaoui, Multiscale nested simulations of Rayleigh–Taylor instabilities in ionospheric flows, *J. Fluids Eng.* 136 (2014) <http://dx.doi.org/10.1115/1.4025657>.
- [535] A. Mahalov, M. Moustaoui, B. Nicolaenko, Three-dimensional instabilities in non-parallel shear stratified flows, *Kinet. Relat. Models* 2 (2008) 215.
- [536] S.L. Ossakow, P.K. Chaturvedi, Morphological studies of rising equatorial spread F bubbles, *J. Geophys. Res.: Space Phys.* 83 (1978) 2085.
- [537] W. Tang, A. Mahalov, Stochastic Lagrangian dynamics for charged flows in the E-F regions of ionosphere, *Phys. Plasmas* 20 (2013) 032305.
- [538] W. Tang, A. Mahalov, The response of plasma density to breaking inertial gravity wave in the lower regions of ionosphere, *Phys. Plasmas* 21 (2014) 042901.
- [539] T. Yokoyama, S.Y. Su, S. Fukao, Plasma blobs and irregularities concurrently observed by ROCSAT-1 and equatorial atmosphere radar, *J. Geophys. Res.: Space Phys.* 112 (2007) 05311.
- [540] T. Yokoyama, T. Horinouchi, M. Yamamoto, S. Fukao, Modulation of the midlatitude ionospheric E region by atmospheric gravity waves through polarization electric field, *J. Geophys. Res.* 109 (2004) 12307.
- [541] T. Yokoyama, M. Yamamoto, S. Fukao, Three-dimensional simulation on generation of polarization electric field in the midlatitude E-region ionosphere, *J. Geophys. Res.* 109 (2004) 01309.
- [542] A. Mahalov, M. Moustaoui, B. Nicolaenko, K.L. Tse, Computational studies of inertia-gravity waves radiated from upper tropospheric jets, *Theoret. Comput. Fluid Dynam.* 21 (2007) 399.
- [543] A. Mahalov, M. Moustaoui, Vertically nested nonhydrostatic model for multiscale resolution of flows in the upper troposphere and lower stratosphere, *J. Comput. Phys.* 228 (2009) 1294.
- [544] A. Mahalov, M. Moustaoui, Time-filtered leapfrog integration of Maxwell equations using unstaggered temporal grids, *J. Comput. Phys.* 325 (2016) 98.
- [545] C.Y. Jung, B. Kwon, A. Mahalov, T.B. Nguyen, Maxwell solutions in media with multiple random interfaces, *Int. J. Numer. Anal. Model.* 11 (2014) 194.
- [546] A. Mahalov, A. McDaniel, Long-range propagation through inhomogeneous turbulent atmosphere: analysis beyond phase screens, *Phys. Scr.* 94 (2019) 034003.
- [547] A. McDaniel, A. Mahalov, Lensing effects in a random inhomogeneous medium, *Opt. Express* 25 (2017) 16.
- [548] A. McDaniel, A. Mahalov, Stochastic mirage phenomenon in a random medium, *Opt. Lett.* 42 (2017) 2002.
- [549] R.W. Schunk, A.E. Nagy, *Ionospheres: Physics, Plasma Physics and Chemistry*, Cambridge University Press, Cambridge, U.K, 2000.
- [550] W.H. Bennett, Magnetically self-focussing streams, *Phys. Rev.* 45 (1934) 890.
- [551] L. Tonks, Theory and phenomena of high current densities in low pressure arcs, *Trans. Electrochem. Soc.* 72 (1937) 167.
- [552] A.S. Bishop, *Project Sherwood: The US Program in Controlled Fusion*, Addison-Wesley, Reading, MA, 1958.
- [553] Y. Maron, Experimental determination of the thermal, turbulent, and rotational ion motion and magnetic field profiles in imploding plasmas, *Phys. Plasmas* 27 (2020) 060901.
- [554] D.B. Sinars, M.A. Sweeney, C.S. Alexander, D.J. Ampleford, T. Ao, J.P. Apruzese, C. Aragon, D.J. Armstrong, K.N. Austin, T.J. Awe, A.D. Baczewski, et al., Review of pulsed power-driven high energy density physics research on Z at Sandia, *Phys. Plasmas* 27 (2020) 070501.
- [555] E.P. Yu, T.J. Awe, K.R. Cochrane, K.C. Yates, T.M. Hutchinson, K.J. Peterson, B.S. Bauer, Use of hydrodynamic theory to estimate electrical current redistribution in metals, *Phys. Plasmas* 27 (2020) 052703.
- [556] D.D. Ryutov, Characterizing the plasmas of dense Z-pinch, *IEEE Trans. Plasma Sci.* 43 (2015) 2363.
- [557] S.A. Slutz, M.C. Herrmann, R.A. Vesey, A.B. Sefkow, D.B. Sinars, D.C. Rovang, K.J. Peterson, M.E. Cuneo, Pulsed-power-driven cylindrical liner implosions of laser preheated fuel magnetized with an axial field, *Phys. Plasmas* 17 (2010) 056303.
- [558] I.R. Lindemuth, R.C. Kirkpatrick, Parameter space for magnetized fuel targets in inertial confinement fusion, *Nucl. Fusion* 23 (1983) 263.

- [559] T.J. Awe, R.D. McBride, C.A. Jennings, D.C. Lamppa, M.R. Martin, D.C. Rovang, S.A. Slutz, M.E. Cuneo, A.C. Owen, D.B. Sinars, K. Tomlinson, Observations of modified three-dimensional instability structure for imploding z-pinch liners that are premagnetized with an axial field, *Phys. Rev. Lett.* 111 (2013) 235005.
- [560] C.E. Seyler, M.R. Martin, N.D. Hamlin, Helical instability in MagLIF due to axial flux compression by low-density plasma, *Phys. Plasmas* 25 (2018) 062711.
- [561] B. Reipurth, J. Bally, Herbig-haro flows: Probes of early stellar evolution, *Annu. Rev. Astron. Astrophys.* 39 (2001) 403.
- [562] A. Ciardi, D.J. Ampleford, S.V. Lebedev, C. Stehle, Curved Herbig-Haro jets: Simulations and experiments, *Astrophys. J.* 678 (2008) 968.
- [563] J.E. Pringle, Accretion discs in astrophysics, *Annu. Rev. Astron. Astrophys.* 19 (1981) 137.
- [564] D. Ryutov, R.P. Drake, J. Kane, E. Liang, B.A. Remington, W.M. Wood-Vasey, Similarity criteria for the laboratory simulation of supernova hydrodynamics, *Astrophys. J.* 518 (1999) 821.
- [565] P.M. Bellan, S. You, S.C. Hsu, Simulating astrophysical jets in laboratory experiments, in: G.A. Kyrala (Ed.), *High Energy Density Laboratory Astrophysics*, Springer, Dordrecht, 2005.
- [566] W.D. Arnett, Supernova theory and supernova 1987A, *Astrophys. J.* 319 (1987) 136.
- [567] W.D. Arnett, J.N. Bahcall, R.P. Kirshner, S.E. Woosley, Supernova 1987A, *Annu. Rev. Astron. Astrophys.* 27 (1989) 629.
- [568] D. Arnett, B. Fryxell, E. Müller, Instabilities and nonradial motion in SN 1987A, *Astrophys. J.* 341 (1989) L63.
- [569] N.J. Hammer, H.T. Janka, E. Müller, Three-dimensional simulations of mixing instabilities in supernova explosions, *Astrophys. J.* 714 (2010) 1371.
- [570] K. Kifonidis, T. Plewa, H.T. Janka, E. Müller, Non-spherical core collapse supernovae-I. Neutrino-driven convection, Rayleigh-Taylor instabilities, and the formation and propagation of metal clumps, *Astron. Astrophys.* 408 (2003) 621.
- [571] K. Kifonidis, T. Plewa, L. Scheck, H.T. Janka, E. Müller, Non-spherical core collapse supernovae-II. The late-time evolution of globally anisotropic neutrino-driven explosions and their implications for SN 1987 A, *Astron. Astrophys.* 453 (2006) 661.
- [572] A.M. Khokhlov, Propagation of turbulent flames in supernovae, *Astrophys. J.* 449 (1995) 695.
- [573] D.L. Meier, R.I. Epstein, W.D. Arnett, D.N. Schramm, Magnetohydrodynamic phenomena in collapsing stellar cores, *Astrophys. J.* 204 (1976) 869.
- [574] J.M. LeBlanc, J.R. Wilson, A numerical example of the collapse of a rotating magnetized star, *Astrophys. J.* 161 (1970) 541.
- [575] J.C. Wheeler, D.L. Meier, J.R. Wilson, Asymmetric supernovae from magnetocentrifugal jets, *Astrophys. J.* 568 (2002) 807.
- [576] I.S. Remming, A.M. Khokhlov, The classification of magnetohydrodynamic regimes of thermonuclear combustion, *Astrophys. J.* 794 (2014) 87.
- [577] I.S. Remming, A.M. Khokhlov, The internal structure and propagation of magnetohydrodynamical thermonuclear flames, *Astrophys. J.* 831 (2016) 162.
- [578] B. Aschenbach, R. Egger, J. Trümper, Discovery of explosion fragments outside the Vela supernova remnant shock-wave boundary, *Nature* 373 (1995) 587.
- [579] N. Bucciantini, E. Amato, R. Bandiera, J.M. Blondin, L. Del Zanna, Magnetic Rayleigh-Taylor instability for pulsar wind nebulae in expanding supernova remnants, *Astron. Astrophys.* 423 (2004) 253.
- [580] Y. Uchiyama, F.A. Aharonian, T. Tanaka, T. Takahashi, Y. Maeda, Extremely fast acceleration of cosmic rays in a supernova remnant, *Nature* 449 (2007) 576.
- [581] P.Y. Chang, G. Fiksel, M. Hohenberger, J.P. Knauer, R. Betti, F.J. Marshall, D.D. Meyerhofer, F.H. Séguin, R.D. Petrasso, Fusion yield enhancement in magnetized laser-driven implosions, *Phys. Rev. Lett.* 107 (2011) 035006.
- [582] B. Srinivasan, X.Z. Tang, The mitigating effect of magnetic fields on Rayleigh-Taylor unstable inertial confinement fusion plasmas, *Phys. Plasmas* 20 (2013) 056307.
- [583] D. Aslangil, Z. Farley, A.G.W. Lawrie, A. Banerjee, Rayleigh-Taylor Instability with varying periods of zero acceleration, *J. Fluids Eng.* 142 (2020) 121103.
- [584] D. Aslangil, D. Livescu, A. Banerjee, Effects of atwood and reynolds numbers on the evolution of buoyancy-driven homogeneous variable-density turbulence, *J. Fluid Mech.* 895 (2020) A12.
- [585] C.M. Athira, G. Rajesh, S. Mohanan, A. Parthasarathy, Flow interactions on supersonic projectiles in transitional ballistic regimes, *J. Fluid Mech.* 894 (2020) A27.
- [586] O.A. Azarova, K.V. Krasnobaev, O.V. Kravchenko, T.A. Lapushkina, A.V. Erofeev, Redistribution of energy in a viscous heat-conductive medium during the interaction of a shock wave with a temperature layered plasma region, in: *J. Phys.: Conf. Ser.*, 1698, IOP Publishing, 2020, p. 012004.
- [587] G. Boffetta, M. Borgnino, S. Musacchio, Scaling of Rayleigh-Taylor mixing in porous media, *Phys. Rev. Fluids* 5 (2020) 062501.
- [588] S.P. Borisov, A.N. Kudryavtsev, Development of the Rayleigh-Taylor instability. Results of numerical simulation at low reynolds numbers, in: *AIP Conf. Proc.*, 2288, AIP Publishing LLC, 2020, p. 030019.
- [589] J. Canfield, N. Denissen, M. Francois, R. Gore, R. Rauenzahn, J. Reisner, S. Shkoller, A comparison of interface growth models applied to Rayleigh-Taylor and Richtmyer-Meshkov instabilities, *J. Fluids Eng.* 142 (2020) 121108.
- [590] V.K. Cheeda, Turbulent flame propagation in corn dust clouds formed in confined and open spaces, *SN Appl. Sci.* 2 (2020) 1415.
- [591] C.A. Di Stefano, F.W. Doss, E.C. Merritt, B.M. Haines, T.R. Desjardins, B.G. DeVolder, K.A. Flippo, L. Kot, H.F. Robey, D.W. Schmidt, M. Millot, Experimental measurement of two copropagating shocks interacting with an unstable interface, *Phys. Rev. E* 102 (2020) 043212.
- [592] A. Do, L.A. Pickworth, B.J. Koziociemski, A.M. Angulo, G.N. Hall, S.R. Nagel, D.K. Bradley, T. McCarville, J.M. Ayers, Fresnel zone plate development for x-ray radiography of hydrodynamic instabilities at the National Ignition Facility, *Appl. Optics* 59 (2020) 10777.
- [593] A.N. Doludenko, Experimental and numerical investigation of the Rayleigh-Taylor instability of the newtonian and dilatant fluid system, *Phys. Scr.* 95 (2020) 115207.
- [594] D. Duda, V. Yanovych, V. Uruba, M. Němc, P. Žítek, Vortices inside a single-stage axial air turbine captured by particle image velocimetry, in: *MATEC Web of Conf.*, 328, EDP Sciences, 2020, p. 05002.
- [595] O. Durand, L. Soulard, L. Colombet, R. Prat, Influence of the phase transitions of shock-loaded tin on microjetting and ejecta production using molecular dynamics simulations, *J. Appl. Phys.* 127 (2020) 175901.
- [596] M. El Rafei, B. Thornber, Numerical study and buoyancy-drag modeling of bubble and spike distances in three-dimensional spherical implosions, *Phys. Fluids* 32 (2020) 124107.
- [597] T. Elizarova, A. Zlotnik, On aggregated regularized equations for homogeneous binary gas mixture flows with viscous compressible components, in: *AIP Conf. Proc.*, 2293, AIP Publishing LLC, 2020, p. 210016.
- [598] Z. Fan, M. Dong, Multiple eigenmodes of the Rayleigh-Taylor instability observed for a fluid interface with smoothly varying density. III. excitation and nonlinear evolution, *Phys. Rev. E* 101 (2020) 063103.
- [599] P.S. Farmakis, P. Tsoutsanis, X. Nogueira, Weno schemes on unstructured meshes using a relaxed a posteriori mood limiting approach, *Comput. Methods Appl. Mech. Eng.* 363 (2020) 112921.
- [600] Y. Fu, C. Yu, X. Li, Energy transport characteristics of converging Richtmyer-Meshkov instability, *AIP Adv.* 10 (2020) 105302.
- [601] F. Gancedo, R. Granero-Belinchón, S. Scrobogna, Surface tension stabilization of the Rayleigh-Taylor instability for a fluid layer in a porous medium, *Ann. Inst. Henri Poincaré, Anal. Nonlinéaire* 37 (2020) 1299.
- [602] F.F. Grinstein, J.A. Saenz, R.M. Rauenzahn, M. Germano, D.M. Israel, Dynamic bridging modeling for coarse grained simulations of shock driven turbulent mixing, *Comput. & Fluids* 199 (2020) 104430.
- [603] X. Guo, Y. Wei, Y. Zhang, Temporal-spatial evolution of kinetic and thermal energy dissipation rates in a three-dimensional turbulent Rayleigh-Taylor mixing zone, *Entropy* 22 (2020) 652.
- [604] X. Guo, Z. Zhai, J. Ding, T. Si, X. Luo, Effects of transverse shock waves on early evolution of multi-mode chevron interface, *Phys. Fluids* 32 (2020) 106101.
- [605] B.M. Haines, R.C. Shah, J.M. Smidt, B.J. Albright, T. Cardenas, M.R. Douglas, C. Forrest, V.Yu Glebov, M.A. Gunderson, C. Hamilton, et al., The rate of development of atomic mixing and temperature equilibration in inertial confinement fusion implosions, *Phys. Plasmas* 27 (2020) 102701.
- [606] B.M. Haines, D.E. Keller, J.A. Marozas, P.W. McKenty, K.S. Anderson, T.J.B. Collins, W.W. Dai, M.L. Hall, S. Jones, M.D. McKay Jr, et al., Coupling laser physics to radiation-hydrodynamics, *Comput. & Fluids* 201 (2020) 104478.
- [607] B.M. Haines, R.C. Shah, J.M. Smidt, B.J. Albright, T. Cardenas, M.R. Douglas, C. Forrest, V.Yu Glebov, M.A. Gunderson, C.E. Hamilton, et al., Observation of persistent species temperature separation in inertial confinement fusion mixtures, *Nat. Comm.* 11 (2020) 544.
- [608] A. Hillier, Self-similar solutions of asymmetric Rayleigh-Taylor mixing, *Phys. Fluids* 32 (2020) 015103.
- [609] X. Hu, H. Liang, H. Wang, Lattice boltzmann method simulations of the immiscible Rayleigh-Taylor instability with high reynolds numbers, *Acta Phys. Sin.* 69 (2020) 044701.
- [610] C.M. Huntington, K.S. Raman, S.R. Nagel, S.A. McLaren, T. Baumann, J.D. Bender, S.T. Prisbrey, L. Simmons, P. Wang, Y. Zhou, Split radiographic tracer technique to measure the full width of a high energy density mixing layer, *High Energy Dens. Phys.* 35 (2020) 100733.
- [611] S.S. Jain, A. Mani, P. Moin, A conservative diffuse-interface method for compressible two-phase flows, *J. Comput. Phys.* 418 (2020) 109606.
- [612] O. Kiprijanović, L. Ardaravičius, J. Gradauskas, Č. Šimkevičius, S. Kersulis, S. Ašmontas, Sn border instability, magnetic flux trapping and cumulative effect during pulsed sn switching of high quality YBaCuO thin films, *Supercond. Sci. Technol.* 33 (2020) 095013.
- [613] Y. Li, R. Samtaney, D. Bond, V. Wheatley, Richtmyer-Meshkov Instability of an imploding flow with a two-fluid plasma model, *Phys. Rev. Fluids* 5 (2020) 113701.

- [614] M. Li, J. Ding, Z. Zhai, T. Si, N. Liu, S. Huang, X. Luo, On divergent Richtmyer–Meshkov instability of a light/heavy interface, *J. Fluid Mech.* 901 (2020) A38.
- [615] Y. Li, C. Diddens, T. Segers, H. Wijshoff, M. Verluis, D. Lohse, Rayleigh–Taylor Instability by segregation in an evaporating multicomponent microdroplet, *J. Fluid Mech.* 899 (2020) A22.
- [616] Z. Li, L. Wang, J. Wu, W. Ye, Numerical study on the laser ablative Rayleigh–Taylor instability, *Acta Mech. Sin.* 36 (2020) 789.
- [617] Y. Liang, L. Liu, Z. Zhai, T. Si, C.-Y. Wen, Evolution of shock-accelerated heavy gas layer, *J. Fluid Mech.* 886 (2020) A7.
- [618] Y. Liang, Z. Zhai, X. Luo, C.-Y. Wen, Interfacial instability at a heavy/light interface induced by rarefaction waves, *J. Fluid Mech.* 885 (2020) A42.
- [619] S. Liu, J. Cao, C. Zhong, Multiscale kinetic inviscid flux extracted from a gas-kinetic scheme for simulating incompressible and compressible flows, *Phys. Rev. E* 102 (2020) 033310.
- [620] H.-C. Liu, Bi. Yu, H. Chen, B. Zhang, H. Xu, H. Liu, Contribution of viscosity to the circulation deposition in the Richtmyer–Meshkov instability, *J. Fluid Mech.* 895 (2020) A10.
- [621] S. Lugomer, Nano-wrinkles, compactons, and wrinkles associated with laser-induced Rayleigh–Taylor instability: I. bubble environment, *Laser Part. Beams* 38 (2020) 101.
- [622] T. Luo, J. Wang, C. Xie, M. Wan, S. Chen, Effects of compressibility and atwood number on the single-mode Rayleigh–Taylor instability, *Phys. Fluids* 32 (2020) 012110.
- [623] C. Matsuoka, Nonlinear dynamics of double-layer unstable interfaces with non-uniform velocity shear, *Phys. Fluids* 32 (2020) 102109.
- [624] C. Matsuoka, K. Nishihara, Nonlinear interaction between bulk point vortices and an unstable interface with nonuniform velocity shear such as Richtmyer–Meshkov instability, *Phys. Plasmas* 27 (2020) 052305.
- [625] C. Matsuoka, K. Nishihara, F. Cobos-Campos, Linear and nonlinear interactions between an interface and bulk vortices in Richtmyer–Meshkov instability, *Phys. Plasmas* 27 (2020) 112301.
- [626] M. Matys, K. Nishihara, M. Kecova, J. Psikal, G. Korn, S.V. Bulanov, Laser-driven generation of collimated quasi-monoenergetic proton beam using double-layer target with modulated interface, *High Energy Dens. Phys.* 36 (2020) 100844.
- [627] F. Nguyen, J.-P. Laval, B. Dubrulle, Characterizing most irregular small-scale structures in turbulence using local Hölder exponents, *Phys. Rev. E* 102 (2020) 063105.
- [628] C.D. Noble, J.M. Herzog, D.A. Rothamer, A.M. Ames, J. Oakley, R. Bonazza, Scalar power spectra and scalar structure function evolution in the Richtmyer–Meshkov instability upon reshock, *J. Fluids Eng.* 142 (2020) 121102.
- [629] S. Oughton, W.H. Matthaeus, Critical balance and the physics of magnetohydrodynamic turbulence, *Astrophys. J.* 897 (2020) 37.
- [630] Q. Peng, B. Bao, C. Yang, L. Zhang, Simulations of young type ia supernova remnants undergoing shock acceleration in a turbulent medium, *Astrophys. J.* 891 (2020) 75.
- [631] F.S. Pereira, F.F. Grinstein, D. Israel, Effect of the numerical discretization scheme in shock-driven turbulent mixing simulations, *Comput. & Fluids* 201 (2020) 104487.
- [632] P. Pfeiffer, Q. Zeng, B.H. Tan, C.-D. Ohl, Merging of soap bubbles and why surfactant matters, *Appl. Phys. Lett.* 116 (2020) 103702.
- [633] D.S. Praturi, S.S. Girimaji, Magnetic–internal–kinetic energy interactions in high-speed turbulent magnetohydrodynamic jets, *J. Fluids Eng.* 142 (2020) 101213.
- [634] R. Ramani, S. Shkoller, A multiscale model for Rayleigh–Taylor and Richtmyer–Meshkov instabilities, *J. Comput. Phys.* 405 (2020) 109177.
- [635] Y. Ruan, Y. Zhang, B. Tian, X. Zhang, Density-ratio-invariant mean-species profile of classical Rayleigh–Taylor mixing, *Phys. Rev. Fluids* 5 (2020) 054501.
- [636] Y.P.M. Sethuraman, K. Sinha, Modeling of thermodynamic fluctuations in canonical shock–turbulence interaction, *AAIA J.* 58 (2020) 3076.
- [637] Y.P.M. Sethuraman, K. Sinha, Effect of turbulent mach number on the thermodynamic fluctuations in canonical shock–turbulence interaction, *Comput. & Fluids* 197 (2020) 104354.
- [638] O. Soulard, J. Griffond, B-J Gréa, G. Viciconte, Permanence of large eddies in decaying variable-density homogeneous turbulence with small mach numbers, *Phys. Rev. Fluids* 5 (2020) 064613.
- [639] S.V. Starinskiy, A.A. Rodionov, Y.G. Shukhov, A.I. Safonov, E.A. Maximovskiy, V.S. Sulyaeva, A.V. Bulgakov, Formation of periodic superhydrophilic microstructures by infrared nanosecond laser processing of single-crystal silicon, *Appl. Surface Sci.* 512 (2020) 145753.
- [640] R. Sun, J. Ding, Z. Zhai, T. Si, X. Luo, Convergent Richtmyer–Meshkov instability of heavy gas layer with perturbed inner surface, *J. Fluid Mech.* 902 (2020) A3.
- [641] P. Sun, J. Ding, S. Huang, X. Luo, W. Cheng, Microscopic Richtmyer–Meshkov instability under strong shock, *Phys. Fluids* 32 (2020) 024109.
- [642] W. Sun, W.M. An, J.Y. Zhong, Two-dimensional numerical study of effect of magnetic field on laser-driven Kelvin-Helmholtz instability, *Acta Phys. Sin.* 69 (2020) 244701.
- [643] Y.B. Sun, C. Wang, Viscous Rayleigh–Taylor and Richtmyer–Meshkov instabilities in the presence of a horizontal magnetic field, *Phys. Rev. E* 101 (2020) 053110.
- [644] Y.B. Sun, C. Wang, A.R. Piriz, A unified model to study the effects of elasticity, viscosity, and magnetic fields on linear Richtmyer–Meshkov instability, *J. Appl. Phys.* 128 (2020) 125901.
- [645] Y.B. Sun, R.H. Zeng, J.J. Tao, Elastic Rayleigh–Taylor and Richtmyer–Meshkov instabilities in spherical geometry, *Phys. Fluids* 32 (2020) 124101.
- [646] J. Tang, F. Zhang, X. Luo, Z. Zhai, Effect of atwood number on convergent Richtmyer–Meshkov instability, *Acta Mech. Sinica* (2020) <http://dx.doi.org/10.1007/s10409-020-01015-5>.
- [647] M. Vadivukkarasan, Temporal instability characteristics of Rayleigh–Taylor and Kelvin–Helmholtz mechanisms of an inviscid cylindrical interface, *Mecanica* 56 (2021) 117.
- [648] A.L. Velikovich, A.J. Schmitt, C. Zulick, Y. Aglitskiy, M. Karasik, S.P. Obenschain, J.G. Wouchuk, F. Cobos Campos, Multi-mode hydrodynamic evolution of perturbations seeded by isolated surface defects, *Phys. Plasmas* 27 (2020) 102706.
- [649] L. Wang, W. Ye, Z. Chen, et al., Review of hydrodynamic instabilities in inertial confinement fusion implosions, *High Power Laser and Part. Beams* 33 (2021) 012001.
- [650] X. Wang, X. Hu, S. Wang, H. Pan, A simplified approximate analytical model for Rayleigh–Taylor instability in elastic-plastic solid and viscous fluid with thicknesses, *Chin. Phys. B* (2020) <http://dx.doi.org/10.1088/1674-1056/abcf44>.
- [651] Y. Wang, G. Dong, Interface evolutions and growth predictions of mixing zone on premixed flame interface during RM instability, *Chin. J. Theor. Appl. Mech.* 52 (2020) 1655.
- [652] M. Xiao, Y. Zhang, B. Tian, Unified prediction of reshocked Richtmyer–Meshkov mixing with K-L model, *Phys. Fluids* 32 (2020) 032107.
- [653] M. Xiao, Y. Zhang, B. Tian, Modeling of turbulent mixing with an improved K-L model, *Phys. Fluids* 32 (2020) 092104.
- [654] K. Xue, X. Shi, J. Zeng, B. Tian, P. Han, Ji. Li, L. Liu, B. Meng, X. Guo, C. Bai, Explosion-driven interfacial instabilities of granular media, *Phys. Fluids* 32 (2020) 084104.
- [655] B. Yan, Q. Li, X. Li, S. Huang, W. Wang, S. Fu, Numerical study of the slip line instabilities in shock-wavywall reflection, *Sci. China-Phys. Mech. Astron.* 50 (2020) 104709.
- [656] P. Yao, H. Cai, X. Yan, W. Zhang, B. Du, J. Tian, E. Zhang, X. Wang, S. Zhu, Kinetic study of transverse electron-scale interface instability in relativistic shear flows, *Matter Radiat. Extremes* 5 (2020) 054403.
- [657] H. Ye, H. Lai, D. Li, Ya. Gan, L. Lin, A. Xu, Knudsen number effects on two-dimensional Rayleigh–Taylor instability in compressible fluid: based on a discrete boltzmann method, *Entropy* 22 (2020) 500.
- [658] D.L. Youngs, B. Thornber, Early time modifications to the buoyancy-drag model for Richtmyer–Meshkov mixing, *J. Fluids Eng.* 142 (2020) 121107.
- [659] B. Yu, M. He, B. Zhang, H. Liu, Two-stage growth mode for lift-off mechanism in oblique shock-wave/jet interaction, *Phys. Fluids* 32 (2020) 116105.
- [660] R. Zanella, G. Tegze, R. Le Tellier, H. Henry, Two-and three-dimensional simulations of Rayleigh–Taylor instabilities using a coupled Cahn–Hilliard/Navier–Stokes model, *Phys. Fluids* 32 (2020) 124115.
- [661] R.H. Zeng, J.J. Tao, Y.B. Sun, Three-dimensional viscous Rayleigh–Taylor instability at the cylindrical interface, *Phys. Rev. E* 102 (2020) 023112.
- [662] Z. Zhai, X. Gu, S. Ting, Experimental study on bubble competition of shock-accelerated saw-tooth interface, *Acta Aerodynamica Sinica* 38 (2020) 339.
- [663] H. Zhang, R. Betti, R. Yan, H. Aluie, Nonlinear bubble competition of the multimode ablative Rayleigh–Taylor instability and applications to inertial confinement fusion, *Phys. Plasmas* 27 (2020) 122701.
- [664] Y. Zhang, Z. He, H. Xie, M. Xiao, B. Tian, Methodology for determining coefficients of turbulent mixing model, *J. Fluid Mech.* 905 (2020) A26.
- [665] Y. Zhang, W. Ni, Y. Ruan, H. Xie, Quantifying mixing of Rayleigh–Taylor turbulence, *Phys. Rev. Fluids* 5 (2020) 104501.
- [666] Y. Zhang, Y. Ruan, H. Xie, B. Tian, Mixed mass of classical Rayleigh–Taylor mixing at arbitrary density ratios, *Phys. Fluids* 32 (2020) 011702.
- [667] Z. Zhang, Q. Fu, H. Zhang, X. Yuan, K. Yu, Experimental and numerical investigation on interfacial mass transfer mechanism for rayleigh convection in Hele-Shaw cell, *Ind. Eng. Chem. Res.* 59 (2020) 10195.
- [668] Y. Zhao, M. Xia, Y. Cao, A study of bubble growth in the compressible Rayleigh–Taylor and Richtmyer–Meshkov instabilities, *AIP Adv.* 10 (2020) 015056.
- [669] Z. Zhao, P. Wang, N. Liu, X. Lu, Analytical model of nonlinear evolution of single-mode Rayleigh–Taylor instability in cylindrical geometry, *J. Fluid Mech.* 900 (2020) A24.
- [670] Z. Zhao, N. Liu, X. Lu, Kinetic energy and enstrophy transfer in compressible Rayleigh–Taylor turbulence, *J. Fluid Mech.* 904 (2020) A37.

- [671] H. Zheng, Q. Chen, B. Meng, J. Zeng, B. Tian, On the nonlinear growth of multiphase Richtmyer–Meshkov instability in dilute gas-particles flow, *Chin. Phys. Lett.* 37 (2020) 015201.
- [672] L. Zou, Q. Wu, X. Li, Research progress of general Richtmyer–Meshkov instability, *Sci. China-Phys. Mech. Astron.* 50 (2020) 104702.
- [673] Y. Zhou, M. Groom, B. Thornber, Dependence of enstrophy transport and mixed mass on dimensionality and initial conditions in the Richtmyer–Meshkov instability induced flows, *J. Fluids Eng.* 142 (2020) 121104.
- [674] Z. Zhou, J. Ding, Z. Zhai, W. Cheng, X. Luo, Mode coupling in converging Richtmyer–Meshkov instability of dual-mode interface, *Acta Mech. Sinica* 36 (2019) 356.
- [675] C. Zulick, Y. Aglitskiy, M. Karasik, A.J. Schmitt, A.L. Velikovich, S.P. Obenschain, Multimode hydrodynamic instability growth of preimposed isolated defects in ablative driven foils, *Phys. Rev. Lett.* 125 (2020) 055001.
- [676] C. Zulick, Y. Aglitskiy, M. Karasik, A.J. Schmitt, A.L. Velikovich, S.P. Obenschain, Isolated defect evolution in laser accelerated targets, *Phys. Plasmas* 27 (2020) 072706.
- [677] B. Bao, Q. Peng, C. Yang, L. Zhang, Evolutions of young type Ia supernova remnants with two initial density profiles in a turbulent medium, *Astrophys. J.* 909 (2021) 173.
- [678] J.D. Bender, O. Schilling, K.S. Raman, R.A. Managan, B.J. Olson, S.R. Copeland, C.L. Ellison, D.J. Erskine, C.M. Huntington, B.E. Morgan, S.R. Nagel, S.T. Prisbrey, B.S. Pudliner, P.A. Sterne, C.E. Wehrenberg, Y. Zhou, Simulation and flow physics of a shocked and reshocked high-energy-density mixing layer, *J. Fluid Mech.* 915 (2021) A84.
- [679] R.A.S. Frantz, G. Deskos, S. Laizet, J.H. Silvestrini, High-fidelity simulations of gravity currents using a high-order finite-difference spectral vanishing viscosity approach, *Comput. & Fluids* 221 (2021) 104902.
- [680] F. García-Rubio, R. Betti, J. Sanz, H. Aluie, Magnetic-field generation and its effect on ablative Rayleigh–Taylor instability in diffusive ablation fronts, *Phys. Plasmas* 28 (2021) 012103.
- [681] F.F. Grinstein, F.S. Pereira, Impact of numerical hydrodynamics in turbulent mixing transition simulations, *Phys. Fluids* 33 (2021) 035126.
- [682] F.F. Grinstein, J.A. Saenz, M. Germano, Coarse grained simulations of shock-driven turbulent material mixing, *Phys. Fluids* 33 (2021) 035131.
- [683] M. Groom, B. Thornber, Reynolds number dependence of turbulence induced by the Richtmyer–Meshkov instability using direct numerical simulations, *J. Fluid Mech.* 908 (2021) A31.
- [684] B.M. Haines, J.P. Sappee, P.A. Keiter, E.N. Loomis, T. Morrow, D.S. Montgomery, L. Kuettner, B.M. Patterson, T.E. Quintana, J. Field, et al., Constraining computational modeling of indirect drive double shell capsule implosions using experiments, *Phys. Plasmas* 28 (2021) 032709.
- [685] L. Heidt, M. Flraig, B. Thornber, The effect of initial amplitude and convergence ratio on instability development and deposited fluctuating kinetic energy in the single-mode Richtmyer–Meshkov instability in spherical implosions, *Comput. & Fluids* 218 (2021) 104842.
- [686] T. Kaman, A. Edwards, J. McGarigal, Performance analysis of the parallel CFD code for turbulent mixing simulations, *J. Comput. Sci. Edu.* 12 (2021) 49.
- [687] Y. Liang, L. Liu, Z. Zhai, T. Si, X. Luo, Universal perturbation growth of Richtmyer–Meshkov instability for minimum-surface featured interface induced by weak shock waves, *Phys. Fluids* 33 (2021) 032110.
- [688] W.H. Matthaeus, Turbulence in space plasmas: who needs it?, *Phys. Plasmas* 28 (2021) 032306.
- [689] S. Pellone, C.A. Di Stefano, A.M. Rasmus, C.C. Kuranz, E. Johnsen, Vortex-sheet modeling of hydrodynamic instabilities produced by an oblique shock interacting with a perturbed interface in the hed regime, *Phys. Plasmas* 28 (2021) 022303.
- [690] N. Peng, Y. Yang, J. Wu, Z. Xiao, Mechanism and modelling of the secondary baroclinic vorticity in the Richtmyer–Meshkov instability, *J. Fluid Mech.* 911 (2021) A56.
- [691] F.S. Pereira, F.F. Grinstein, D.M. Israel, R. Rauenzahn, Molecular viscosity and diffusivity effects in transitional and shock-driven mixing flows, *Phys. Rev. E* 103 (2021) 013106.
- [692] S.A. Piriz, A.R. Piriz, N.A. Tahir, S. Richter, M. Bestehorn, Rayleigh–Taylor Instability in elastic-plastic solid slabs bounded by a rigid wall, *Phys. Rev. E* 103 (2021) 023105.
- [693] S.I. Podvalny, E.M. Vasiljev, Intensification of heat transfer in chaotic modes, in: IOP Conf. Ser., 1035, IOP Publishing, 2021, p. 012046.
- [694] B. Popescu Braileanu, V.S. Lukin, E. Khomenko, Á. de Vicente, Two-fluid simulations of Rayleigh–Taylor instability in a magnetized solar prominence thread. I. effects of prominence magnetization and mass loading, *Astron. Astrophys.* 646 (2021) A93.
- [695] J. Pulido, R.D. da Silva, D. Livescu, B. Hamann, Multiresolution classification of turbulence features in image data through machine learning, *Comput. & Fluids* 214 (2021) 104770.
- [696] N. Sabet, H. Hassanzadeh, A. De Wit, J. Abedi, Scalings of Rayleigh–Taylor instability at large viscosity contrasts in porous media, *Phys. Rev. Lett.* 126 (2021) 094501.
- [697] J.A. Saenz, D. Aslangil, D. Livescu, Filtering, averaging, and scale dependency in homogeneous variable density turbulence, *Phys. Fluids* 33 (2021) 025115.
- [698] Y. Song, P. Wang, L. Wang, Numerical investigations of Rayleigh–Taylor instability with a density gradient layer, *Comput. & Fluids* 220 (2021) 104869.
- [699] T.J. Vogler, M.C. Hudspeth, Tamped Richtmyer–Meshkov instability experiments to probe high-pressure material strength, *J. Dynamic Behavior Mater.* (2021) <http://dx.doi.org/10.1007/s40870-020-00288-y>.
- [700] Z. Wang, K. Xue, P. Han, Bell–Plesset Effects on Rayleigh–Taylor instability at cylindrically divergent interfaces between viscous fluids, *Phys. Fluids* 33 (2021) 034118.
- [701] J. Wu, H. Liu, Z. Xiao, Refined modelling of the single-mode cylindrical Richtmyer–Meshkov instability, *J. Fluid Mech.* 908 (2021) A9.
- [702] M. Xiao, Y. Zhang, B. Tian, A K-L model with improved realizability for turbulent mixing, *Phys. Fluids* 33 (2021) 022104.
- [703] L. Xu, H. Shen, J. Wei, Mathematical foundations of the three-dimensional neutron hydrodynamics coupled transport equations, *Ann. Nucl. Energy* 156 (2021) 108198.
- [704] D.A. Yoder, P.D. Orkwis, On the use of optimization techniques for turbulence model calibration, *Comput. & Fluids* 214 (2021) 104752.
- [705] K.A. Yuana, B. Jalaali, E.P. Budiana, Pranowo, A. Widayaparaga, Indarto, Deendarlianto, Lattice Boltzmann simulation of the Rayleigh–Taylor instability (RTI) during the mixing of the immiscible fluids, *Eur. J. Mech. B Fluids* 85 (2021) 276.
- [706] T. Zhu, Z. Jia, X. Wang, L. Zhang, Z. Yang, R. Lin, J. Liu, Experimental and simulation study of forced convection in vertical eccentric annular space, *Int. J. Therm. Sci.* 161 (2021) 106735.
- [707] A. McDaniel, A. Mahalov, Coupling of paraxial and white-noise approximations of the Helmholtz equation in randomly layered media, *Physica D* 409 (2020) 132491.
- [708] B. Cheng, J. Glimm, D.H. Sharp, The  $\alpha$ s and  $\theta$ s in Rayleigh–Taylor and Richtmyer–Meshkov instabilities, *Physica D* 404 (2020) 132356.
- [709] J. Glimm, B. Cheng, D.H. Sharp, T. Kaman, A crisis for the verification and validation of turbulence simulations, *Physica D* 404 (2020) 132346.
- [710] K. Narayanan, R. Samtaney, On the role of thermal fluctuations in Rayleigh–Taylor mixing, *Physica D* 402 (2020) 132241.
- [711] C.H. Chang, R.W. Douglass, Numerical simulations of onset and growth of Rayleigh–Taylor instability involving solids in converging geometry, *Physica D* 411 (2020) 132607.
- [712] J.T. Horne, A.G.W. Lawrie, Aspect-ratio-constrained Rayleigh–Taylor instability, *Physica D* 406 (2020) 132442.
- [713] B.E. Morgan, W.J. Black, Parametric investigation of the transition to turbulence in Rayleigh–Taylor mixing, *Physica D* 402 (2020) 132223.
- [714] N.O. Braun, R.A. Gore, A passive model for the evolution of subgrid-scale instabilities in turbulent flow regimes, *Physica D* 404 (2020) 132373.
- [715] F.F. Grinstein, Coarse grained simulation of convectively driven turbulent mixing, transition, and turbulence decay, *Physica D* 407 (2020) 132419.
- [716] X. Bian, H. Aluie, D. Zhao, H. Zhang, D. Livescu, Revisiting the late-time growth of single-mode Rayleigh–Taylor instability and the role of vorticity, *Physica D* 403 (2020) 132250.
- [717] I.W. Kokkinakis, D. Drikakis, D.L. Youngs, Vortex morphology in Richtmyer–Meshkov-induced turbulent mixing, *Physica D* 407 (2020) 132459.
- [718] S. Kurien, F.W. Doss, D. Livescu, K. Flippo, Extracting a mixing parameter from 2d radiographic imaging of variable-density turbulent flow, *Physica D* 405 (2020) 132354.
- [719] O. Soulard, F. Guillois, J. Griffond, V. Sabelnikov, S. Simoëns, A two-scale langevin pdf model for Richtmyer–Meshkov turbulence with a small atwood number, *Physica D* 403 (2020) 132276.
- [720] W. Guo, Q. Zhang, Universality and scaling laws among fingers at Rayleigh–Taylor and Richtmyer–Meshkov unstable interfaces in different dimensions, *Physica D* 403 (2020) 132304.
- [721] C.D. Noble, J.M. Herzog, A.M. Ames, J. Oakley, D.A. Rothamer, R. Bonazza, High speed PLIF study of the instability upon Richtmyer–Meshkov re-shock, *Physica D* 410 (2020) 132519.
- [722] L.G. Margolin, C.S. Plesko, J.M. Reisner, A finite scale model for shock structure, *Physica D* 403 (2020) 132308.
- [723] O. Schilling, A buoyancy–shear–drag-based turbulence model for Rayleigh–Taylor, reshocked Richtmyer–Meshkov, and Kelvin–Helmholtz mixing, *Physica D* 402 (2020) 132238.
- [724] K.O. Mikaelian, B.J. Olson, On modeling Richtmyer–Meshkov turbulent mixing widths, *Physica D* 402 (2020) 132243.
- [725] D. Aslangil, D. Livescu, A. Banerjee, Variable-density buoyancy-driven turbulence with asymmetric initial density distribution, *Physica D* 406 (2020) 132444.
- [726] M.J. Wadas, E. Johnsen, Interactions of two bubbles along a gaseous interface undergoing the Richtmyer–Meshkov instability in two dimensions, *Physica D* 409 (2020) 132489.
- [727] T.-W. Lee, Lagrangian transport equations and an iterative solution method for turbulent jet flows, *Physica D* 403 (2020) 132333.

- [728] M. Groom, B. Thornber, The influence of initial perturbation power spectra on the growth of a turbulent mixing layer induced by Richtmyer-Meshkov instability, *Physica D* 407 (2020) 132463.
- [729] W.T. Buttler, R.K. Schulze, J.J. Charonko, J.C. Cooley, J.E. Hammerberg, J.D. Schwarzkopf, D.G. Sheppard, J.J. Goett III, M. Grover, B.M. La Lone, S.K. Lamoreaux, R. Manzanares, J.I. Martinez, J.D. Regele, M.M. Schauer, D.W. Schmidt, G.D. Stevens, W.D. Turley, R.J. Valencia, Understanding the transport and break up of reactive ejecta, *Physica D* 415 (2021) 132787.
- [730] M.G. Probyn, R.J.R. Williams, B. Thornber, D. Drikakis, D.L. Youngs, 2d single-mode Richtmyer-Meshkov instability, *Physica D* 418 (2021) 132827.
- [731] D. Livescu, T. Wei, P.T. Brady, Rayleigh-Taylor Instability with gravity reversal, *Physica D* 417 (2021) 132832.
- [732] S. Dalziel, V. Mouet, Rayleigh-Taylor Instability between unequally stratified layers, *Physica D* (2021) <http://dx.doi.org/10.1016/j.physd.2021.132907>.